Mechanistic selection and growth of twinned bicrystalline primary Si in near eutectic Al-Si alloys

by

Choonho Jung

A dissertation submitted to the graduate faculty

in partial fulfillment of the requirements for the degree of

DOCTOR OF PHILOSOPHY

Major: Materials Science & Engineering

Program of Study Committee:
Ralph E. Napolitano, Major Professor
R. William McCallum
Iver E. Anderson
Scott Chumbley
Frank Peters

Iowa State University

Ames, Iowa

2006

Graduate College
Iowa State University

This is to certify that the doctoral dissertation of

Choonho Jung

has met the dissertation requirements of Iowa State University

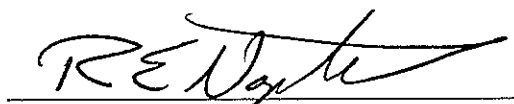

Major Professor

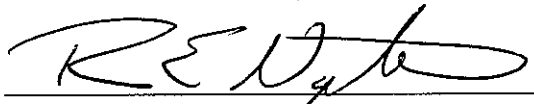

For the Major Program

For my daughter, Hailey, who is still in mom's tummy

TABLE OF CONTENTS

LIST OF FIGURES

ACKNOWLEDGMENTS

I would like to express my appreciation to Dr. Ralph Napolitano, my major professor, for being an excellent advisor and giving me the opportunity to do what I really want to do. I would like to thank my committee members, R. William McCallum, Iver Anderson, Scott Chumbley, and Frank Peters, for their insight and opinions. I would also like to thank Rohit Trivedi, the former committee member, for his sincere advice. Additionally, I would like to thank Emrah Simsek, Alfred Kracher, and Fran Laabs for their willing assistance. I wish to express my gratitude to the former and current solidification group members for sharing their knowledge. My appreciation is also extended to Melis Serefoglu, Amie Yang, Jeongyun Choi, Jongho Shin, and Dongwon Shin, for their encouragement and valuable comments. Special thanks need to be extended to my family, especially to my mother-in-law. Without her endless love, I could not have finished my study. I would like to memorize two persons: Dr. Kim, who had passed away before my study in the U.S and my mother, who has passed away in Dec. 2003. She deserves to be happy with me in heaven. Finally, I would like to thank my wonderful wife, Seyoun Chu with a little girl in her tummy. It is no exaggeration to say that her sacrifice and love has completed my accomplishment.

The work presented in this dissertation was performed under the Solidification Science focus area within the Ames Laboratory Materials and Engineering Physics Program and was made possible by support from the Division of Materials Science, Basic Energy Science, Office of Science, U.S. Department of Energy, under Contract No. W7405-Eng-82. The United States government has assigned the DOE Report number IS-T 2475 to this thesis.

ABSTRACT

Morphological evolution and selection of angular primary silicon is investigated in near-eutectic Al-Si alloys. Angular silicon arrays are grown directionally in a Bridgman furnace at velocities in the regime of 10^{-3} m/sec and with a temperature gradient of 7.5×10^3 K/m. Under these conditions, the primary Si phase grows as an array of twinned bicrystalline dendrites, where the twinning gives rise to a characteristic 8-pointed star-shaped primary morphology. While this primary Si remains largely faceted at the growth front, a complex structure of coherent symmetric twin boundaries enables various adjustment mechanisms which operate to optimize the characteristic spacings within the primary array. In the work presented here, this primary silicon growth morphology is examined in detail. In particular, this thesis describes the investigation of

- morphological selection of the twinned bicrystalline primary starshape morphology;
- primary array behavior, including the lateral propagation of the starshape grains and the associated evolution of a strong <100> texture;
- the detailed structure of the 8-pointed star-shaped primary morphology, including the twin boundary configuration within the central core;
- the mechanisms of lateral propagation and spacing adjustment during array evolution; and
- the thermosolutal conditions (i.e. operating state) at the primary growth front, including composition and phase fraction in the vicinity of the primary tip.

Experimental methods include directional solidification, high-resolution serial milling, electron-probe microanalysis, backscattered electron diffraction, and high resolution transmission electron microscopy techniques. The following key observations are made here.

- It is found that slightly hypereutectic Al-Si alloys, directionally solidified at rate below 1μm/s, exhibit rapid emergence of a strong <100> texture, associated with the selection and lateral propagation of the star-shaped growth mode. The dominant silicon morphology in this array is an 8-pointed star-shape "dendrite" with sideplates at alternating angles of 37° and 53°. Large domains of identically oriented silicon dendrites

evolve, suggesting that the entire twinned domain originates from one twin-pair of silicon grains.

- Analysis of the detailed structure within the twinned core reveals that {210}/{310} coherent twin boundaries comprise the core structure of the 8-pointed star-shape. These crystal defects, with a high migration tendency, provide the core with an essential mechanism for the faceted interfaces to grow. Thus, the twin structure plays a crucial role in the morphological/ mechanistic selection of the primary silicon morphology in these Al-Si alloys at low grow rates.
- Examination of the overall array structure and dynamics with regard to several mechanisms of branching and spacing adjustment shows that primary tip splitting/joining, tertiary branching, and related twin boundary migration in the core are the main mechanisms for array evolution. Although the Al phase has no preferred orientation with respect to the axial growth direction, its grain structure seems to be influenced by the side branching of silicon, resulting in the polycrystalline grains with no more than one grain between two silicon secondary plates.
- Primary and inter-plate spacing have been measured and the result suggests that overall growth is a diffusively coupled "cellular" growth. In order to model the overall low-velocity growth of Al-Si alloys, which have a kinetically limited twinned Si array, we propose a "mesoscopic" envelope and some relevant experiments such as corner growth experiments and directional growth at hypoeutectic compositions for the quantification of supersaturaton and tip temperature, combining with phase fraction measurements near the primary tip.

Through the observations and analyses highlighted above, the growth of the faceted silicon bycrystalline structure in near eutectic Al-Si has been comprehensively understood. Phase fraction, composition, interface structure, and spacing in the interdendritic region behind the growing tip suggest that overall microstructure evolution occurred by a very tiny decoupled primary tip, followed by an Al "halo-like" structure surrounding the silicon star-shape. Overall microstructure evolution proceeds with the assistance of crystal defects (i.e. twinning in the silicon dendrite core) and this mechanistic self-optimization by twinning allows the strongly anisotropic faceted crystal-melt interfaces to respond to local fluctuations, selecting the distinct star-shaped silicon morphology which best satisfy long-range diffusion fields.

CHAPTER 1

General Introduction

Controlling microstructure is a key to achieving desired properties during materials processing, and understanding microstructural selection is critical for intelligent materials design. Here, the role of the complex thermodynamic and kinetic factors must be understood for prediction and control of microstructure and associated properties, where multi-step processes are often required for engineered materials, often involving several thermal, mechanical, and/or chemical stages. Among these, it is clear that the phase transition from liquid to solid is one of the most important processes[1], where changes in solidification conditions give rise to dramatic differences in microstructure. Hence, scientific advancements are clearly linked to potential capabilities through the fundamentals of solidification and the selection of solidification microstructures observed in all places, from daily life to industry.

Solidification science has played a very important role in both academic accomplishments of material science and practical industrial products[1]. For instance, dendritic microstructures are commonly seen in solidification of metals [2] or crystallization in supersaturated solutions[3]. In such cases, a quantitative understanding of dendritic evolution is required to optimize the quality of the final product, as observed in a wide rage of solidification processes, from casting to welding. In order to describe and understand the microstructure of final products at various length scales from atomic structure to casting defects, fundamental knowledge of microstructural evolution and morphological selection, associated with the intrinsic behavior of solid-liquid interfaces must be established. Most of all, the structure and behavior of crystal-melt interfaces must be examined based on both atomic structure and thermodynamic properties. In addition, basic parameters that govern the behavior of interfaces allow one to describe interfacial dynamics.

In this study, critical topics for Si and Al-Si alloys, where Si is a well known faceted non-metallic material, will be studied. Accordingly, the investigation of faceted primary Si using directional solidification will provide a fundamental understanding of kinetically limited faceted primary growth in alloys. In the Chapter 2, some important fundamentals of crystal-melt interfaces are summarized, and an overview of various morphologies that emerge during directional solidification is given. Chapter 3 will talk about motivation, objectives, and significance of this primary silicon growth in near eutectic Al-Si alloys. The scientific basis for this study and the technical approach used to accomplish these goals are summarized in Chapter 4. In

the chapters that follow, we investigate further the growth morphology of the low-rate Al-Si eutectics. First, we examine the selection of the "star-shaped" morphology and the evolution of the preferred texture in Chapter 5. Second, we investigate the detailed morphology of the star-shaped silicon overall growth structures and core structure, with respect to the crystallography of solid silicon and its defects in Chapter 6. Array structure and branching mechanisms of this distinct faceted morphology, associated with spacing adjustment will be discussed in Chapter 7. A careful examination in the vicinity of the growing faceted tip region will be discussed in Chapter 8 in order to describe the overall growth model of faceted primary silicon phase with Al matrix. Finally, the dissertation will be completed summarizing all efforts to understand kinetically limited faceted growth in this study, and some potentially useful experimental and theoretical investigations are proposed for further research.

CHAPTER 2
Technical Background

It is well known that crystal-melt interfaces and their crystallographic characteristics play an important role in microstructural evolution during solidification. Detailed knowledge of the microstructure, dynamics, and thermodynamics of the crystal-melt interface is central to the full understanding of such important phenomena as near-equilibrium crystal growth and homogeneous nucleation as well non-equilibrium solidification. In this chapter, several critical issues regarding the fundamental behavior of solid-liquid interfaces are discussed. In addition, the particular issues of microstructure evolution in Al-Si alloys are addressed.

2.1 Structure of crystal-melt interfaces

Until the middle of the twentieth century, the study of crystal-melt interfaces had faced a difficulty due to experimental limitations and the absence of a model for interfacial structure. Since Turnbull's homogeneous nucleation experiments[4], many scientists have proposed the structure of crystal-melt interfaces, taking the atomistic structure of the liquid into account. More recently, atomistic simulations have become a valuable tool to examine interface structure and dynamics. In the following sections, we examine recent theoretical and experimental approaches and summarize our current state of understanding.

2.1.1 Atomic structure near a crystal-melt interface

Atoms at crystal-melt interfaces are in an environment that is markedly different from the environment of atoms in the bulk of the solid. There might be fewer nearest neighbor atoms, and these neighbors become more anisotropic than in the bulk. Thus, we need to be able to quantify the excess properties of crystal-melt interfaces. Before the thermodynamic and kinetic approach to crystal-melt interfaces, atomic structure of both bulk phases as well as interfaces must be described.

Solid (crystalline structure) vs. liquid structure

Before examining the crystal-melt interfaces itself, it is prudent here to briefly discuss the structure of the bulk phases which are divided by such an interface. Crystal structure is well established despite uncertainty of liquid structure. A solid with a regular atomic arrangement has a site for each atom, determined by its geometric relationship with the crystal lattice. Precisely

speaking, the site is not fixed but the mean position of the atom with thermal vibration. It should be mentioned that the crystalline state includes crystal defects such as vacancies, dislocations, and grain boundaries, etc.

It is much more difficult to describe the structure of liquid. In the earliest models of crystal-melt interfaces[5], the specific structure of liquid is ignored by the assumption of a considerable density deficit that makes a clear dividing interface. Most works on the structure of liquids come from Bernal's pioneering "ball-bearings" experiments[6]. He suggests that tetrahedral coordination is another characteristic of a liquid, maximizing short-range density through the dense random packing. Moreover, he reported clusters of five-fold symmetry as a key ingredient in the structure of liquid.

This five-fold symmetry causes the lack of translational symmetry and, therefore, long-range order disappears, in contrast to the crystalline state. Owing to the short range order but lack of long rage order, the diffraction halo observed for liquids is a well known experimental result. The detailed structure of a liquid might come from X-ray diffraction patterns in terms of various radial distribution functions that describe the atomistic structure. The simplest distribution function is the so-called pair correlation function[7], g(r). This pair correlation function can be theoretically computed and compared with the structure factor from X-ray diffraction experiments to investigate the atomic structure of liquid phase. Let n(r) be the average number of particle centers found in the shell defined by two spheres of radii r and r+Δr from the center of a test particle. The pair correlation function, g(r) is then defined as

$$g(r) = \frac{1}{\rho} \frac{n(r)}{4\pi r^2 \Delta r} \tag{1}$$

where ρ is the density of the material and $4\pi r^2\Delta r$ is the volume between two particles of radii r and r+Δr, centered at the reference particle. Thus, it reflects atom whose center lies at a radius, r, from the reference point.

$$\lim_{r\to\infty} g(r) = 1 \tag{2}$$

This *g(r)* function tells us the probability of finding two atoms a distance r apart, the next nearest neighbors are likewise ordered around the first group of r_0. At larger distances, however, there is no correlation with respect to the reference atom. Thus, a characteristic of the liquid state is that clear order can extend over only a few atomic distances. As seen in Fig.2-1(a), the peaks in the *g(r)* wave for a liquid show clear short range ordering in liquid. Because, even in liquid state, the atoms are very restricted in their motion and positioning with respect to one another, a reference

atom or molecule has only slightly fewer nearest-neighbors than in a close-packed crystal, typically nine to eleven instead of twelve.

Diffraction techniques have historically been the primary means for probing and pair correlations in liquids as well as in solids. In X-ray diffraction, a resultant wave scattered by all the atoms of a crystal unit cell is called the structure factor, because it describes how the atom arrangement, given by the position vector *uvw* for each atom, affects the scattered beam. A quantitative object of the measurements, therefore, may be the structure factor *S(k)*. For instance, the structure factor of a monatomic system is defined by[8]

$$S(k) = 1 + \frac{4\pi\rho}{k}\int_0^\infty (g(r)-1) r \sin(kr) dr \qquad (3)$$

where ρ is the density of the material, and k is the scattering wave vector modulus, expressed by

$$k = 4\pi / \lambda \sin(2\theta).$$

S(k) contains information on the radial distribution function *g(r)* defined above. Using the simple Fourier transformation technique, Eq.3 can be inverted to obtain an experimental determination of *g(r)*. In Fig.2-1(b), the most recent results by neutron diffraction techniques about structure factors and radial distribution functions for liquid Si are shown[9].

In order to resolve a crystal-melt interface in terms of order and to interpret simulation results, various order parameters have been applied as local probes of structure.[10, 11, 12, 13, 14] Such order parameters are essential and useful to decide whether a particle belongings to the crystal or to the melt, particular in metallic systems where interfaces are general rough and fluctuations continually obscure the interface location. For examples, Briels and Tepper[13] introduced a simple order parameter, Ψ, to discriminate between the crystal and liquid phases,

$$\Psi = \sqrt{\frac{\langle X^2 \rangle - \langle X \rangle^2}{\langle X \rangle^2}}. \qquad (4)$$

Here, the function of X(r) takes the same value for every vector r pointing from a central particle to one of its nearest neighbors and the average is taken over all neighbors residing within some cutoff radius. The distributions of the values of Ψ during a simulation of a pure crystal and a pure liquid are plotted in Fig.2-2. It is seen that by calling crystal particles those particles for which Ψ <0.5(solid line) and liquid particles for which Ψ >0.5(dashed line).

Recently, Hoyt et al. proposed a parameter to identify the position of the crystal-melt interface in simulated(MD) systems by labeling an atom as belonging to either the liquid or crystal[15],

$$\phi = \frac{1}{12}\sum_{i}\left|\vec{r}_i - \vec{r}_{fcc}\right|^2 . \tag{5}$$

where the sum is taken over the 12 nearest neighbors about a central atom. One can compute the distance the neighbor makes from the ideal fcc positions of the crystal in the given orientation for any of the 12 nearest neighbors of a given atom. As the solid-liquid interfaces are traversed, the interface position changes very abruptly, indicating relaxation over interface width as shown in Fig. 2-3.

On the other hand, Davidchack and Laird[13] introduced an orientational order parameter to determine the origin of the expansion of the lattice plane spacing in their MD simulations of face-centered cubic (100) and (111) crystal-melt interface using hard spheres model as shown in Fig.2-4. It is defined as

$$q_n(z) = \left\langle \frac{1}{N_z}\sum_{i,j,k}\cos\{n\theta_{xy}(i,j,k)\}\right\rangle, \tag{6}$$

where n is an integer, i, j, and k are nearest neighbor atoms,

$$\theta_{xy}(i,j,k)$$

is the bond angle formed by i, j, and k projected on the x, y plane, and N_z is the total number of atoms taken in the sum.

As seen in above examples, the order parameters at crystal-melt interfaces have been used to distinguish if atom belongs to liquid or solid in MD simulations. In addition to a purpose of a useful parameter for simulations, they can be used to examine intrinsic characteristics of interface such as a width of interface or a structure of interface[16, 22, 23].

Relaxation near the interface

Turnbull's significant experiments [17] for undercooling at the crystal-melt interface provided the proof of existence of an effective barrier against crystal nucleation. Though the density and bonding of solid and liquid had been known to be very similar, these experiments proposed that the liquid structure is fundamentally different from that of the crystal and ordering of liquid atoms occurs near the interfaces, resulting in an entropy decrease. This argument, however, did not produce any specific liquid structure model. Frank [18] proposed a polytetrahedral structure for a simple monatomic liquid with short range order and Spaepen developed a model for structure of crystal-melt interfaces[19] based on Burnal's dense random packing[6].

Physical modeling[19,20], analytic studies, and computer simulation[21,22] of the crystal-melt interfaces in simple systems (hard sphere, Lennard-Jones, and etc.) produced similar atomic density profiles, proposing a relaxation near crystal-melt interfaces. This relaxation from crystalline to liquid can be observed in several parameters, such as density, diffusion coefficient or pressure etc. Davidchack and Laird performed MD simulations of the hard sphere crystal-melt interface[23]. Their results, showing two major parameters, are given in the Fig.2-5. The average of atomic density is very similar in both solid and liquid but a decaying wave is seen from solid to liquid, revealing an interface thickness on the order of a few interatomic distances with bonding and coordination showing only small variation from solid to liquid. This change in order becomes a key factor in interfacial behavior. Indeed, many properties of crystal-melt interfaces can be described in terms of the change in configurational entropy, as will be discussed in the next section.

2.1.2 Thermodynamic treatments of S-L interfaces

Atoms at crystal-melt interfaces are in an environment that is markedly different from the environment of atoms in the bulk of the solid as discussed in the previous sections. As a result, the ordering decay of various parameters may occur at the interfaces from the solid to liquid due to the broken bonding and more configurational entropy. Accordingly, the interfacial energy cannot be isotropic because the broken bonds strength depends on the orientation of the crystal and we need to be able to quantify the excess properties of interfaces. In this subsection, several thermodynamic and kinetic approaches to crystal-melt interfaces will be summarized and discussed based on anisotropic interfacial free energy and broken bond model. In the following section, the theoretical prediction and experiment of critical parameters of interfacial properties are discussed.

Enthalpic/entropic contributions

In order to make sure the technical terms such as surface, interface and surface tension or energy, let us briefly define these terms. While interface is a general term used for boundaries of two different phases, surface is the term normally for solid-gas and liquid-gas boundaries. The isotropic surface tension, σ, can be defined as an excess surface stress per unit surface area. It is appropriate when referring to liquids, because liquids cannot support shear stresses and atoms in the liquid can diffuse fast enough to accommodate any change in the surfaces area. The surface energy, γ, is defined as the energy of creation of a new equilibrium surface of unit area by dividing a crystal into two separate parts.

As mentioned before, since the atomic structure of the interfacial layers is different from that found in either bulk phase, the enthalpy and entropy in the solid-liquid interface may be different from those of bulk state as well. Consider a large homogeneous solid that contains N atoms and is surrounded by plane surfaces. Note that interfaces are assumed to be between solid and gas phase. The energy and entropy of the solid (per atom) are denoted by E_s and S_s. The specific surface energy, E_I (per unit area), is defined by the relation

$$E = NE_S + AE_I, \tag{7}$$

where E and A are the total energy and surface area of the solid, respectively. Thus AE_I is the excess of the total energy E that the solid has over the value NE_S, which is the value it would have if the surface were in the same thermodynamic state as the homogeneous interior.

To create a surface we have to do work on the system that involves breaking bonds and removing neighboring atoms. At constant T and P, the reversible surface work dW required to increase the surface area A by an amount dA, in a one –component system, is given by

$$dW_{I(T,P)} = \gamma dA, \tag{8}$$

where γ is called the surface energy and its units are J/mm^2. Thus, with $G=G(T, P, A)$, the differential total free energy of a one component system with the inclusion of the increase of free energy with increasing surface can be written as

$$dG = -SdT + VdP + \gamma dA. \tag{9}$$

We note that the crystal-melt interfacial energy consists of an enthalpy contribution due to bond energies and an entropy contribution due to a specific structure of the interface[24, 25]. Based on these enthalpy and entropy contributions to the interface structure, following two treatments are basic interface models.

Gibbs dividing interface

The thermodynamic treatment of interfaces was first introduced by Gibbs based on the surface tension for isotropic systems. Gibbs[26] has pointed out that a simple phenomenological treatment of the complex interface can be given if the transition layer is replaced by a hypothetical geometrical interface which he called a dividing surface. In his model, the dividing surface has no thickness and only gives a geometrical separation of the two homogeneous phases.

Now, we derive the change in the surface internal energy with a system of two isotropic phases, solid and liquid with multiple components to define the surface tension. The total internal energy is given by

$$dU = TdS - pdV + \sum \mu_i dn_i \tag{10}$$

The internal energy for each solid and liquid phase separately is

$$dU^S = TdS^S - pdV^S + \sum \mu_i dn_i^S \tag{11}$$

$$dU^L = TdS^L - pdV^L + \sum \mu_i dn_i^L \tag{12}$$

where the superscripts S and L refer to the solid and liquid, respectively. Since the Gibbs dividing surface is only a geometrical surface with no thickness and thus has no volume, combination of Eqs.10, 11, and 12 yields

$$dU^I = dU - dU^S - dU^L, \tag{13}$$

therefore,

$$dU^I = TdS^I + \sum \mu_i dn_i^I . \tag{14}$$

The exact position of the geometrical surface can be changed. When the location of the geometrical surface is changed while the form of a system is left unaltered, the internal energy, entropy, and excess moles of the interface vary. For systems where the thickness of the real physical interface is much smaller than the curvature of the interface, Gibbs showed that the dividing surface could be positioned such that the contribution from the curvature of the interface is negligible and an infinitesimal change in the surface internal energy is

$$dU^I = TdS^I + \sigma dA + \sum \mu_i dn_i^I . \tag{15}$$

Assuming the surface to have such a position, only the term related to a change in the interfacial area needs to be considered and the surface tension, σ, is

$$\sigma = \left(\frac{\partial U}{\partial A} \right)_{S,V,n_i} \tag{16}$$

This is the definition of the surface tension according to the Gibbs surface model. According to this definition, the surface tension is related to an interface, which behaves mechanically as a membrane stretched uniformly and isotropically by a force which is the same at all points and in all directions. The importance, here, is the formation of a surface always leads to a positive Gibbs free energy contribution. It should be also noted that the volumes of both phases involved are defined by the Gibbs dividing surface that is located at the position which makes the contribution from the curvature negligible.

Gibbs adsorption theory

Gibbs was the first to show that there is a thermodynamic relationship between the work required to reversibly create unit are of new surface, γ, and the number of atoms adsorbed per unit area. The totally differentiated internal energy of the surface is

$$dU^I = TdS^I + S^I dT + \sum \mu_i dn_i^I + \sum n_i^I d\mu_i + \sigma dA + Ad\sigma . \quad (17)$$

Comparison with modified Eq.17 with surface tension yields

$$0 = SdT + \sum n_i^I d\mu_i + Ad\sigma \quad (18)$$

or in per unit area

$$d\gamma = -S^i dT - \sum_{i=1}^{n} \Gamma_i d\mu_i , \quad (19)$$

which is the Gibbs adsorption equation. For a two-component system at constant temperature, Eq.19 reduces to

$$d\gamma = -\Gamma_A d\mu_A - \Gamma_B d\mu_B . \quad (20)$$

Combining the Gibbs-Duhem equation give rise to

$$-(d\gamma / d\mu_B)_T = [\Gamma_B - (X_B / X_A)]\Gamma_A , \quad (21)$$

where the " Gibbs adsorption coefficient " is

$$\Gamma_i = \frac{n_i^I}{A}$$

and it is the number of moles of species i absorbed at unit surface area. Eq.21 is a well-known relationship for a two-component system, and it applies to any case of equilibrium adsorption at constant temperature and overall composition. Each phase is assumed to be homogeneous right up to this dividing interface so that thermodynamics of homogeneous phases can be applied to each phase.

Spaepen's model

Spaepen proposed a model for the crystal-interface based on the dense random packing of hard spheres developed by Bernal and coworkers[6, 27]. He considered the specific case of the interface between a close packed crystal plane and a dense random packed melt phase. Using the following rules,

- form tetrahedral holes preferentially,
- disallow all octahedral holes and

- maximize the density.

He could deposit three layers of atoms on the crystal and showed that density of atom centers as a function of distance perpendicular to the interface decayed over three atomic layers. In addition, Spaepen derived crystal-melt interfacial energy, of entropic origin, for his model. The Helmholtz free energy at equilibrium (i.e. at T_m) is given by

$$\Delta F = \left(U_C - T_M S_C\right) - \left(U_L - T_M S_L\right) = 0 \ . \tag{22}$$

Therefore, the entropy of fusion is equal to

$$\Delta S = S_L - S_C = \Delta U / T_M$$

and consist of two components: a vibrational entropy due to the increased local volume available to the liquid atom for motion around its average position, and a configurational entropy due to the number of configurations that are possible for a given energy of the random assembly of liquid atoms. Assuming the atomic volume of the liquid is constant up to the interface, the vibrational entropy is the same at the interface as in the bulk liquid. Obviously, since the structure of the crystal has not changed, its entropy is constant up to the dividing surface. Therefore, the only quantity that changes because of the existence of the interface is the configurational entropy, and the crystal-melt free energy of Spaepen's model can be derived as follows.

The difference in free energy between a system at temperature T_M containing an interface, and a bulk crystal (taken here as the ground state) is

$$T_M \left[S_{config}\left(bulk\right) - S_{config}\left(surface\right)\right]$$

per atom of the interface. The interfacial free energy per atom in the crystal plane is therefore

$$\gamma_{SL} = \frac{N_I}{N_C} T_M \left(\frac{\Delta S^B_{config} - \Delta S^I_{config}}{\Delta S} \right). \tag{23}$$

N_I : *No.* of atoms in interface

N_C: *No.* of atoms in crystal plane

where γ_{SL} is the interfacial free energy per atom in the crystal plane, ΔU is the heat of fusion per atom, and ΔS is the entropy of fusion per atom. Superscript *B* and *I* represent bulk and interface, respectively. Spaepen calculated the configurational entropy of the crystal-melt interface based on various approximations and estimated the interfacial free energy. In this model, however, there exist only three layers of atoms for interface and is only considered for interfacial free energy.

Chemical free energy of interfaces

The classical approach to thermodynamics of crystal-melt interfaces is valid for homogeneous systems or very thick interface regions. Based on classical density functional theory, Cahn & Hillard[28] developed a method for interfacial free energy of a nonuniform system. In their method, the various spatial derivatives of density or composition were treated as independent variables. They derived total free energy of a nonuniform system and interfacial free energy of a flat interface. The total free energy in one dimension which they obtain in their treatment is

$$F = N_V \int_V \left[f_0(c) + k(dc/dx)^2 \right] dx . \tag{24}$$

It reveals that the free energy of a small volume of nonuniform solution can be expressed as the sum of two contributions, one being the free energy that this volume would have in a homogeneous solution and the other a "gradient energy" which is a function of the local composition. Note that the composition varies continuously and $f_0(c)$ is defined over the full range. The minimum of this integral of Eq.24 with respect to a one dimensional composition or density variation corresponds to free energy of a flat interface,

$$\sigma = 2N_V \int_{C_\alpha}^{C_\beta} \left[k\Delta f(c) \right]^{\frac{1}{2}} dc . \tag{25}$$

This continuum treatment of interfaces in microstructures has been the basis of numerous analytical and numerical treatments of thermodynamics and kinetics in real material systems.

Faceted/nonfaceted interfaces

With interfacial free energy included in the total free energy of a material system, microstruture becomes a necessary parameter in the description of thermodynamic equilibrium. Equilibrium interface shapes can be described in terms of interfacial energy by thermodynamic approach. At the equilibrium state, the interfacial energy and its orientation dependence associated with the existence of facets can be shown in the γ-plot. Interfacial energy, γ, is plotted on a polar diagram such that the length of the radius coordinate is proportional to interfacial free energy. On an arbitrary plane, the interfacial energy can be written as a function of only a single rotation angle, θ, as shown below.

$$\gamma(\theta) = \gamma_0 \left(1 + \sum_{m=2}^{\infty} \varepsilon_m^{hkl} \cos(m\theta) \right) \tag{26}$$

where γ_0 is the mean interfacial free energy, and m indicates the rotational symmetry of the crystal on the plane given by *{hkl}*. From the *γ-plot* for the interface between two phases, it is possible to determine the equilibrium shape of the interface. If planes are drawn perpendicular to the radius vectors where they cut the *γ-plot*, then the inner envelope of these planes corresponds to the equilibrium shape. The reverse is not necessarily true, however, as many crystals exhibit equilibrium shapes in which certain high-energy orientations are not present. For example, the {001} section of the *γ-plot* for a cubic metal would exhibit four-fold symmetry, and the interfacial free energy may be approximated as

$$\gamma(\theta)=\gamma_0\left(1+\varepsilon_4^{001}\cos(4\theta)\right) \tag{27}$$

where the anisotropy is described with a single parameter, ε_4. If Eq.27 is plotted for the system where there is no orientation dependence, the γ-plot will be circular as shown in Fig.2-6(ϵ_4=0). On the other hand, the first and second derivatives of Eq.27 give us,

$$\frac{d\gamma}{d\theta}=\gamma_0\left(-4\varepsilon_4^{001}\sin(4\theta)\right)$$

and

$$\frac{d^2\gamma}{d\theta^2}=\gamma_0\left(-16\varepsilon_4^{001}\cos(4\theta)\right), \tag{28}$$

respectively. The general curvature undercooling can be expressed as

$$\Delta T_r=\frac{K}{\Delta S_f}\left(\gamma+\gamma'\right)=\Gamma K\,. \tag{29}$$

where ΔS_f is the entropy of fusion and Γ is stiffness which is defined as sum of interfacial free energy and its secondary derivative. Stiffness as a function of orientation is, therefore, given by

$$\tilde{\gamma}(\theta)=\gamma_0+\gamma_{\theta\theta}=\gamma_0\left(1-15\varepsilon_4^{001}\cos(4\theta)\right). \tag{30}$$

The magnitude of this stiffness is much more anisotropic than the interfacial free energy as shown in Fig.2-7. From Eq.30, at

$$\varepsilon_4^{001}=1/15,$$

a negative stiffness emerges, indicating missing orientations occur, as shown in Fig.2-6. Therefore, for low values of anisotropy (less than 0.067), the graph of $\gamma(\theta)$ is equivalent to the equilibrium shape as shown in Fig.2- 8(a). Above this value of 0.067(1/15), equilibrium shape is not anymore

similar to γ-plot as shown in Fig.2-8(b). However, equilibrium shapes exhibit missing orientations only when the anisotropy exceeds a value which is approximately 0.067.

The most interesting feature of the equilibrium shape emerging from the γ-plot is the presence of facets corresponding to the cusps in the stiffness as a function of orientation. At higher anisotropy enough, for example, cusps are clearly shown in Fig.2-7(b) with corresponding to the faceted equilibrium shape as shown in Fig.2-8(b) due to the sufficient missing orientations. While a metallic crystal and its melt has a very small magnitude of anisotropy of interfacial energy typically exhibiting no missing orientations, materials with high anisotropy such as silicon and germanium, therefore, has a faceted morphology at equilibrium, resulting in the different growth behavior from the non-faceted metallic growth.

The roughening transition

One of the most interesting phenomena regarding facets on surfaces is a thermal roughening transition[29, 30, 31]. Generally speaking, it is a phase transition which occurs on a crystal surface at the roughening temperature T_R. According to Kosterlitz and Thouless[32], it is a phase transition of infinite order. This implies that the edge free energy γ_e vanishes continuously below the critical temperature.

The phenomenon of roughening transition has a firm thermodynamic basis. The concept has been introduced as a TLK (Terrace-Ledge-Kink) model in a famous paper of Burton et al.[33]. Because the free energy, required to form an edge or step, vanishes when actual temperature is equal or larger than T_R, steps propagate and flat surfaces may become rough on the microscale. On the mesoscopic scale, this roughening transition causes height fluctuations, which diverge with the distance probed on the surface. This makes the flat faces disappear from the macroscopic equilibrium crystal shape. The decrease in free energy of the step is due to an increase the entropy of the step caused by the increased jaggedness of the step. The step disappears into the noise on a rough surface, as illustrated in Fig.2-9.

Thermodynamic treatment for this transition is well summarized by Howe[34]. Consider a unit area of a {111} surface of an f.c.c. crystal in which the atoms are bounded by nearest neighbors with bond energy ϵ_b. To create a vacancy, we remove a surface atom, breaking nine bonds, and replace it at a kink site, restoring six bonds. Thus, the net energy of forming a vacancy is $3\epsilon_b$. If we now create n_v vacancies per unit area of surface, the energy of vacancy formation is

$$E_V = 3\varepsilon_b n_V - \frac{6\varepsilon_b n_V^{\,2}}{N_{S\{111\}}}, \tag{31}$$

where the second term arises as a correction for surface divacancies, and $N_{S\{111\}}$ is the number of surface sites per unit area on the {111} surface and n_v times $6\varepsilon_b n_v$ is the number of divacancies.

If we assume that an atom cannot occupy a site overhanging a vacancy, the number of ways of distributing n_v vacancies among N_S sites is

$$\xi = \exp\frac{S}{k_B} = \frac{N_S!}{(N_S - n_V)!\, n_V!} \tag{32}$$

Applying Stirling's approximation, the Helmholtz free energy of formation of n_v vacancies is

$$F = E_V - TS = 3\varepsilon_b n_V - \frac{6\varepsilon_b n_V^{\,2}}{N_{S\{111\}}} \\ -k_B T\left[N_S \ln N_S - (N_S - n_V)\ln(N_S - n_V) - n_V \ln n_V\right] \tag{33}$$

We can then obtain the equilibrium concentration of vacancies from the condition that

$$\frac{\partial F}{\partial n_V} = 0,$$

yielding

$$\frac{n_V}{N_{S\{111\}} - 3n_S - n_V} = \exp\left[-\left\{\frac{3\varepsilon_b}{k_B}\left(1 - 4\frac{n_V}{N_{S\{111\}}}\right)\right\}\right]. \tag{34}$$

For a {100} surface of a f.c.c crystal or a simple cubic crystal, we can similarly obtain the expression

$$\frac{n_V}{N_{S\{100\}} - n_S - n_V} = \exp\left[-\left\{\frac{2\varepsilon_b}{k_B}\left(1 - 2\frac{n_V}{N_{S\{100\}}}\right)\right\}\right]. \tag{35}$$

In the case of adatoms, adatoms might be constrained to occupy only the normal f.c.c sites, therefore the derivation of n_a follows the above treatment for n_v exactly and an equation like Eq.35 results, with n_a and n_v simply interchanged.

$$\frac{n_a}{N_{S\{100\}} - n_V - n_a} = \exp\left[-\left\{\frac{2\varepsilon_b}{k_B}\left(1 - 2\frac{n_S}{N_{S\{100\}}}\right)\right\}\right] \tag{36}$$

Noting, in this case, that n_a=n_v and letting X=X_v=X_a, where X_v is the mole fraction of vacancies and X_a is that of adatoms, Eq.35 and 36 both become

$$\frac{X}{1-2X} = \exp\left[-\left\{\frac{2\varepsilon_b}{k_B T}(1 - 2X)\right\}\right]. \tag{37}$$

We can define the surface roughness s as the number per site of free bonds parallel to the surface, which in the case of {100} gives

$$s = \frac{E_V}{N_S(\varepsilon_b/2)} = 8X(1-X). \tag{38}$$

Although the behavior of the surface roughness is qualitatively described by the Eq.38, the nearest neighbor bond model cannot be used to determine the actual temperature dependence for a particular material.

In order to describe the behavior of a Burton's TLK model of a surface with respect to temperature, we need to consider roughening of ledges in addition to roughening of the terraces. If we take the case of a <110> ledge on an {111} f.c.c surface, the energy of formation of n_v^l ledge vacancies is

$$E_V^l = \varepsilon_b n_V^l - \left\lfloor \varepsilon_b \left(n_V^l\right)^2 / N_l \right\rfloor, \tag{39}$$

where N_l is the number of available ledge sites. Continuing as in the previous treatment of terraces, we obtain

$$\frac{n_V^l}{N_l - n_V^l - n_a^l} = \exp\left[-\frac{\varepsilon_b}{k_B T}\left(1-2X_V^l\right)\right] \tag{40}$$

and

$$\frac{n_a^l}{N_l - n_a^l - n_V^l} = \exp\left[-\frac{\varepsilon_b}{k_B T}\left(1-2X_a^l\right)\right]. \tag{41}$$

In this case, the energy of formation of defects is much less than in the case of the low-index surface, and roughening typically becomes appreciable at temperatures of approximately one-half the melting point of a material. Leamy and Gilmer have examined the equilibrium structures of <100> oriented steps on vicinal {100} surfaces by Monte Carlo methods[35]. The energy of the ledge E_l is shown as a function of temperature in Fig.2-10. The energy of the ledge first rises with temperature as a result of thermal excitation until, in a critical region, E_l decreases rapidly to zero at the roughening temperature T_r. This result also predicts that at the roughening transition, the cusp in the *Wulff* plot for a low index surface vanishes. The effect of surface roughening on the equilibrium crystal shape[36] is illustrated schematically in Fig.2-11.

Jackson's α parameter-kinetic approach

There are basically two types of atomic structure for crystal-melt interfaces[83]. One is an atomically flat "faceted" interface and the other is an atomically rough "nonfaceted" interface. The classification of substances into faceted and non-faceted types is based on their growth

morphology. Metals usually solidify with atomistically rough (macroscopically smooth) crystal-melt interfaces and exhibit no facets in spite of their crystalline nature. An atomically rough interface always exposes a lot of favorable sites for the attachment of atoms from liquid. Such an interface tends to remain rough and leads to smooth crystals which are non-faceted at the microscopic scale and exhibit low kinetic undercoolings.

Moving to the faceted interface, systems that have a high fusion entropy change and interfacial free energy typically exhibit crystal-melt interfaces that are flat at the atomic scale. This atomically flat interface will maximize the bonding between atoms in the crystal and those in the interface. Thus, such an interface will expose few bonds to atoms arriving via diffusion through the liquid. This leads to crystals which are faceted at the microstructure scale and usually exhibit higher kinetic undercoolings.

Jackson approached the crystal-melt interface structure by atomic attachment kinetics and derived the Eq.42 from crystal growth rates theory[37]. He introduced a dimensionless entropy, $\alpha(\Delta S_f/R)$ to classify interface structures in atomic scale[37, 38].

$$V = Jv' = v'J_0^+ \exp\left[-\frac{Q}{RT}\right]\left(\frac{\Delta S_f}{R}\right)\left(\frac{\Delta T}{T}\right)f[hkl] \qquad (42)$$

This criterion is convenient and practical to predict a structural behavior of crystal-melt interfaces. If α is less than 2 in materials, they tends to be non-faceted during crystal growth. Materials in which α is more than 2 tend to exhibit faceted growth[37, 39] as summarized in Table 1.

2.2 The intrinsic behavior of crystal-melt interfaces

Microstructure selection, particularly morphological selection during the solid-liquid transition may be governed by various factors such as partitioning or diffusion of solute or heat, convection of liquid and even nucleation. However, responding of crystal-melt interfaces to above extrinsic factors contributes to overall microstructural selection through the phase transition by the intrinsic interfacial properties. Any interface can locally be described by the intrinsic variables, stiffness and mobility, where stiffness is quantifies resistance to curvature and mobility defines resistance to motion.

2.2.1 Intrinsic response of crystal-melt interfaces

In the preceding discussion, we examined the structure of crystal-melt interfaces. In the context of phase transformation, the value of understanding interfacial structure lies in its

connection to interface behavior and its role in microstructural evolution. Most basically, we can describe any 2 phase microstructure in terms of the positions ($\vec{r}$) of the interfacial elements S_i.

Thus for any interfacial element we can define the two fundamental state variables, curvature (K) velocity (v):

The unit tangent vector at a point on P on the curve at the interface in 3 dimensions is defined as

$$\hat{t} = \frac{d\vec{r}(s)}{ds} \tag{43}$$

where s is the arc length and ds is the element of arc length of the curve $\vec{r}$. Because $\vec{r}$ is between points infinitesimally separated on the space curve at any point, it is tangent to the curve at that point. The curvature of the interface, K, is equal to the rate at which the tangent vector changes as the curve is transverse and is therefore given by the relation,

$$\frac{d\hat{t}}{ds} = K\hat{n} \tag{44}$$

where $\hat{n}$ is the normal vector. Curvature of interfaces is a basic variable that describes a simple geometric shape of interfaces. For any surface element, the mean curvature of interface is defined as the change in the slope over a length of arc,

$$K = \left(\frac{1}{r_1} + \frac{1}{r_2}\right). \tag{45}$$

In the case of a sphere, $r_1 = r_2 = r$ so that $K=2/r$ and, for a cylinder, r_1 is infinite and $r_2 = r$ so that $K=1/r$. As an intrinsic factor, the interfacial stiffness is a quantity that includes the amount of energy required to curve the interface.

The interfacial free energy between a crystal and its melt is generally dependent on the crystallographic plane which is presented to the liquid. The effect of this orientation dependence on the equilibrium shape of the interface was considered by Herring in his analysis of the variation of free energy associated with local shape change[40]. Herring's well-known result implies that the local driving force is related to the principal interfacial curvatures, K_1 *and* K_2.

$$\Delta T_r = \frac{1}{\Delta S_f}\left[K_1\left(\gamma(n) + \frac{\partial^2\gamma(n)}{\partial n_1^2}\right) + K_2\left(\gamma(n) + \frac{\partial^2\gamma(n)}{\partial n_2^2}\right)\right] \tag{46}$$

where ΔS_f is the entropy of fusion, $\gamma(n)$ is the anisotropic interfacial free energy, n is the interface normal vector, and K_1 and K_2 are two principal curvatures. If one of the principal curvatures is zero, then the orientation can be substituted by θ, the angle between a reference direction and the interfacial normal,

$$\Delta T_r = \frac{K}{\Delta S_f}\left(\gamma + \frac{\partial^2 \gamma}{\partial \theta^2}\right) = \Gamma K \tag{47}$$

where Γ is an orientation dependent stiffness coefficient as discussed before.

In the case of moving interface, interfacial mobility is defined as how much energy is required to move the interface,

$$\Delta G_K = \frac{V \Delta S}{\mu(\theta)} \tag{48}$$

and the kinetic component of interface undercooling is, thus,

$$\Delta T_K = \frac{V}{\mu}. \tag{49}$$

Like interfacial energy, the interface mobility is anisotropic, depending on the crystal plane presented to the liquid.

We have, so far, learned that the intrinsic response of crystal-melt interfaces depends critically on interfacial free energy and mobility, which have anisotropic characteristics. These two properties determine the interface shape and rate and, indeed, select morphology of the phase during solidification. Furthermore, due to the anisotropic nature of these key factors, faceted interfaces can emerge in a certain system during the growth. This faceted growth is typically restricted to a certain growth direction with the consequence that the interfaces cannot respond to local instability. Indeed, the system may have to find efficient growth mechanisms, so that morphological selection would be enhanced by the alternatives. Therefore, in some cases, crystal defects might play a certain role in the morphological selection of kinetically limited faceted interfaces to reach and maintain a stability of growth.

2.2.2 Experimental measurement of μ, γ

Recognizing the importance of interfacial properties during solidification, several attempts have been made to obtain the interfacial free energy and anisotropy. Turnbull's nucleation rate experiments in 1950 were the first attempt to measure interfacial free energy[4], when nucleation was homogeneous at the maximum undercooling. Because solidification should occur at limited conditions of homogeneous nucleation and maximum undercooling in this method, ES (Equilibrium Shape) and GBG (Grain Boundary Groove) methods become widely used to establish interfacial free energy and anisotropy of crystal-melt interfaces.

Jones and Chadwick obtained equilibrium shapes of liquid droplets in the solid for camphene, succinonitrile and white phosphorous. They found that the aspect ratios of

equilibrium shapes were within a few percent of unity, and concluded that the anisotropy effect was small. Glicksman et al.[41, 42] measured interfacial free energy of transparent materials using equilibrium shape method. It is, however, difficult for opaque metal systems. Chadwick and Miller[43] extended this technique and measured interfacial free energy of alloys such as Bi-Cd and Zn-Pb using a fine dispersion of liquid droplets. Unfortunately they, however, did not measure anisotropy. The GBG (Grain Boundary Groove) method[44, 45, 46] has also been one of the techniques for measuring γ. Moreover, Hunt et al.[47, 48] have reported interfacial free energy of Al alloys and Sn alloys using GBG. It should be noted that the measured interfacial energy is a mean value without anisotropy.

In spite of the difficulty due to a small variation of γ, this quantity has been measured for some transparent organic materials[49, 50, 51]. More recently, Napolitano et al. measured the anisotropy of interfacial energy for Al-Cu and Al-Si alloys[52] and Al-Sn[53], using the equilibrium shape method. In addition, they proposed a GBG method that can be used to determine anisotropy from experimental measurements[54].

Like the interfacial free energy, the mobility of the crystal-melt interface and its mobility have a critical influence on the morphology of microstructures, especially at large undercoolings. The kinetic coefficient, μ, has been experimentally measured in only a few cases. Glicksman and Schaefer[55] measured it for phosphorus and Rodway and Hunt[56] attempting to determine the mobility of Pb. Surprisingly, the dependence of mobility on growth direction has been barely reported experimentally for a metal.

2.2.3 Theoretical predictions of μ, γ

Due to the considerable importance of μ and γ for numerical calculations of morphological evolution, many authors have tried to calculate the material parameters associated with various potential models. Molecular-dynamics (MD) simulation techniques have recently been applied to the determination of these parameters. Broughton and Gilmer[57] made the first such theoretical estimation for γ using the Lernard-Jones (L-J) system. They used an "adiabatic cleaving" technique to create a solid-liquid interface. With this method, they made the first MD-based theoretical estimates of γ, but did not report any orientation dependence. Subsequently, MD-based estimates of the crystal-melt interfacial energy and its anisotropy have been reported for a hard sphere system[13, 58], the Lennard-Jones system[57, 59], and for several EAM potentials[60, 61, 62, 63]. In addition, direct calculation of crystal-melt interfacial free energy has been reported for the Lennard-Jones system[64, 65, 66].

Moving to the theoretical estimates of μ, the pioneering work on MD simulations of crystallization kinetics was performed by Broughton, Gilmer, and Jackson (BGJ)[67]. In their study of the L-J system, The BGJ simulation represents the MD equivalent of a directional solidification experiment. By varying the velocity, the relationship between velocity and undercooling, $V(\Delta T)$, and hence μ, could be determined.

There exist several techniques capable of extracting μ from MD simulations. The various attempts to compute μ fall into three broad categories: forced velocity simulations[68], free solidification methods[12, 69] and fluctuation or random walk techniques15[7071]. The most common method is the free solidification technique[12, 69], which involves applying a thermostat to all atoms of the system and, where the velocity vs. undercooling behavior is found by tracking the solid-liquid interface motion as the system solidifies at some temperature below T_M. The forced velocity and free solidification methods determine μ by mapping out the entire velocity vs. undercooling behavior. In random walk methods, by monitoring the fluctuations in the average position of the interface for a system maintained at the melting temperature, μ can be found directly.

2.3 Overall behavior of crystal-melt interfaces

While the intrinsic behavior of a crystal-melt interface originates from the fundamental properties of the interface itself, a crystal-melt interface can be significantly affected by external variables. Both extrinsic and intrinsic factors contribute to the overall driving force. In this section, overall behavior of interfaces, associated with complex relationships between intrinsic and extrinsic factors, will be summarized. As a result of these connections of interfacial behavior, various emerging morphologies will be briefly reviewed.

2.3.1 Overall equation at state for an interface

Both intrinsic and extrinsic contributors are taking into acount, overall undercooling which can be expressed by

$$\Delta T = (\Delta T_R + \Delta T_K)_I + (\Delta T_D)_E . \tag{50}$$

Each term of intrinsic contributions can be reproduced without anisotropic interfacial considerations.

$$\Delta T = \frac{v}{\mu} + \Gamma K + \Delta T_D \tag{51}$$

Local response of crystal-melt interfaces depends critically on the partitioning of these shape (curvature) and velocity (mobility) contributions to the local undercooling. The last term in Eq.54

drives all extrinsic processes such as the solute and heat diffusion. Therefore, both intrinsic and extrinsic driving forces determine the local interfacial condition and microstructrue can evolve with selected morphologies.

2.3.2 Constrained vs unconstrained growth

The stability of crystal-melt interfaces depends on the direction of the heat flow. The liquid temperature always decreases from the interface in the unconstrained condition and the heat flow direction for solidification, therefore, is as same as the crystal growth direction. Here, "unconstrained" means that heat dissipation from the crystal-melt interfaces are not mainly controlled by the external heat sink. This type of growth can be observed often in an undercooled melt such as emulsion or levitation experiments of solidification as well as in the equiaxed region of ingot casting. However, sometimes crystal growth is constrained in its direction and the melt temperature increases from the solid-liquid interfaces. Consequently, heat is sinked into the solid. This phenomenon is observed at the wall of casting mold showing columnar cell or dendrite. Directional solidification is one of the constrained solidification processes and it is an important technique in the industry as well as academia due to the reproducible and reliable characteristics of controlling the interface. Therefore, various morphologies observed in this constrained directional growth will summarized in the next section.

2.3.3 Directional solidification morphologies in alloys

Directional solidification has been an excellent method for solidification and interface science because of its unique advantages as mentioned before. The microstructures that emerge under this constrained condition are not only governed by the cooling conditions, specifically temperature gradient and growth velocity, but by alloy compositions as well. During the growth, the temperature gradient can be fixed and moving velocity of interface can be easily controlled. These simply controlled conditions allow observations of microstructural evolutions and provide a reasonable analytical approach to complex interfacial properties. In this section, various morphologies, which might be observed in directional solidification, are summarized.

Cellular and dendrite array

When alloys are directionally solidified arrays of cells or dendrites can be produced. They grow with an average spacing and a tip undercooling which can be measured. Papapetrou first described a dendritic growth as a paraboloid of revolution with fixed tip radius and Ivantsov solved the thermal diffusion equation for the parabolic needle. Since Ivantsov's accomplishment, numerous dendritic/cellular growth models have been developed. Among them, however,

critical equations for constrained alloy dendrite and cell growth are summarized and, especially are plotted for Al-Si alloys system at the specific solidification conditions, for example. Note that all symbols are defined at the end of this section.

A. Dendritic growth

Assuming that the thermal contribution to the tip is negligible for the directional growth of dendrites,

$$R^2V = \frac{4\pi^2 D\Gamma}{\Delta T_0 k}, \tag{52}$$

The fully developed dendrite with side branches can be approximated by an ellipsoid of revolution for hexagonal array,

$$\lambda = 4.3\left(\frac{D\Gamma\Delta T_0}{k}\right)^{0.25} V^{-0.25} G^{-0.5} \tag{53}$$

Trivedi et al.[72] extended this equation by using the marginally stable tip radius for low Peclet numbers and proposed

$$\lambda = 6\left(\Delta T_0 k D\Gamma\right)^{1/4} V^{-1/4} G^{-1/2}\left[1-\left(DG/V\Delta T_0 k\right)\right]^{1/2}. \tag{54}$$

Spacing λ was expressed by velocity and temperature gradient in Eqs. 53 and 54. Note that, with regard to λ, none of these models represents well the real behavior. They are useful only for making qualitative estimates of λ.

B. Cellular growth (Hunt[73, 74])

Hunt et al.[75, 76] have extensively studied cellular/dendritic growth, using numerical finite element methods. By suitable non-dimension treatments, relatively simple analytic expressions can be used to fit their numerical results.

$$\lambda = 4.09k^{-0.335}\left[\frac{\Gamma}{mC_O(k-1)}\right]^{0.41}\left(\frac{D}{V}\right)^{0.59} \tag{55}$$

This expression provides an insight into the cellular and dendritic growth processes and may be useful for comparing theory with experiment.

Eutectic growth (Jackson and Hunt[77], Trivedi's parameter[78])

Eutectic structures may exhibit a wide variety of morphologies but only the broad classifications of regular and irregular will be considered here. A general solution to the regular eutectic lamellar or rod growth has been developed by Jackson and Hunt. They approached the

problem by calculating the average total undercooling at the interface in terms of a lamellar spacing λ. The resultant equation contains only the variables λ, v, and ΔT, and may be written as

$$\Delta T = K_1 \lambda V + \frac{K_2}{\lambda}. \tag{56}$$

For minimum undercooling at a given velocity,

$$\lambda^2 V = \frac{K_2}{K_1}. \tag{57}$$

Irregular eutectics tend to grow at higher undercoolings and the spacing has a strong thermal gradient dependence. Because one of the phases involved in irregular eutectic growth exhibits faceted solid-liquid interface and thus, preferred growth directions, the resulting microstructure consists of converging and diverging lamellae with a wide range of spacings that are larger than that observed in regular eutectic growth. Equations for irregular eutectic growth are given by

$$\Delta T = \frac{\left(\phi^2 + 1\right) K_2}{\lambda},$$

$$\frac{\Delta T}{\sqrt{V}} = \left(\phi + 1/\phi\right)\sqrt{K_1 K_2},$$

and

$$\lambda^2 V = \phi^2 \left(\frac{K_2}{K_1}\right),$$

where Φ is dimensionless operative parameter. Both equations are derived at the extremum, where the minimum undercooling for growth at a given velocity coincides with the maximum growth rate for a given undercooling. Thus, eutectic spacing can be measured and compared to these traditional equations.

As we have seen various models for a pattern formation, spacing, undercooling, and supersaturation, associated with a composition field are important factors to describe morphological evolution during directional solidification. By careful measurements of above values, overall growth behavior can be explained and described well.

R: Dendrite Tip Radius

ΔT: Undercooling

ΔT_0: Freezing range

λ: Spacing (m)

D: Diffusion coefficient (m^2/sec)

Γ: Gibbs-Thomson coefficient (mK)

V: Growth velocity (m/sec)

G: Temperature gradient (K/m)

k : equilibrium partition coefficient

K_2, K_1, $\varnothing$: constant

m: Liquidus slope (K/wt%)

2.4 Solidification in Al-Si alloys

The morphology of silicon growing from a melt is of interest in several different processes from casting of Al-Si alloys to silicon thin films laser technology. In particular, the morphologies of the eutectic Si and primary Si in Al-Si alloys, and the associated growth mechanism, have been widely studied[78, 79, 80, 81] intensively in relation to controlling the microstructure and improving properties of casting products. In this section, various Si morphologies, associated growth and transition mechanisms, will be summarized. Particularly, primary Si and eutectic Si related to twinning will be focused. In Fig.2-12, equilibrium Al-Si binary alloy phase diagram[82] is shown.

2.4.1 Eutectic morphologies (coupled growth)

Al grows in a non-faceted manner like other metallic elements while a faceted flake-type is a representative Si morphology in Al-Si eutectics. This faceted-nonfaceted irregular eutectic is commonly observed in conventional casting products without any modification and its structure is characterized by large silicon flakes. The broad plane of flakes are parallel to the {111} planes of the diamond cubic Si and there are no known crystallographic relationship between Al and Si. The flake exposes its {111} surface to the adjacent eutectic Al phase. The parallel {111} twins within the flake produce a stable 141° reentrant groove also faced by {111} planes at the growing tip. The groove is efficient in retaining silicon atoms deposited from the melt and promotes faster growth along <112>. According to coupled zone calculations[83], Al-Si alloy has a right-skewed coupled zone due to the faceted Si during the eutectic growth.

2.4.2 High rate transitions

The solidification microstructures in the Al-Si alloys vary widely because of intrinsic morphologies of faceted Si that vary with solidification conditions such as growth velocity and thermal gradient. While the flake type is normal for Si morphologies in conventional casting processes, high growth rates give rise to a morphological transition, from a faceted flake to a non-

faceted rod-like morphology[79]. A large contribution of kinetic undercooling results in this transition, limiting anisotropic growth of Si.

2.4.3 Impurity modification (important because of twinning)

Impurity modification for faceted Si at low growth rates causes a similar result for quenched modification, enabling reentrant twin plains to play a role in selection of growth direction and morphological optimization in response to local solutal and thermal fluctuation. In spite of similar morphologies of Si particles to that of quench modification, impurity atoms cause twinning on a very fine scale as shown in Fig.2-13. Therefore, twinning is a much more important growth mechanism in this mode. The twin plane reentrant edge (TPRE) mechanism is a well-known theory[84, 85] for this transition and will be discussed later in detail. The resulting microfaceted structure with a high density of reentrant twin plane edges permits the silicon phase to self-optimize by responding to local thermal and solutal fields in a manner similar to a nonfaceted phase.

2.4.4 Solidification in eutectic/hypereutectic

Primary Si in hypereutectic Al-Si alloys has been extensively studied[86, 87]. A series of primary morphologies has been reported:[88] plate-shaped crystals of hexagonal form, octahedral equiaxed crystals, equiaxed crystals containing varying numbers of parallel twins, star-like crystals containing two to five radiating twin planes, and spherical crystals. Atasoy et al.[89] observed primary silicon morphologies in directionally grown hypereutectic eutectics and found that octahedral crystals, twinned {111} and twin-free, predominated over a wide range of growth velocities.

There is another interesting morphological transition from randomly oriented flakes to angular morphologies in near eutectic Al-Si alloys at certain G/V regime. This phenomenon has been reported by several authors[90, 91, 92, 93]. The first careful examination of the low velocity Al-Si eutectic morphologies was reported by Day and Hellawell. Depending on the magnitude of the thermal gradient, they reported a transition from uncoupled growth at very low rates (i.e. 0.1 to 1 μm/s) to a coupled growth morphology characterized by large connected branched silicon structures as show in Fig.2-14. In addition, they reported several characteristic features of the low-velocity coupled growth morphology. Most notably, they observed a strong <001> Si texture associated with this structure. In addition, they observed side-plates which were either smooth with broad {001} faces or corrugated with alternating {111} faces, meeting along a common [011] direction. The detailed features of Si structure have been examined by Shamsuzzoha et all[92, 94].

They have revealed similar side-plate structures emanating in <001> directions from a twinned central stem. In spite of excellent crystallographic works, twin structures of the 8- pointed angular Si remains in ambiguity and the growth and branching mechanisms of faceted angular Si have not fully understood yet.

2.4.5 Growth mechanism of silicon

Pure silicon can be doped with boron, gallium, phosphorus, or arsenic to produce silicon for use in transistors, solar cells, rectifiers, and other solid-state devices which are used extensively in the electronics and space-age industries. In addition to its applications for electric devices, silicon is an important alloying element in Fe based or Al based alloys. Growth mechanisms of Si crystals are of interest because in many alloys Si occurs as a pure and distinct phase[95]. Therefore, intrinsic twinning of diamond cubic Si is an essential to understand Si growth mechanisms in both pure Si and alloys.

Solidification in pure silicon

The morphologies in the previous section are readily observed for crystals in an alloy matrix. In contrast, traces of the growth morphology in pure silicon are more difficult to detect. In connection with its use as a semiconductor[96], much attention was paid in the past century to purification and single crystal growth of silicon.

The Czochralski process is commonly used to produce single crystals of silicon used for solid-state or semiconductor devices. In this technique, high purity polycrystalline silicon is melted down in a crucible and a small piece of a single crystal seed is placed on the molten liquid. As the seed is slowly rotated and pulled from the melt, the surface tension between the seed and the liquid silicon causes the liquid to rise with the seed and freeze into a single crystalline ingot.

Float zone crystal growth method[97] is another commercial process to produce silicon single crystal. This technique is done in an inert gaseous atmosphere, vertically placing a polycrystalline rod and a seed crystal face to face. Both are partially melted and the melted zone is gradually moved upwards rotating with the seed crystal until the entire polycrystalline rod has been converted to a single crystal.

Growth mechanisms

Si has been believed to show lateral growth, giving a faceted morphology near to equilibrium at low growth velocities, but normal non-faceted growth at high velocities. In lateral growth, atomic steps on the growing interface are essential for interface propagation. Atoms

jumped from the liquid can be easily attached to these steps. Steps can be provided by defects in the crystal, such as twins and screw dislocation[98, 99].

More recently, research has focused on melt undercooling, crystal morphology, growth mechanisms, and metastable phase formation in undercooled melts for both germanium[100] and for silicon[101, 102]. Levitation is a well-known method to observe morphological transitions of pure Si at high undercooling. A summary of growth morphologies [103] of silicon at different undercoolings is shown in Fig. 2-15.

Hogan et al.[104] have reported that the majority of the primary silicon crystals grown in Al-Si castings can be identified as variants of octahedral crystals with {111} facets despite wide variations in morphology. No evidence of TPRE assistance was found in the growth of the octahedral-type crystals studied. They proposed that the observed dislocation spirals on {111} facets provide a major source for layer growth of the crystal facets. Plate-like Si crystals growing by the TPRE mechanism are also observed. A subsequent research by the same authors[104] proposed 3 stages of complex primary Si morphology evolution from spherical to hollow as shown in Fig.2-16. The spherical morphology of their observation came from a quenching effect near the mold wall.

The twin plane reentrant edge (TPRE) mechanism[105, 106] is a process by which a crystal can grow at terminal twin plane grooves and continually generate new grooves. As discussed in eutectic morphologies, TPRE is a major growth mechanism for eutectic Si flakes as well as primary Si. However, for angular morphology of Si, although TPRE is proposed in order to explain the growth mechanism, the growth mechanism and the role of twinning are not fully understood.

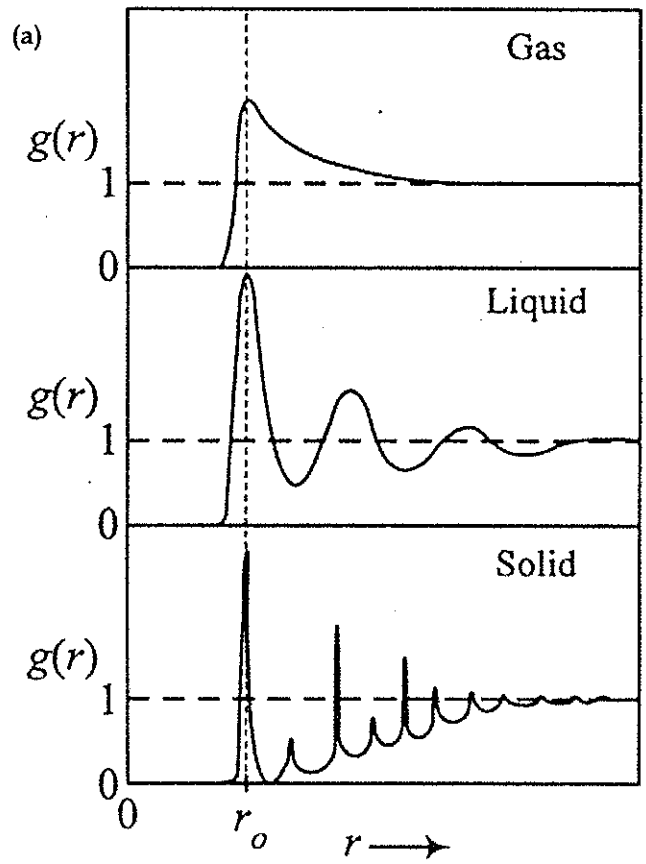

Figure 2-1. (a) Pair correlation function for gas, liquid, and solid phase.

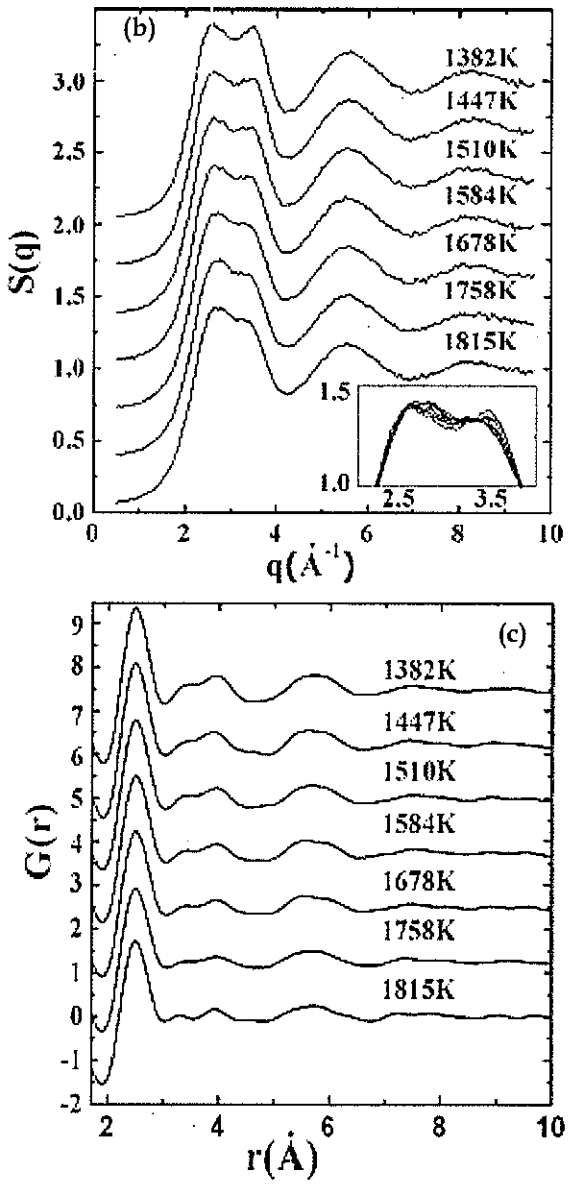

Figure 2-1. Continued. (b) Structure factors and (c) reduced radial distribution functions for liquid Si, obtained neutron diffraction patterns, from the reference [9].

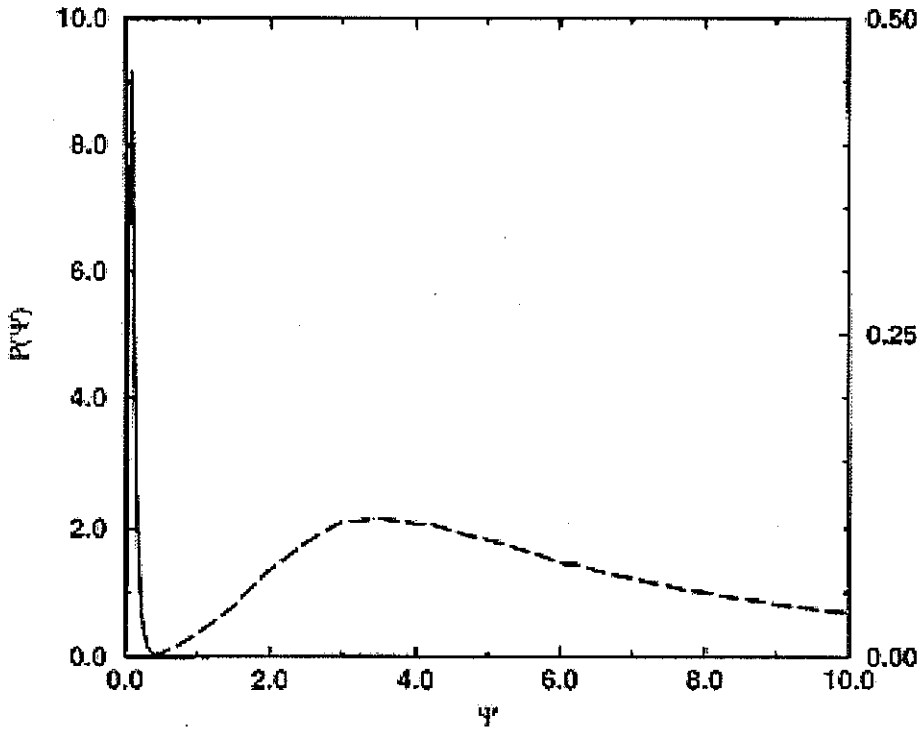

Figure 2-2. The distributions of the values of Ψ during a simulation of a pure crystal and a pure liquid. From the reference [12].

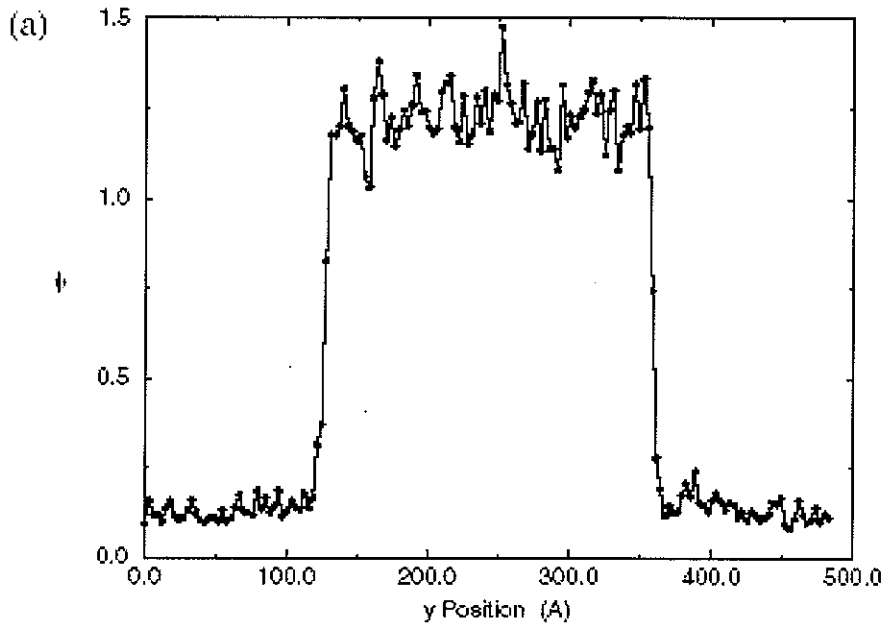

Figure 2-3. Plot of the order parameter, at a point along the interface during an MD simulation. From the reference [15].

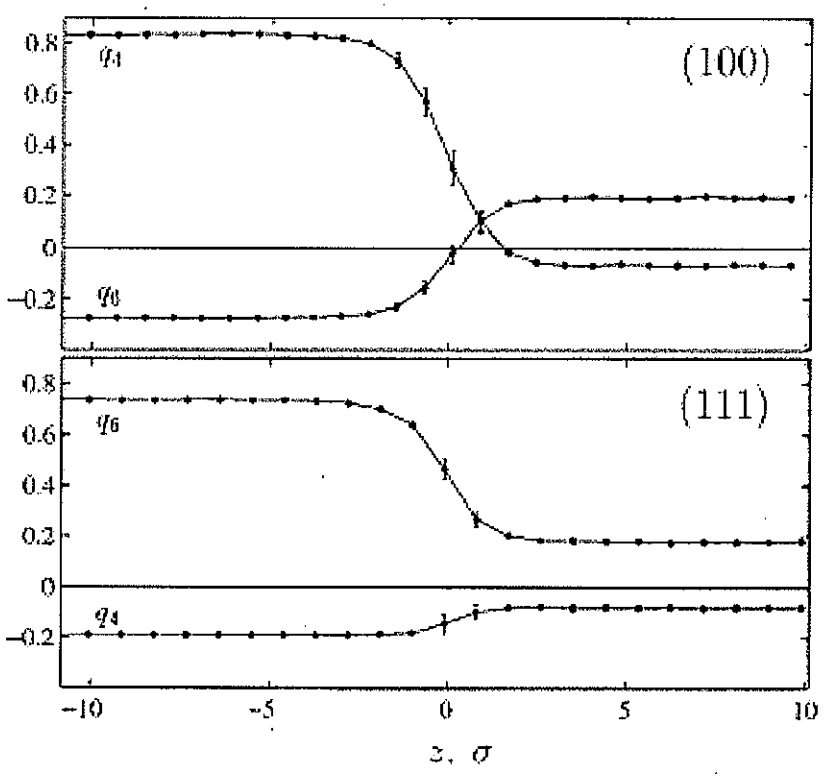

Figure 2-4. Orientational order parameter profiles measured on a uniform coarse-scale. From the reference [13].

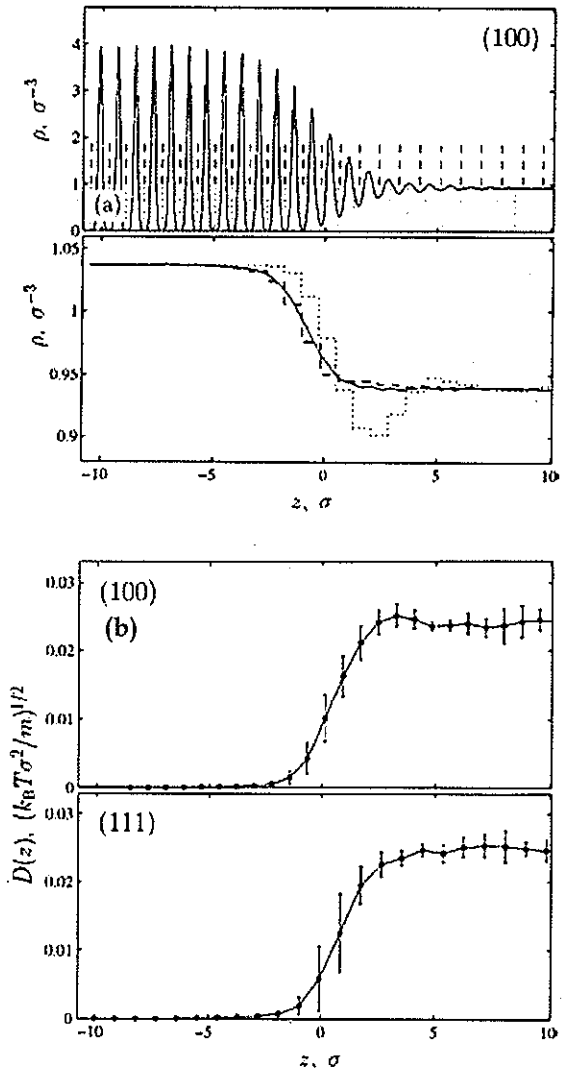

Figure 2-5. (a) Fine scale density profiles for the (100) crystal-melt interface (upper) and Density profiles on the uniform (dotted line) and the non-uniform (dashed line) coarse scales (lower). (b) Diffusion coefficients for the (100) and (111) crystal-melt interfaces. Those are from the simulation of the hard-sphere crystal-melt interface. From the reference [13].

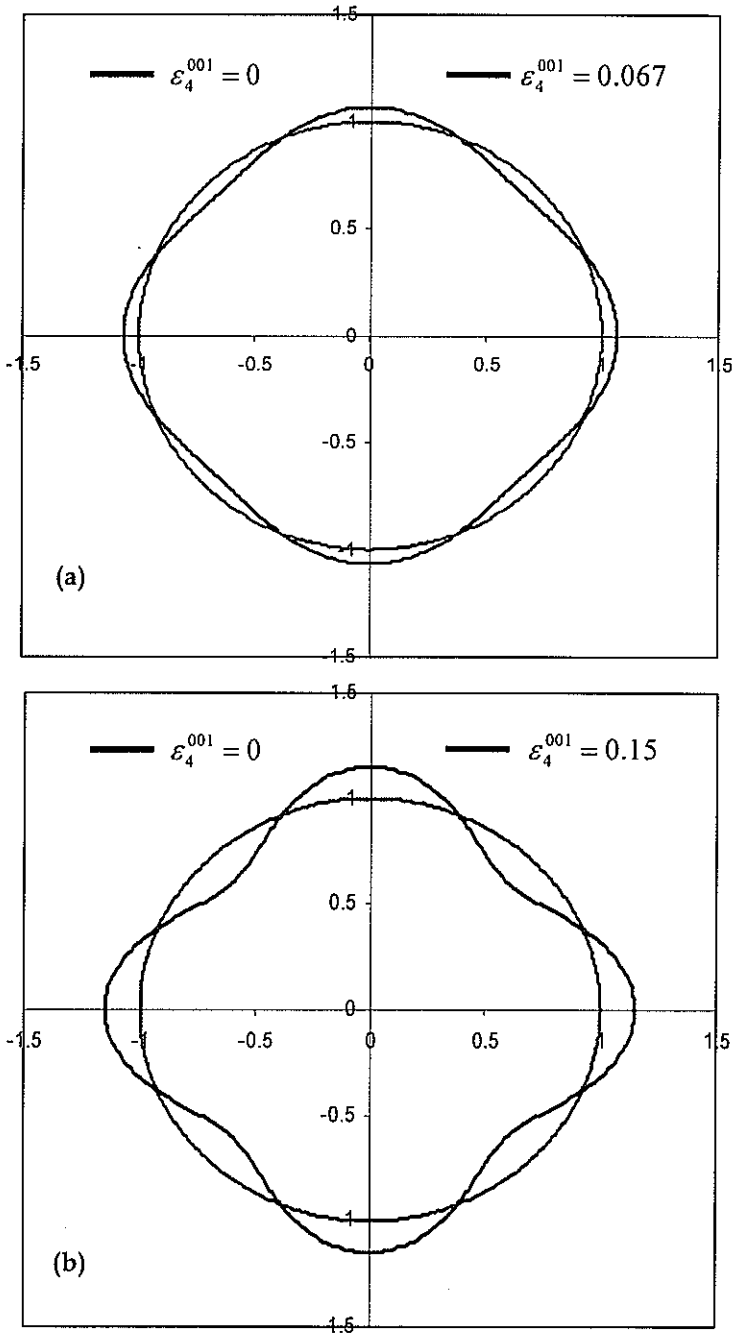

Figure 2-6. Interfacial free energy (4 fold symmetry) as a function of ø at different anisotropy of values. (a) Anisotropy is 0.067 and (b) anisotropy is 0.15. For both cases, anisotropy is zero for the red circles.

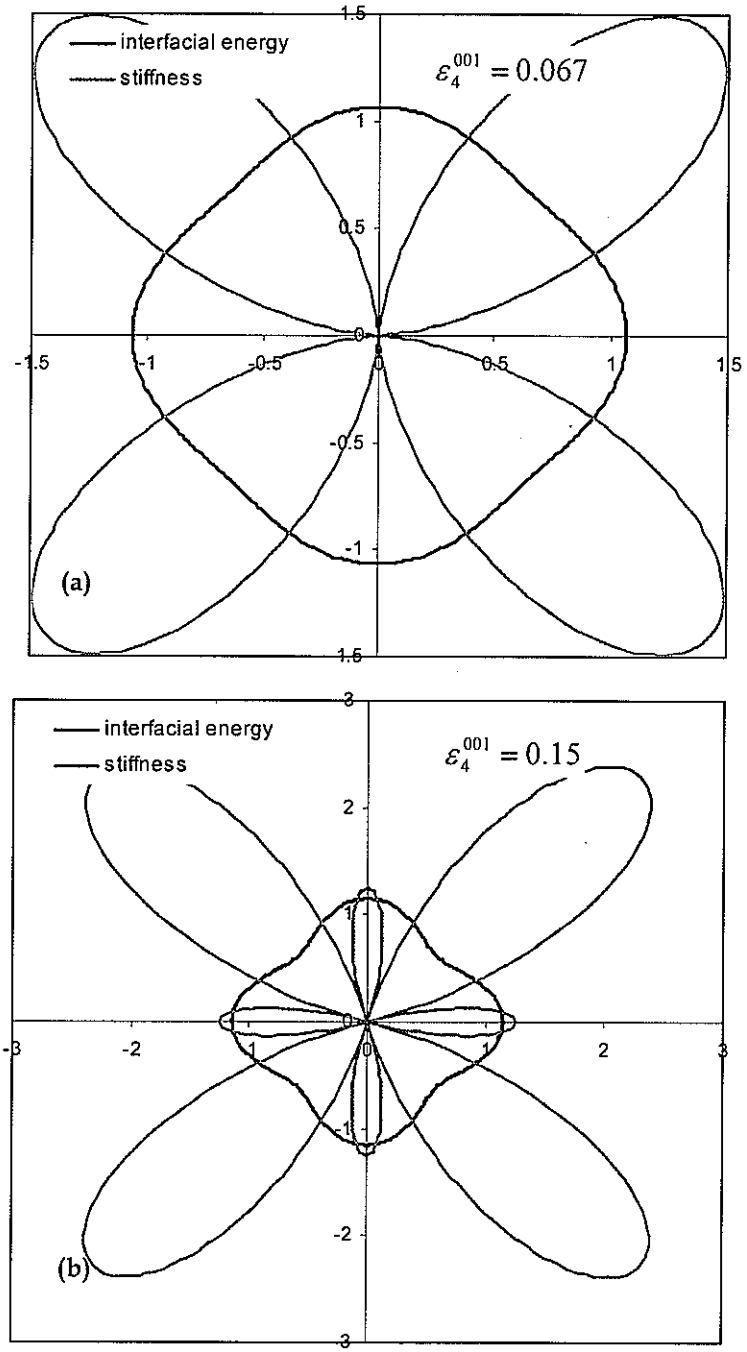

Figure 2-7. Stiffness and interfacial free energy (4-fold symmetry) as a function of ø at different anisotropy values. (a) Anisotropy is 0.067 and (b) anisotropy is 0.15.

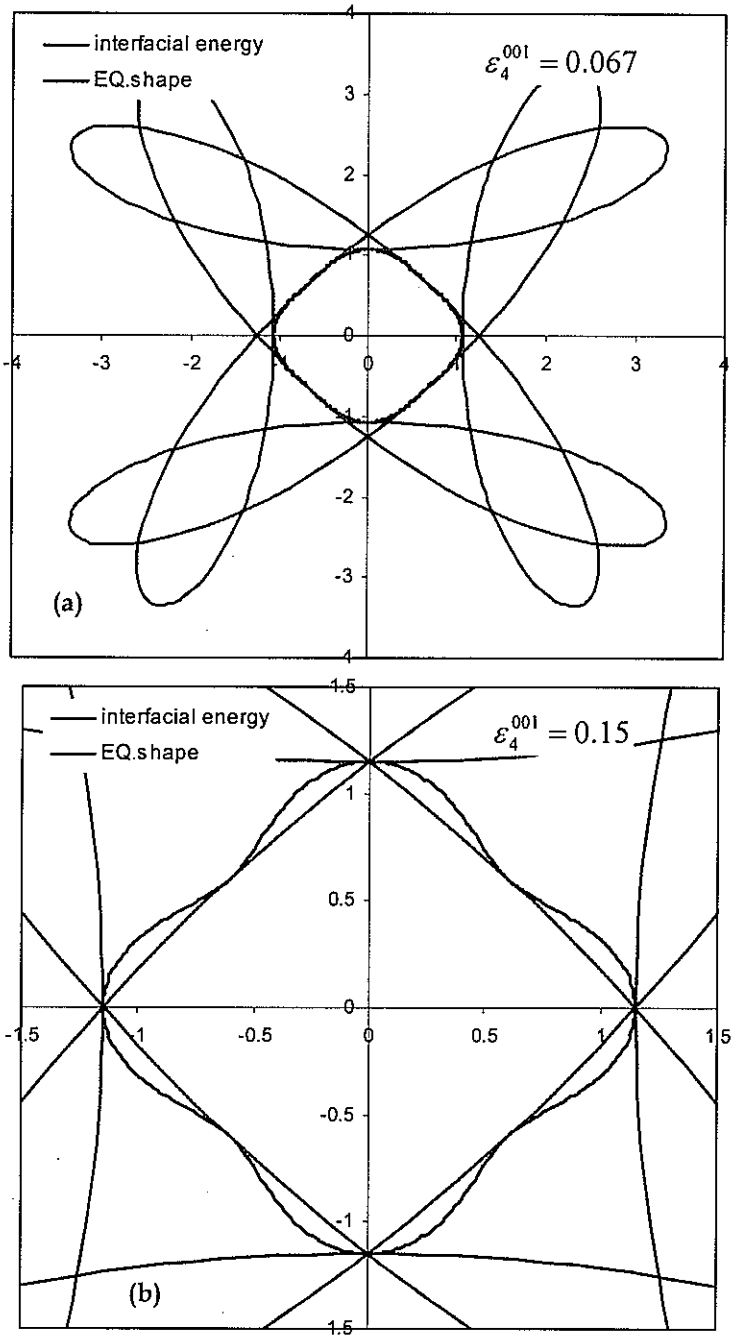

Figure 2-8. Equilibrium shapes corresponding to Fig.2-6 and 2-7. (a) Anisotropy is 0.067 and (b) anisotropy is 0.15 and inner envelope is equilibrium shape.

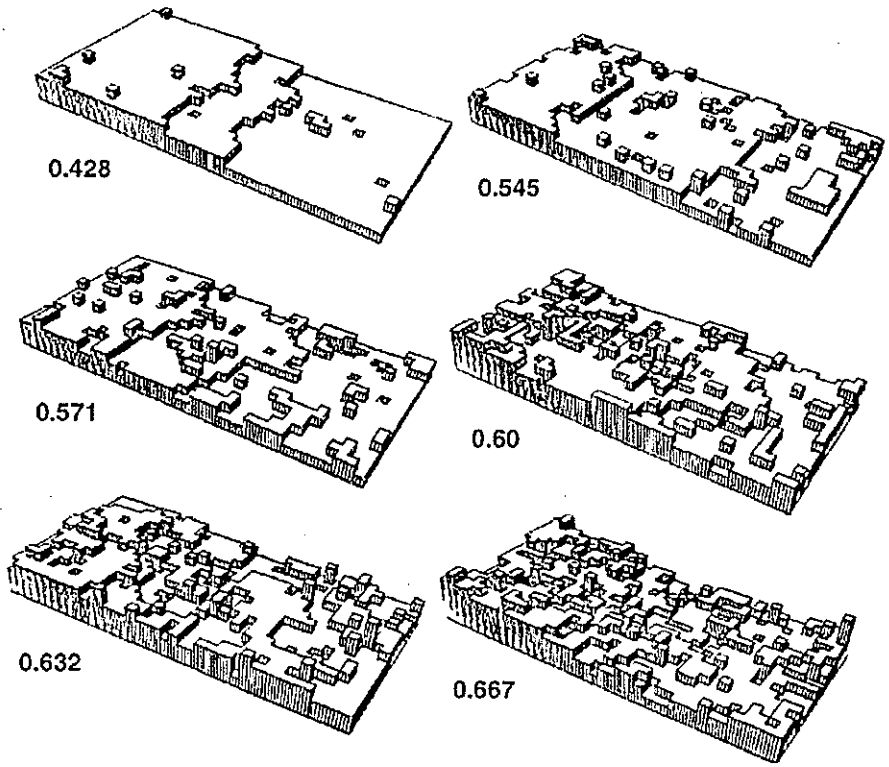

Figure 2-9. Computer simulation of surfaces with various roughness for {21 1 0} surface configurations at various values of K_BT/e_b. From the reference [35].

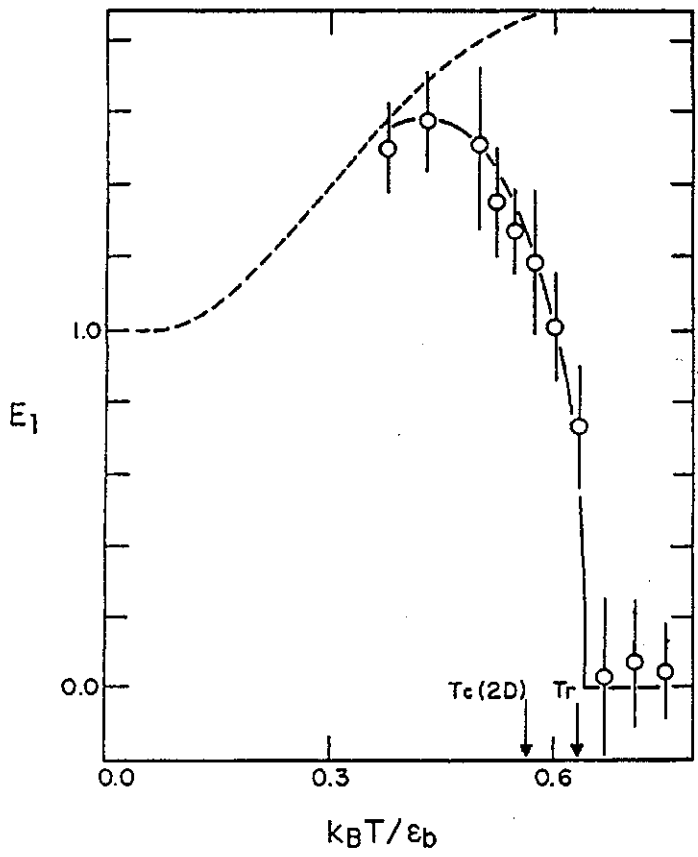

Figure 2-10. Temperature dependence of the energy of an isolated <100> ledge on the {100} surface of a simple cubic crystal. From the reference [35].

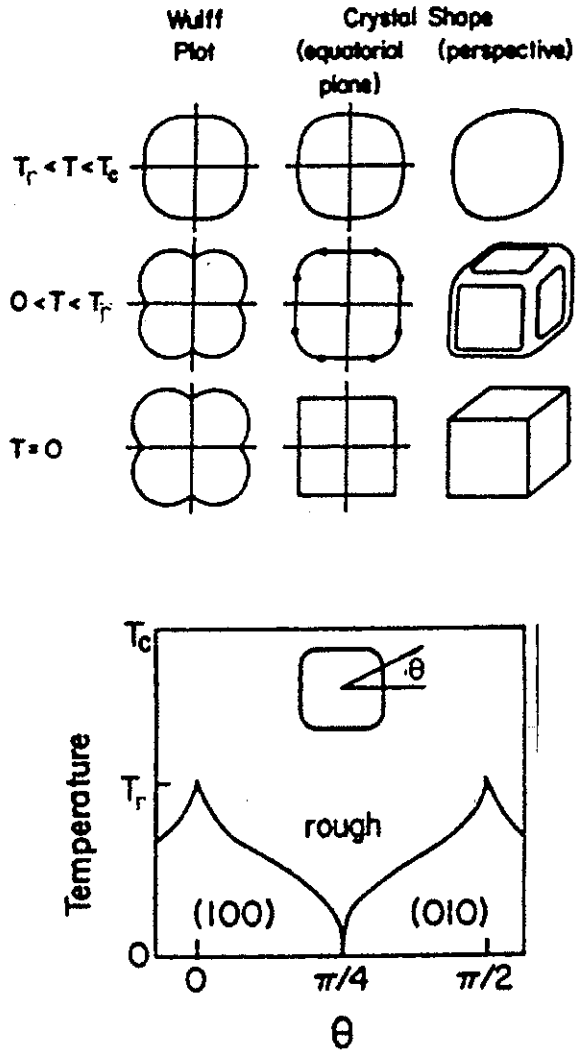

Figure 2-11. Equilibrium shape of nearest-neighbor simple cubic crystal as a function of temperature T (upper). The evolution of the edge position in the equatorial plane is shown in the phase diagram in the lower plot, where T_r is the roughening temperature of the {100} surface and θ is the angle of the surface normal from {100}. From the reference [36].

Table 1. Various $\alpha(\Delta S_f/R)$ values for materials. Those bolded are well known to be faceting on at least one orientation[107].

Material	$\alpha(\Delta S_f/R)$	Material	$\alpha(\Delta S_f/R)$
Potassium	0.825	Lead	0.935
Copper	1.14	Silver	1.14
Mercury	1.16	Cadmium	1.22
Zinc	1.26	Aluminum	1.36
Tin	1.64	Gallium	2.18
Bismuth	2.36	Antimony	2.57
Germanium	**3.15**	**Silicon**	**3.56**
Water	2.62	CBr4	1.27
yclohexanol	0.69	Succinonitrile	1.40
enzil	6.3	Salol	7

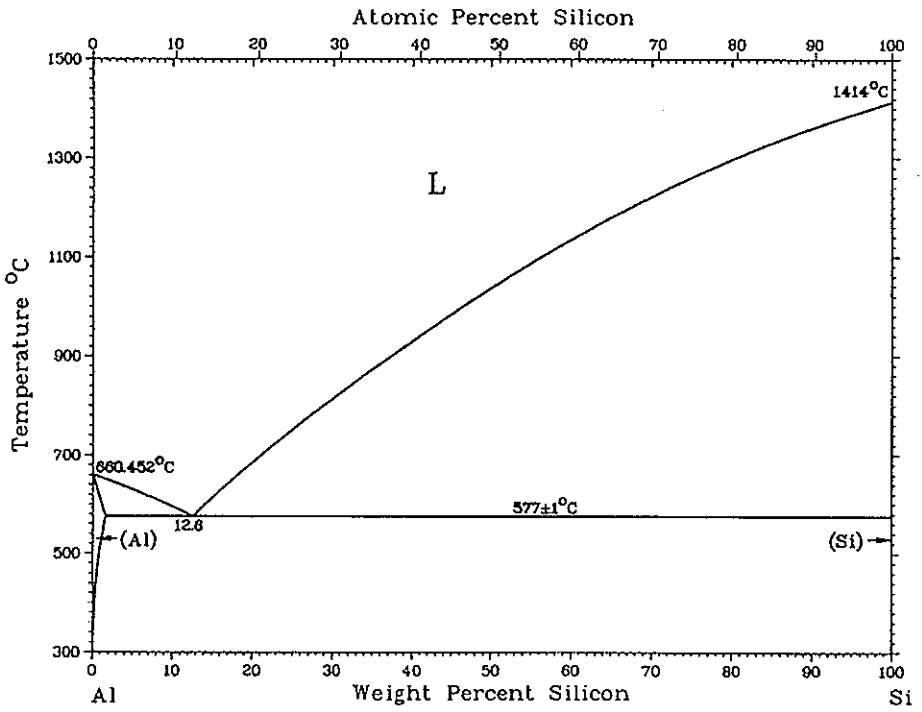

Figure 2-12. Equilibrium phase diagram of binary Al-Si alloys[82].

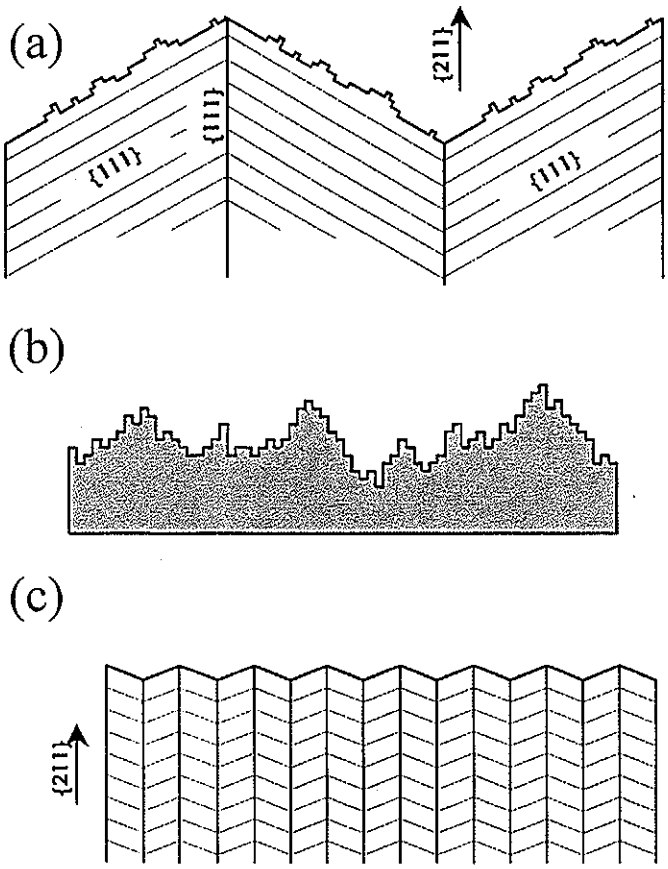

Figure 2-13. Schematic diagram illustrating the effect of twin density on growth mode. Note that impurity modified growth has a fine micro-facets while quenched modified growth has rough interfaces[79].

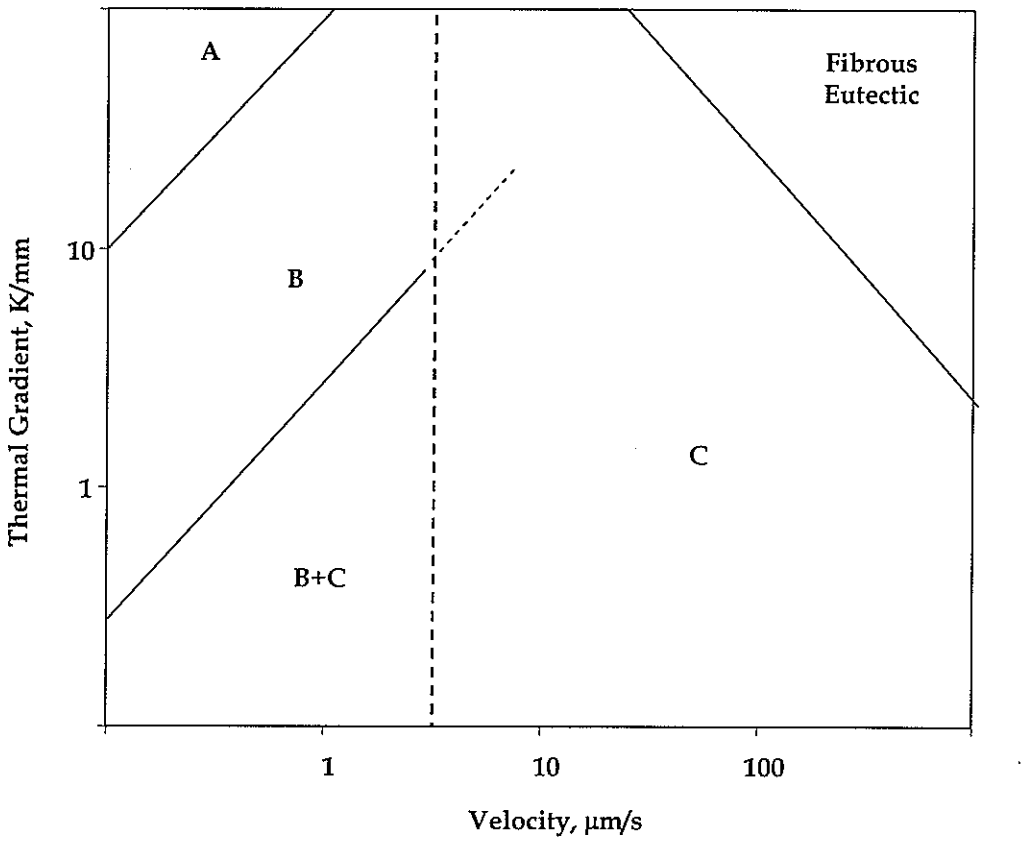

Figure 2-14. The effect of growth rate(V) and temperature gradient (G) on prevailing growth mechanisms and the resulting morphologies of Si classified according to Day and Hellawell[90] where the region A, B and C denote A: Long-range diffusion between large Si particle at a planar aluminum front. B: Short –range diffusion between Si fibers and varioius plate-like morphologies possessing <100> texture. C: Short-range diffusion between Si particles containing multiple {111} twins.

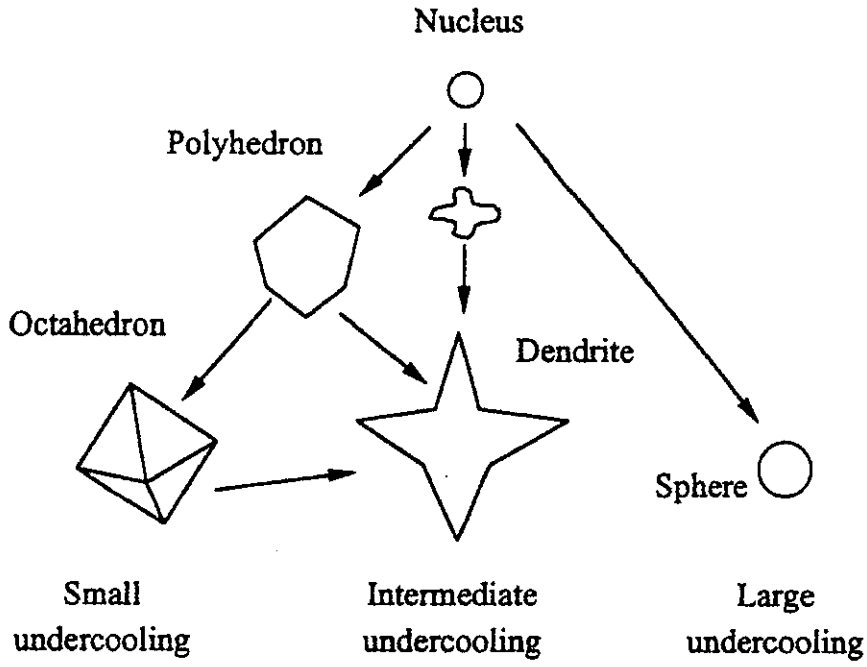

Figure 2-15. Summary of growth morphologies of pure silicon at the different undercoolings. From the reference [103].

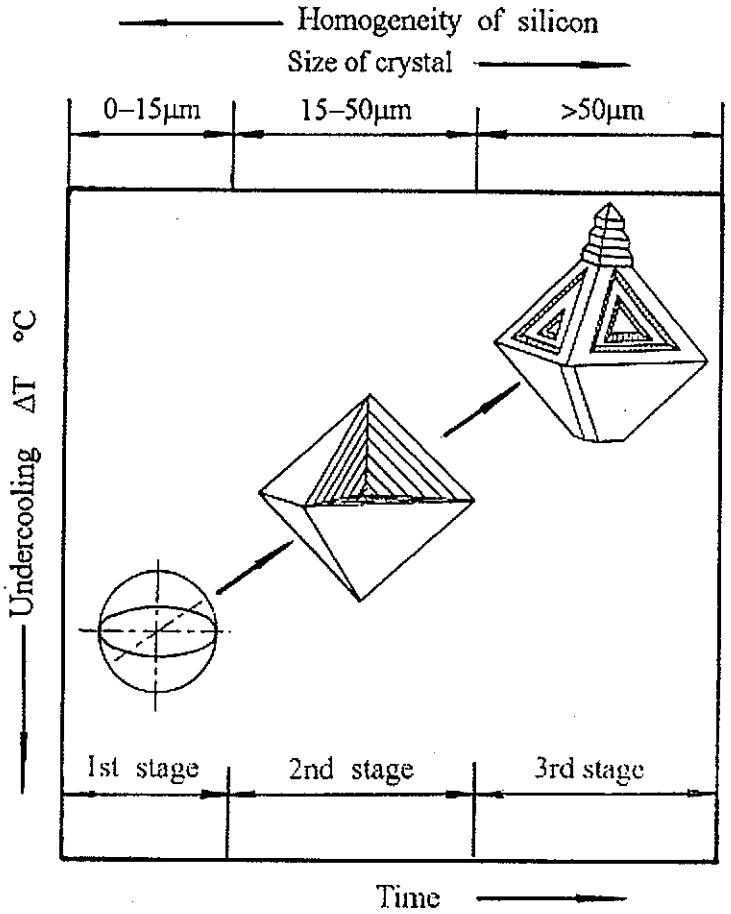

Figure 2-16. Various silicon growth mechanisms in hypereutectic Al-Si alloy, showing spherical, octahedral, and hopper-like growth. From the reference [104].

CHAPTER 3

Motivation, Objectives, and Significance

3.1 Motivation

Although transition from normal flakes to angular morphologies has been reported by several authors, they approached this transition by examining the morphology itself, as a kind of eutectic morphology. There is, however, no clear evidence that the star-shape Si is a part of coupled growth because a coupled zone may be unclear at low growth rates and undercooling. In addition, because the silicon phase grows with a diamond-cubic structure with strongly anisotropic interfacial properties, a fundamental understanding of critical contributions of these interfacial properties and non-intrinsic defect-assisted growth mechanisms is essential to describe a growth mechanism of primary Si as well as its effect on overall microstructure evolution of Al-Si alloys.

Due to the intrinsic interfacial properties of faceted Si, kinetically limited growth is favored in near eutectic Al-Si systems. Therefore, crystal defects might play a role in critical responses to external driving forces. Particularly, it is uncertain why and how twin formations have an influence on the branching and lateral propagation of star-shaped Si rods observed at low growth rates. Furthermore, subsequent questions regarding atomistic structures of twin boundaries are arising. Atomic attachment to the crystal-melt interfaces, on the order of interatomic thickness, might be important for twinning events during growth. Here, arising questions from the distinct twinned faceted primary silicon array evolution are summarized:

- Where can we observe the transition from the normal flakes to angular silicon morphology?
- What is the structure of dominant 8-pointed star-shaped primary silicon and how does it evolve from the non-faceted/faceted crystal-melt interfaces in Al-Si alloys?
- How does twinning of silicon influence on the overall structure of star-shaped silicon and what is the role of twinning in growth mechanisms?
- What are the mechanisms of lateral propagation of relatively regular faceted silicon array?
- What are the mechanisms of branching and spacing adjustment of primary silicon dendrites?

- What is the overall growth mode of this faceted silicon bicrystalline array and what is exactly happening at the vicinity of the growing primary tip?

3.2 Objectives

It is hoped that an understanding will be developed regarding the possible ways twins affect the overall microstructure selection process which gives rise to the observation of textured regions of star-shaped silicon particles. The structure of the star-shaped silicon raises a number of questions with regard to its propagation mechanism. These questions are: (i) what is the underlying mechanism that gives rise to lateral propagation of textured starshape domains, (ii) how do these dendritic bicrystal arrays adjust their spacing, (iii) what is the underlying reason for the selection of the textured star-shape domains over the irregular eutectic morphology, and (iv) what is the exact role played by the twins within the core? In order to answer these arising questions and understand overall growth mechanisms of faceted primary silicon growth, several sub-objectives are summarized here.

- Investigation of texture and grain evolution related to lateral propagation of faceted silicon in Al-Si alloys at low growth rates during directional solidification.
- Study of splitting and branching mechanisms associated with twinning in the core of primary 8 pointed star-shaped morphology.
- Three dimensional characterizations for branching and splitting of star-shaped Si rod and reconstruction of the crystal-melt interfaces.
- Observation of detailed interface structures and coherent twin boundaries in eight pointed angular silicon and atomistic structure studies for the role of crystal defects in morphological selection and local spacing adjustments in faceted silicon array.
- To develop an overall growth model of primary faceted Si array in near Al-Si eutectics that grows in kinetically limited conditions.

Based on these objectives, appropriate scientific strategies will be set up in the next chapter.

3.3 Significance

It is well known that most metallic systems are generally non-faceted and have relatively low interfacial free energy and weak anisotropy. Therefore, various microstructures can emerge because of the high responsiveness of non-faceted interfaces with respect to thermal fluctuation and local solute distribution, resulting from their rough surface in atomic scale. Faceted crystal-melt interfaces, however, cannot respond easily to local solute or thermal field due to the strong

anisotropic interfacial properties. In this case, crystal defects play very important role in microstructure evolution. The solidification microstructures of Al-Si eutectics are controlled by the kinetically limited faceted silicon phase. Indeed, silicon twinning plays critical role in determining the overall microstructure in several Al-Si growth modes. At low growth rates studied here, twinning occurred in the growing primary silicon tip governing the morphological selection, branching, and array evolution, eventually enabling the growth mode transition from the normal eutectic flakes to the angular silicon morphology.

In a nutshell, the most significance component of this morphological transition regime is the twinning within the dendritic core due to the kinetic constraints of the faceted crystal-melt interfaces. Thus, mechanistic nature of crystal defects must be cooperated with morphological selection of the primary angular silicon in Al-Si near eutectics. In this work we establish a hybrid mechanistic and morphological selection phenomenon and make a direct connection between the atomistic structure of the twin boundaries on the growth interface, twin boundary migration during primary growth, the mechanism of sideplates formation, and evolution of the overall primary morphology. Such connection may be a critical step in the understanding of growth phenomena in more complex phase, such as multifunctional or coupled-response materials. Thus, the importance of the twinned-dendrite growth mode investigated here is discussed below.

(1) Morphological selection of faceted Si

The solidification microstructures observed in Al-Si alloys vary widely, and various silicon morphologies can exist at different process conditions as summarized in the previous literature review. This variety exhibited by this system can be attributed to the irregular faceted-nonfaceted nature of the eutectic, and more specifically to the rate-dependent transitions in the operative growth mechanisms for the silicon phase. Both impurity and quenching modifications have been extensively studied with respect to the morphological selection of silicon, associated with twinning and kinetic roughening effect, respectively. However, an understanding of the mechanisms and kinetics of Si growth and branching within the various microstructures of Al-Si alloys remains as the principal barrier to the development of a more general growth theory for this system, where a faceted phase leads the overall crystal-melt interfaces. Accordingly, morphological transition from flakes to angular Si at low growth rates can give us more understandings for microstructure evolution with faceted crystal-melt interfaces.

(2) The role of twinning in faceted crystal growth

Through a careful examination of the twinned core of eight-pointed star-shaped bicrystalline silicon, detailed twin boundaries in the diamond cubic structure of silicon will be

clearly shown. Based on the geometry of coherent twin boundaries, we can understand how twinning occurs in the core. Although it seems certain that the presence of twins at the core affects the overall growth morphology and kinetics, their exact role and formation mechanisms are not well understood. Therefore, investigating twinning and its role during growth is the focal point of this study. Indeed, we can learn how the crystal defect contributes to faceted crystal growth and what is happening exactly in the core during the crystal growth.

(3) Branching and lateral propagation of primary silicon array

Mechanisms of lateral propagation of strong textured array and spacing adjustments of primary silicon dendrites will be obtained. Branching and spacing adjustments of faceted primary phase have never been studied before. For instance, eight-pointed angular silicon has been thought as a kind of eutectic morphology without serious considerations of diffusion coupling or cooperative growth of two phases. The conventional irregular eutectic models, however, cannot be applied to the relatively regular silicon array in this study. Therefore, mechanisms of propagation and branching of silicon can lead us to the deeper understanding of diffusional optimization of primary faceted array.

Identical faceted primary silicon array and distinct 8-pointed dominant star-shaped silicon morphology have been observed in this study. The critical observations above imply that the multiple length scales from the atomic structure to macroscopic texture as well as time scales from atomic attachment kinetics to array evolution are associated with morphological selection and microstructure evolution in the dynamic sense. It should be also stressed that this fundamental research of faceted primary growth will lead not only a rigorous scientific understanding but also engineered microstructure evolution of faceted materials. Due to the intrinsic characteristics of faceted crystal-melt interfaces of silicon, crystal defects may have to emerge at the interfaces for partitioning of the local extrinsic variables, finding the efficient way of solute/heat diffusion. Twinning in silicon has been intensively studied in the case of twin-assisted growth and branching of eutectic flakes/fibers and primary hopper-like morphology of hypereutectic Al-Si alloys. In this study, further understanding of the role of crystal defects in faceted silicon growth will be obtained. Furthermore, a self-optimization of twin-assisted bicrystalline dendrites may be important in the industrial crystal growth process of composite materials that need to be designed with certain crystallographic orientations with a regular array structure.

CHAPTER 4

Scientific Approach

As described in Chapter 3, in order to understand texture evolution/domain structure of faceted silicon array, detail structures of 8-pointed star-shaped silicon bicrystalline and its core, mechanisms of lateral propagation and spacing adjustment, characteristics of branching and splitting of silicon dendrites, and the overall growth mode selection of kinetically limited growth of Al-Si alloys, we perform directional solidification experiments, characterization of morphology and crystallographic orientations of twinned bicrsyal, and comparison of experimental with theoretical calculations.

In this section, detailed technical plans are categorized into three major parts. First of all, solidification experiments to obtain samples for characterization of morphology and other useful information such as general crystallography of directionally solidified Al-Si alloys with and without a seed will be covered. Second, various morphology characterization techniques are treated to understand morphological selection and growth mechanisms of primary Si and detailed crystallography of twinned Si bicrystalline. Third, based on above experimental plans, spacing, composition, and phase fraction at the vicinity of the primary tip region measurements will be measured for the comparison to the theoretical expectations. Through this comparison, overall strategy of modeling a microstructure evolution in near eutectic Al-Si alloys will be proposed.

4.1 Solidification experiments

The Al-Si rod samples were prepared from pure Al (99.99%) and Si (99.99%). Alloys with near eutectic composition (13wt% Si) were obtained by melting Al and Si under vacuum in a graphite crucible. In addition, compositions of 11, 12, 14, and 15 wt% Si are selected for coupled zone experiments of Al-Si alloys. The samples were arc-melted and direct-chill cast into rods of slightly over 5mm diameter and then swaged to approximately 5mm.

The rods were inserted in Alumina ampoule with 5.5mm diameter and the directional growth experiments were carried out at velocities ranging from 0.5μm/s to 10μm/s in order to reach the region where star-like Si morphology can occur using the setup illustrated in Fig.4-1. In addition, an Al single crystal seed was used to evaluate how a single grain of Al effects the texture development of Al-Si alloy. When 2mm of the single crystal seed was melted, the

interface was allowed to grow. The furnace was held at least for one and half hour at 1173K and the ampoule was immersed into the cooling chamber for the purpose of achieving good thermal conditions. Once the travel distance was over 6cm, the sample was quenched immediately at a velocity of 17mm/s for the normal condition and 71mm/s for the "rapid quenching" experiment. The whole procedure of growth and quenching was controlled by the computer system (XWARE4.0) to avoid any error.

4.2 Characterization techniques

4.2.1 Sectioning and serial milling

Each directional solidified sample was sliced every 0.25 or 0.5mm from the initial point to the quenched interface to examine time evolution of microstructure and crystallographic orientation by conventional diamond wheel saw machine and metallography. In addition to the conventional sectioning, ultra serial milling technique has been used as summarized[108] in Fig.4-2. This sectioning method is for detailed 3-dimensional analysis of faceted silicon bicrystal, especially for branching, splitting, and lateral propagation of twinned bicrystal morphology during the directional growth. Images of cross sections in z-direction (growth direction) in Fig.4-2 were taken at regular intervals of 4~5 microns or more by ultra-milling using attached optical microscope to keep the position at every sectioning sequence. These sequent images merged, aligned, and reconstructed using Image Pro as shown in Fig.4-2.

4.2.2 Microstructure analysis

Optical microscope and electron microscopes are main equipment for the microstructure analysis in this study. Detailed defect structures and crystallography in Al-Si alloys has been investigated using several types of electron microscopy such as SEM, TEM, OIM, and μ-probe.

A. Optical Microscopy and image analysis

Optical microscopy is a basic tool to investigate a distribution of angular silicon morphology during directional solidification. An image analysis software package (Image Pro Plus 5.0) was used for detailed measurements of eutectic and primary Si. In order to observe Al grains, the well-known Keller's reagent was used. Combining with a serial milling technique, sequential images and three-dimensional reconstruction of microstructure could be obtained to investigate lateral propagation, tip splitting, branching mechanisms, and overall microstructure evolution.

B. Scanning Electron Microscope/Micro-probe

In order to find twin boundaries in the core of Si bicrystal and classify the possible twin boundaries, secondary electron images were used and backscattered electron images are taken to verify the twin boundaries. Samples were prepared by a conventional metallograpy procedure without any chemical etching to observe twin boundaries in the core stem. In addition, interfacial morphologies of primary silicon were characterized by chemically removal of Al phase at the quenched crystal-melt interfaces using Keller's reagent with a composition of (by volume) 2.5% HCl, 1.5% HNO_3, 1% HF and balance H_2O.

For the composition analysis at the crystal-melt interfaces, electron microprobe microanalysis (EPMA) was used combining serial milling technique. Average liquid compositions as a function of distance to the primary tip were obtained as well as other useful composition profiles in the microstructure. The beam condition of μ-probe are 5Kv and 1μm step for a high resolution of chemical analysis. In addition to above microscopes, a high resolution TEM has been used to verify the twin boundaries in the central stem of dendritic silicon.

C. Electron Backscattered Diffraction Pattern Analysis

OIM (Orientation Image Microscope)[109] is a very powerful and convenient tool to examine crystallographic orientations of materials. A detector for backscattered electrons can be attached to the conventional SEM without dedicated equipment setup for orientation analysis. The sample preparation is also easier than that of TEM. This microscope has many advantages to examine detailed crystallography of primary Si and its branching and propagation because Si has a strong anisotropic interfacial properties and a complex twinning nature in its growth. In this study it has been used for two main purposes. First, texture analysis was performed at a sectioned sample as a function of growth distance. Second, detailed twin boundaries of eight-pointed star-shaped Si were investigated, mapping the Dingley patterns into Inverse pole figure images by computing Euler angles through the computer software. Overall scheme of OIM is given in Fig.4-3.

4.3 Microstructural analysis

Most of growth theories for morphological evolution such as dendrite, cellular, and eutectic are generally divided into two categories. The first is the characterization of the conditions at the tip of an advancing cell or dendrite. The second is the description of all of the phenomena which occur in the two phase region behind the tip, where the microstructure evolves. These two areas are then related simply because they are each described in terms of the

same principal solidification parameters which are the growth velocity and the temperature gradient.

In order to describe mushy zone phenomena, various relationships describing the prevailing growth conditions in terms of V, G, and ΔT have been developed before. In the case of dendritic growth, a tip radius, R, is a well-known parameter that describes a local equilibrium. This parameter can not be used because of a difficulty of measuring R as well as intrinsic nature of faceted Si. In this study, primary spacing, inter-plate spacing, interdendritic liquid composition, and phase fraction as a function of distance to the growing tip were measured and compared with analytical models. In the following subsections, several microstructural analyses conducted to quantify the above variables and phenomena in this study will be summarized.

4.3.1 Quantification of primary silicon tip

During the array evolution of faceted primary bicrystal, the growing tip is the most important part in morphological section of overall microstructure. Therefore, primary spacing measurements and analysis of primary silicon array gave us much more understanding of the tip dynamics.

A. Eutectic and primary spacing

Eutectic spacing parameters were measured on transverse sections taken from at least 40 local areas at a location within 10 mm of the quenched interface using the line intercept method. The number of Al/Si boundary intersections per unit length N_L was directly measured and averaged. This spacing indicated the average inter-plates spacing. For an array of faceted Si, the primary spacing of star-shaped Si was also measured at the same microstructures. To obtain reliable data, consistent rules were applied for measuring. Note that only distances between two stems were counted in when no plates from the tertiary star-shaped silicon interrupted the straight line between them.

B. Statistical and numerical analysis of primary silicon array

In addition, the statistical and numerical analysis has been possible for primary silicon particles such as Voronoi polygon and Minimum Spanning Tree (MST) that are broadly used in primary dendrite morphologies. Ordering in the primary array at various distances from initial growth interface was quantified by using minimum spanning tree (MST). In the MST approach, all points were connected without any closed loop, giving a minimum total length as described in Fig.4-4. For that purpose, Prim's algorithm was implemented in order to find the tree connecting all dendrite cores for which the sum of the edge lengths was minimal. Here, the distribution of

edge lengths was unique, and the average edge length (m) and the standard deviation (σ) were characteristic of the arrangement of points. Any irregularity in the arrangement of an array, as determined by the MST approach, can be descriptive of the array selection. The positions of the silicon dendrite cores were digitalized on sequential transverse cross-sections and were used in MST calculation of the degree of array ordering during growth. The degree of ordering in the growing array of dendrites has informed us qualitatively about the possible spacing adjustment mechanisms controlling the diffusive optimization processes.

Voronoi tessellation has been used to examine the degree of disorder in the distribution of faceted silicon array in this study. Voronoi tessellation is a mathematical method of partitioning space with several points by drawing the smallest convex polygon from bisectors of every point in the space as described in Fig.4-5. Every point in a given polygon is closer to its origin point than to any other primary positions. Therefore, the number of sides of a Voronoi polygon in the array provided the useful information of neighboring points.

C. Volumetric approach

Due to the limitation of experimental and theoretical measurements of tip temperature and tip radius for the faceted silicon tip, volumetric approach has been introduced in this study. Using serial sectioning at the quenched crystal-melt interfaces, phase fractions for Al, Si, and liquid phase have been measured as a function of distance to the tip. This volumetric quantity might be another quantity for the tip condition. In this study, between secondary branched plates from the core, Scheil model was applied for the simple non-equilibrium solidification of Al phase since the sideplates spacing was less than approximately 50 microns and remaining interplate liquid might be considered fully mixed with no solid diffusion.

4.3.2 Core structure of twinned bicrystalline

It was essential to examine the core structure to understand morphological selection and spacing adjustment of faceted silicon array because crystal defects may play critical role in array evolution including lateral spreading, sideplates branching, and diffusional optimization of array. We have classified and verified twin boundaries in the dominant 8-pointed star-shaped morphology, combining electron microscopies and statistic analytical method to quantify the distribution of coherent twin boundaries in the core. In addition, twin boundary migration in the core has been confirmed by the time evolution of twin boundaries.

4.3.3 Chemical analysis

Composition profiles in the vicinity of the primary tip have been analyzed by the micro-probe mentioned above. Two main areas were selected to measure average Si compositions in Al and liquid phase, as a function of the distance to the tip, by the area mapping with the beam conditions of 5KeV and 1μm step. Here, a serial milling was a key procedure for the construction of composition profiles. Combined with phase fraction measurements at the same area, the phase fraction has given rise to understanding of the overall growth mode selection of Al-Si near eutectic alloys at low growth rates.

Summary

Directional solidification experiments, characterizations of microstructure, and computational techniques have been performed to understand morphological selection mechanisms and crystallographic orientations of 8-pointed star-shaped Si bicrystal. Combining all of data we could get and analyze as summarized in this chapter, we have understood mechanistic/morphological selection of twinned bicrystalline Si and have successfully shown the role of mechanistic twinning in the growth of twinned bicrystalline dendrites. In addition, we have explained the overall growth mode of microstructure evolution of near eutectic Al-Si alloys at low growth rates and proposed the appropriate approach to establish a strong analytical and numerical model for the faceted silicon bicrystalline array, based on the measurements summarized here.

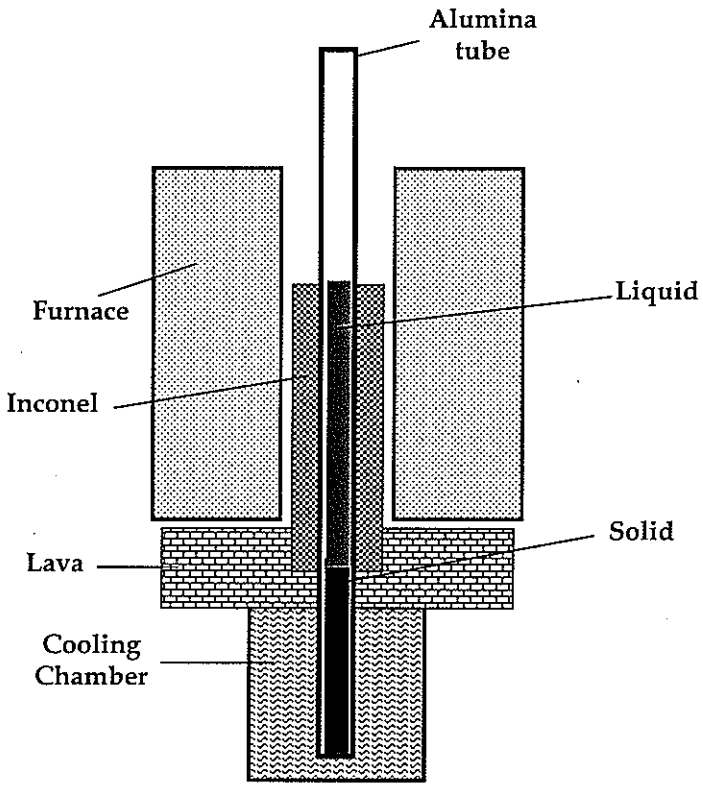

Figure 4-1. Schematic of the directional solidification experiment.

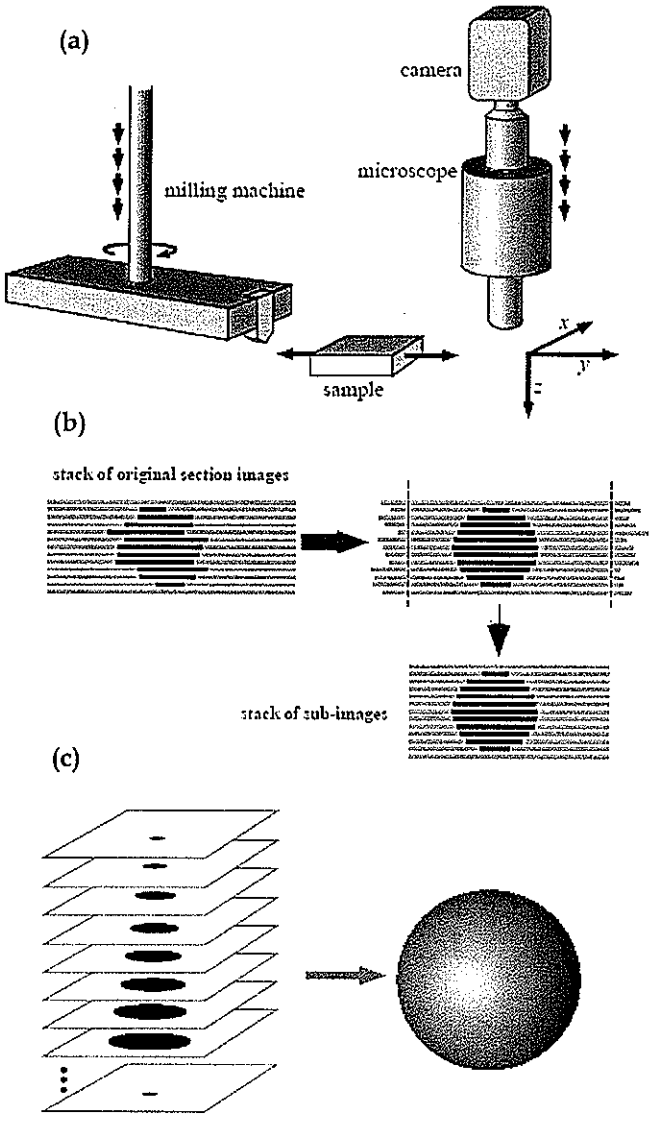

Figure 4-2. (a) Schematic illustration of serial sectioning procedure, (b) alignments of images procedure, and (c) The three-dimensional reconstruction can be achieved from the stack of cross sections[108].

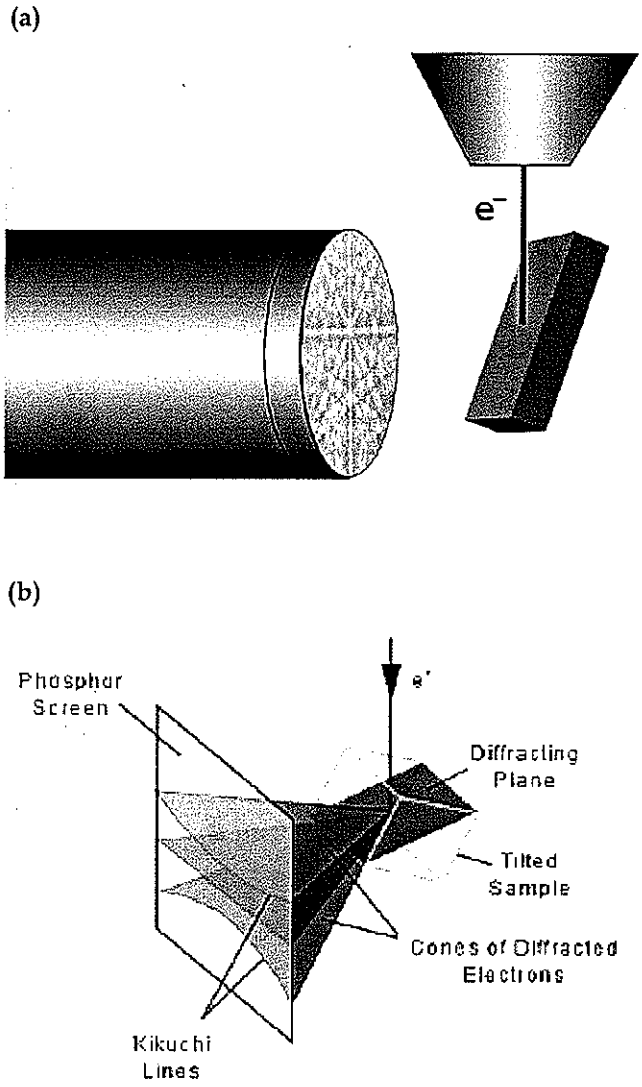

Figure 4-3. Illustrations showing principle of Orientation Image Microscope. (a) Sample is tilted 70degrees with respect to the horizontal and the diffraction pattern is imaged on a phosphor screen. (b) The bands in the pattern represent reflecting planes in the diffracting crystal volume[109].

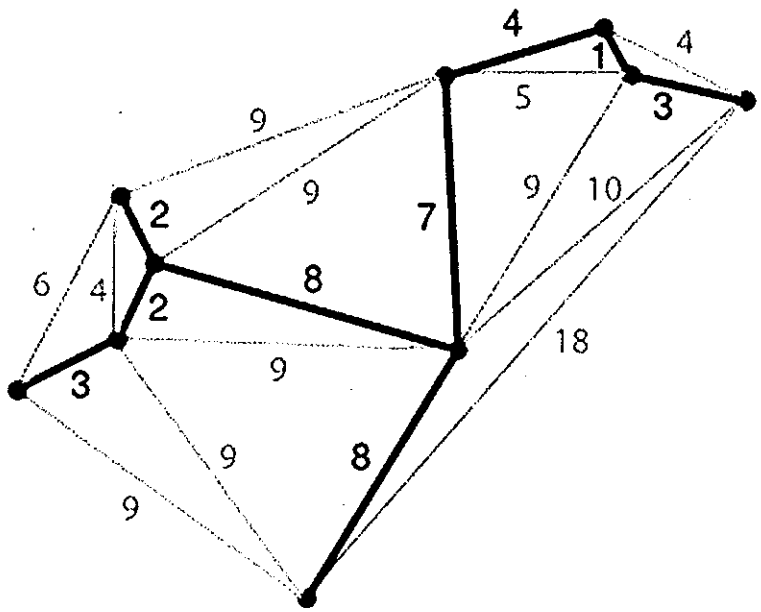

Figure 4-4. An example of MST (Minimum Spanning Tree). Here, the numbers indicate length between two points and thicker segments are spanning tree, providing the minimum total length without any close loop.

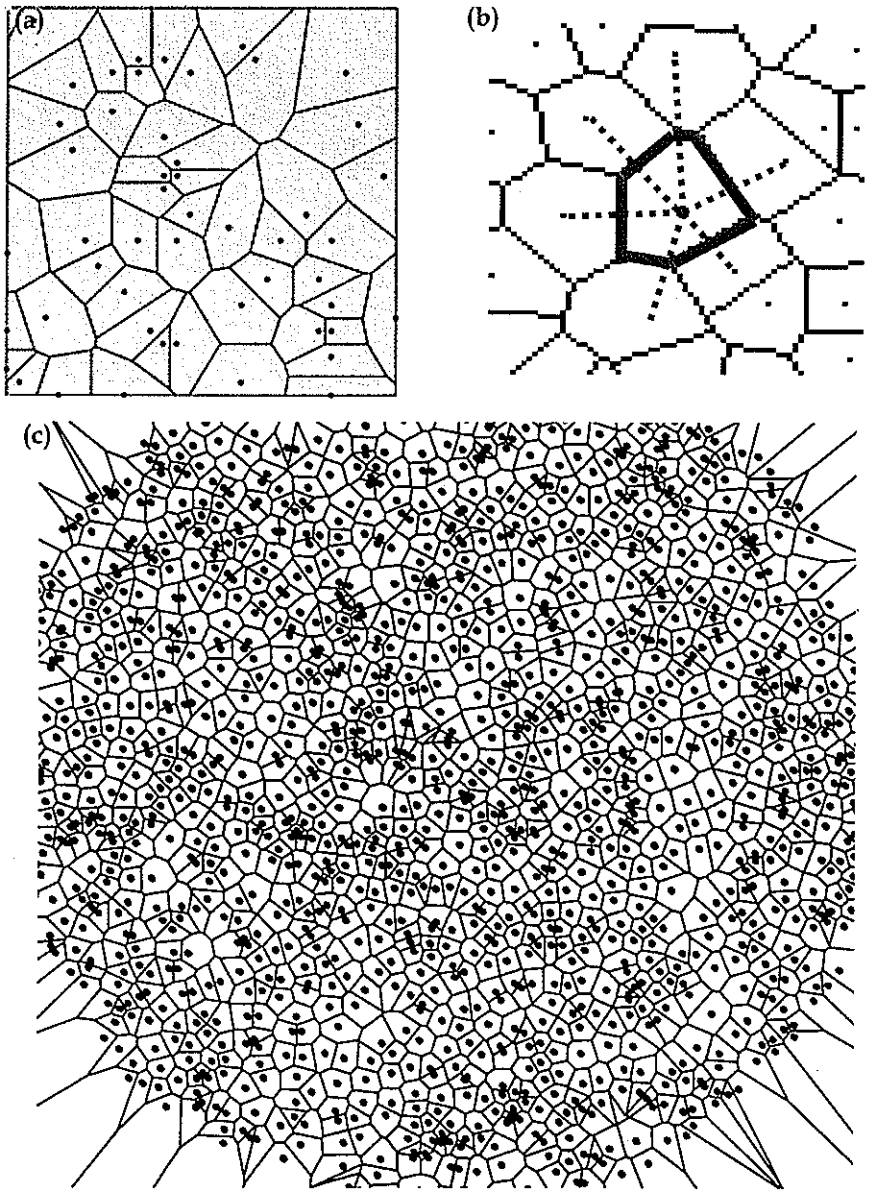

Figure 4-5. (a) An example of Voronoi polygons from random points (b) The point has a neighbors in this case and each side of the polygon is the bysector of two adjacent points. (c) A constructed from the real whole cross section of silicon array, for example.

CHAPTER 5

Morphological Selection and Texture Evolution

The overall selection of the star-shaped primary silicon structure is discussed in this chapter. This includes the initial emergence of the <001> textured star-shaped grains and the evolution of the associated domain structure. In subsequent chapters, the detailed structure within the dendritic core is examined, along with spacing adjustment mechanism and tip phenomena.

5.1 Morphological transitions

The Al-Si alloys exhibit a wide range of eutectic solidification structures. The most common of these structures includes a faceted flake-type silicon morphology, as shown in Fig.5-1(a). This classic example of a faceted-nonfaceted irregular eutectic is commonly observed in conventional shape castings, where no specific refinement modification has been made. Trace ternary additions of certain elements (e.g. Sr, Na, Ce), result in another common eutectic structure, where the kinetic effects give rise to a fibrous or rod-type Si morphology. Without such ternary modifications, a flake to fiber transition is also observed at high growth rates, typically between $5x10^{-4}$ and $1x10^{-3}$ m/s, as shown in Fig.5-1(b). While the fibrous morphologies resulting from ternary modification and from high velocity growth appear to be generally similar, the mechanisms by which they form are indeed very different, and these differences have been reported by several authors [5,6] and summarized in the literature review of Chapter 2.

Beside the importance of morphological transition by modification, faceted crystal-melt interfaces select interesting silicon morphologies at kinetically limited growth conditions, due to the strong anisotropic interfacial properties of silicon, resulting in the restriction of certain crystallographic orientations. A transition from the flake-type Si morphology to a more connected angular or script morphology than flakes is observed as the velocity drops below approximately $2x10^{-5}$ m/s, as shown in Fig.5-1(c). Here, we observe that, with decreasing velocity, the spacing between the "stems" of the eight-pointed star-shaped particles increases and the overall structure of the silicon becomes more disconnected. With further decreases in the growth rate (typically < 1μm/s), the angular silicon morphology becomes increasingly disconnected, giving rise to the distinct star-shaped rod morphology shown in Fig.5-1(d). Furthermore, pictured in Fig.5-1(d), the low-rate mode gives rise to a relatively regular array of star-shaped

silicon rods, each consisting of a set of side-plates extending radially outward from a central core which is oriented along the primary growth direction.

Fig.5-2 shows a microstructure of the longitudinal section of the directionally solidified Al-Si which corresponds to the cross section of Fig.5-1(d). Note that the growth has occurred from the bottom upward. These micrographs were taken near the quenched interface where the steady state growth was reached. In this micrograph, the corrugated plates, which might be a part of growing angular Si plates, have been observed. This interesting growth behavior of continuous zigzag patterns will be revealed within the detailed primary silicon structure in a later section.

Microstructures of transverse sample sections grown at various rates and compositions are shown in Fig.5-3~Fig.5-6. We have observed the morphological transition from flakes to angular in the faceted silicon phase in 13 wt% Si which is very near to eutectic composition (12.6wt%) in Al-Si binary system. Based on these observations in Fig.5-1, it is necessary to find solidification conditions, particularly alloy composition and growth rate because this transition seems to have a kinetic dependency at lower growth rate extreme. The similar morphological selection has occurred in 11, 12, 14, and 15 wt% Si, off-eutectic compositions as shown in Fig.5-3, 4, 5, and 6, respectively. The interesting observation of morphological selection of the dominant 8-pointed star-shape is that lower growth rates are needed at hypoeutectic composition. The 8-pointed star-shape is, however, dominant angular silicon morphology in all compositions performed in this study around 1 μm/s growth late. Moving to slightly higher growth rates regime, the transition from flake silicon to the angular morphology has been observed between 7 and 8μm/s growth rates, for example, as shown in 14wt% Si microstructures of Fig.5-7. No angular silicon morphologies have emerged at 8μm/s. Though the transition regime of flakes to angular silicon has not been investigated for all alloy compositions, a similar exposure of new growth mechanism of faceted silicon has observed at 13 and 15 wt% compositions. It should be mentioned that all results are done at the same temperature gradient (7.5mm/K). The significance of this morphological selection at the low extreme corresponds to the transition from flakes to fibrous morphology by the impurity modification in terms of the role of twining in the morphological selection mechanisms. This key issue in faceted silicon crystal growth with respect to the twining will be comprehensively studied in the subsequent Chapters 6 and 7, based on the thorough analysis of its structure and branching.

5.2 The twinned bicrystalline morphology

We now examine the detailed structure of the star-shaped silicon particles. The angular star-shaped silicon rods, shown in the cross-section, Fig.5-1(d), are typically comprised of long plates which are approximately 10 microns in thickness. The plates extend radially from a central stem or core, which may be compact and roughly cylindrical or elongated and irregular in shape. The angular rods tend to have eight side-plates, but fewer or more side-plates are commonly observed. A typical eight-pointed star-shaped rod is shown in Fig.5-10(a), revealing that the angle between side plates typically alternates between 37°and 53°. This angular relationship between sideplates is generally observed in all of the silicon particles at low growth rates.

In Fig.5-8, Kikuchi patterns produced by backscattered electron diffraction reveal that there are only two different orientations from all 8 points of each side arm. The pole near the center in (a) and at right-center in (b) is the [011] pole. The {001} and {011} great circles are shown with dashed lines in two different colors. Consequently, each of the side-plates extends radially in a <100> direction. The solution of two distinct Kikuchi patterns in Fig.5-8 suggests that the star-shaped particle indeed consists of two interpenetrating four-pointed stars, each of a single crystallographic orientation, with a rotation between the two sets that is consistent with {210} twinning. Note that the normal growth direction, [001] pole is indicated at the upper-right of the solutions in Fig.3-3. The alternating orientations are shown with optical image of 8-pointed angular silicon in Fig. 5-10 (a) and the constructed [100] projection indicates that two grains are sharing the {210} type twin plane with 37° and 53°, off-set angles as shown in Fig.5-10(b).

From the previous EBSD patterns It is deduced that two grains (each a 4-pointed subunit) compose the overall 8-pointed star-shape structure. In Fig.5-11, interpenetrating grains are clearly seen and the silicon phase, in a given textured domain, is comprised of two interpenetrating four-pointed stars which themselves consist of two sets of intersecting planes and extending along the primary [001] axis. In addition, it has been observed that silicon orientations of each grain are all identical to each other. A question arises here regarding how exactly two grains interpenetrate each other in the central stem and have the same identical orientation in the given domain. To answer this, a careful three dimensional structure analysis must be performed to proceed into detailed core structures. This will be done in the subsequent chapter.

5.3 Strong selection of the twinned bycrystalline morphology

The first careful examination of the low velocity Al-Si eutectic morphologies was reported by Day and Hellawell[90] as summarized in the review section. Most notable observation

of their research is a strong <001> Si texture with angular silicon shape. This texturing phenomenon has transient characteristics, in that it evolves from randomly oriented Si particles for typical growth as shown in Fig.5-12. It is shown that (a) randomly dispersed silicon and (b) star-shaped domain coexist in the transverse section at 10 mm grown at 0.92μm/s. Once the steady state is reached, the angular Si particles have all been oriented along <001> directions in the whole cross section as shown in Fig.5-13. This overall <001> texture is revealed by pole/inverse pole figures in Fig.5-14 obtained from backscattered electron diffraction patterns, taken over several regions of inside and outside of the star-shape domain. The pole figures and inverse pole figures in Fig.5-14(a) and (b) indicate that no preferred orientation with respect to the growth direction outside the star-shape domain. Inside the star-shape domain, however, a strong <001> crystallographic orientation is, however, clearly shown in (c) and (d), pole figures and inverse figures from the correspondent 8-pointed star-shaped region. Note that Fig.5-14 (a) and (c) come from the area (a) and (b) in Fig.5-12, respectively. The interesting thing that must be mentioned from the pole figure of (d) is, while the normal direction of the sample indicates a strong <001> orientation, family of 8 different <001> types are also seen along the great circle of {001} planes in the projection. Thus the distribution of family orientations must come from dominant 8 branched sideplates. The orientation of the angle variants corresponds well to the identical orientation of arranged silicon particles of the micrograph at the right side. This also confirms the previous Kikuchi patterns, revealing detailed primary silicon structure.

We have investigated the evolution of the textured morphology during the initial stages of directional growth by the ultra serial milling at every 5μm at the transverse section. The selected microstructures show that <001> texture laterally proceeds as shown in Fig.5-15. The initial solidification front exhibits randomly oriented plates with some angular rod-like features.

In addition to the early stage observations, the entire textured domain evolutions at a velocity of 0.5, 0.92 and 1μm/s were examined by sectioning transversely in increments of 5 mm for the purpose of further understanding of domain propagation during the growth. The sequence in Fig.5-16(0.92μm/s) shows that within the first 10 mm of growth, the textured star-shape morphology begins to emerge. Then, rather than a gradual increase of the preferred <001> texture by the appearance of multiple separate regions of star-shaped silicon, the texture develops essentially as one or two continuous domains of the star-shaped morphology which spread rapidly across the specimen at a relatively high rate. The similar lateral expansion of domains over the complete transient period is illustrated in Fig.5-17, showing that the process is complete after roughly 55 mm (a) and 35mm (b) of axial growth at 0.5 and 1μm/s respectively. In this case, two domains finally survived while there is one single domain in Fig.5-16. The average

rate of lateral expansion during this period was about 0.2μm/s, a significant fraction of the axial velocity (~20%). Moreover, closer examination reveals that the entire textured domain not only shares a common <100> direction, but that the whole domain consists of only a few different secondary orientations or, in some cases, a single grain. This characteristic suggests that the star-shaped structures propagate in a manner similar to the lateral growth of a nonfaceted dendritic crystal by secondary and tertiary branching and indicates the operation of one or more low-undercooling mechanisms for the generation of new central cores. The key issue of lateral propagation of identically oriented primary structure will be discussed in chapter 7, where the structure of the overall array is examined.

5.4 Al-Si orientation relations

In comparison to the preferred orientation of Si texture, the fcc Al phase does not show any orientation dependence to growth direction at low growth rates. For unmodified flakes Al-Si eutectics, the morphology of Si is flakes and the aluminum phase has been shown to be polycrystalline with randomly oriented fine grains. These very small grains give a similar size to inter-flake spacing in its size. However, Shamsuzzoha et al. reported[92] that the aluminum grains with star-shaped silicon are relatively large and extend over several silicon stars.

In the present investigation, no associated texture evolution was observed in the aluminum solution phase, where a fine-grained polycrystalline structure was observed. This is consistent with the observations of Shamsuzzoha et al[92]. and Hogan and Song[80]. Since the formation behavior of Al grains and the transition of grain size might be related to Si spacing and nucleation of Al at faceted silicon plates, there would be numerous challenging studies for grain nucleation and evolution. To begin to investigate this question, we employ a seeded growth method, as described below.

We conducted a set of directional solidification experiments using a <001> oriented aluminum single-crystal seed. A very tiny part of Al single crystal seed was melted and mixed with alloy melts then Al-Si crystal nucleate and evolved from the seed. The microstructure was observed to be very similar to that of samples grown at the same velocity without seeds. The micrographs of the sample grown from a single crystal seed are shown in Fig.5-18. We have seen the clear interface between the Al single crystal and the solidified Al-Si alloy in Fig.5-18 (a) and (c). We have also observed eutectic Al grains as soon as the growth begins. This is shown in Fig.5-18 (a). In addition, the independent Al grains are observed at the side of growing Si in Fig. 5-18 (c). Note that (a) and (b) in Fig. 5-18 are as-cast longitudinal sections while (c) and (d) are chemically etched to see the grain structure of Al phase at the different positions of the same

sample. To summarize our findings, subsequent Al-Si growth was unaffected by the presence of the seed and a randomly oriented fine-grained aluminum phase structure was quickly established.

Even though we have verified the polycrystalline structure of the Al phase, the grain structure and orientation of the Al phase have been examined by orientation imaging from backscattered electron diffraction. An example is shown in Fig.5-19. While strong <100> texture of silicon phase is emerging, no preferred orientation of Al phase has been identified indicating as similar as the result from pole figures in the previous texture analysis. Dominant Al grain structure is slightly low angle sub-grains between secondary branched silicon plates. Two or more Al grains between side branched arms of original star-shaped dendrite, however, have been observed with significantly different orientations at the center of this image with three different colors. Furthermore, one Al grain was never observed to contain two or more silicon rods. Secondary side branching at the right behind of silicon tip may influence on Al grain nucleation and separate Al grains. There is no axial preferred orientation of Al grains, but we cannot rule out the possibility that an epitaxial orientation relationship exists between silicon plates and Al phase. Although this critical issue is out of the scope in this study, we offer this OIM observation as motivation for further research of grain structure and evolution.

Summary of key points in this chapter

- The transition from flake silicon to the angular morphology has been observed between 7 and 8μm/s growth rates. At lower growth rates, typically less than 1 μm/s, the dominant morphology was an 8-pointed star-shape consisting of two interpenetrating four-pointed rods.
- One or more domains of the strong <001> textured silicon array emerged at the beginning and propagated rapidly over the transverse, while Al phase has no axial preferred orientations, exhibiting the polycrystalline grain structure.
- In the given domain, all silicon dendrites are arranged to the identical crystallographic orientation having the same angle variants (37° and 53°) in the individual 8-pointed star-shape.

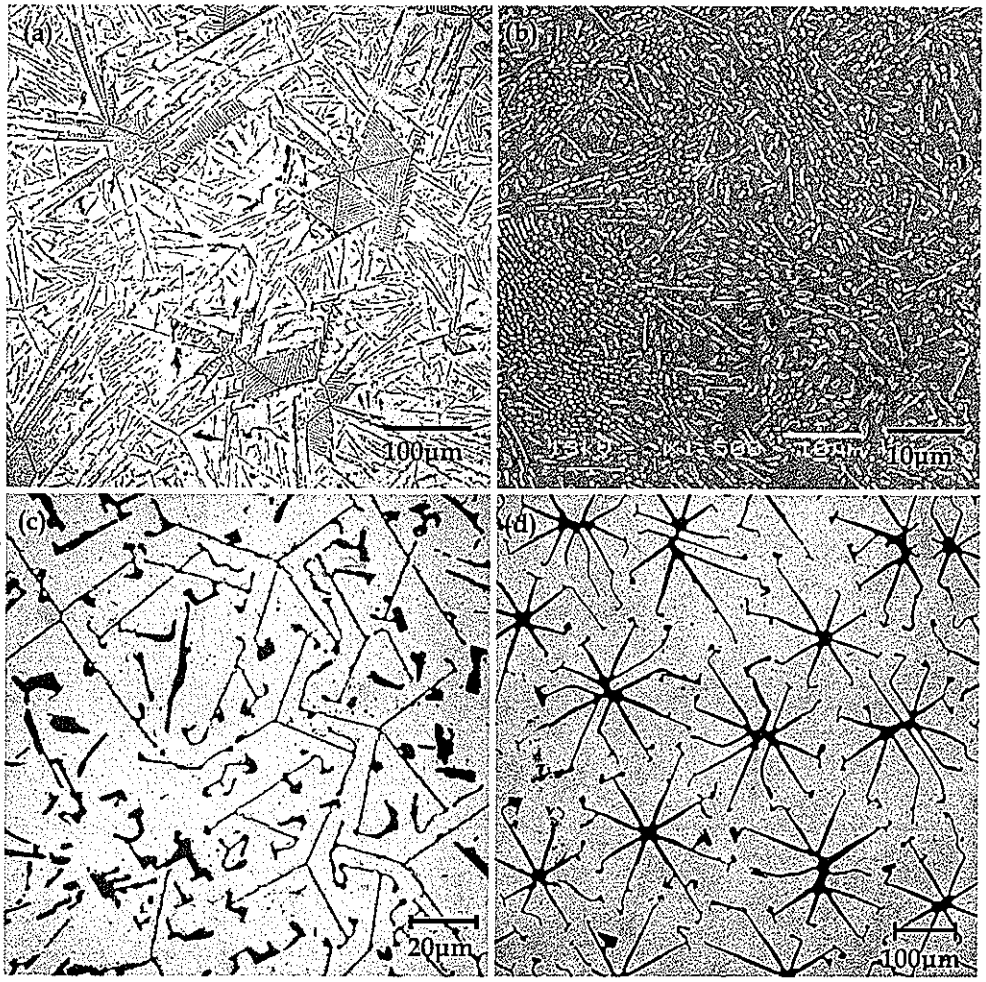

Figure 5-1. Some typical Al-Si eutectic solidification structures: (a) typical flake morphology, (b) fibrous morphology formed at high rates (1 mm/s), (c) angular or script morphology formed at 5 μm/s and (d) at 0.5μm/s.

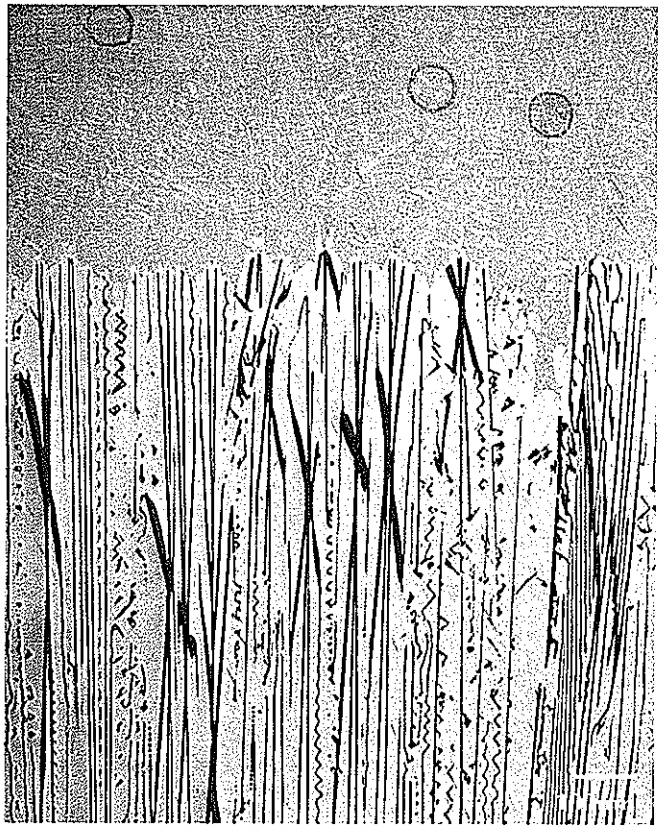

Figure 5-2. Microstructures of longitudinal sections at the quenched interface at 0.5μm/s in 13wt%Si alloy, showing non-isothermal crystal-melt interfaces and aligned silicon plates to the axial growth direction.

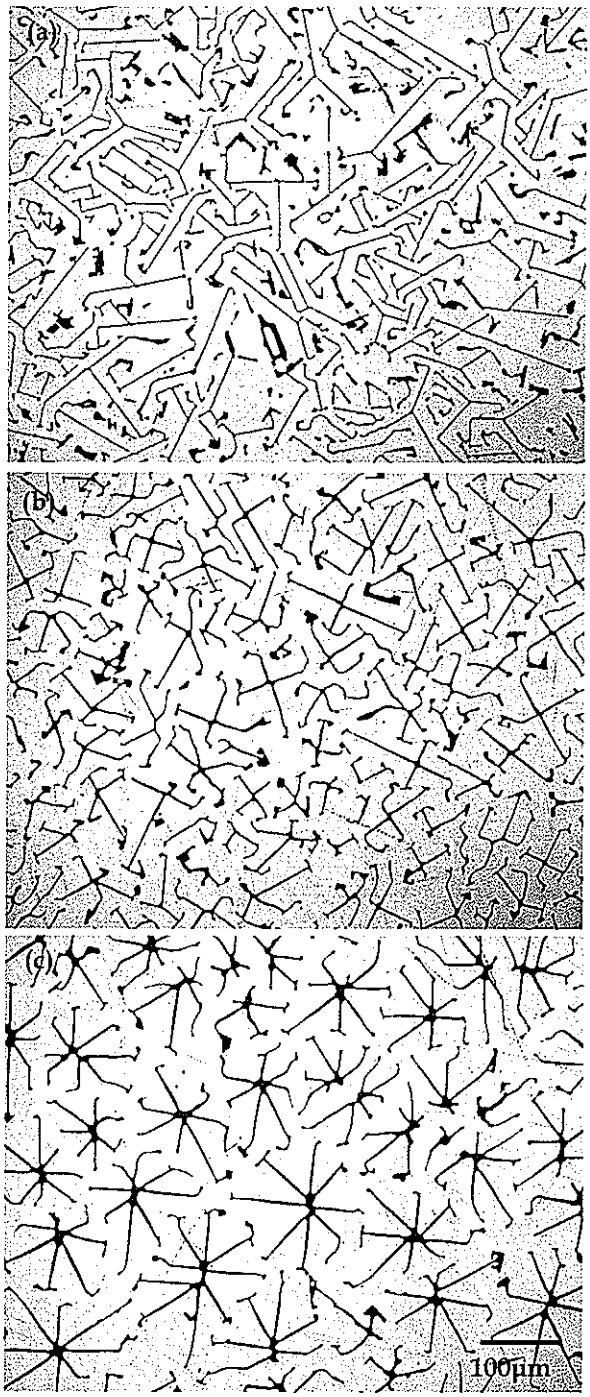

Figure 5-3. The characteristic microstructure in an Al-11wt%Si alloy observed after directional solidification (G=7.5 K/mm) at (a) 2 μm/s, (a) 1 μm/s and (c) 0.5 μm/s.

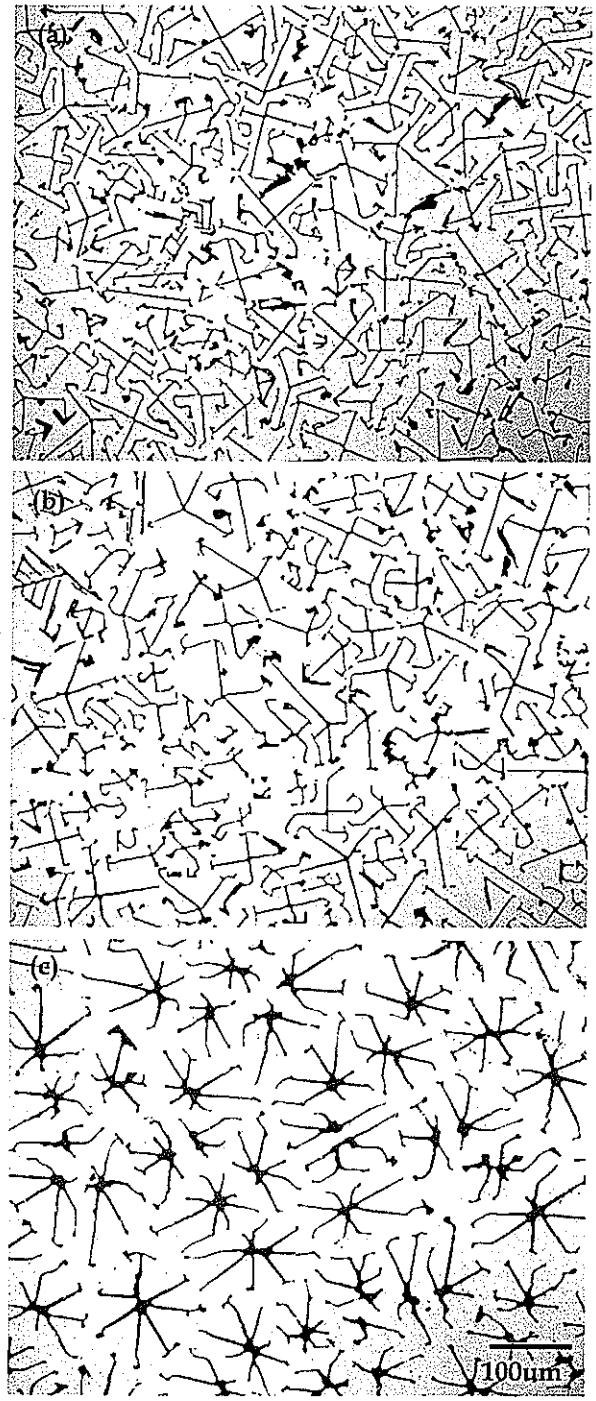

Figure 5-4. The characteristic microstructure in an Al-12wt%Si alloy observed after directional solidification (G=7.5 K/mm) at (a) 2 μm/s, (a) 1 μm/s and (c) 0.5 μm/s.

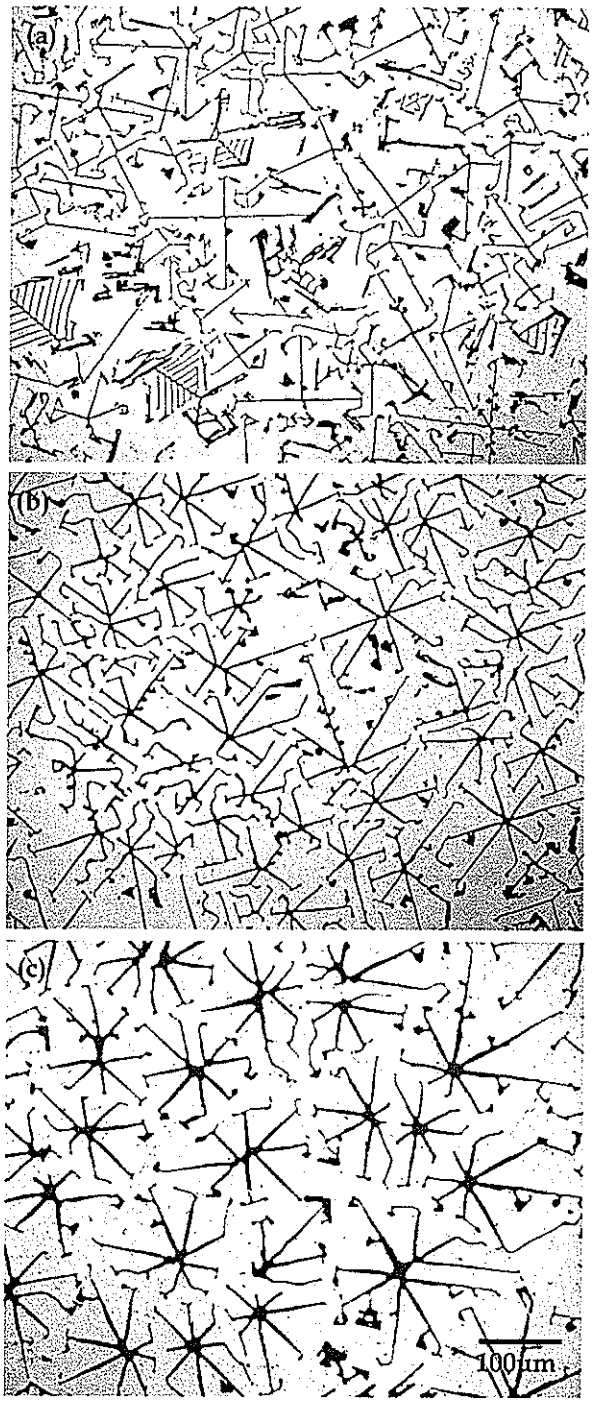

Figure 5-5. The characteristic microstructure in an Al-14wt%Si alloy observed after directional solidification (G=7.5 K/mm) at (a) 2 μm/s, (a) 1 μm/s and (c) 0.5 μm/s.

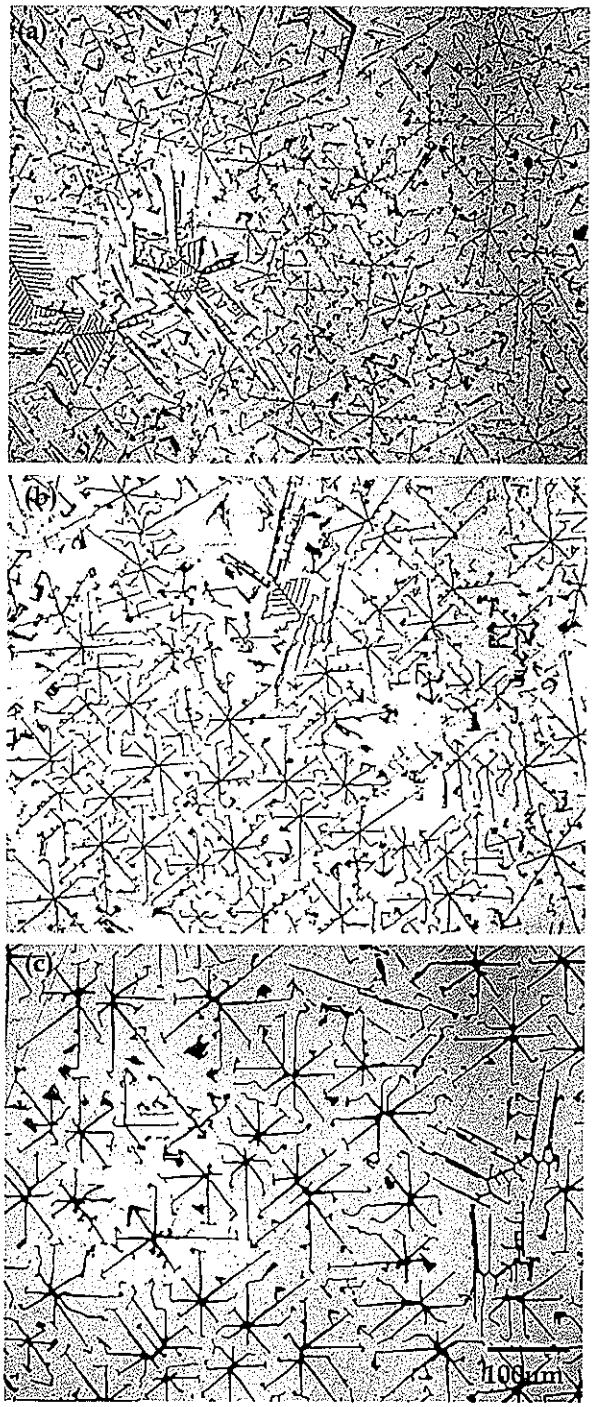

Figure 5-6. The characteristic microstructure in an Al-15wt%Si alloy observed after directional solidification (G=7.5 K/mm) at (a) 2 μm/s, (a) 1 μm/s and (c) 0.5 μm/s.

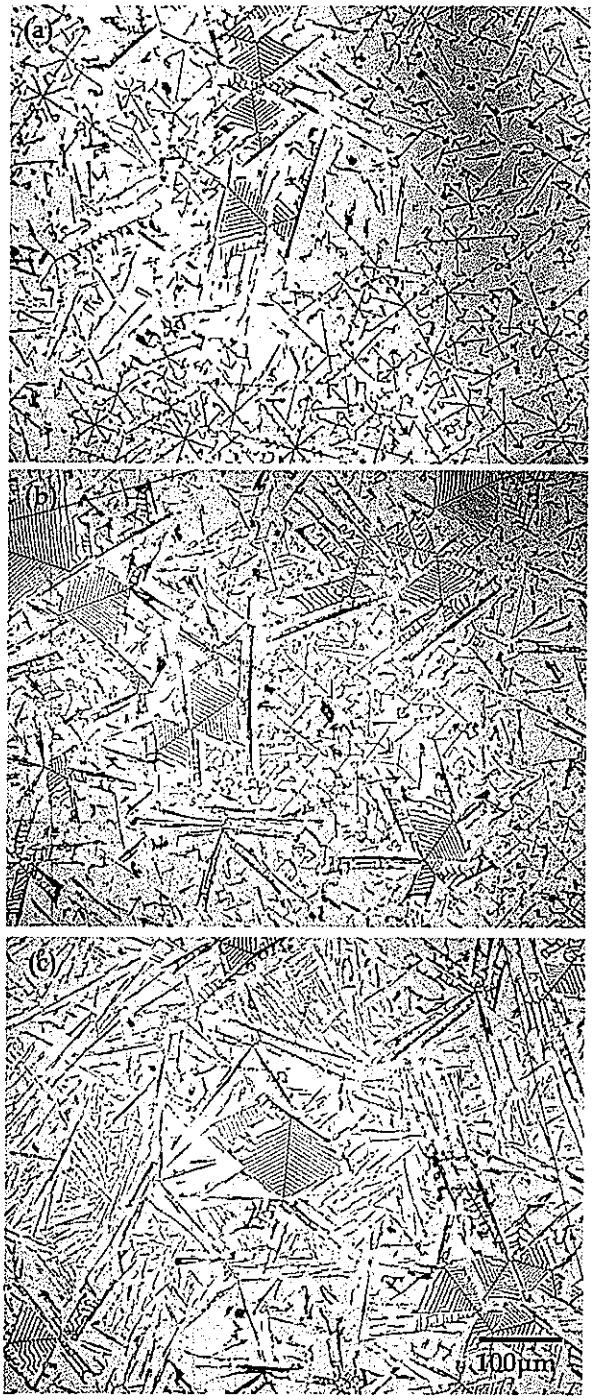

Figure 5-7. The characteristic microstructure in an Al-15wt%Si alloy observed after directional solidification (G=7.5 K/mm) at (a) 5 μm/s, (a) 7μm/s and (c) 8 μm/s.

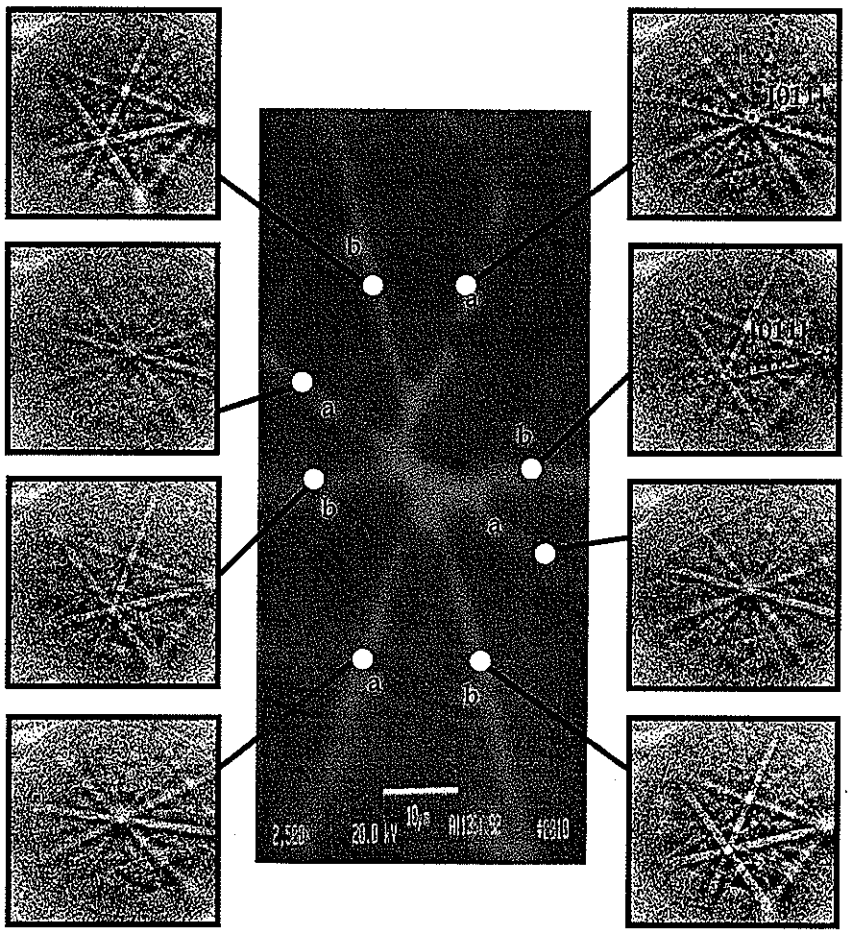

Figure 5-8. Kikuchi patterns generated with backscattered electron diffraction, showing that the star-shaped structures consist of two interpenetrating grains. The pole near the center in (a:blue) and at right-center in (b:red) is the [011] pole. The {001} and {011} great circles are shown with dashed lines in two different colors.

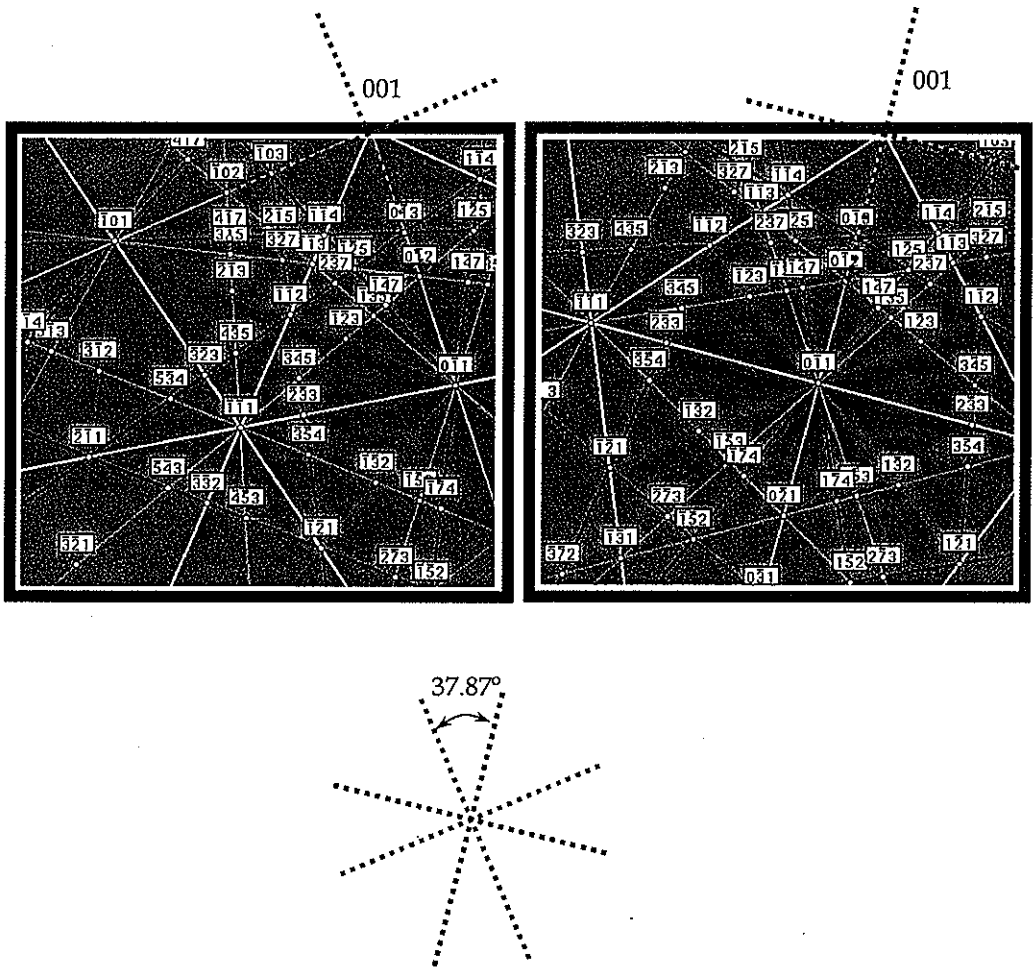

Figure 5-9. Kikuchi pattern analysis for two grains revealing that the two grains are offset by a 37° rotation, characteristic of {210} twinning.

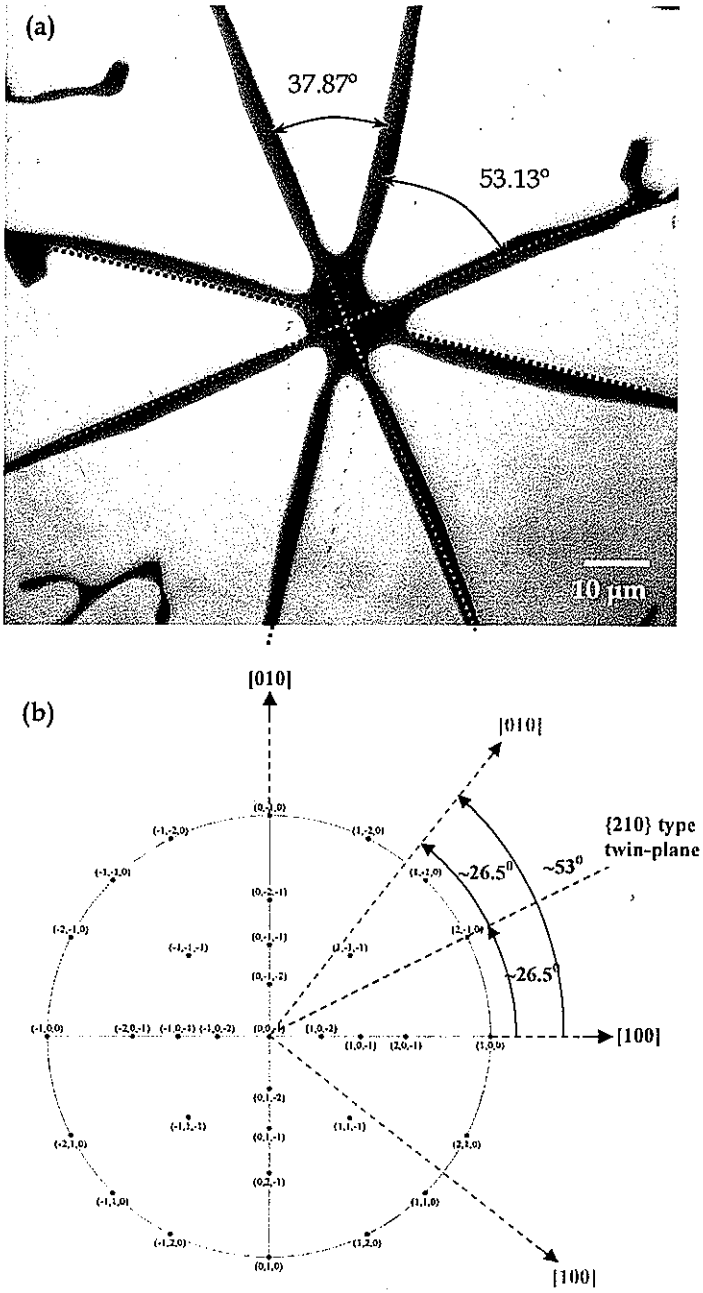

Figure 5-10. An example of an eight-pointed star-shaped silicon rod, showing the alternating 37°/53° angles between the sideplates (a). These angles indicate twinning about {210} planes, as illustrated in (b).

Figure 5-11. An inverse pole figure map showing interpenetrating structures of alternating orientations, rotated about the primary axis. This map is [011] inverse pole figure map to observe two different plane orientations sharing the same axial growth direction [001].

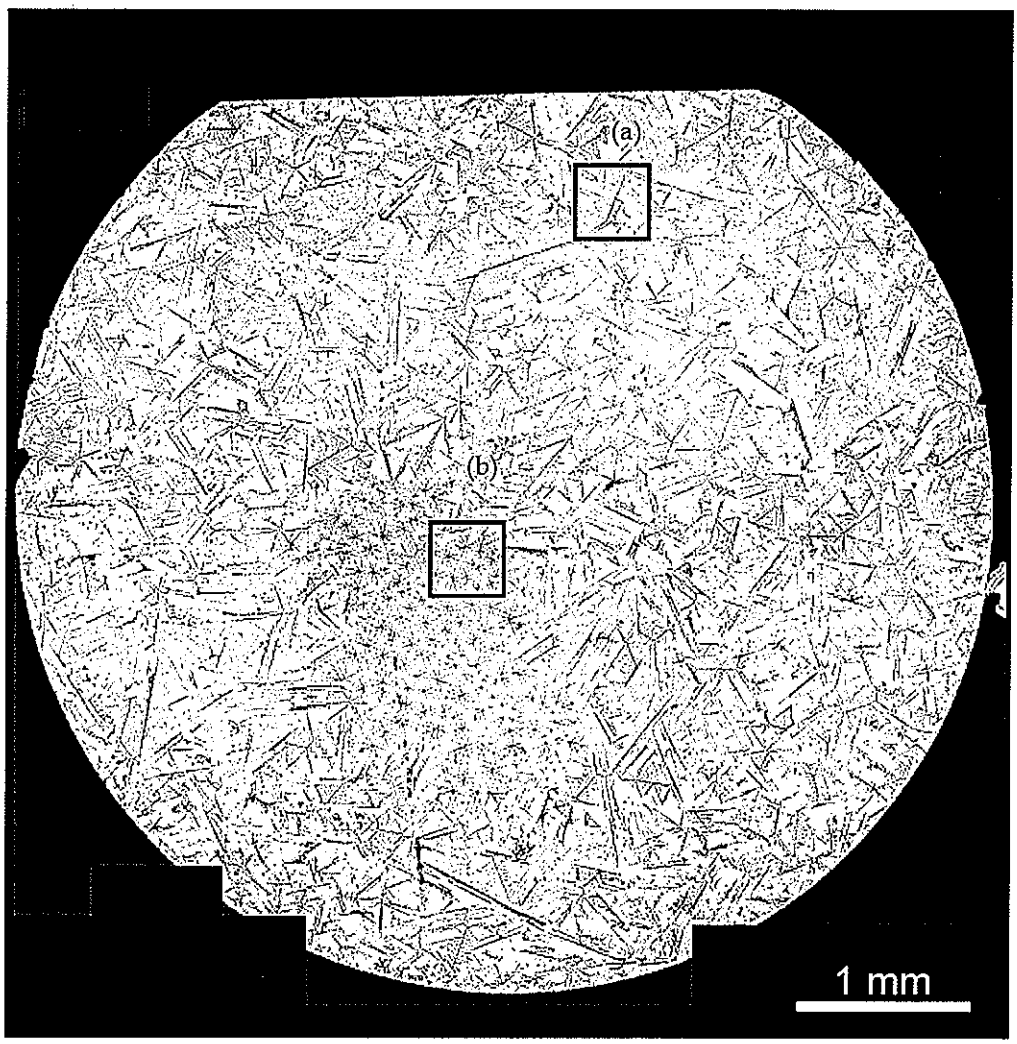

Figure 5-12. The evolution of <100> texture at z=10mm during directional solidification (G=7.5 K/mm, V=0.92 μm/s). (a) The selected area without angular rods and (b) The area showing the growing domain of the angular rod morphology.

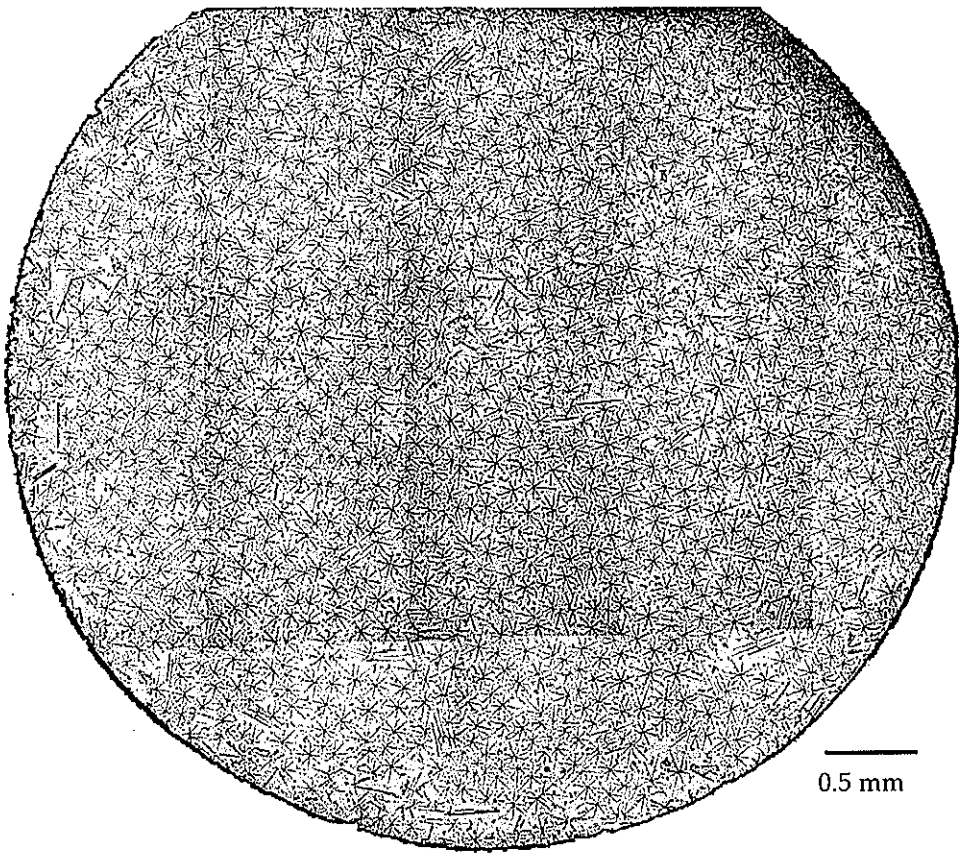

Figure 5-13. The evolution of <100> texture at z=65mm during directional solidification (G=7.5 K/mm, V=0.5 μm/s).

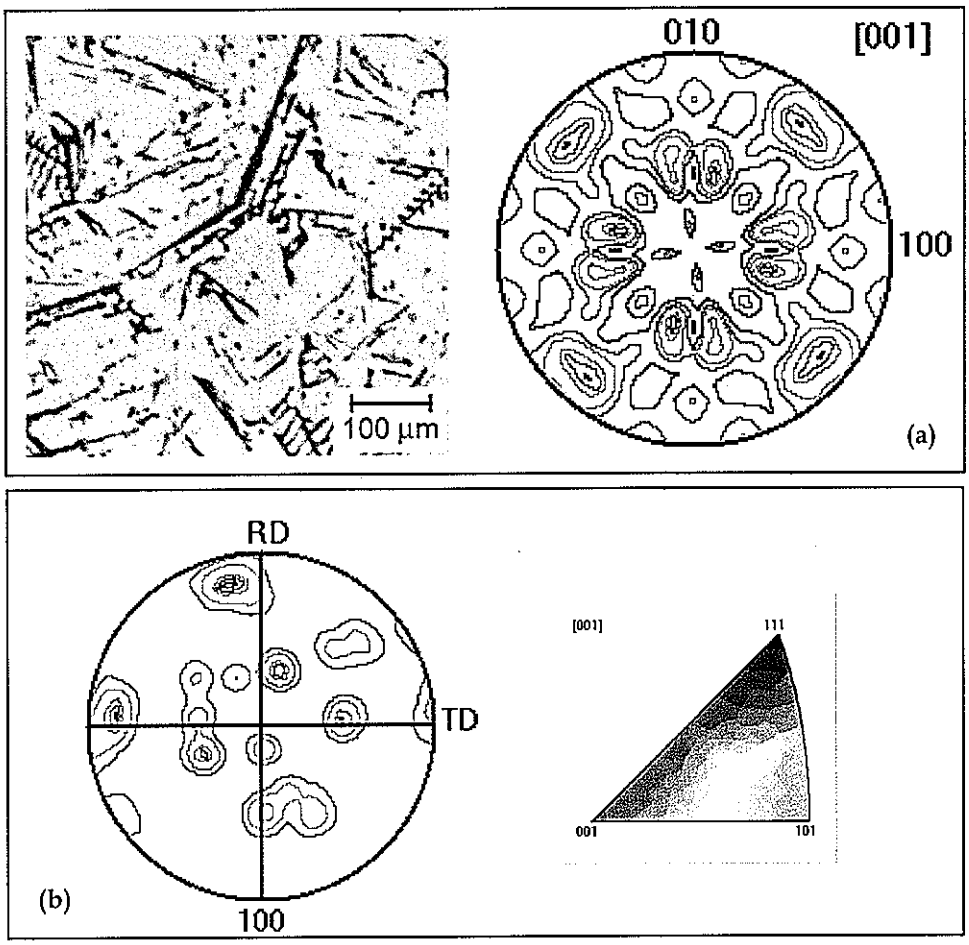

Figure 5-14. (a) Enlarged views outside the angular-rod domain from Fig.9 and the distribution of axial crystallographic orientations in the silicon phase. (b) Correspondent inverse pole figures of (a) with orientations legend of inverse pole figures.

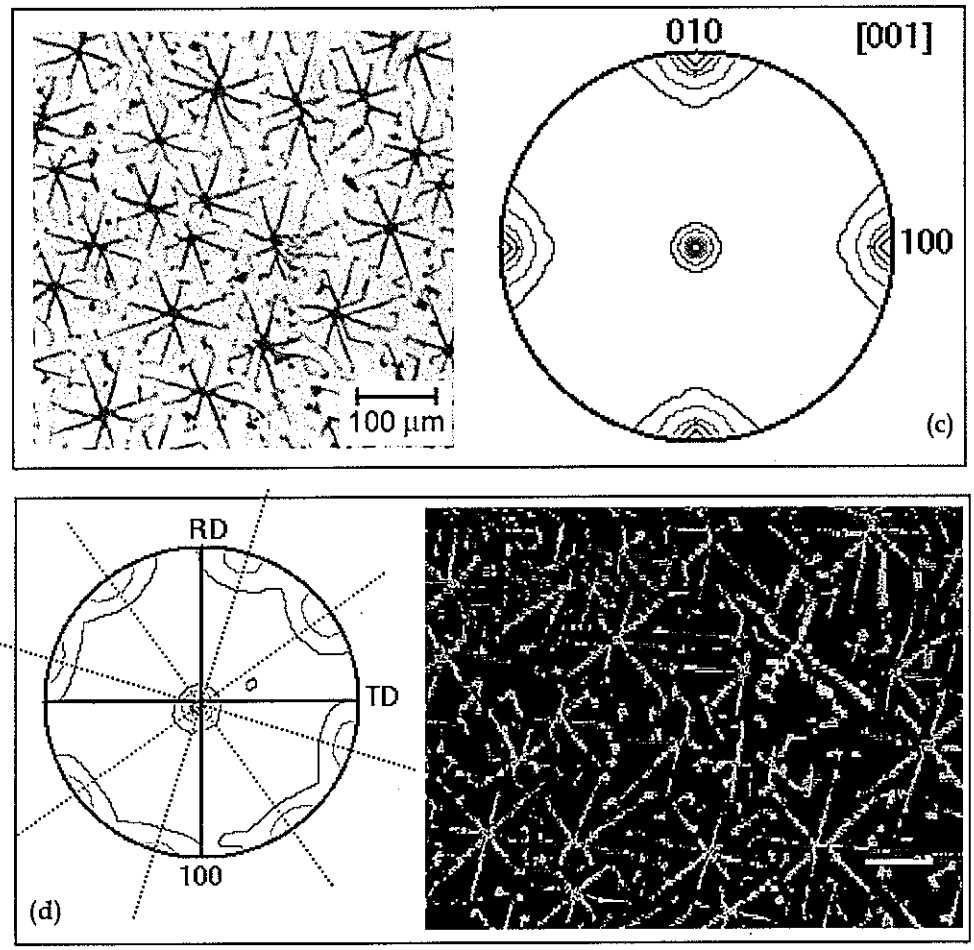

Figure 5-14. Continued. (c) Enlarged views inside the angular-rod domain from Fig.9 and the distribution of axial crystallographic orientations in the silicon phase. (b) Inverse pole figures of the left micrograph with silicon array, showing [001] normal orientation with family <001> directions from the side arms.

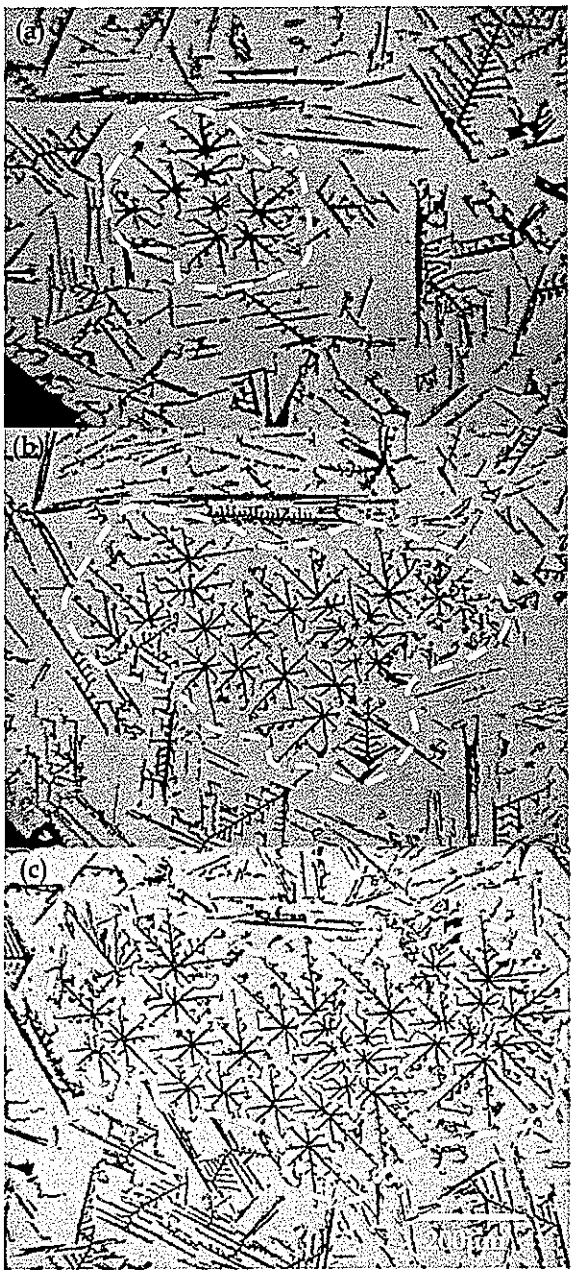

Figure 5-15. Transverse cross-section of the directionally grown sample showing the development of textured dendritic silicon domains at the early stages of growth. The relative distance between section (a) and (b) is 1000 μm, and the section (b) and (c) is 750 μm. The boundary separating textured and randomly oriented silicon structures are separated by the dotted lines.

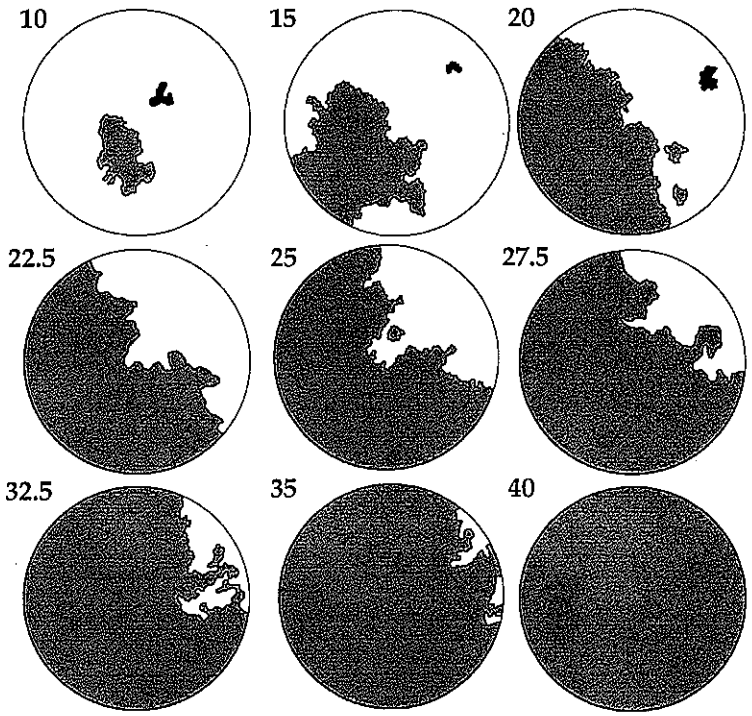

Figure 5-16. <100> texture evolution during directional solidification (G=7.5 K/mm) at 0.92 μm/s. The gray colored region indicates angular rod domains. The upper left number indicates the growth distance.

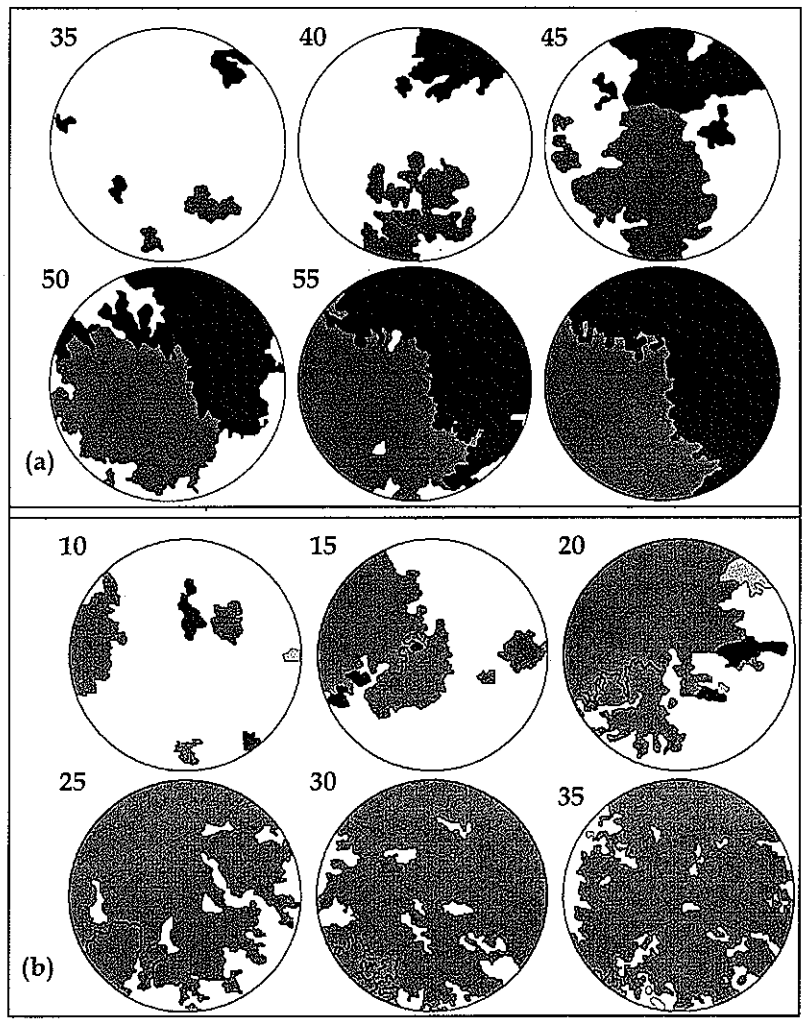

Figure 5-17. <100> texture evolution during directional solidification (G=7.5 K/mm) (a) at 0.5 μm/s, and (b) at 1 μm/s. The colored regions indicate angular rod domains. The upper left number is the growth distance where the cartoon is constructed. The sample solidified at 0.5 μm/s exhibits multiple domains each with a different in plane secondary orientation. The cartoon shown in (b), on the other hand, shows multiple orientations only in the initial stages.

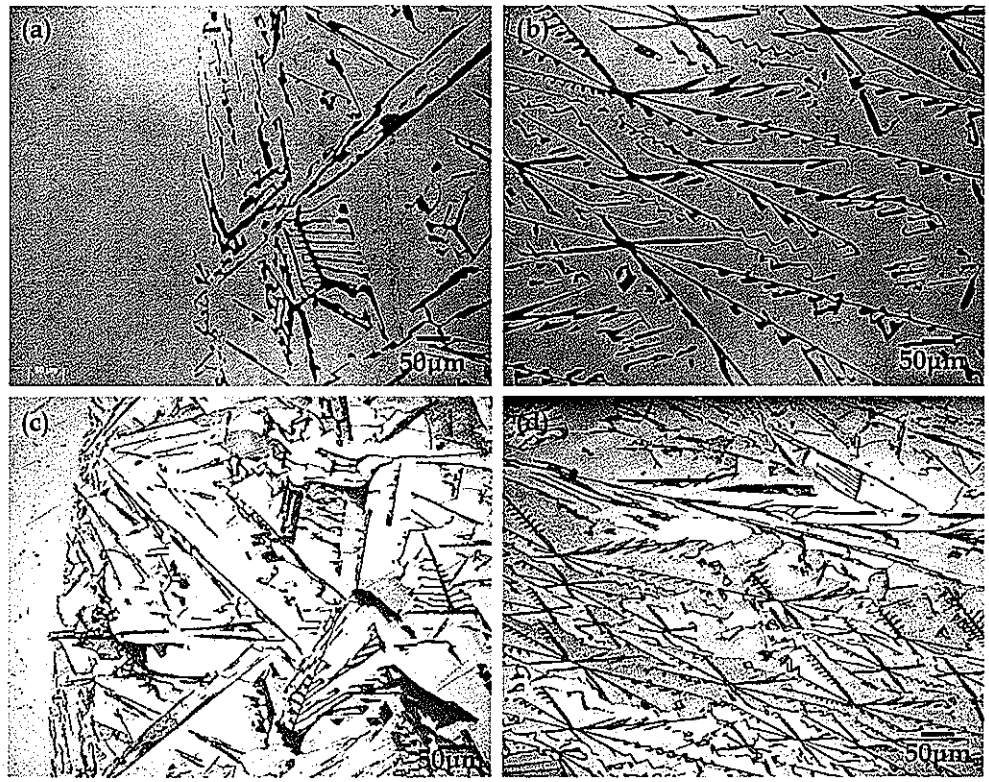

Figure 5-18. (001) Al single crystal seed experiment at 1μm/s of 13 wt% Si alloy. (a) and (b) are not chemically etched and (c) and (d) are etched by Keller reagent. The growth direction is from letf to right and the unmelted single crystal seed is located at the left side of (a) and (c).

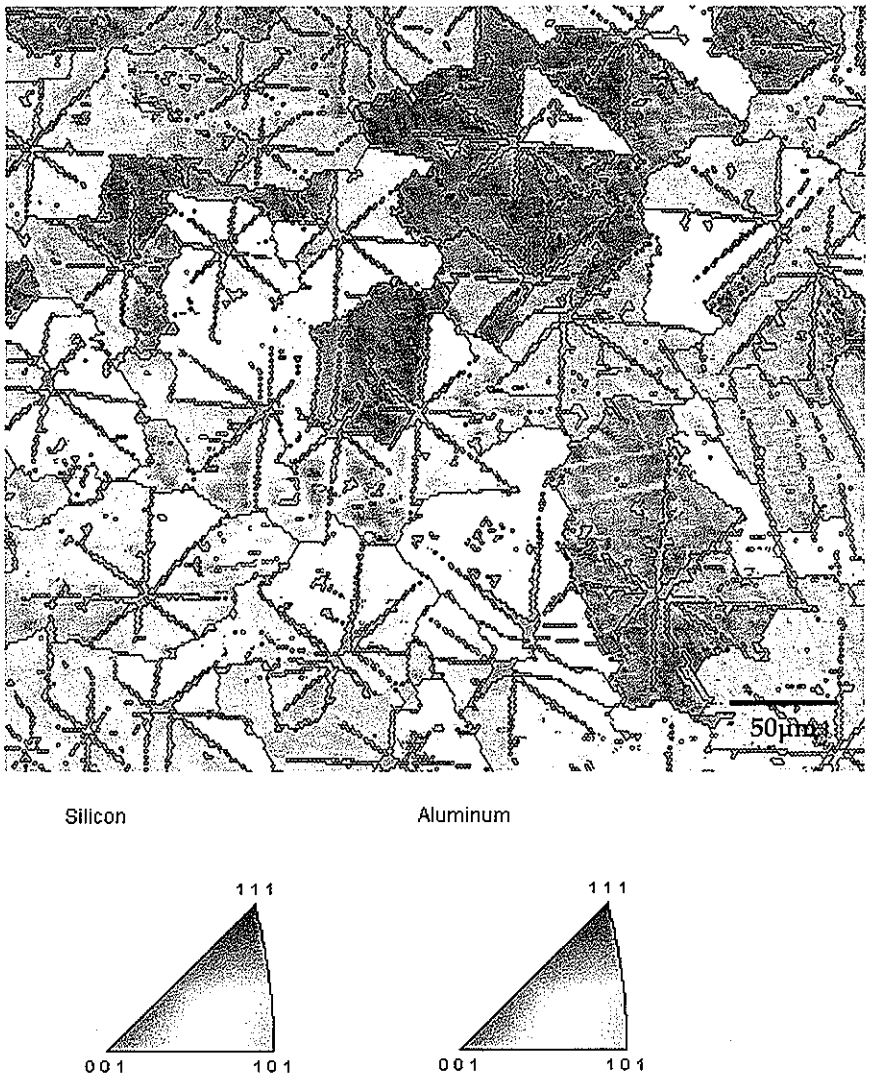

Figure 5-19. Color coded [001] inverse pole figure map, showing <001> texture of silicon phase and poly crystalline of Al phase.

CHAPTER 6

Detailed Structure of Primary Silicon

In Chapter 5, we have examined the morphological transition from normal flake silicon to the angular or "script" structure and finally to the faceted star-shaped morphology. In this growth mode, the strongly texture domains of relatively regular faceted silicon "dendrites" continuously propagate during directional growth. Arising questions from the distinct angular morphology are:

- How the crystal structure evolves in 3-dimensions with interpenetrating twins in the core?
- What is the exact twin structure within the core and what governs the selection of this 8-pointed branched morphology in the overall microstructure evolution?

Accordingly, the dominant morphology, 8-pointed angular silicon of the textured domains was intensively studied in terms of twin boundaries and their migration in the dendritic core. Our findings related to these issues are discussed in this chapter.

6.1 Three dimensional morphology

For microscopic observation of the primary twinned structure, we used a deep-etching technique, where chemical removal of the aluminum-rich phase reveals the detailed morphology of the silicon phase at the quenched interface or at any selected location in the two phase region, as shown in Fig.6-1, 2, and 3. While the position of the aluminum-rich phase in the growth front cannot be determined here, it is clear that the star-shaped silicon rods grow as a leading primary array of pointed angular structures with a distinct secondary plate morphology. Such an array is shown in Fig.6-2 (a), where chemical etching reveals the tips of several star-shaped growth features. The detailed view in Fig.6-2 (b) shows the faceted nature of the side plates. The point at which all of the eight lamellae intersect is the tip of the growing dendrite-like structure. Here, the {111} family of planes are exposed to the melt at the edge of each lamellae and the tip assumes an extended octahedral shape. We have clearly determined that the leading edge of each sideplate is comprised of two {111} planes that intersect along a <110> direction making an angle of 135° with the primary growth axis. It must be emphasized here that the adjacent {111} planes on the leading edge of any given side-plate exhibit an octahedral relationship, where the angle between the two faces is 109.47°. The structure is illustrated schematically in Fig.6-4, showing that the 4-branch

subunit of Fig.6-4(b) is actually an extended octahedron. Two of the 4-pointed extended units eventually make one fully 8-pointed star-shaped structure as shown in Fig.6-4 (c). Considering two grains in an 8-pointed silicon rod, a nice illustration is given in Fig.6-5(a) with two different color codes. Fig.6-5(b) is the end-on view of the growth tip after chemically removal of Al phase around the tip region. While we see here that the two twinned grains intersect in the core, the detailed core structure cannot be explained from this structure analysis.

Due to the limitation of chemical removal, an extended octahedron cannot be seen easily in Fig.6-3 in spite of a clear dendritic tip shape. Thus all stacks of 52 micrographs are reconstructed far enough from the tip using alignment, rescaling, and volume rendering techniques. Three snapshots from the reconstructed sequent animation are given in Fig.6-6 and these verify the 8-pointed star-shaped structure with extended octahedral plates. One can clearly see the overall structure in three-dimensions. Note that tertiary branching from the secondary plate is also shown in the reconstructed series. These additional structures within the overall array will be discussed in the later section.

The dominant 8-pointed morphology is analogous to that observed in the growth of primary Si crystals from a uniformly undercooled melt, where so-called "hoperlike dendritic crystals" have been observed with a strong octahedral faceting tendency. The star-shaped rod-like features, indeed, appear to be the directional solidification counterpart to these "hoperlike" structures.

6.2 Core structure

We have observed rapid lateral propagation of bicrystal grains during low velocity directional solidification in Chapter 2 and the previous sections of this chapter, suggesting that crystal twinning is a principal contributor to the observed dominance of the corresponding textured dendritic array. Presently, we focus on the fundamental issue of self-optimization and examine the structure and growth mechanisms within the central core of these faceted dendrites.

Before considering the crystallographic nature of these twinned dendrites, we examine the overall geometry of the twin boundaries within the core. For the sake of the current discussion, we consider only the typical eight-pointed structure of the primary silicon and note that several twin boundary configurations are possible as given in examples of Fig.6-7. Categorizing these according to the in-plane connectivity of the two twins, we formulate a structural basis set of sorts, including the three possible configurations (types I, II, and III) and their inverses, as illustrated in Fig.6-8.

In each case, regardless of the specific connectivity, we can identify generally eight radial subgrain boundaries. Indeed, we have observed each of these configurations within a single bicrystal, as shown in Fig.6-9(a-i). Twinning about the {210} planes has been reported in these growth structures, and the sideplates in Fig.2 exhibit rotational offsets of 53.13 and 36.87 about the <001> axis, which is consistent with {210} twinning as discussed earlier. However, we point out now that this {210}||{210} relationship provides only two possibilities for twin boundary orientations within a given core and note that a higher number of possible twin plane orientations is required for the observed complex twin boundary configurations shown in Fig.6-9, and even in Fig.6-7.

Both {210} and {310} symmetric coherent twins have been proposed for the diamond cubic silicon [I. Hornstra, *Physica* 26, 409 (1959)][110]. The essential feature regarding these particular twin orientations is that they are complementary angles and, because the grain rotation is about a four-fold axis, both twin types can exist at the same grain misorientation (i.e. a rotation of 53.1309°) about the [001] axis. The atomic structure of these {210} and {310} coherent twins is given in Fig.6-10 (a) and (b) respectively. Therefore, both twin boundary types can exist within the same bicrystal. In fact, a single twin boundary can exhibit segments of each type. Such a configuration increases the number of independent twin planes within a given bicrystal to four, sufficient for generating the twinned core configurations shown in Fig.6-9. Accordingly, we propose a complex twin configuration, comprised of both {210}||{210} and {310}||{310} twin boundary segments, where both types are fully coherent and symmetric about the [001] primary growth axis. A detailed example of the atomistic structure within a core exhibiting a Type I geometry is given in Fig.6-11.

Indeed, we have measured the twin boundary orientations in over 100 dendritic cores relative to a crystallographic arbitrary reference. First, we have measured the angle between each segment and the reference and then measured the length of each segment. The example of the measurements is given in Fig.6-12. Subsequent normalizing, numerical fitting by Fourier function, and the derivative of this fitted normalized length as a function of angle give us a distribution of twin boundary orientation angles, shown in Fig.6-13. In addition, geometrically computed twin angles of possible {130} and {120} twins for each grain are compared to this distribution. It indicates that the {130}||{130} and {120}||{120} twins are dominant within the dendritic cores, with the {130}||{130} variant being favored.

Corresponding to each type of coherent twin boundary, the colored area in Fig.6-14 (a) and (b) is a measure of the distortion energy, and the twin boundary energy is related to the number of distorted bonds and the magnitude of bond distortion. This should scale with the twin

boundary angle. Therefore, the ratio of these twin boundary angles is simply a measure of the ratio of respective specific twin boundary free energies. Thus, we estimate the ratio of γ_{210} to γ_{310} to be 1.5. Indeed, this is the same ratio of the two corresponding peak areas, approximated as shown on the plot above, using the FWHM positions. This analysis supports the argument that both boundaries exist in roughly the proportion given by their twin energies. High resolution TEM image in Fig.6-15 confirms that twin boundaries in the cores do consist of segments of both types.

6.3 Twin boundary migration

The interface morphology of star-shaped rod, shown in Fig.6-1 and 6-5 (b), reveals various steps and grooves which may be important for growth, but these images provide no clear evidence for the role of twinning. However, the longitudinal view of a silicon rod tip is shown in Fig.6-16, where a line of dark/light contrast along the axial direction indicates twinning. Furthermore, a deep groove is observed at the tip where the twin intersects the solid-liquid interface, suggesting that the twin-plane groove is an important feature in the growth of these solidification structures. This observation suggests growth kinetics are enhanced by a defect mechanism where it is easier for Si atoms to attach themselves near the twin boundary/growth tip intersection.

In addition to its contribution to the growth kinetics at the tip, the critical role of twinning in the formation of secondary sideplates is certain. The original four-pointed substructure described previously can form without any twinning, with the solute gradient around the advancing tip creating the conditions for radial instability and sideplate development. Because of the strong faceting tendency of the growing Si phase, however, growth is suppressed in all but the low-stiffness high-mobility <001> directions, giving rise to the "secondary side-plate" morphology shown in Fig.6-1. The secondary structures extend radially, locally relieving the supersaturation but still constrained to grow in their respective <001> directions bounded by broad {100} side-faces and {111} facets at the advancing edges. The initiation of a twinned region, either at the core or along a growing sideplate, provides a means for the growth of additional sideplates, further improving the efficiency of solute redistribution. These additional sideplates also extend radially in <001> directions, where the {210} or {310} twin orientations gives rise to the 37°/53° relationship between sideplates that is observed in virtually every star-shaped rod.

With convincing evidence related to the twin structure within the bicrystalline dendritic cores, we now note that the utility of the twin configurations in mechanistic selection relies on the

ability of the twin boundaries to reconfigure themselves, according to the requirements of the local driving forces. Simple examples are shown in Fig.6-14(c) and (d). Experimental observation also confirms this reconfiguration of the core structure in Fig.6-17. Thus, it is critical that the twin boundaries in the core have a reasonable migration mobility in terms of lateral propagation during growth. In this case, a given twin boundary will readily migrate laterally as new atoms are added to the growing crystal, permitting branch generation in the most advantageous locations, as dictated by the governing solute field. The critical dependence of new sideplate generation on the location of the twin boundaries within the core is indicated very clearly in Fig.6-18, where the early stages of sideplate formation are evident. Based on the evidence of twin boundary structure we have presented thus far and on the requirement for twin boundry migration in the overall scheme of selection dynamics, we propose a two-atom twin-boundary migration mechanism in Fig.6-19, and assert that such a mechanism would provide the responsiveness required to enable rapid twin reconfiguration as needed for efficient sideplate formation and optimization of solute redistribution during growth.

While the twinned-sideplate mechanism gives rise to a much higher efficiency with regard to solute redistribution at the growth front, the local solute gradient surrounding the sideplates may become substantial with increasing radial extension from the central core. This drives the formation of additional or "tertiary" structures within the overall array, and we have observed several mechanisms by which this may occur. The sideplate may become "fluted" by extending in the two <110> directions on either side of the plate, favoring facets on alternating {111} planes, as shown in Fig.6-20(a). By this mechanism, the sideplate increases its effective thickness as it "opens up" into the interplate region as shown schematically in Fig.6-20(b). Growth of these fluted structures cannot be sustained for large radial distances, and one of the two <110> directions will ultimately be selected, depending on the solute field on either side of the sideplate. In this case, the plate will grow radially in this <110> direction. However, the kinetic constraints give rise to a corrugated structure to maintain broad {111} facets, as shown in Fig.6-21(c). The extreme regularity of the corrugations suggest that the corrugated structure results from end-on growth in the radial direction, rather than growth in alternating direction along the primary growth axis. A third mechanism involves tertiary plates, which develop as a regular array of vanes emanating from one or both sides of a parent plate, as shown in Fig.6-21(d). They are generally observed to extend from near the core to the leading growth edge, and the extension away from the parent sideplate is governed by the local solute field. Certain tertiary plates may offer a substantial benefit to local dissipation of supersaturation, particularly at the location of branching. Growth at these intersection points will be favored and the interface may

locally advance quickly toward the growth front, assuming the <001> primary direction and moving ahead of the parent sideplate from which it originated. This proposed mechanism may provide a means for the generation of new primary rods and the propagation of the overall structure.

Summary of the key points of this chapter with respect to the core structure

- Two grains of Si interpenetrates each other, producing the complex twin boundaries in the dendritic core. For the typical morphology, 8-pointed starshape silicon, Type I, II, and III twin configurations can exist in the core based on the geometric constraints and we have identified and confirmed all of them.
- Both {210} and {310} symmetric coherent twin boundaries can exist within the same bicrystal, and we have verified it by measurements and observation.
- These coherent twin boundaries must migrate for the mechanistic reconfiguration in the core to respond to the local fluctuation, resulting in the sideplates formation or optimization of solute redistribution during growth.
- Therefore this "mechanistic" twin boundary migration play very critical role in the morphological selection of faceted silicon phase.

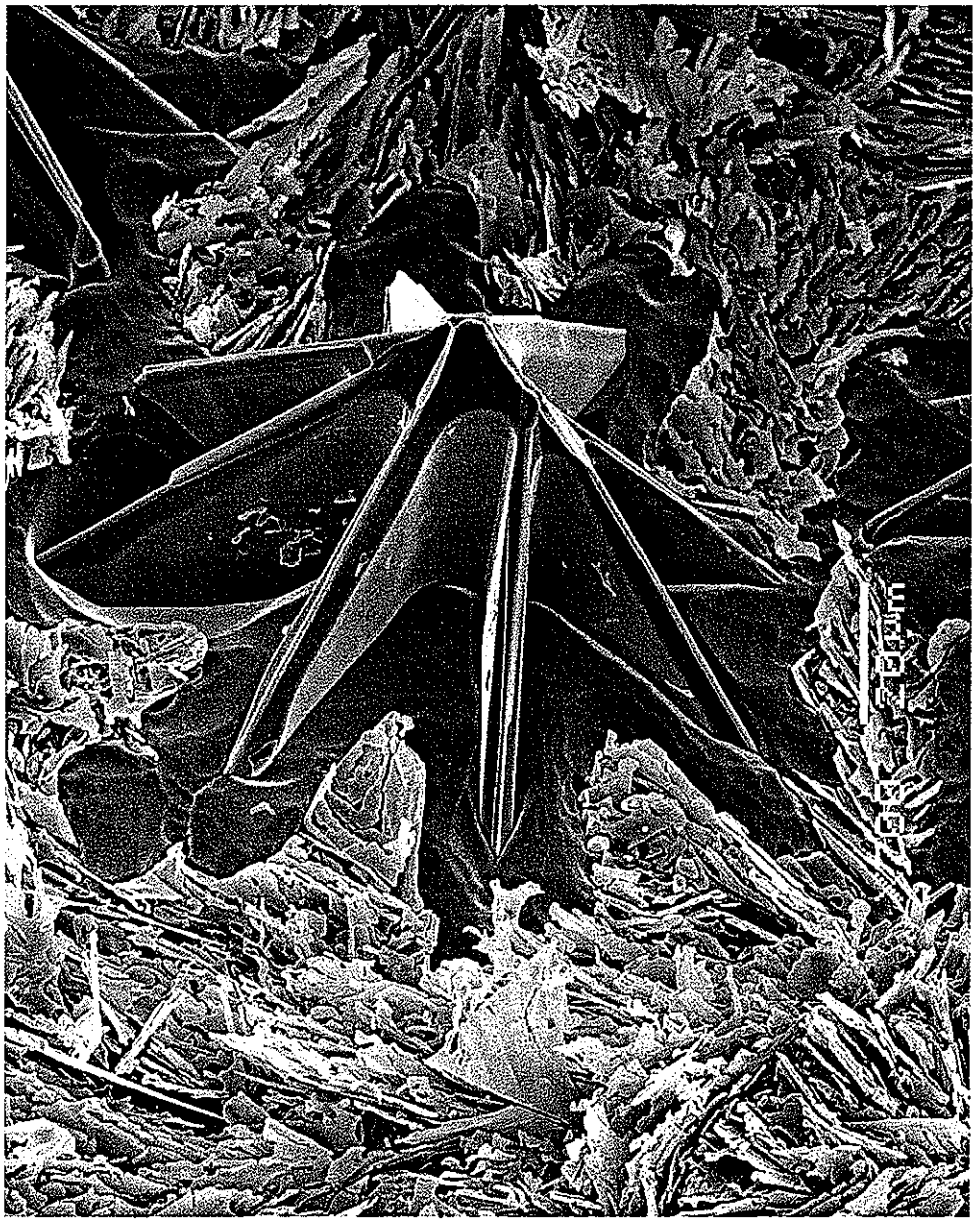

Figure 6-1. Octahedral tip of 8-pointed star-shape silicon. Al phase and quenched liquid were chemically removed.

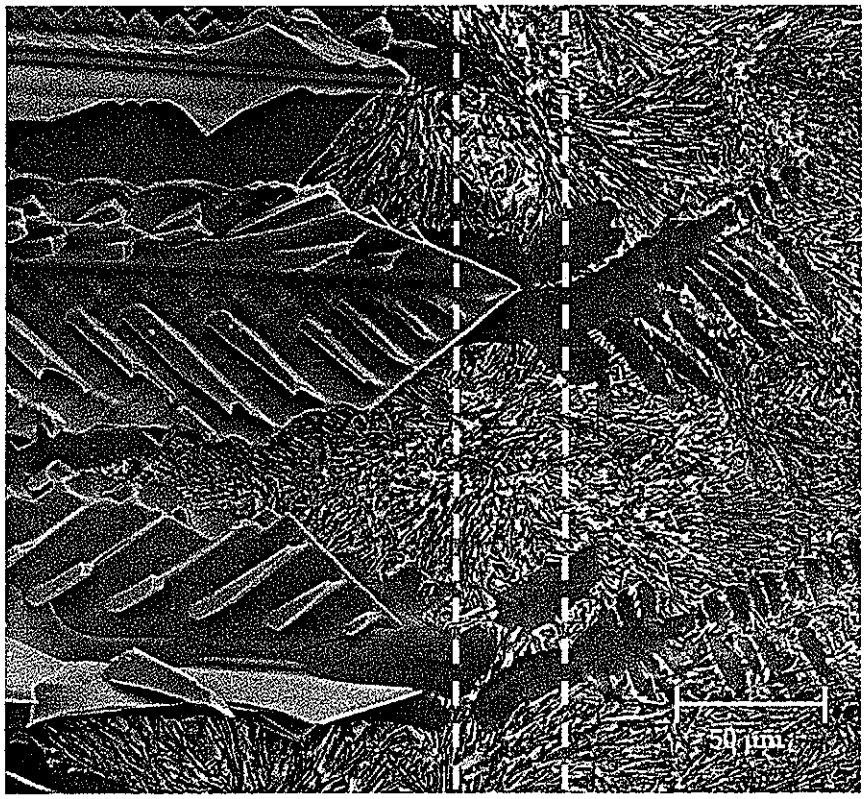

Figure 6-2. A longitudinal view of the quenched solid-liquid interface, showing the structure of the growth front and the leading silicon phase. (Growth conditions: G=7.5 K/mm, V=0.92 μm/s.) Chemical removal was applied from the quenched liquid to the interface as indicated dotted lines.

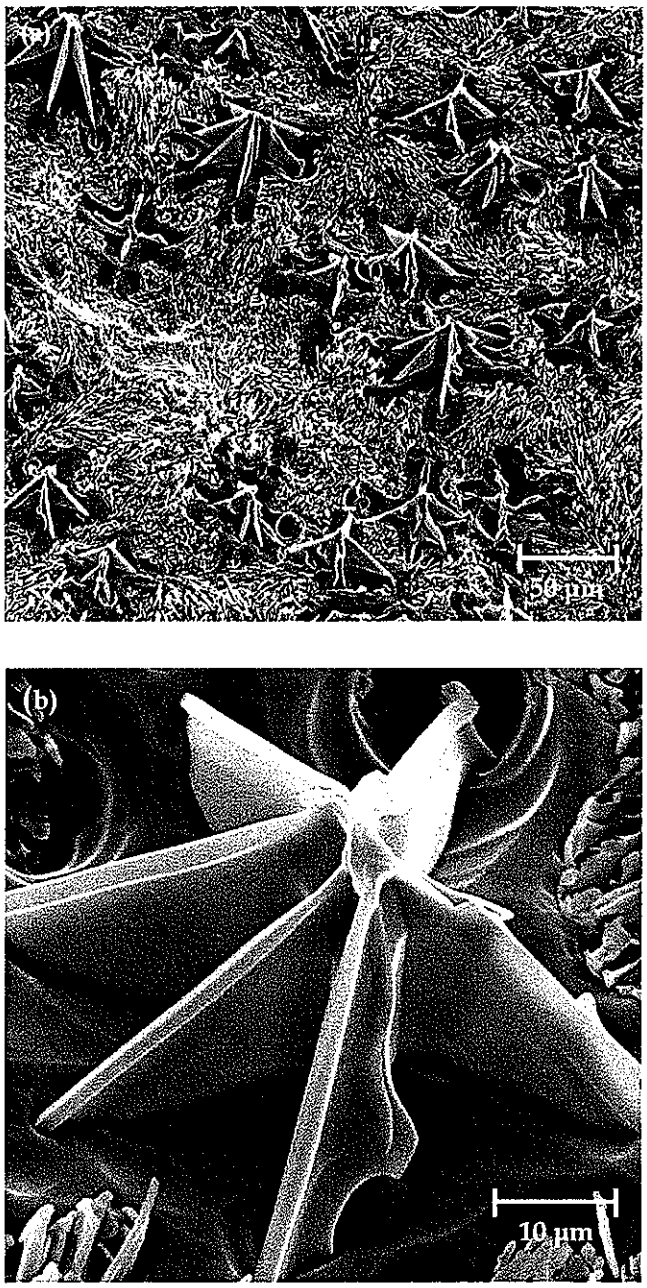

Figure 6-3. The interface structure of the star-shaped angular silicon rods revealed by chemical removal of the surrounding quenched liquid: (a) the overall array of silicon, showing only the tips of the rods protruding from the surrounding quenched liquid; (b) a detailed view of a single star-shaped rod, showing {111} facets intersecting on <110> directions along the leading edges of the sideplates; and (Growth conditions: G=7.5 K/mm, V=0.92 μm/s).

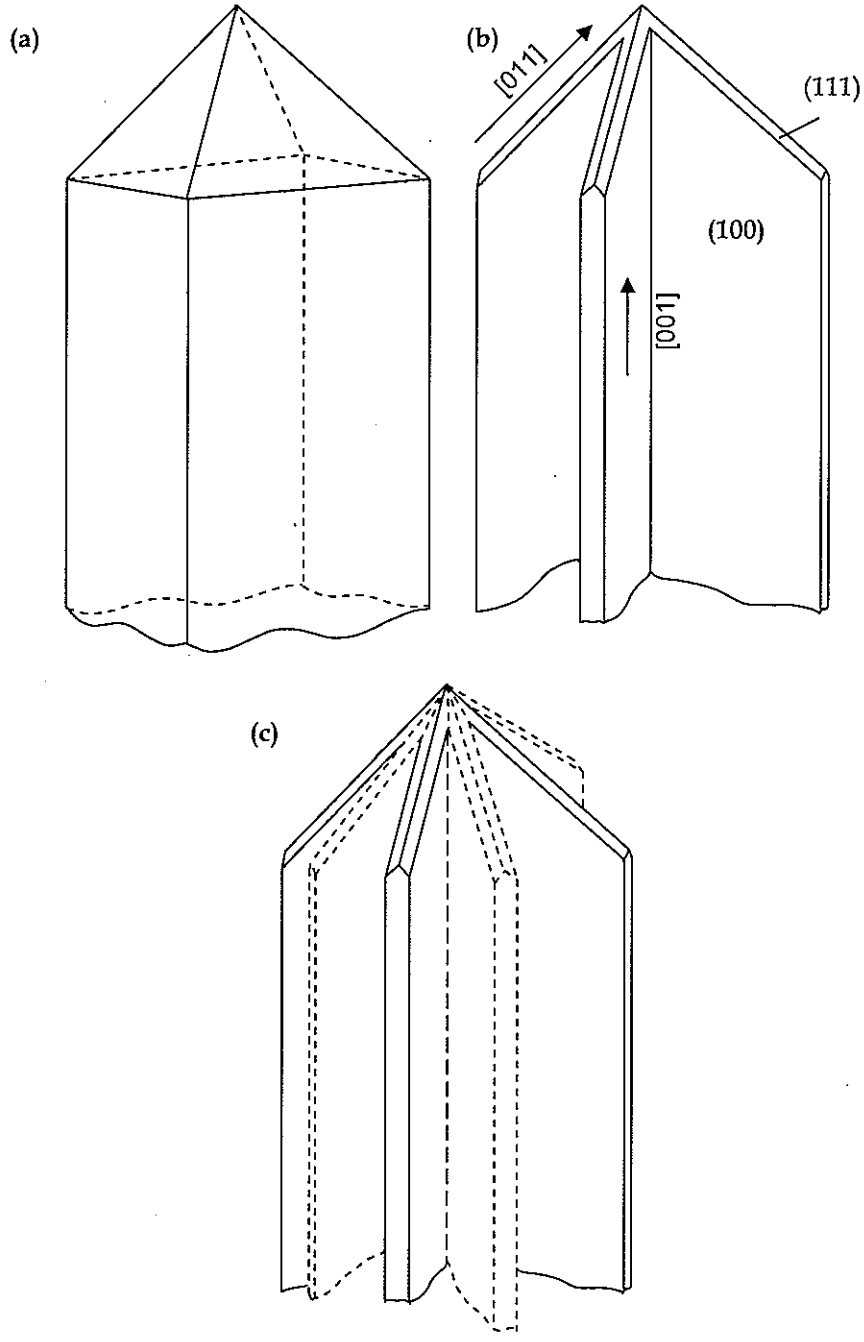

Figure 6-4. A schematic representation of the structure of the star-shaped silicon rod: (a) the basic octahedral shape, (b) the faceted "extended" octahedral 4-sideplate subunit, and (c) the 8-sideplate rod morphology that must include a twinned core structure.

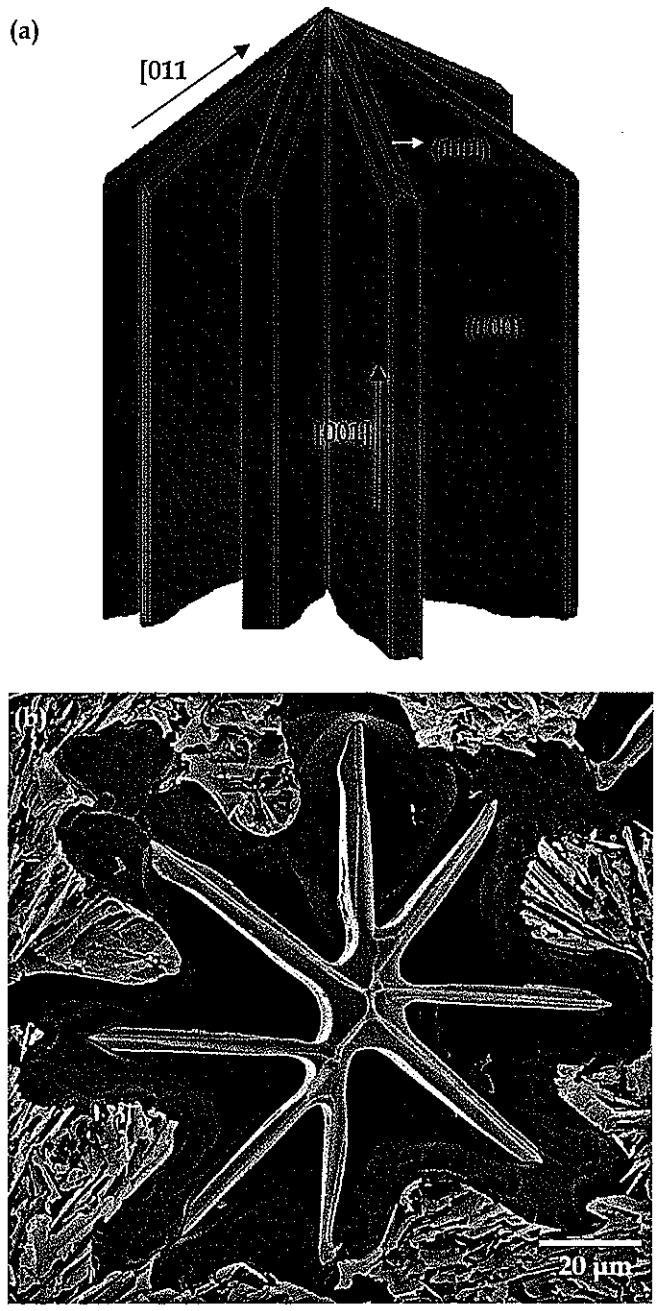

Figure 6-5. (a) An illustration showing two interpenetrating sets of four-point octahedral plates with crystal orientations (b) An end-on view of the growth tip after chemical removal of Al phase.

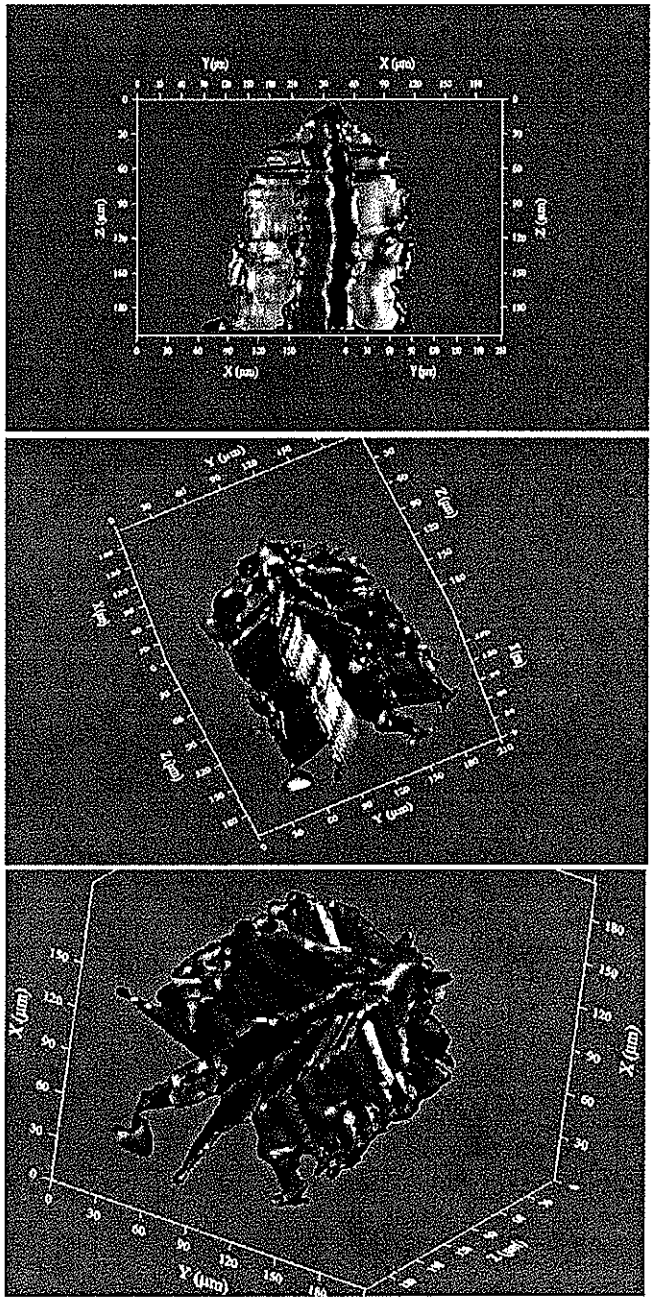

Figure 6-6. Snapshots of tree dimensional reconstruction at various view angles showing octahedral growing tip, secondary add tertiary branched plates. Reconstructed from 52 serially sectioned images at every 4μm/s.

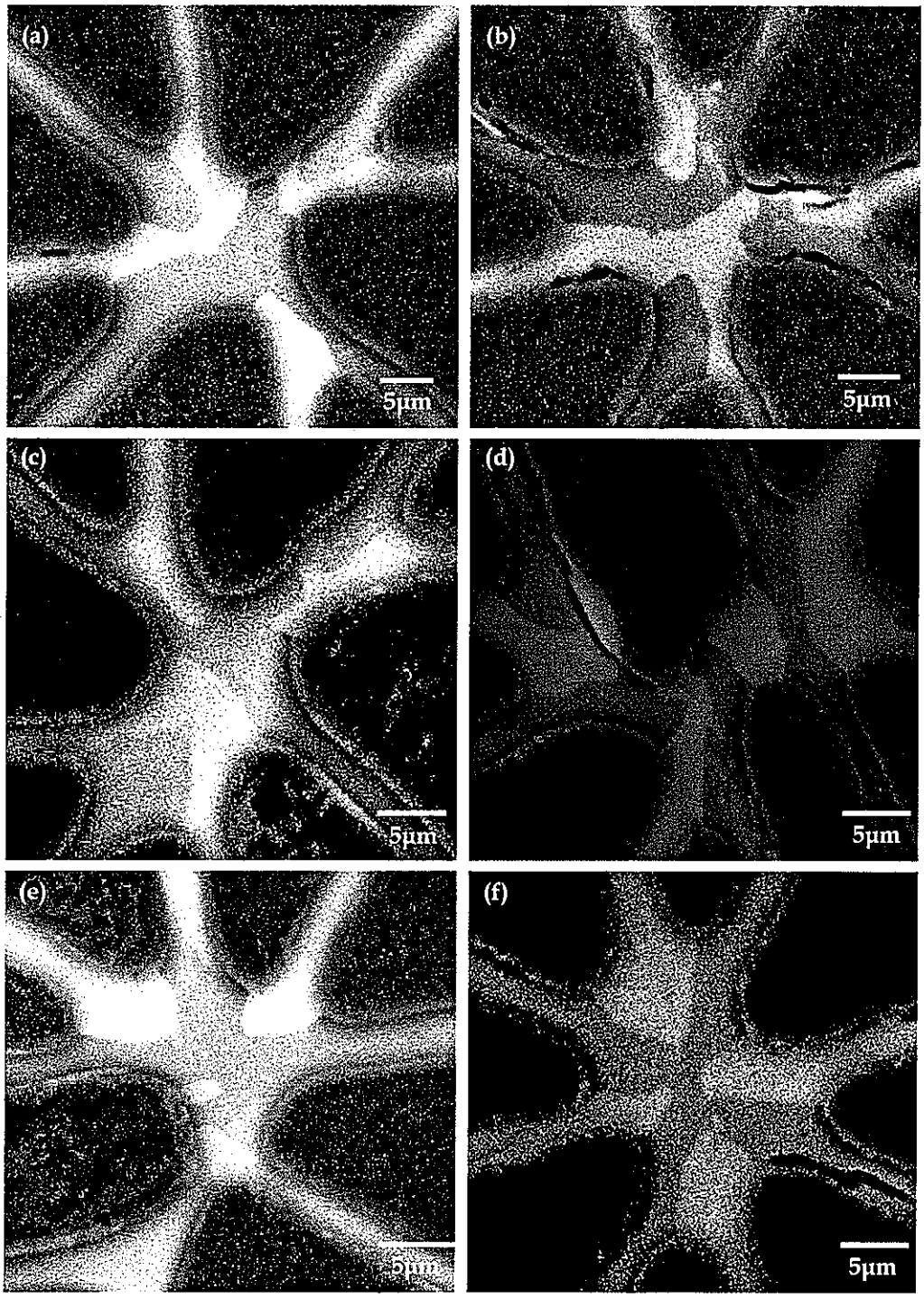

Figure 6-7. BSE images of core structure showing several complex twin boundaries configurations. Note that all configurations of twin boundaries except (f) are not of any Type I, II, and III proposed in Fig.6-8. (f) Type I twin structure. All pictures are from BSE imaging.

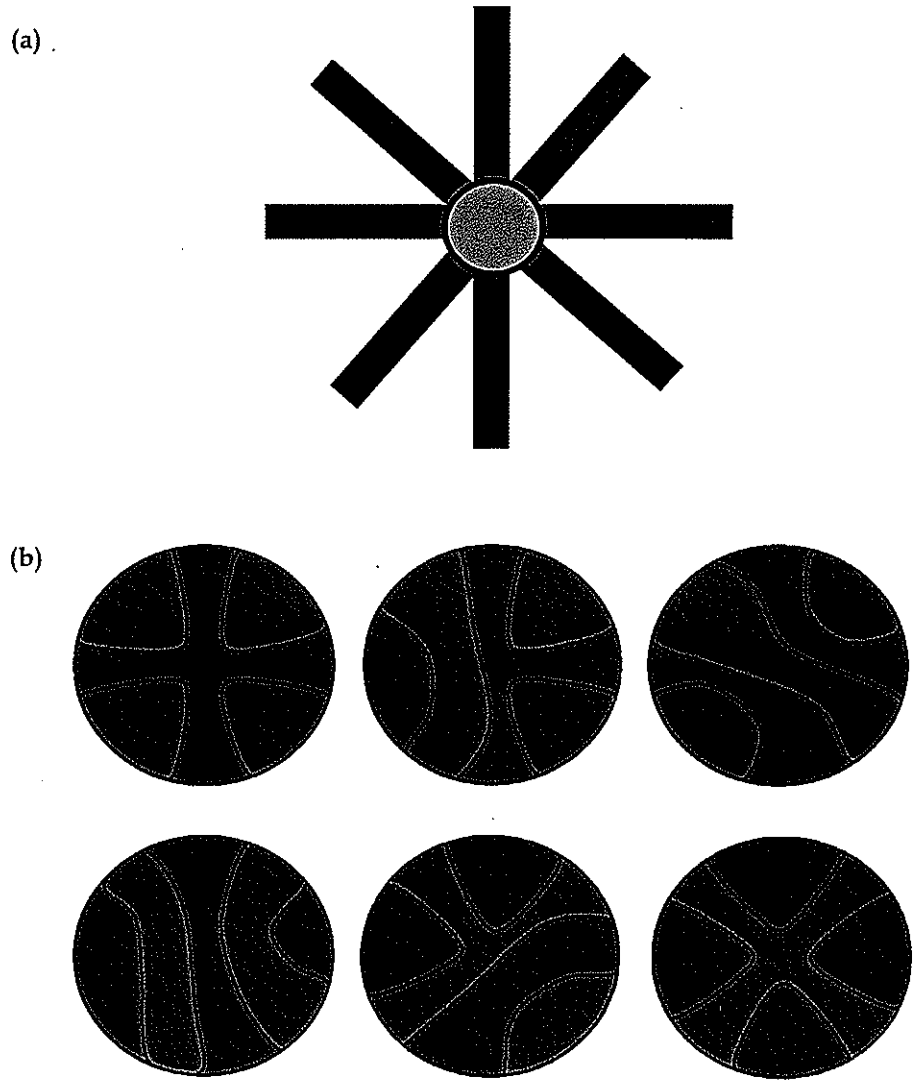

Figure 6-8. (a) Schematic cartoon of two grains sharing the central stem. (b) Three possible twin configurations in the core and (c) their inverse.

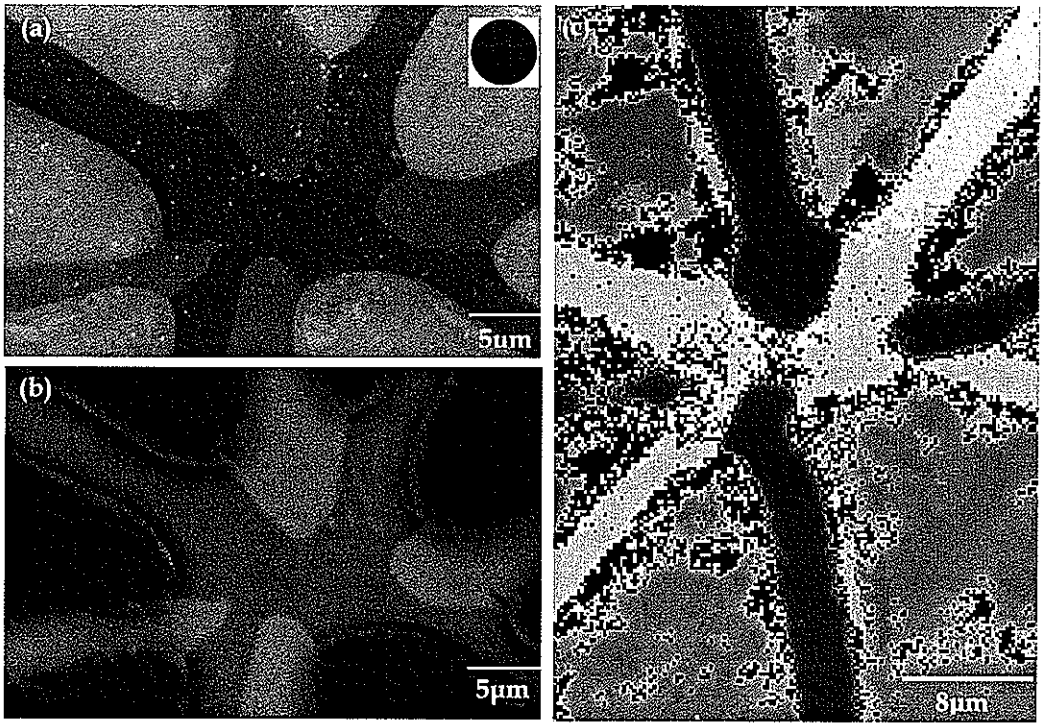

Figure 6-9. Type I twin configuration in the core. The black and white micrographs are (a) secondary and (b) backscattered electron SEM images, while (c) the color micrograph are the orientation image maps obtained from EBSD analysis.

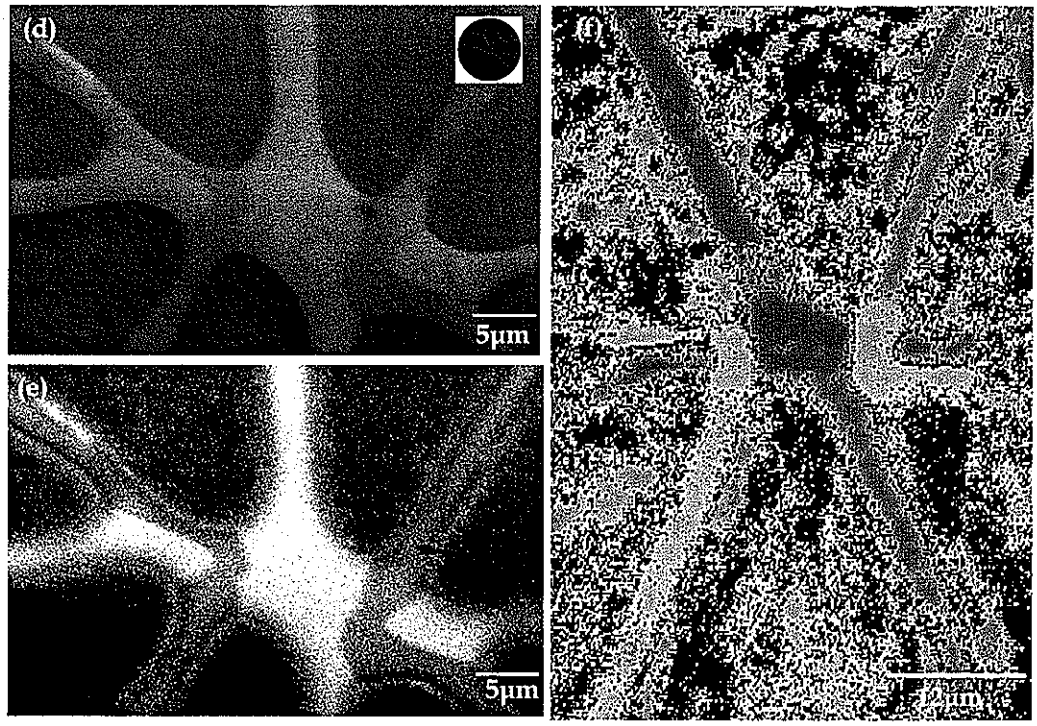

Figure 6-9. Continued. Type II twin configuration in the core. The black and white micrographs are (d) secondary and (e) backscattered electron SEM images, while (f) the color micrograph are the orientation image maps obtained from EBSD analysis.

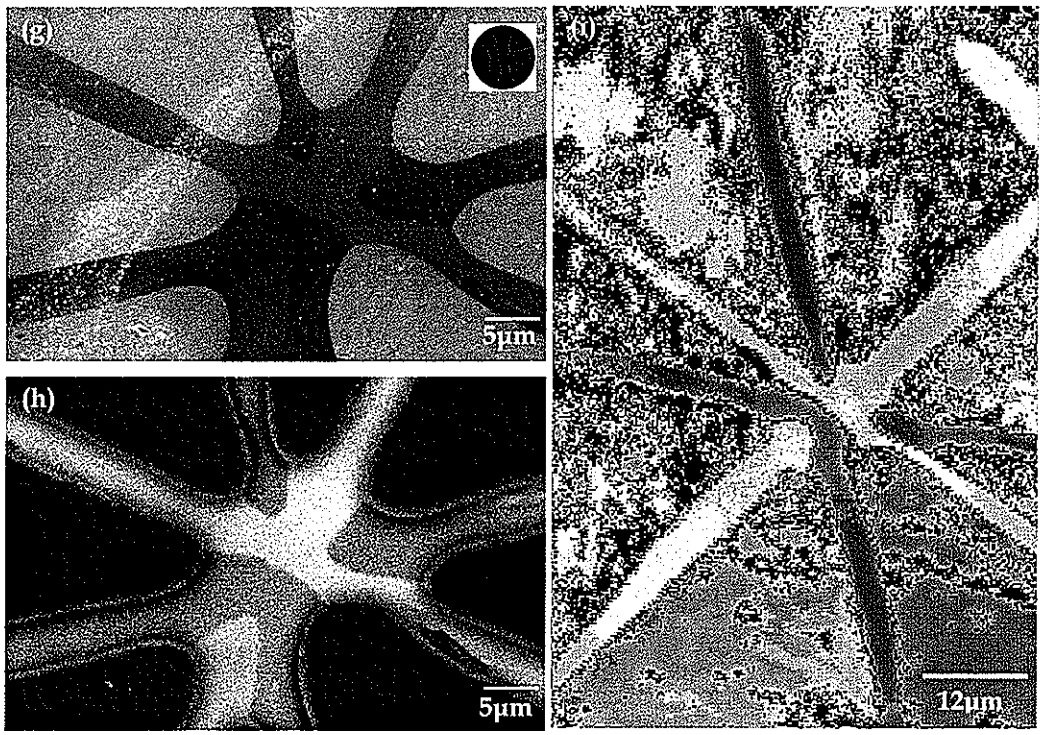

Figure 6-9. Continued. Type III twin configuration in the core. The black and white micrographs are (g) secondary and (h) backscattered electron SEM images, while (i) the color micrograph are the orientation image maps obtained from EBSD analysis.

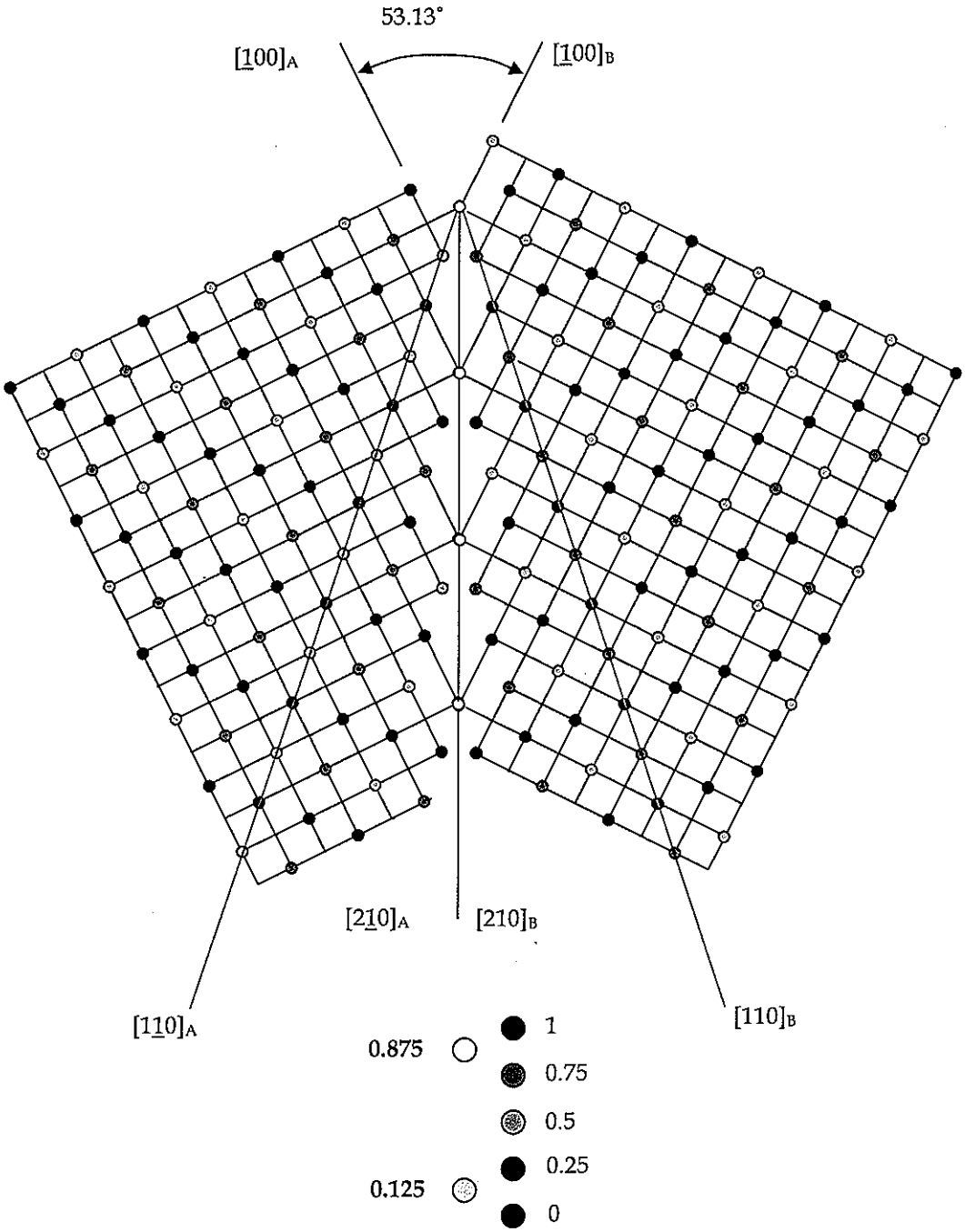

Figure 6-10. (a) Atomic structure of (210) coherent twin boundaries in the diamond cubic structure.

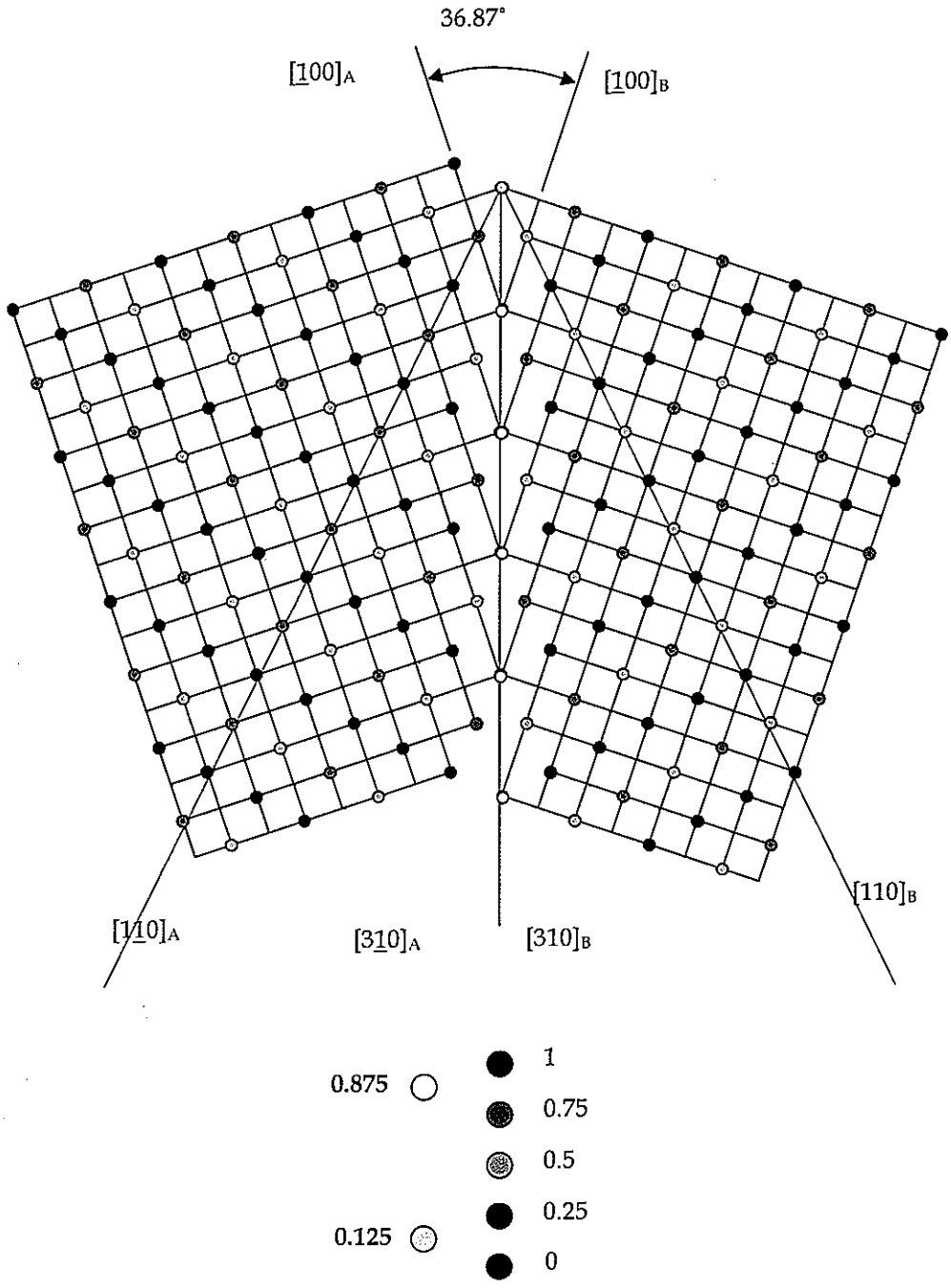

Figure 6-10. Continued. (b) Atomic structure of (310) coherent twin boundaries in the diamond cubic structure.

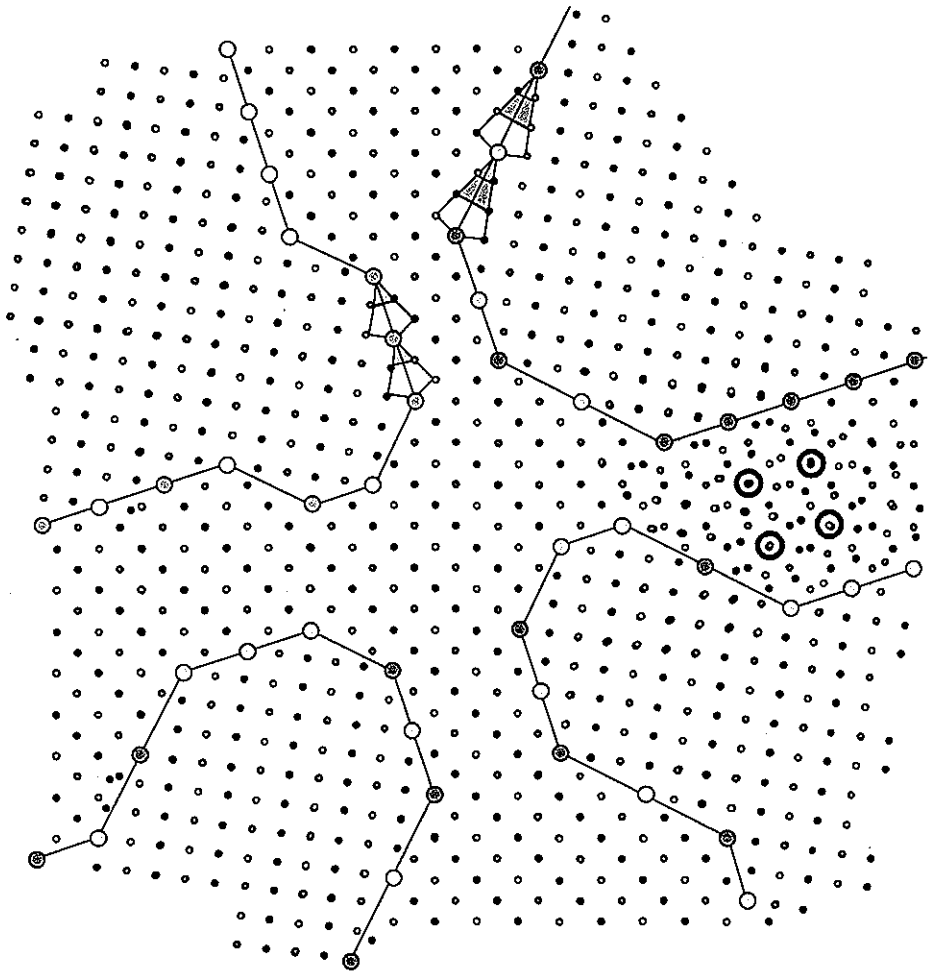

Figure 6-11. Imaginary Type I core structure comprised of two grains, indicating that it can be constructed by only two coherent twin types. The legend for relative heights of a regular diamond cubic crystal structure and relative heights of atomic position from coherent twin boundaries are same as Fig.6-10.

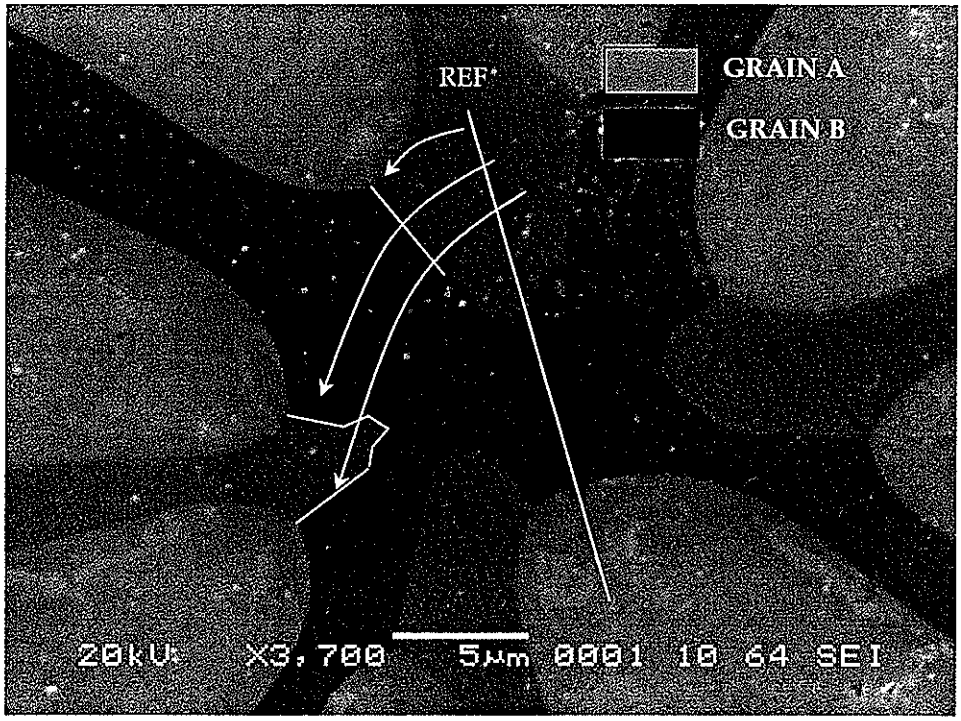

Figure 6-12. An example of twin orientation angle measurement and corresponding segments. White lines indicate some of segments and a yellow line is a reference plane. Note that the reference plane is parallel to one of grains, A in this case.

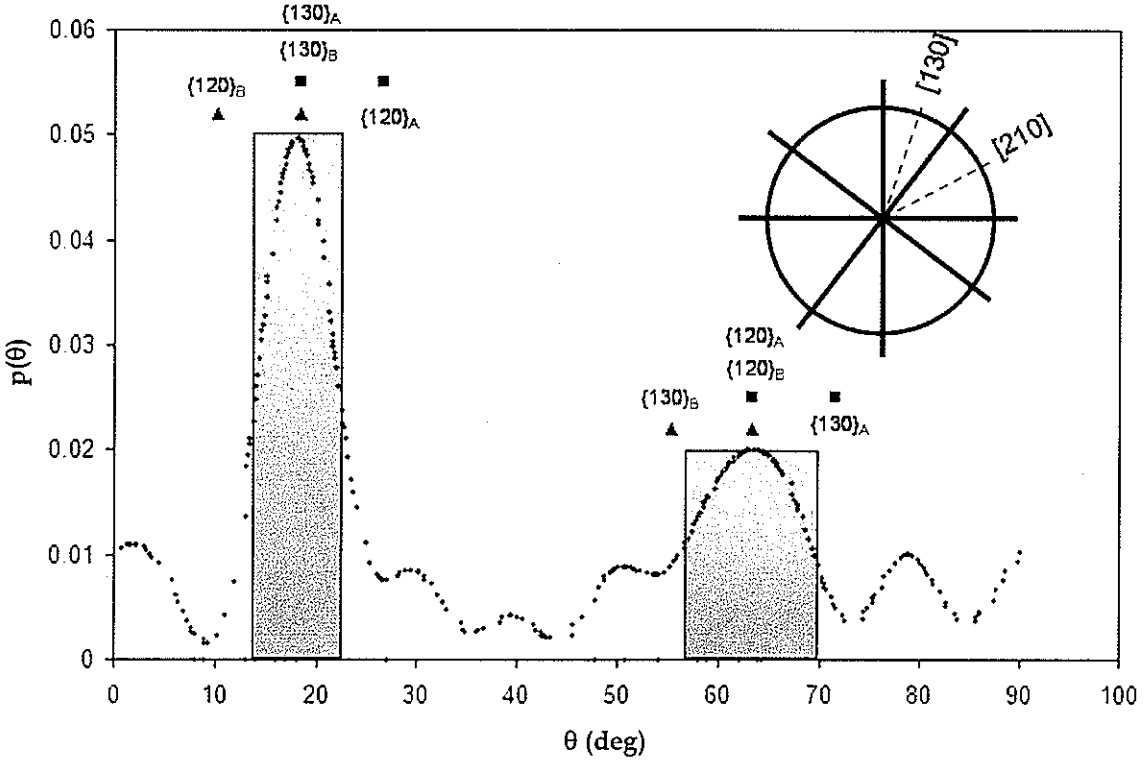

Figure 6-13. The distribution probability of twin boundaries angle. Grain A and B are distinguished in different color code, blue and red respectively, showing {130| |130} variant is favored in the core.

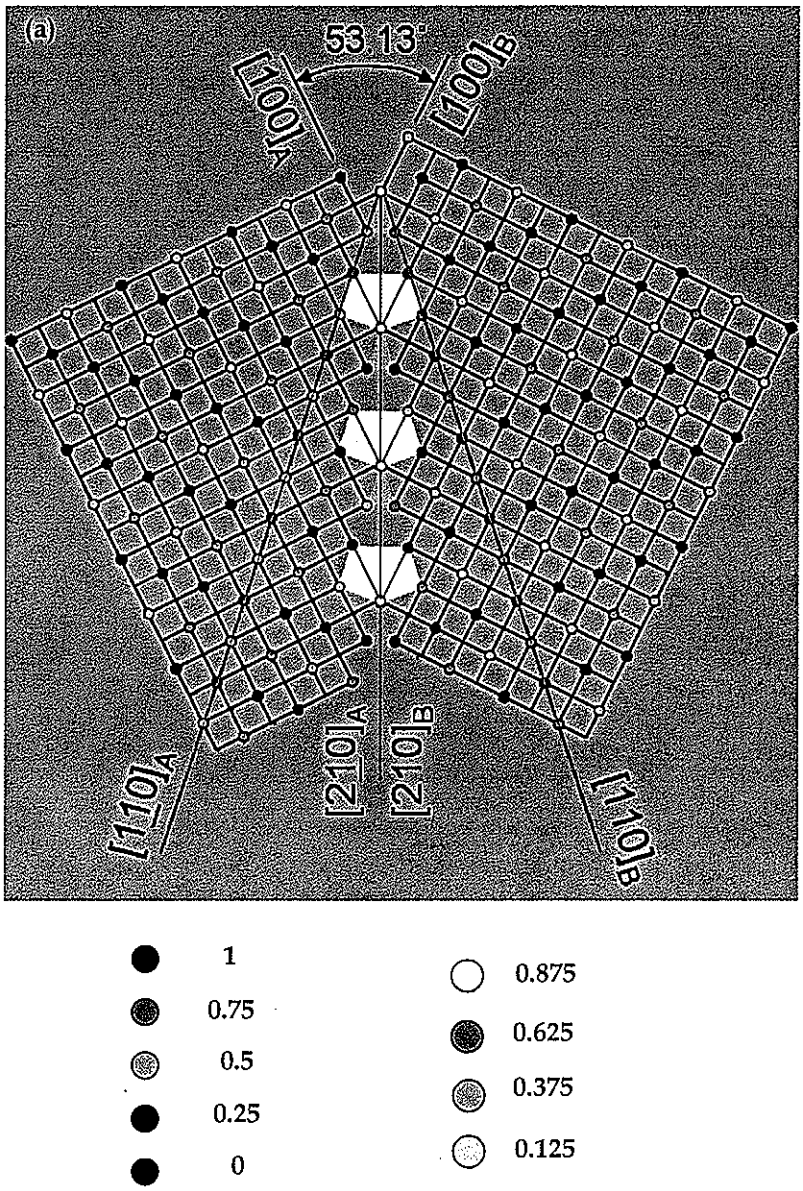

Figure 6-14. (a) Atomic structure of {210} type of twin boundaries and its boundaries area in color.

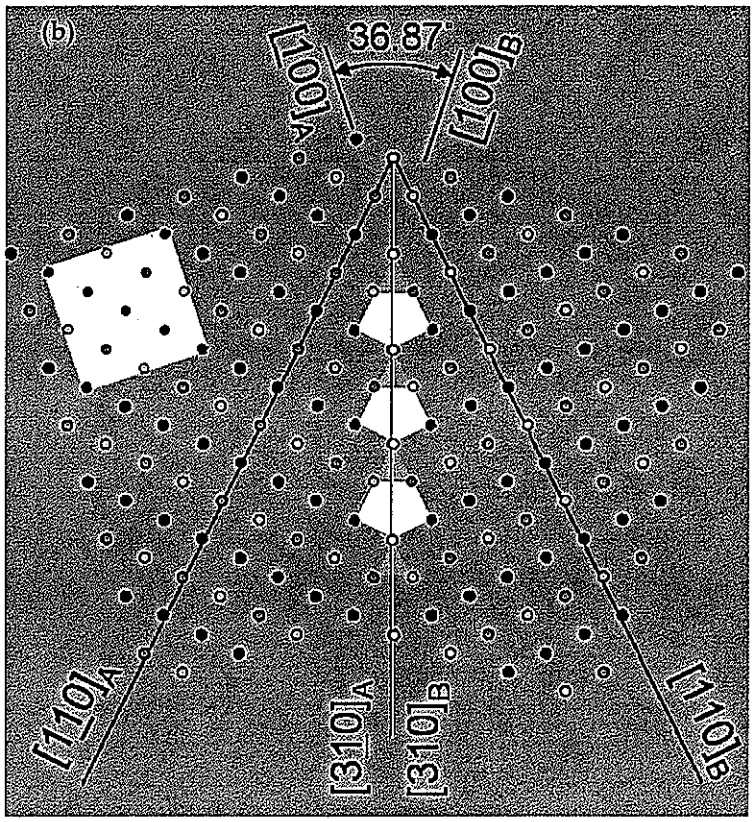

Figure 6-14. Continued. (b) Atomic structure of twin boundaries of {310} type and its boundaries area in color showing the twin boundary unit area is smaller that that of {210} type.

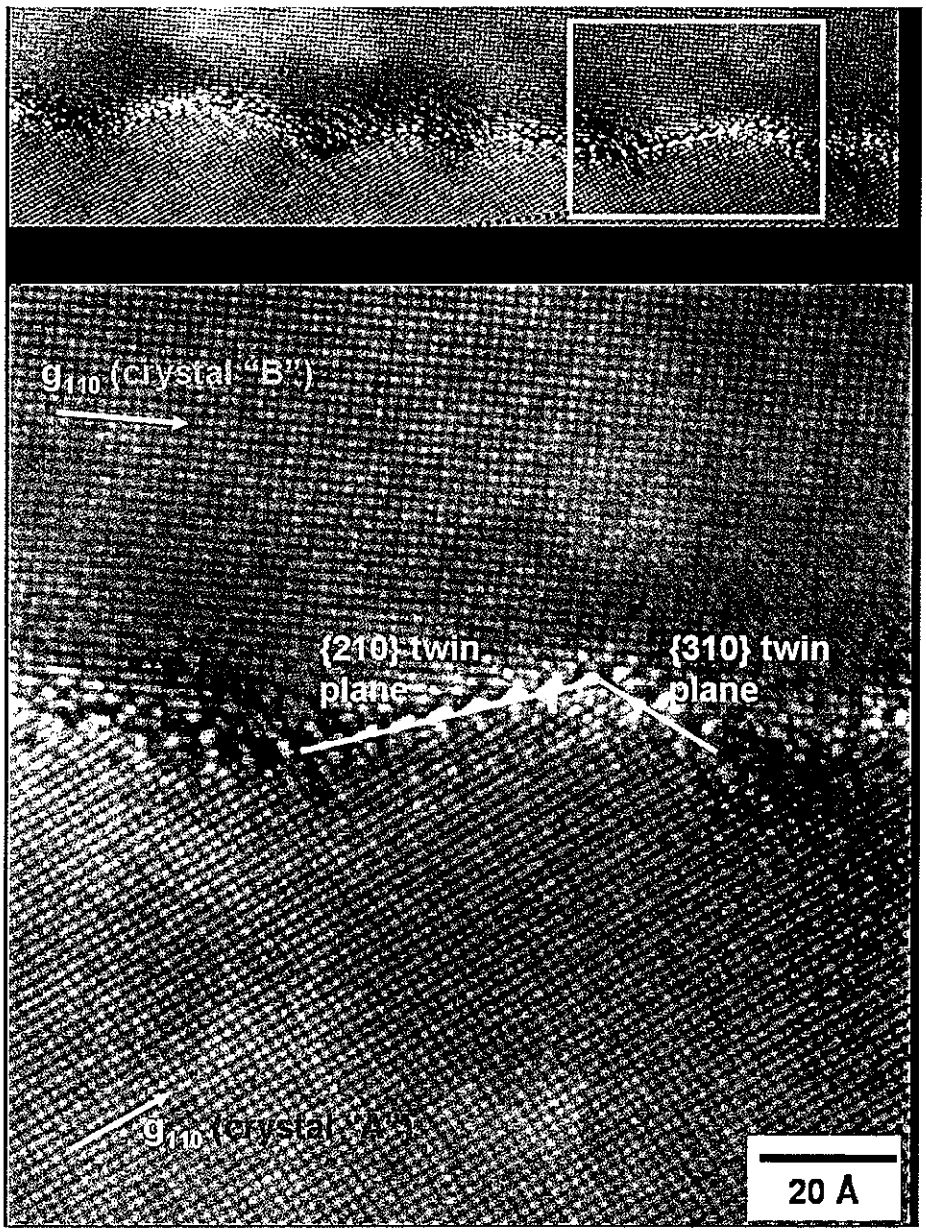

Figure 6-15. High resolution TEM image taken from the core of a star-shaped silicon particle.

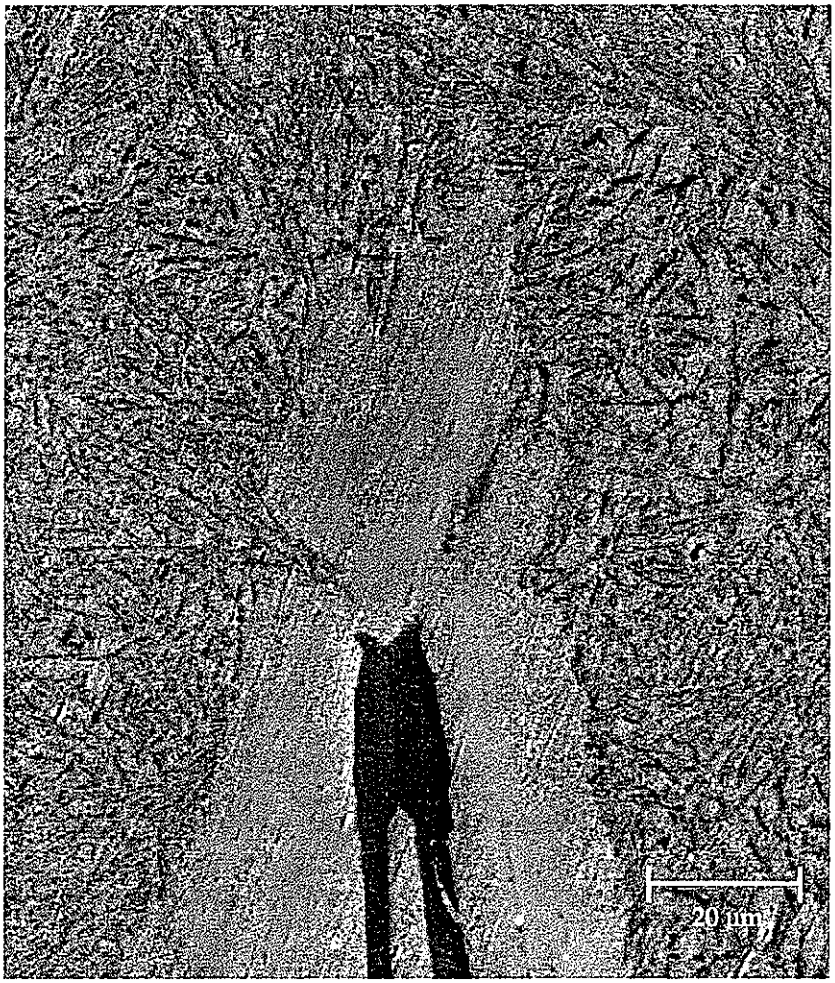

Figure 6-16. A longitudinal view of a star-shaped rod, revealing an axially oriented twin plane and an associated groove at the solid-liquid interface.

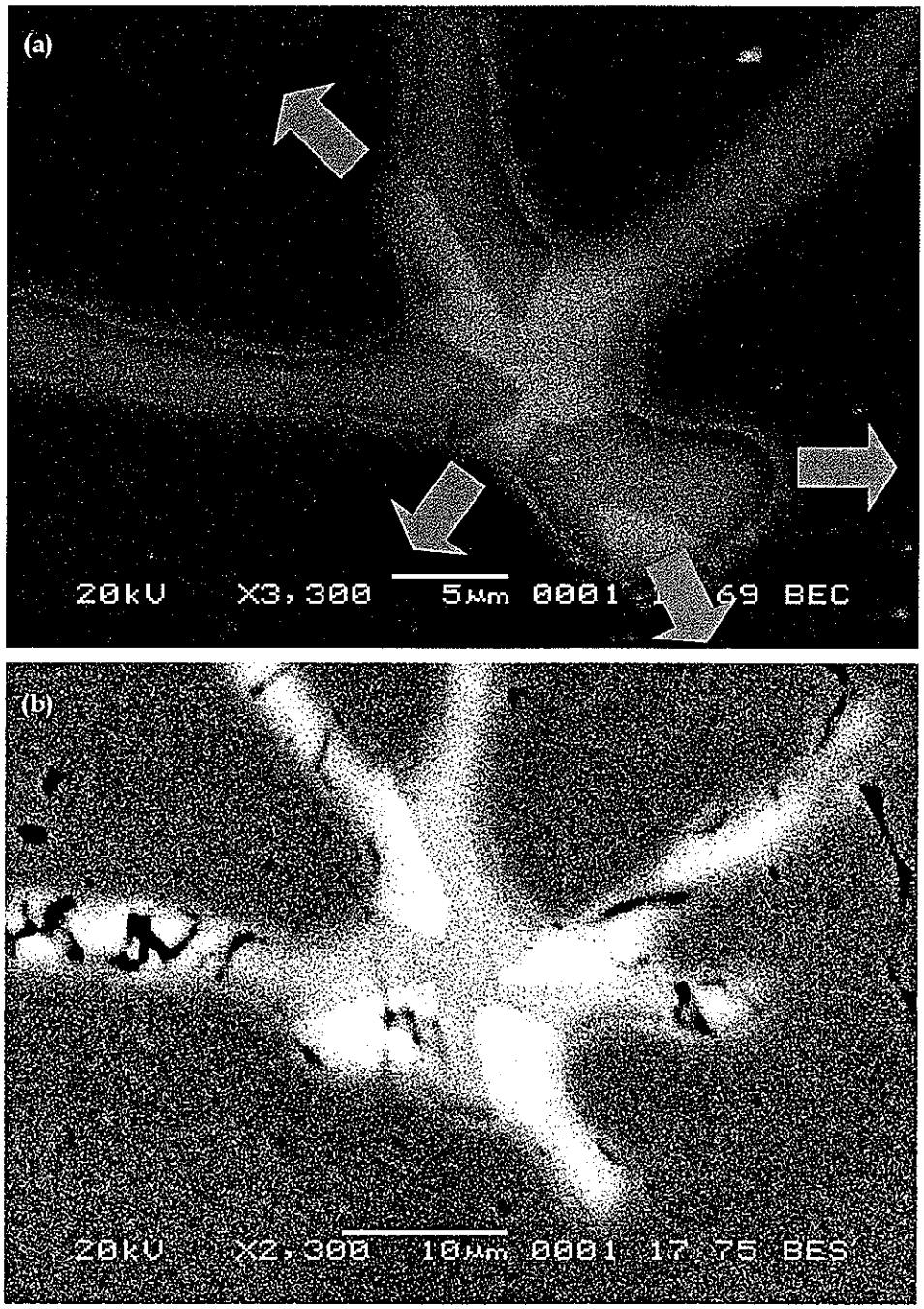

Figure 6-17. (a) Interface instability leads side branching from the core and (b) after 300μm growth from (a), twin boundaries reconfiguration occurred with branching.

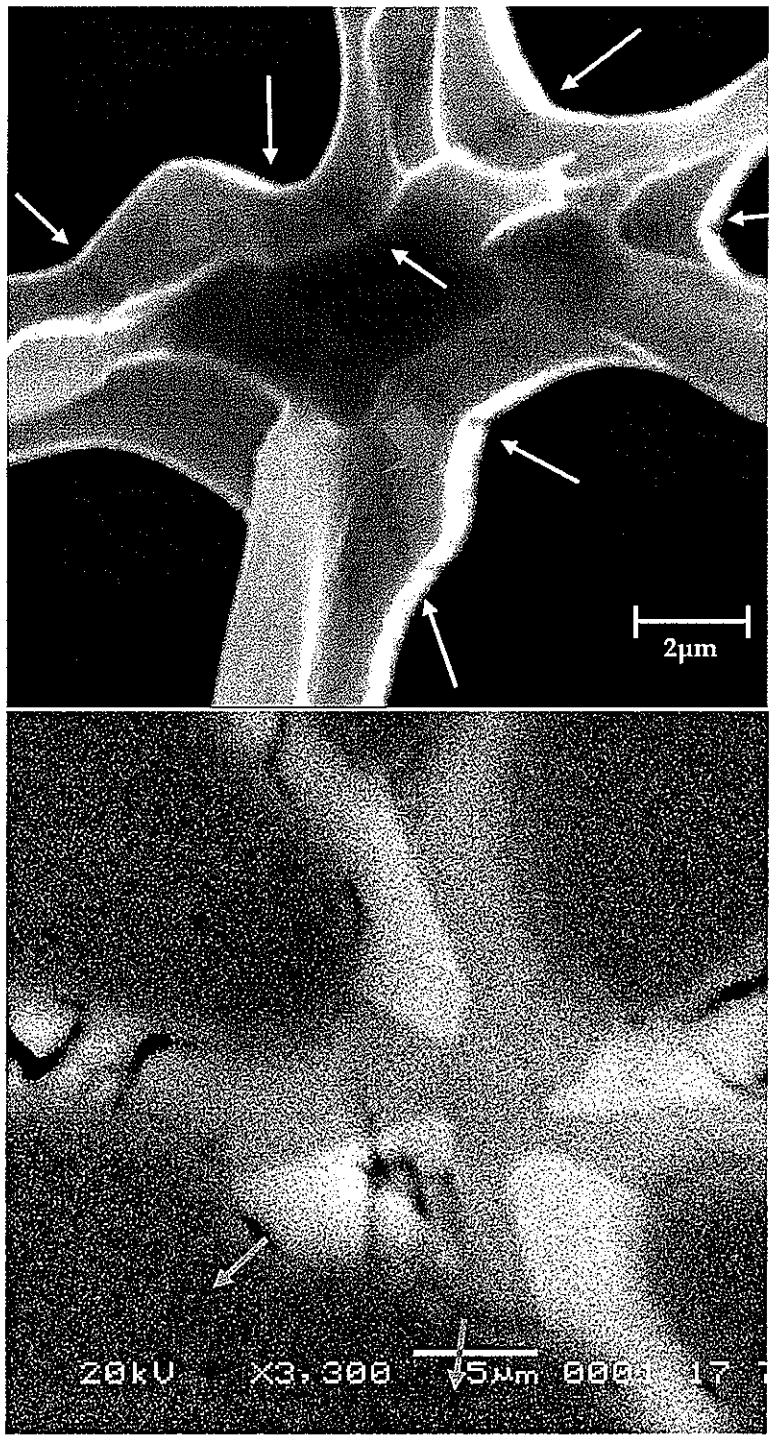

Figure 6-18. Early stage of star-shaped silicon evolution showing radial instability leads to a new secondary sideplate at the twin orientation.

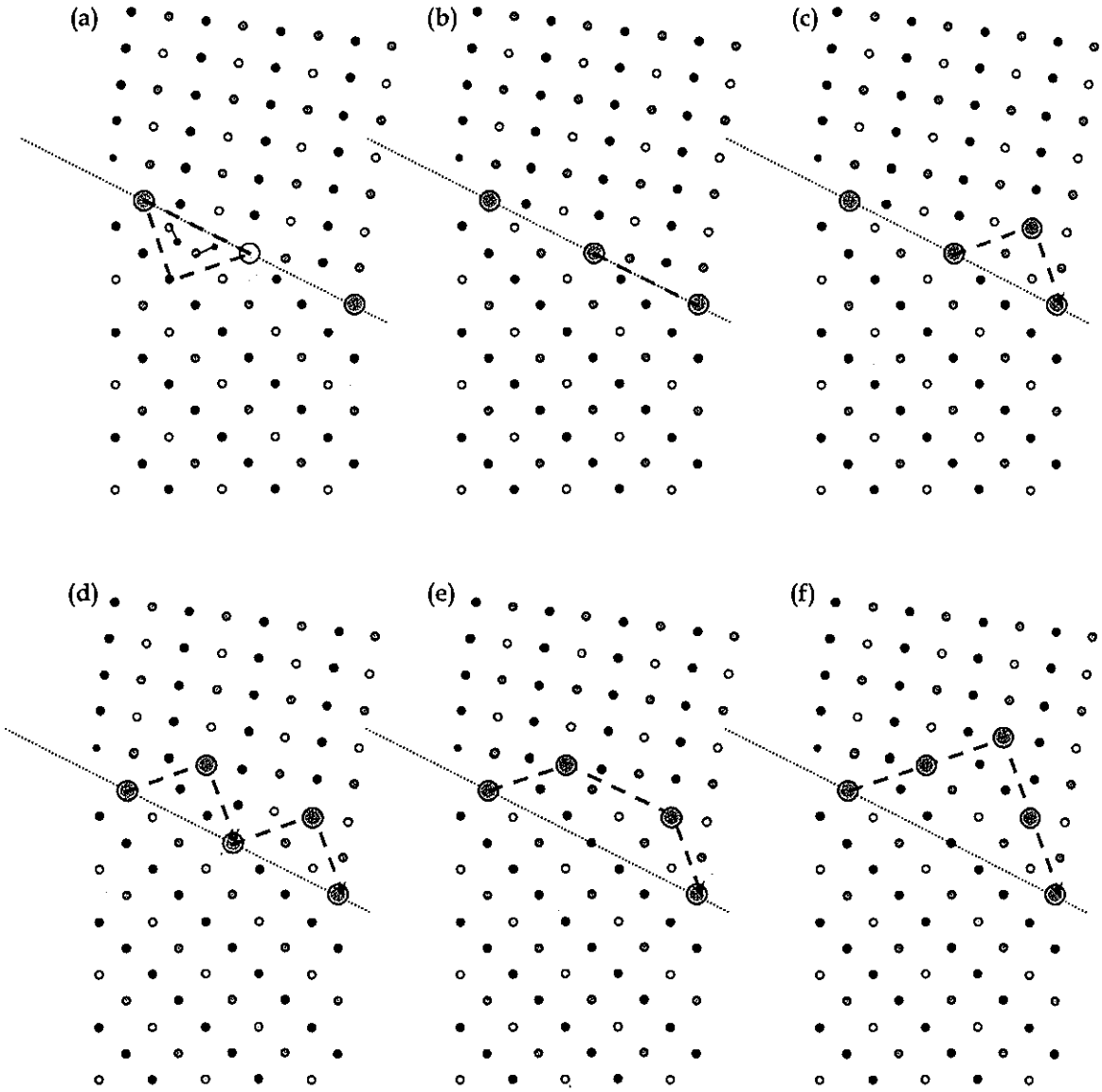

Figure 6-19. Proposed "two-atom" twin boundary migration mechanism. In this case, the migration occurred from (a) to (f), from {210}to{310}.

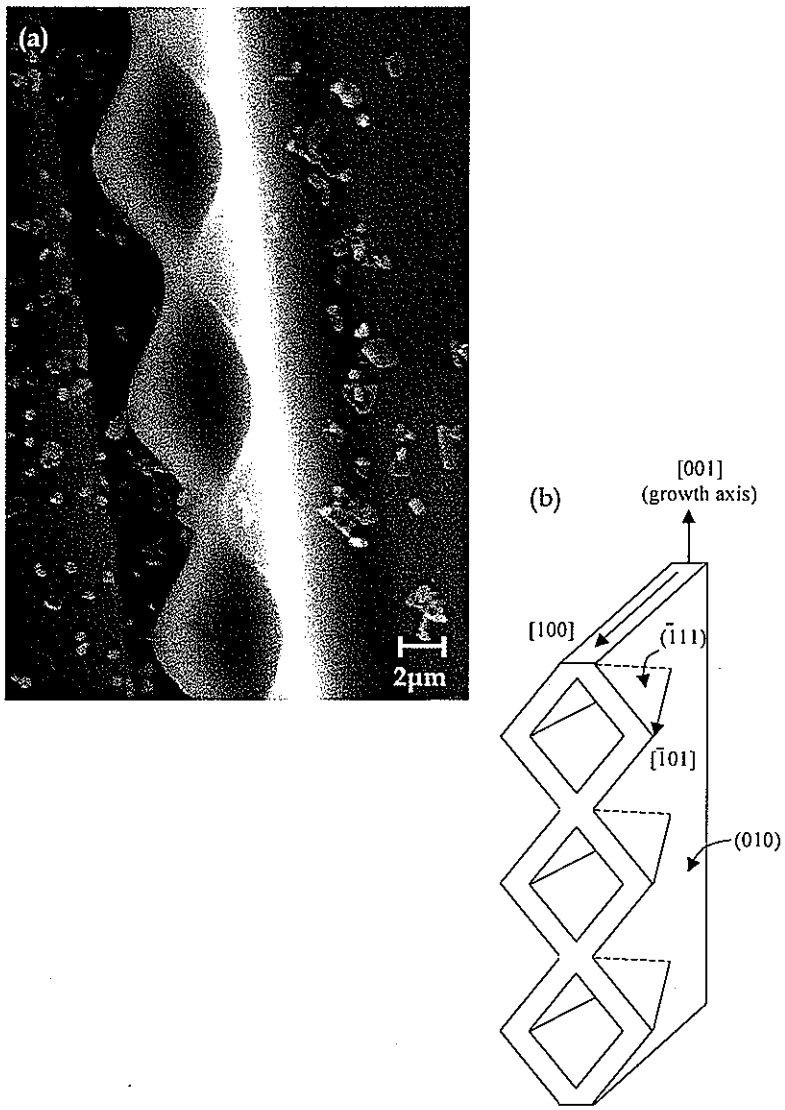

Figure 6-20. (a) Examples of the fluted structure and (b) Schematic illustration of (a). The overall growth direction is vertically upward in each image.

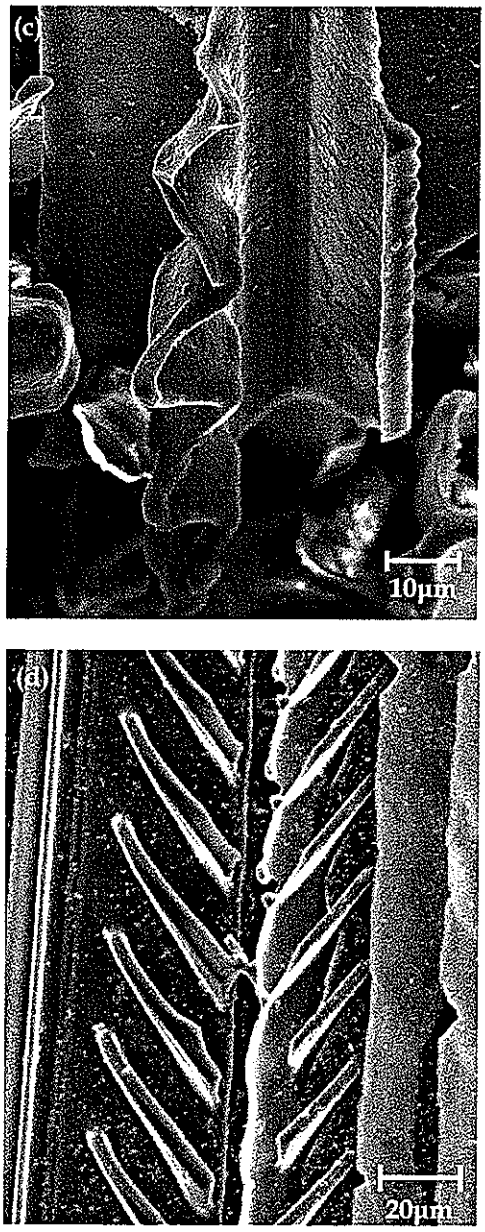

Figure 6-20. Continued. (c) Corrugated structure and, (d) Tertiary sideplate structure in the star-shapes silicon rods. Specimens were deep-etched to remove the aluminum-rich phase. The overall growth direction is vertically upward in each image.

CHAPTER 7

Array Structure and Spacing Adjustment

In the preceding chapter, it was shown quite definitively that coherent symmetric {210} and {310} twins are essential for the selection of the stars-shaped faceted growth mode and that these coherent twins play an essential role in morphological and mechanistic selection of silicon phase in Al-Si alloys, which determines overall microstructure in both eutectic and off-eutectic alloys. The propagation of faceted silicon domains, discussed in Chapter 5, might have a similar trend as seen in metallic dendritic array evolution. A careful examination is, however, desired to evaluate this relatively regular faceted array since complex branching and morphological selection occur behind the faceted silicon tip by a self-motivated way of twinning in the core that may not be seen in the metallic cellular and dendritic growth.

In this chapter, we examine the primary faceted array structures and investigate the mechanisms of lateral domain spreading and spacing adjustment of primary silicon phase during directional solidification in hypereutectic Al-Si alloys. A careful observation and measurement of complex branching and spacing of faceted primary bicrystalline silicon will provide further understanding of array evolution and associated spacing adjustment of the primary phase array, in combination with the critical role of twin boundary migration.

7.1 Array evolution

In the conventional dendritic array evolution, individual dendrite tips are decoupled to a regime of isolated self optimization while a cellular growth seems to have an overall array optimization characteristic with strong interactions between the cells. The structural difference of these two patterns is that dendrites can be distinguished by the presence of side branches and cells are defined as a non-parabolic and periodic pattern with missing branches. Accordingly, the tree-like morphology of angular silicon tip shown in Fig.6.1 implies that the silicon rods with side branches emanating along <100> at low growth rates might be considered as a dendritic diffusive coupling growth with relatively strong anisotropic interfacial properties of faceted silicon. This key issue will be discussed in Chapter 8 because we need to collect proper, exact, and essential tip conditions to describe overall growth mode of low-velocity off-eutectics. We will, thus, focus on the lateral propagation mechanisms and related branching events in detail.

The transverse sample cross-sections in Fig.5-15 show the evolution of the microstructure at different positions along the growth axis. An interesting feature in these micrographs is the emergence of a novel microstructure in the form of star-shaped silicon particles as discussed in Chapter 5 and 6. These textured domains grow laterally at a relatively rapid rate, on the order of approximately 10% of the overall growth rate. Arising questions from this lateral propagation of faceted silicon array are what the mechanisms of multiplication are and how they occur during the growth. As shown in Fig.6-17 and 6-18, a specific configuration of twin boundaries and their mobility must be the answer for the question. Furthermore, we will look at the detail processes in a higher length scale to investigate array dynamics.

Fig.5-17 shows a series of such transverse cross-sections where the textured dendritic array spreads laterally into regions of non-textured and randomly oriented silicon phase, and eventually across the whole sample cross-section. We can see that there are, in fact, more than one textured domain with slightly differing in plane orientations, as shown in Fig.5-17(a) and (b) with different color codes. Roughly speaking, the whole cross section is covered by the textured domains after 50mm and 35mm growth distances at 0.5μm/s and 1μm/s growth velocities respectively. A same colored domain consists of identical twinned bicrystalline of silicon rods. Indeed, we have identified several mechanisms for the formation of new primary dendrite cores spreading laterally. These include tip-splitting and tertiary growth from sideplates, both analogous to mechanisms of lateral propagation in non-faceted dendritic crystals. These mechanisms will be discussed in the later section, associated with branching and spacing adjustment of primary silicon.

It is worthwhile to recall the two key observations of growth orientations from star-shaped domains. First of all 36.87° and 53.13° between side branched arms are obviously coherent {210} or {310} twin angles, constituting a core structure of faceted silicon rods and assisting a branching of second arms. The second orientation relationship only to the identical twin angles is that each silicon rod has an identical orientation to the reference in the same domain. Since a single domain of textured silicon consists of dendrites having common sidearm orientations, it is highly unlikely that the newly formed dendrites at the periphery of the domain are due to nucleation events. However, the presence of a single grain orientation suggests that the textured regions of primary silicon arrays develop from the occurrence of a single silicon dendrite which has formed during the earlier stages of growth. Accordingly, the fact that side plate orientations (hence, twin orientations) are identical within the given domain suggests that the entire twinned domain originates from one twin-pair of two silicon grains.

7.2 Analysis of array dynamics

7.2.1 MST calculation

One example of MST at the cross section of 55mm and 70mm growth distance is plotted in Fig.7-1 (a) and (b) respectively. The mean edge length is calculated for cross-sections taken at increasing relative distances from the initial interface. Average minimum edge length, m shows interesting behavior as a function of the growth distance in Fig.7-1(c). The m of both two velocities indicated by closed triangles and circles with solid lines in Fig.7-1(c) decreases by 35mm (1μm/s) and 50mm (0.5μm/s), and then increases to roughly constant values. The normalized lengths ($\sqrt{A/N}$) for two velocities shown as open triangles and circles with dotted lines in Fig.7-1(c) are also similarly decreasing and increasing around this point, where A is array area and N is the number of points. Both MST calculations and normalized lengths indicate that the density of silicon dendrites in a given domain decreases during propagation but increases and reaches to constant representing spacing adjustment has been accomplished during the faceted array evolution. This behavior implies that there might be different contributions to the faceted array evolution before and after this critical point.

7.2.2 Voronoi tessellations

The regime between 50mm and 70mm at 0.5μm/s, where m is increasing, the Voronoi diagrams are compared in Fig.7-2(a) and (b). Though the constructed area is a middle of the sample, a density of points is also significantly decreasing resulting in spacing increments at this regime. The cluster of points which represent the position of twinned star-shaped silicon is vanishing between these two cross sections. The frequency of number of side for Voronoi polygons constructed at different growth distances is plotted in Fig.7-2(c). This directionally solidified sample at 0.5μm/s has a clearly sharper and more symmetrical shape in the frequency at 70mm growth than that of shorter growth distances. It is not surprising that the most probability of polygons is hexagonal as similarly observed in cellular or dendritic array.

The fact that clusters of silicon rods are dispersed indicates that the primary spacing within the cluster is under the stability limit of the faceted silicon array. Therefore, Voronoi diagrams from the different positions support that a gradual spacing adjustment occurs after the critical growth distance. The reason why this critical point exists during array evolution of faceted silicon can be explained by the domain propagation and consecutive spacing adjustments. Before the critical growth distance, the domains propagate laterally at a relatively higher rate than the axial growth rate. Althought there might be a local spacing adjustment by a dynamical

branching of secondary or tertiary arms, the lateral spreading of faceted silicon bicrystalline makes a main contribution to overall array structures. On the other hand, after the lateral propagation is accomplished over the whole cross section, spacing adjustments occur dominantly around clusters of silicon rods. A notable feature of Voronoi polygons clearly substantiates this criterion of dynamic array evolution of faceted silicon in Fig.7-2. The frequency of six-sided polygon at 70mm is 0.35 with more symmetric shape. From array analysis for deep cells of Al-Cu alloy by Tewari et al [ref], the probability of hexagonal polygon is over 0.45. Although the probability of a hexagonal polygon in our faceted silicon array is less than that of Al-Cu alloys, the hexagonal is a predominant polygon in Voronoi diagrams after spacing adjustment of the silicon array in this study.

7.3 Branching and spacing adjustments

The star-shaped silicon particles must be connected throughout the whole sample even if they look like separate features in a two-dimension. This necessitates the evolution of the microstructure similar to that in a single crystal casting where the textured dendritic microstructure is a result of tip splitting and other requisite branching events operative during growth. In a similar fashion, the star-shaped silicon grows and spreads laterally by the continuous branching from the sideplates, thus, replacing the randomly textured silicon microstructure formed during the transient period. In this chapter we will examine detailed diffusion optimization processes, namely branching and splitting.

7.3.1 Tip dynamics

Tip-splitting phenomenon during dendritic growth of silicon crystals was observed as shown in microstructure series of Fig.7-3(a). These cross-sections are separated from each other by a nominal distance of 10 microns showing a tip splitting event results in the formation of a new dendrite. A tip of the growing silicon dendrite may assume a variety of shapes; it may have a compact core with secondary branches emanating outwards or an extended core which may split into two compact cores, emerging in Fig.6-1. As the dendrite tip splits, the point of separation is then occluded by the surrounding aluminum phase. Tip splitting steps are also schematically depicted in Fig.7-3(b). For an easier splitting of primary tip, the migration of twin boundaries must be essential in the core.

There is a close link between the star-shaped silicon dendrites and the spider-web morphologies observed during the transient period where the strong <100> texture was not firmly established as well as at steady state. The picture (Fig.7-4 and 5) shows the coexistence of

the spider-web morphology with the star-shaped dendritic morphology. Here, especially in the deeply etched microstructure in Fig.7-5, one can see that the spider-web morphology does not grow parallel to the overall growth direction as opposed to the star-shaped dendritic arrays. Due to this non-directional growth behavior, growth path of the textured star-shaped regions and of the spider-web particle coincide. This convergence in the growth path of the two morphologies results in the convolution of the solutal fields of the two distinct regions. The intervening solutal field also gives rise to the disappearance of some of the side arms of both features, as shown in Fig.7-4. This convolution may cause the termination of a number of star-shaped particles as they approach near the spider-web morphology. In the case of Fig.7-4, however, two particles have survived and occupied their own positions slightly migrated from the original positions.

For the selected local area, positions of the silicon dendrite cores were recorded at different cross-sections in Fig.7-6. It reveals that the tips of the silicon dendrites tend to migrate towards seemingly more spacious regions in terms of silicon phase fraction. These regions having a relatively low silicon phase fraction are indicative of solute-rich (silicon-rich) regions. Therefore, the diffusive optimization process is constantly carried out through this type of "tip migration "processes at the growth front. Note that there are two or three complex spider-webs in the real microstructure of the position map. It means that there must have been the interactions between primary rods and spider-webs, as discussed above.

7.3.2 Sideplate branching

Significant observation in the lateral propagation of array is a new star-shaped evolution branching from secondary or tertiary arms. These branching events are particularly important for the peripheral dendrites that surround the textured region since they reside near the boundary where the supersaturation should be relatively high, a conclusion inferred from the fact that branching necessitates solute-rich regions. The branched arms from the parent stem which is on the face of domain are mainly interacting with non-textured region. In the Fig.7-7, one branched arm of the eight-pointed silicon rod is dynamically responding to the not-textured region during only 6μm growth distance and new angular silicon evolves. Note that the parent silicon particle is placed in the outer textured domain. Although there is no quantitative analysis showing the dominant process for the domain propagation, it seems that secondary or tertiary branching is more likely to be a main mechanism for the lateral propagation of array than tip splitting. Thus branching from secondary or tertiary arms is a main mechanism of lateral propagation of star-shaped domain as similar as dendritic array evolution. Indeed, the microstructural evidence

shows that there are several tertiary branches on the side plates of a typical star-shaped structure, as discussed earlier in Chapter 3.

In a system with pronounced anisotropy, such as during the growth of a faceted crystal, sidebranches form readily when the local spacing is large. In the inter-silicon dendrite region, the liquid that is solidifying in the last place may be highly supersaturated since silicon atoms are being rejected from the solidifying Al phase and a parent silicon rod has to find an easier way to respond to this relatively higher supersaturation. Thus tertiary or secondary arms are dynamically branching toward solute-rich liquid of inter-plate. The evidence for this active response of sideplates is firmly shown in the Fig.7-8.

When a whole cross section of the sample is covered with faceted primary silicon particles, the sequent pictures reveal that new star-shaped silicon from the tertiary branched arm emerges near to a domain boundary between the slightly different orientations as shown in Fig.7-9. The only difference between Fig.7-7 and Fig.7-9 is that the former is taken during the period of lateral domain propagation and the latter is attained when the propagation of domain is near completion.

7.3.3 Spacing adjustments

Accordingly, spacing adjustment can be facilitated in a number of ways, such as (i) by the formation of new primary trunks as a result of tip splitting, (ii) by the formation of new primary arms from secondary branches, (iii) by tertiary branching from the side plates as a consequence of keeping up with the solute redistribution at the growth front, and (iv) by lateral position changes of the growing "dendritic" tip in accord with the governing solute fields ahead of the interface. As seen in Voronoi diagram in Fig.7-2, changes in primary spacing may result from two distinctly different mechanisms: the tip elimination and splitting. When the local spacing is smaller than the characteristic spacing, one of the tips is eliminated to increase the spacing. Once a tip is eliminated, the adjoining primary silicon rods reorganize. On the other hand, branching is operative when the local spacing is larger than the characteristic spacing. In this case, the tip assumes an elongated shape and then splits into two, thereby creating an additional space, as shown in Fig.7-10. The mechanisms of branching and elimination continue until a characteristic spacing is established.

This criterion is very similar to that of Hunt and Lu[73] who discussed the array stability limit and the upper spacing limit. Hunt and Lu suggest that tip splitting is likely to occur for a cellular growth and a tertiary branching seems to easily occur in a dendritic array for a spacing adjustment at the upper spacing limit. Although we observed the branching from tertiary

sideplates as well as the tip splitting in the faceted silicon array, a tip splitting may occur at a regime with a higher spacing to dissipate local solutes. As mentioned before, new primary rod from tertiary sideplates results mainly from lateral spreading of array. The sideplate makes a contribution to the local spacing adjustment far from the tip, changing its direction as shown in Fig.4-11.

Another interesting observation of spacing adjustment is the competition between neighboring dendrites, splitting and joining events occurring at the tip region. Fig.7-10 shows the competition between two dendrites and the resulting disappearance of one of the dendrites as shown by the arrows in circles in Fig.7-10(c) ~ (f). Here, one can also observe the splitting and subsequent rejoining of a dendrite tip indicated by the arrows in (a) and (b) of Fig.7-10. The competition with neighboring Si dendrites by splitting and joining events at the tip is one of the spacing adjustment mechanisms for efficient solute redistributions.

Spacing can provide us valuable information regarding the nature of growth. However, due to the limitation of the star-shaped morphology to a certain velocity range, microstructures having a more eutectic character form at higher velocity regimes. For this reason, one needs to define two types of spacing, namely primary and eutectic spacing, in order to compare these two structures. Note that only distances between two stems are counted in when no plates from the tertiary star-shaped silicon interrupt the straight line between them.

The primary and eutectic spacing measurements obtained from samples prepared at different directional solidification velocities and compositions are plotted in Fig.7-11. The primary spacing is found to decrease with increasing growth velocity in a manner that obeys $\lambda^2 V$=const relationship, where λ is the cell spacing and V is the growth velocity. This relationship is common to all diffusive transformations and it implies a more stringent diffusive coupling between individual star-like features. The way that this diffusive coupling is established can also shed light into various diffusive optimization processes operative during growth. The diffusive optimization is achieved by ordering of the whole array to facilitate more efficient chemical diffusion, similar to cellular growth in single phase solidification. Therefore, the increase in mean edge length after 35 and 50mm in Fig.7-1(c) is a measure showing the increase in array ordering, which is further evidence for diffusive optimization via spacing adjustment by splitting and joining of growing tips as well as creation, annihilation and progression of new side branches.

Summary of key points in this chapter

- Branching occurs in the form of tip splitting or side plates branching events. The latter is, however, a main mechanism of lateral propagation of array during the directional growth in near eutectic Al-Si alloys.
- The density of primary silicon rods increases when the lateral propagation is dominant during the array evolution. Once the spreading of faceted array is accomplished over the whole transverse of the sample, spacing adjustment occurred by the tip migration, splitting/joining, and dynamic tertiary branching to find an efficient solute redistribution.
- Minimum edge length, Voronoi polygons, and spacing measurements suggest that some level of diffusive optimization has occurred during the array evolution.

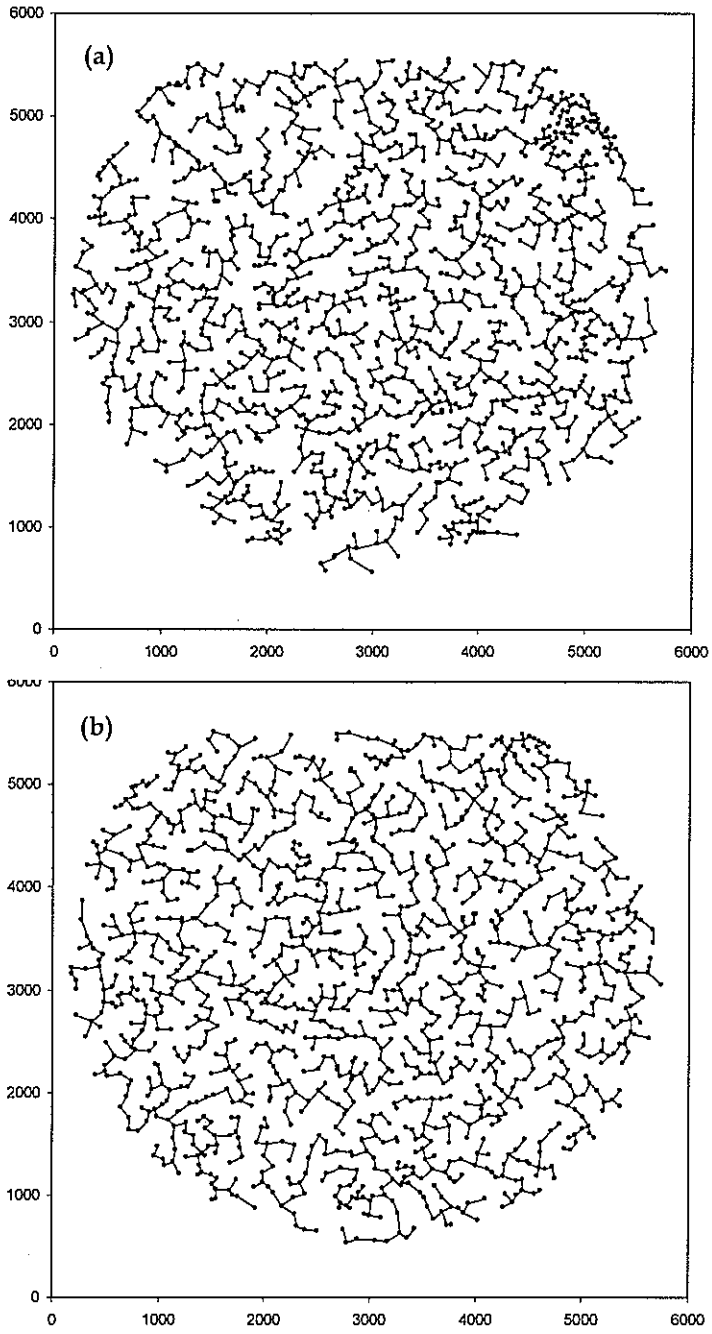

Figure 7-1. (a) and (b): Examples of MST at 55mm and 70mm growth distance respectively.

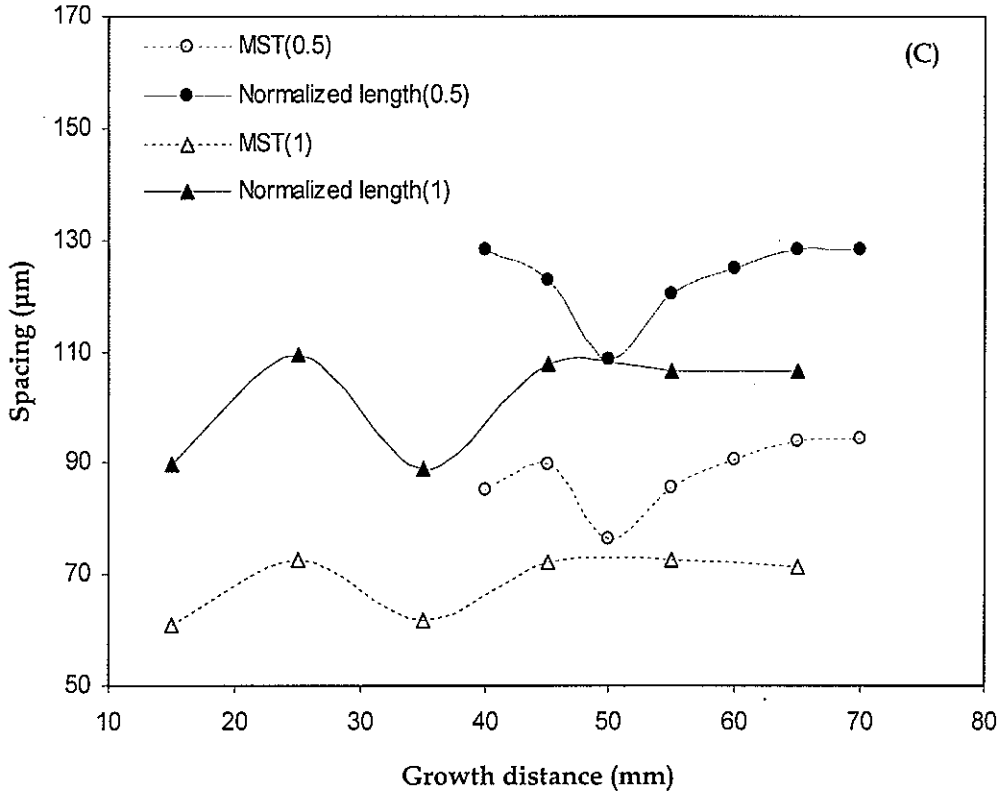

Figure 7-1. Continued. (c) Both of average minimum edge and normalized lengths are decrease and increase to constant as function of growth distance.

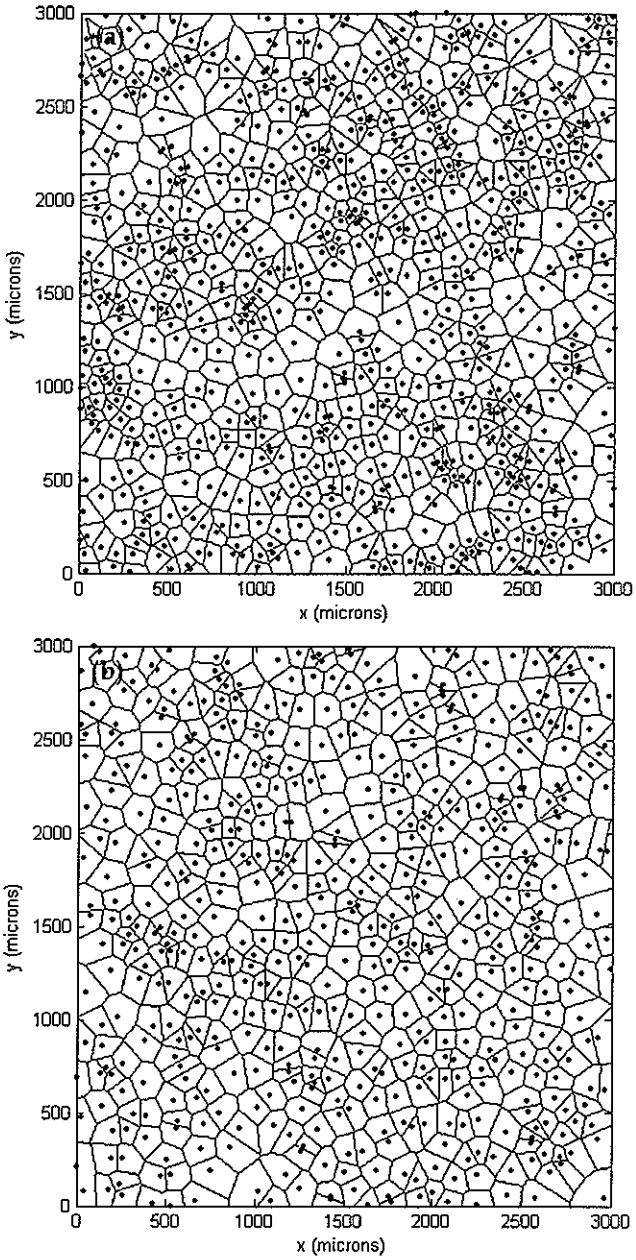

Figure 7-2. (a) and (b); Examples of Voronoi diagram at 55mm and 70mm, respectively.

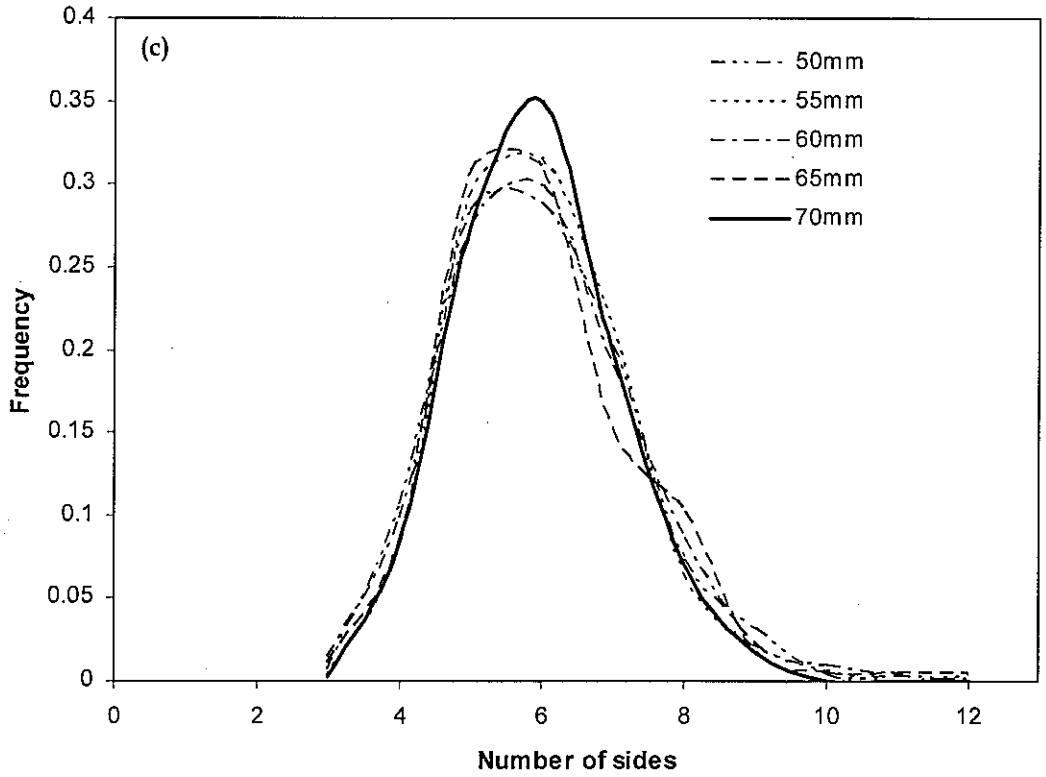

Figure 7-2. Continued. (c) The frequency of number of polygon sides goes to six and the distribution shape become more symmetric after spacing adjustments.

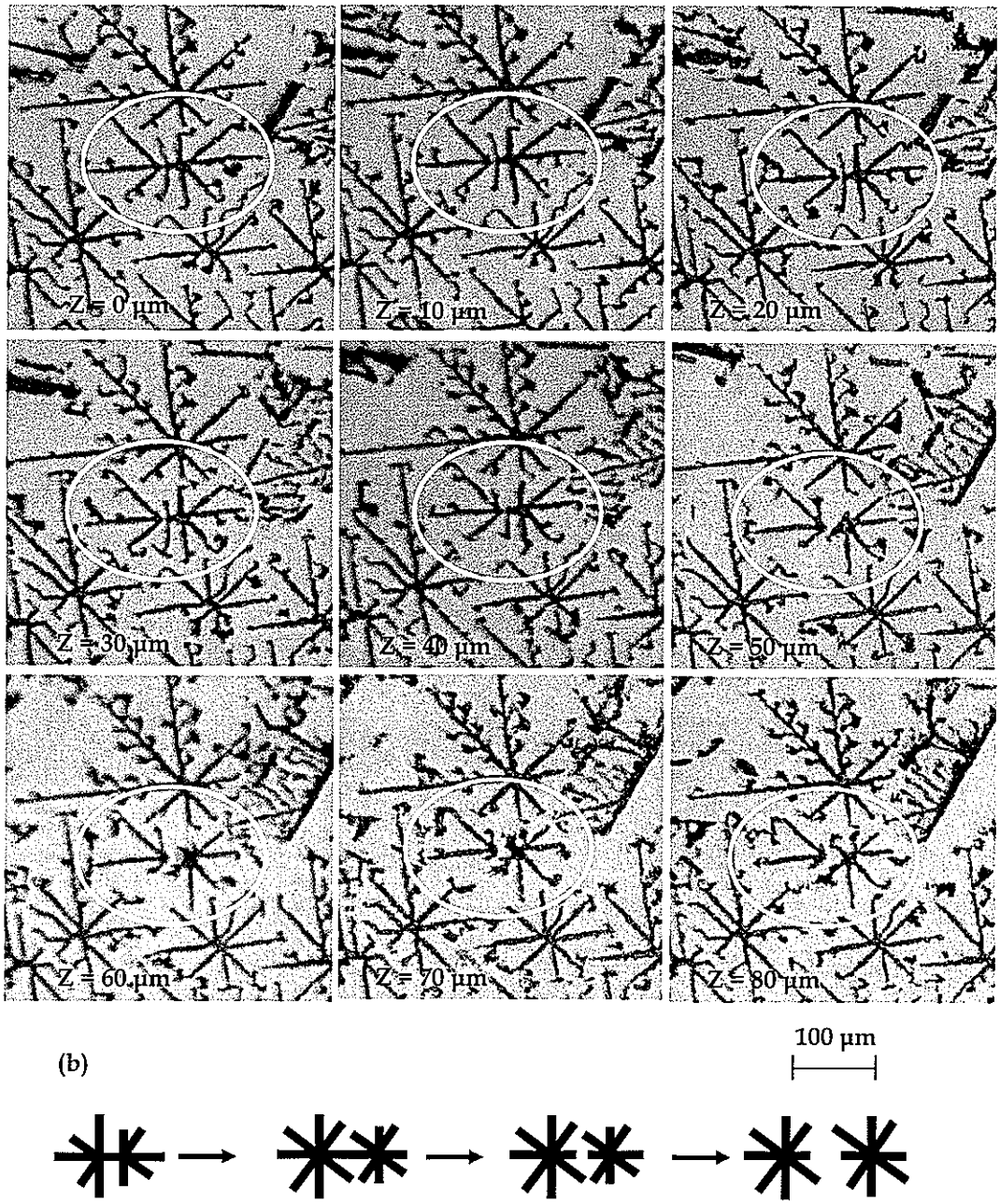

Figure 7-3. Formation of a new star-shaped angular silicon by splitting of the core structure. The silicon dendrite that undergoes tip splitting is encircled. The microstructures are from cross-sections perpendicular to the growth direction and are 10 microns apart. Relative elevation, Z, increases along the growth direction.

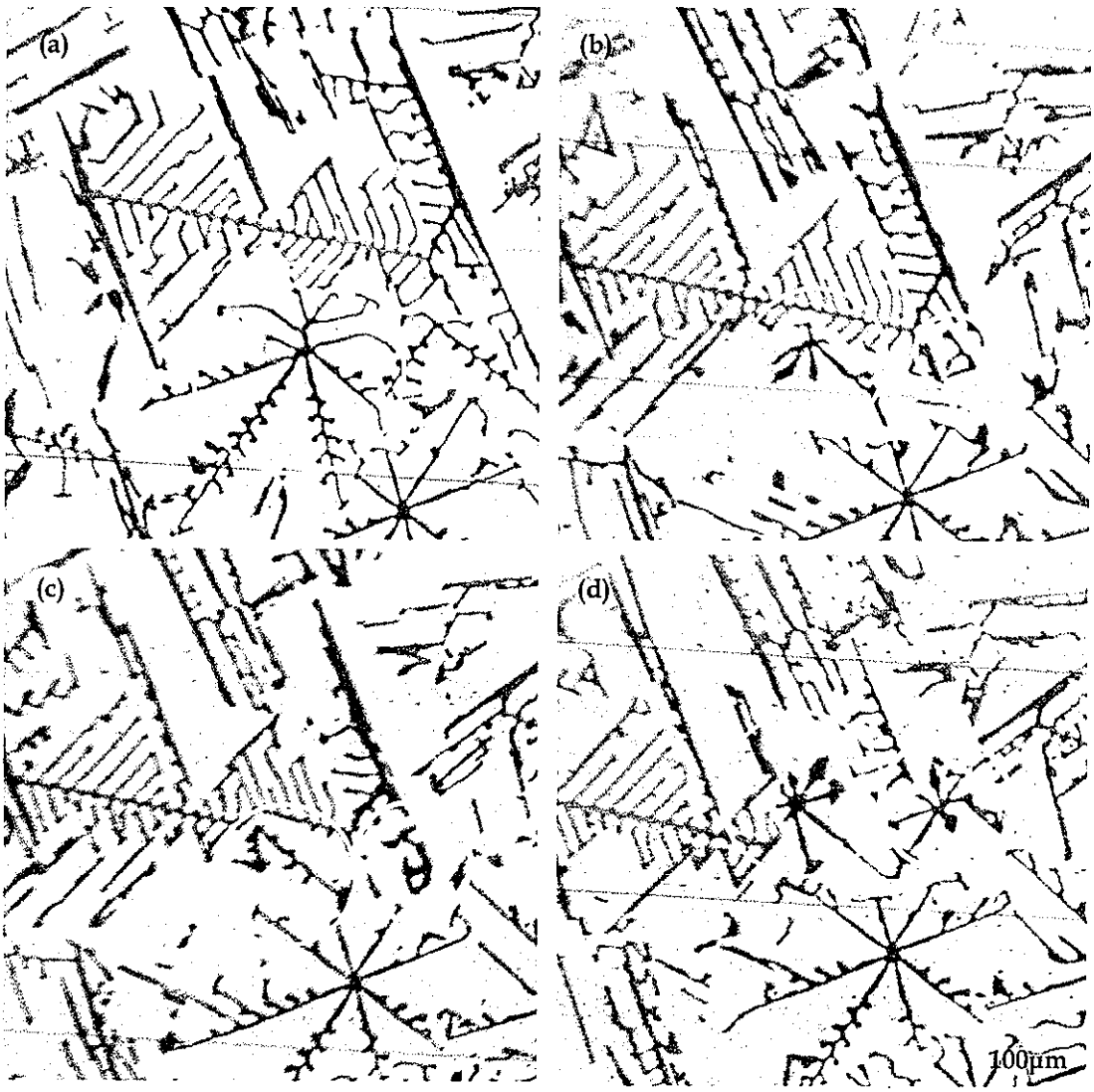

Figure 7-4. The competition between a starshaped silicon particle (indicated with the circles) and a spider-web morphology. The distance between the serial cross-sections are: (a-b) 95, (b-c) 35, (c-d) 55 microns, where axial positions of the cross-sections from the initial interface in increasing distance are (a)<(b)<(c)<(d). Here, solute fields of both structures interact, and the end effect on the microstructure manifests itself as missing sidebranches in both of the growth morphologies. In the end, the starshaped silicon shown in the circles prevail and continue to grow.

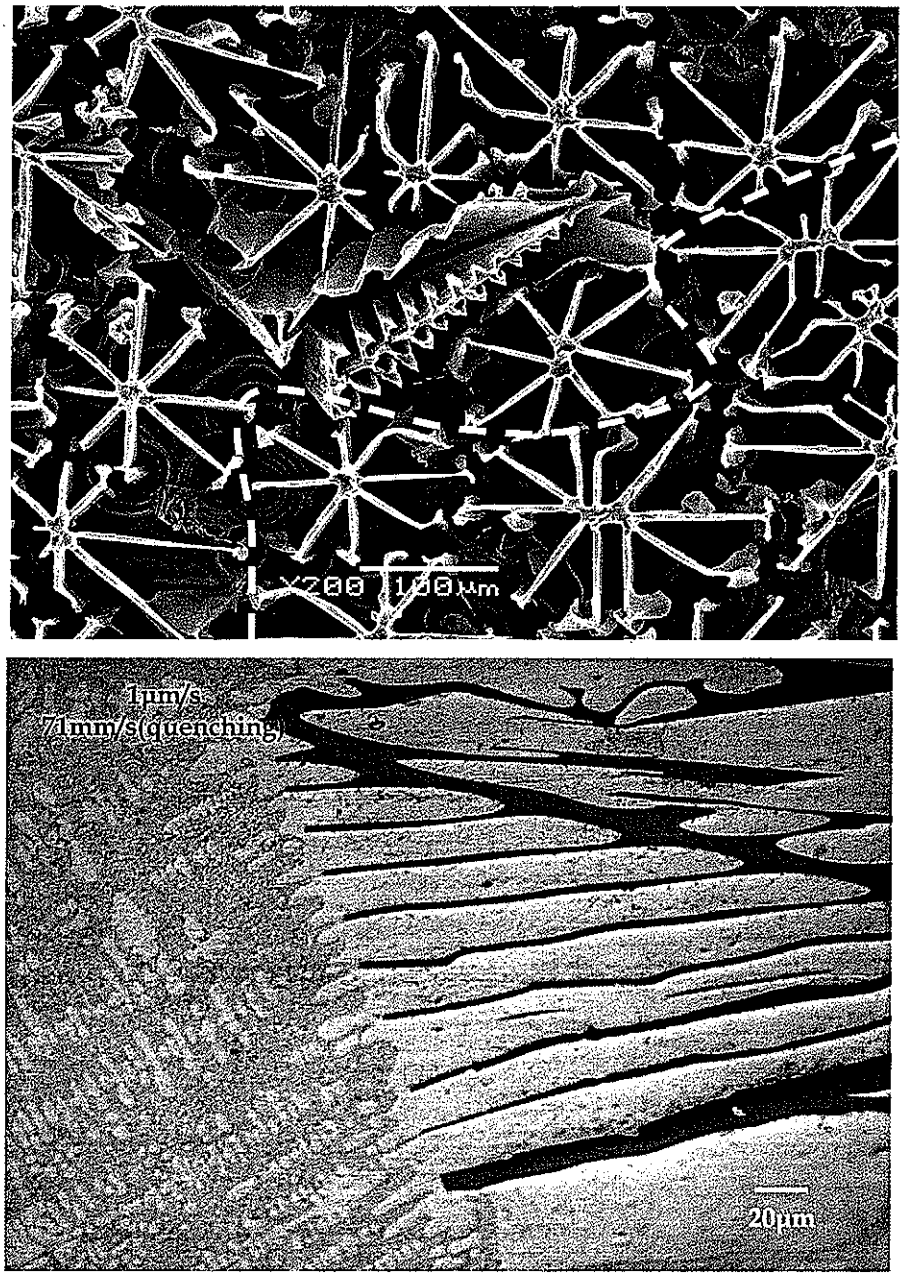

Figure 7-5. This deep-etched transverse cross-section shows the non-directional growth behavior of remnant spiderweb morphology. Also, note the two different rotation variants of the star-shaped sideplates.

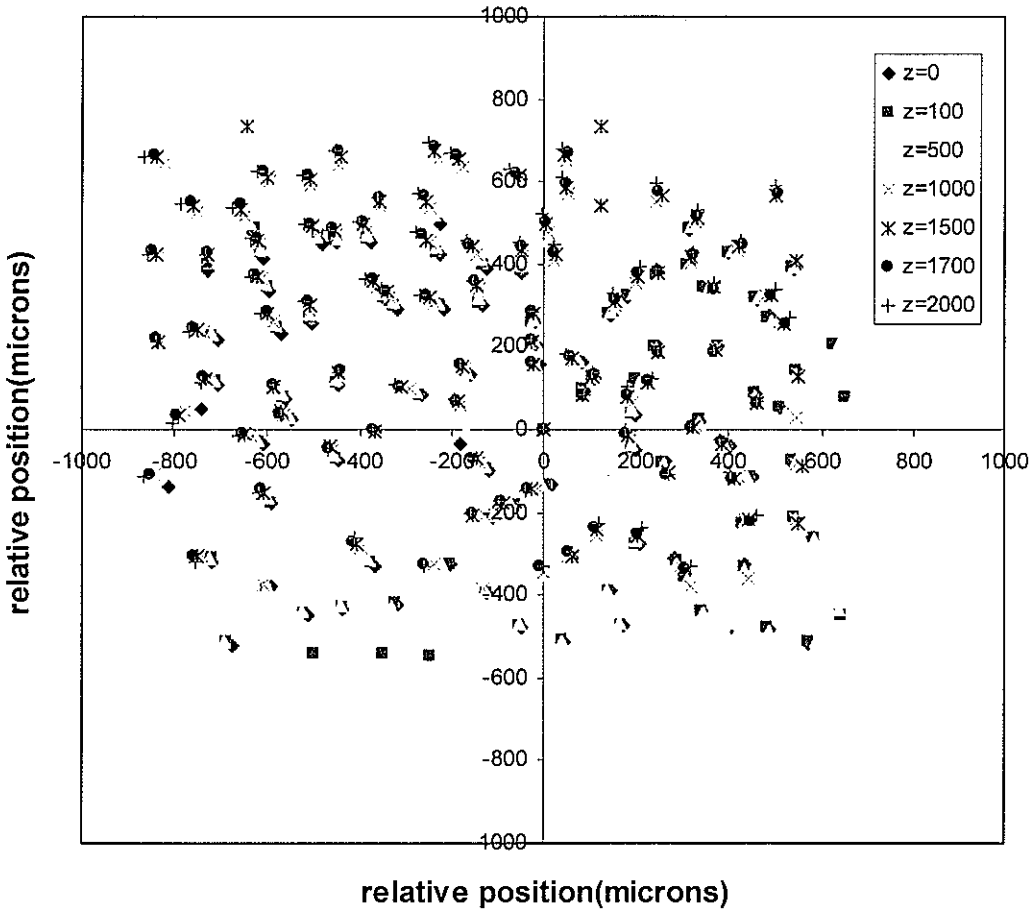

Figure 7-6. Primary core positions map, showing migration of tip during growth.

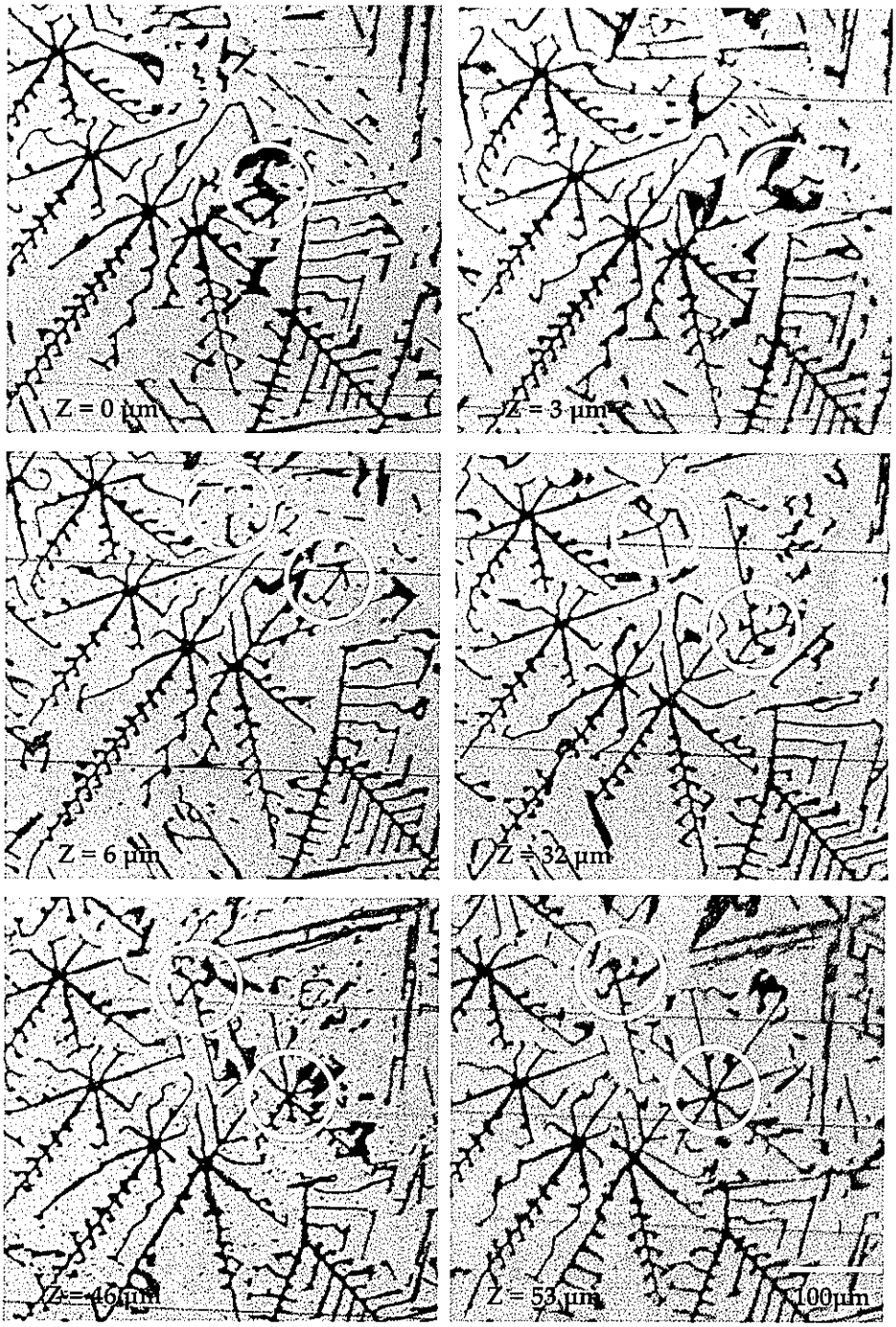

Figure 7-7. Formation of a new star-shaped angular silicon from the tertiary branched arm. Relative elevation, Z, increases along the growth direction, indicated in the lower left. The new silicon dendrite keeps the same orientation to the origin.

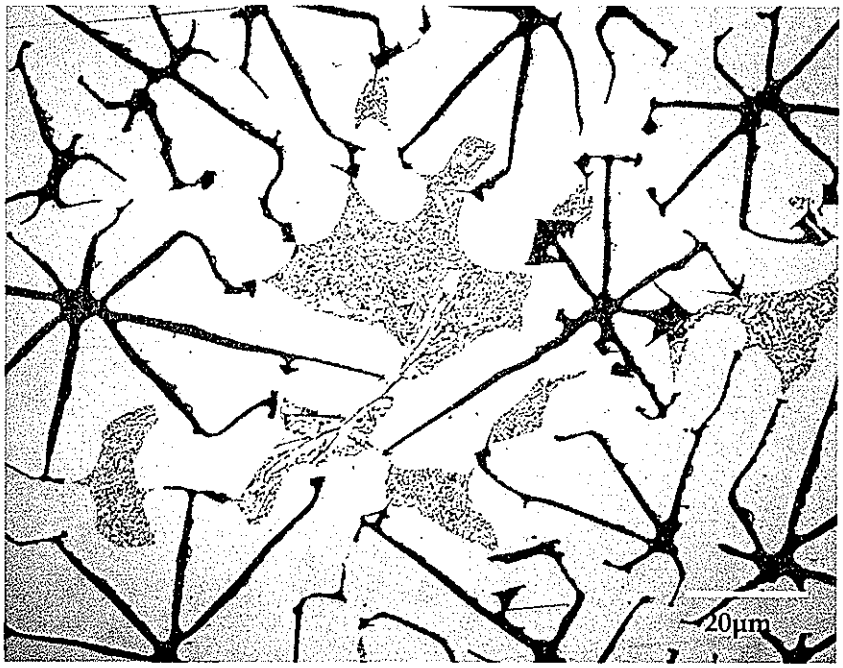

Figure 7-8. Microstructure at the quenched interface. The secondary branching arms are dynamically changing their radial direction toward interdendritic liquid with tertiary arms.

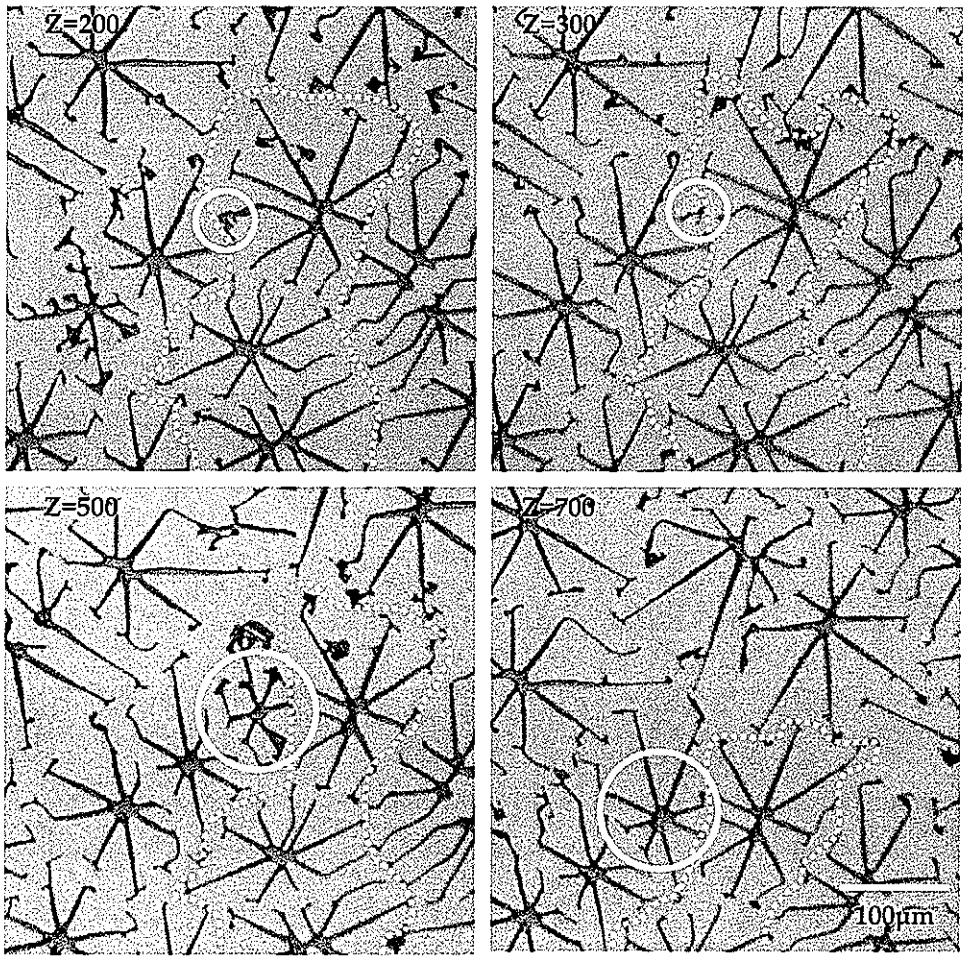

Figure 7-9. Formation of a new star-shaped angular silicon from the tertiary branched arm. This is occurring during the spacing adjustment regime as domain boundaries are indicated between two textured regions, not propagating to randomly oriented silicon plates shown in Fig.5-15.

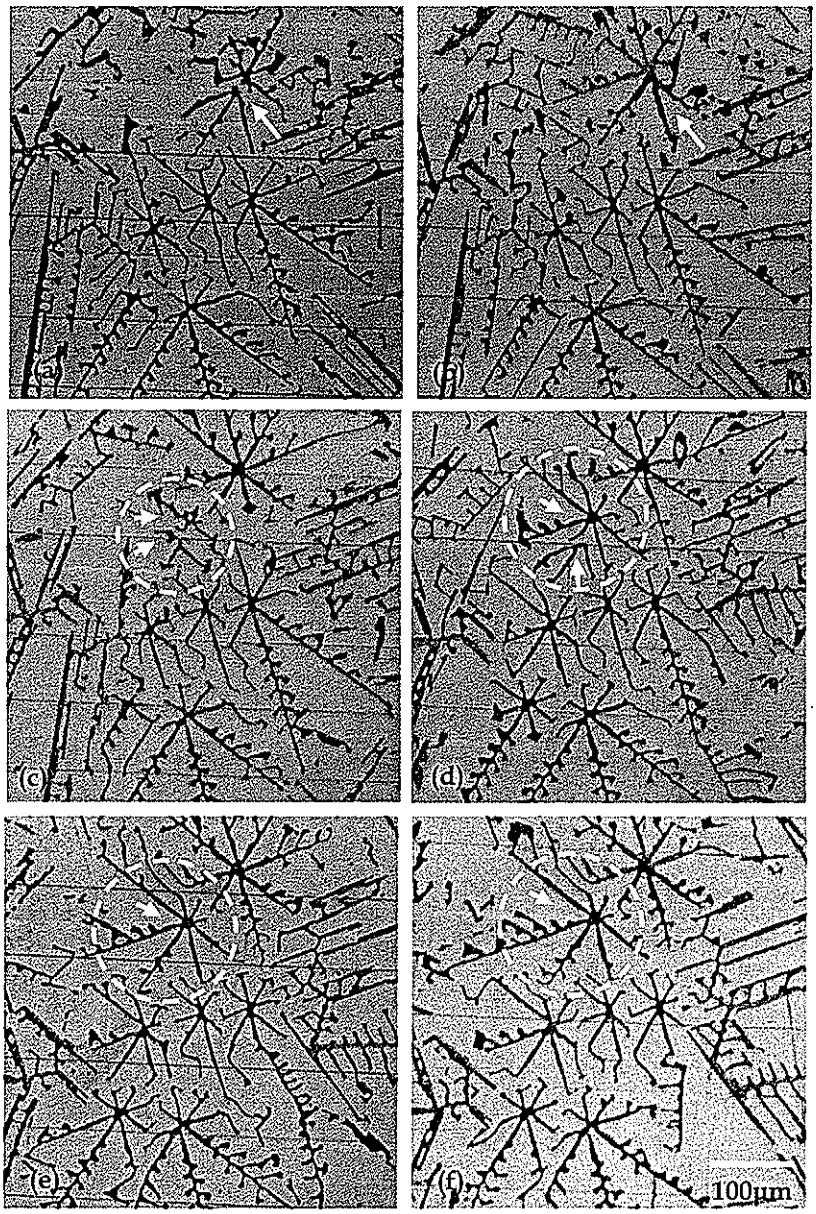

Figure 7-10. (a) and (b); Tip joining, (c), (d), (e), and (f); Competition between growing dendrites and subsequent elimination of a dendrite. The distance between each cross-section is 100 microns and the growth direction is from (a) to (f).

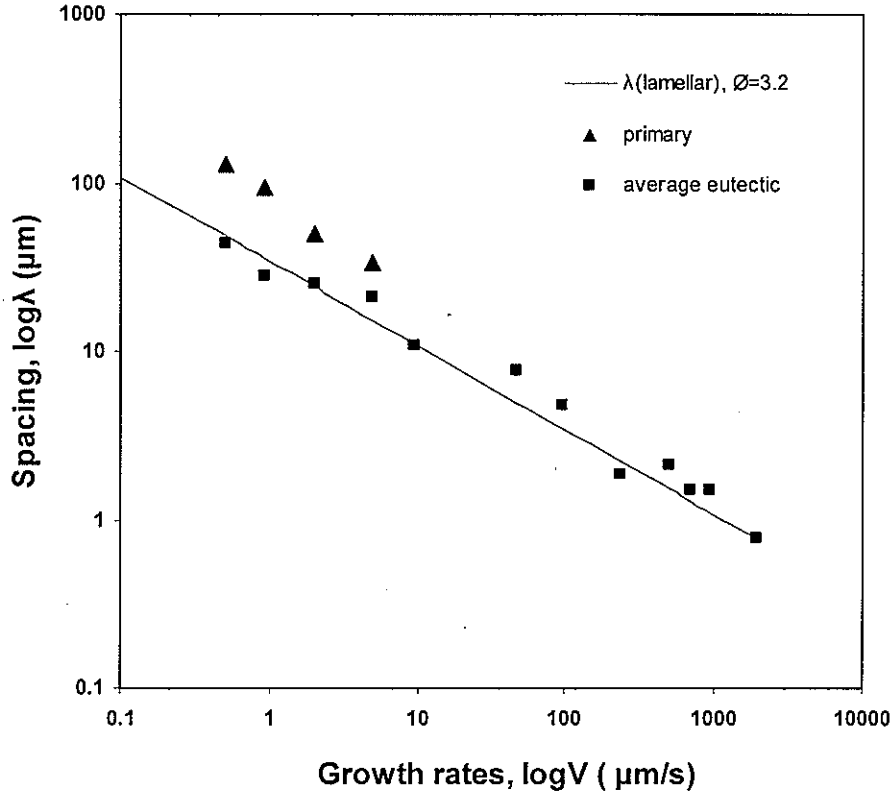

Figure 7-11. Primary spacing (between star-like silicon structures) and eutectic spacing measurements show a $\lambda^2 V$=const. type relationship.

CHAPTER 8

Phenomena in the Region of Primary Tip

We have examined the structure of 8-pointed star-shaped silicon and its growth mechanism with regard to {210} and {310} twin boundaries in the core. Array evolution and tip dynamics are also studied, revealing the mechanisms of branching and spacing adjustment of faceted primary silicon. The growing silicon octahedral tip is the most important part in this microstructure evolution. Especially, the migration ability of two coherent twin boundaries in the core is critical to the tip kinetics, the secondary structure, lateral propagation, and spacing adjustment. Now we examine the overall microstructure evolution that should start at the tip. In order to describe overall growth mode in detail, we need tip temperature that gives undercooling, liquid composition that determines supersaturation, and the primary spacing that is the characteristic length scale of cellular or dendritic growth. It must be mentioned, however, that tip temperature of primary silicon may not be directly measured due to the experimental limitation from the length scale of tip.

8.1 Composition profiles

Most of all, both liquid compositions at the tip and interdendritic region are critical to solute redistribution phenomenon in octahedral shaped silicon bicrystalline. At the growing tip, depending on the local supersaturation, tip migration and optimal secondary branching occur, assisted by mechanistic twin boundary migration, for the solute dissipation. Branching associated with interfacial kinetics of faceted silicon sideplates determine the interdendritic liquid composition. In addition, Al nucleation and growth must be deeply related to overall composition profile behind the tip.

Silicon compositions in Al phase has been measured first with spiral positions in the inter-plate region as shown in Fig.8-1 (a). Line composition profiles are plotted in Fig.8-1(b). When silicon compositions are plotted as a function of radial distance from the core center, not even shown in the dissertation, they did not give us enough information of solute distribution. It looked like discrete and arbitrary data.

In Fig.8-2 (a), a silicon dendrite with two small liquid envelopes was chosen and four line composition profiles have been plotted in Fig.8-2 (b) and (c). We have expected that there might be a gradual increase in silicon composition in Al phase to the liquid. The results, however, show

two or three measured points between Al phase and liquid, implying these gradients between two phases in Fig. 8-2 (b) and (c) came from the beam resolution limit. Though silicon compositions in liquid may be approximated to 20wt% by taking average of the points, the number of points is not sufficient to quantitative analysis. Therefore, as an alternative method, area mapping has been used for composition measurements. The silicon composition in Al phase, however, seems to be very uniform under 2wt% in the preliminary composition measurements, even in one dimensional line profile.

Two primary 8-pointed star-shapes have been chosen for micro-probe area mapping. All measurements have been carried out at the same beam conditions of 5keV acceleration voltage and 1μm step. In order to save a measurement time, a triangle between two secondary plates and a quadrant rectangle were investigated as shown in Fig.8-4(a) and (b) respectively. By 5μm decrements of surface by serial milling, we have got composition maps as a function of distance, Z, from the tip. Note that Z is the approximated distance from the measured height to the tip in the mush zone region of non-isothermal interfaces and the growth direction is, therefore, downward from the plane.

Fig.8-4 is a series of composition map on the triangle microstructure. Si composition is categorized into 9 ranges. As shown in (a), Al phase between two side plates indicates that it has almost uniform silicon content, similar to that of limited line measurements. Interesting feature of Fig.8-4(a) is that there is a slightly local fluctuation in the left secondary plate. Thus, we can expect that there might be a tertiary branching at the right there. In Fig.8-4(b), we have observed a tertiary branching that dissipates a local supersaturation in the interdendritic region as discussed in chapter 3. That means that there must be a highly supersaturated liquid in front of the tertiary at the lower Z (closer to the tip). It is also revealed that a tertiary plate of the right secondary plate is changing its growth direction to the remained liquid to respond to the local supersaturation. The expectations are clearly shown in Fig.8-4(c). Interdendritic liquid has caused a tertiary branching that would dynamically interact with liquid. Qualitatively, one can notice that a strong blue color region (30-45 wt% Si) is reduced from (c) to (b). In addition, average silicon compositions in Al phase as a function of the distance from the tip are potted in Fig.5-5. Roughly speaking, silicon amount in the solid solution is slightly decreased as the distance to the tip increases far from the tip because the final liquid composition is expected to reach equilibrium eutectic composition.

Unfortunately, the liquid phase fraction from this triangle area has not significantly changed from Z=70μm since the target silicon particle is too close to the lower silicon dendrite.

Thus, area with more spacing will give us much more information of liquid compositions as a function of Z.

Four micro-probe results of the quadrant rectangular area are shown in Fig.8-7 (a), (b), (c), and (d). The distance from the tip for each composition map is 70, 40, 20, and 0μm respectively. Note that at Z=0μm, as shown in the lower-left corner of the microstructure, a very tiny tip exists. Since additional serial milling will entirely pass it, we assume this is the tip position in this study. From (a) Z=70μm to (c) Z=20μm, silicon composition of 20-30wt% regime is replaced to the light blue, indicating that interdendritic liquid composition increases in the deeper position from the tip. As Al phase grows from the primary silicon, the rejected solute (silicon) from the Al phase result in this composition increments. This can be easily expected from the simple solute redistribution phenomenon. The composition in liquid at (d) Z=0, however, seems to be much higher than that of (c) Z=20μm. This confusing opposite behavior of solute redistribution might be due to the quenched Al phase at the vicinity of the tip. This argument may be very critical in phase fraction measurements in the later analysis. In addition, if Z is increased from (a), similarly in Fig.8-4 (a) and (b), the silicon composition of remaining liquid will be decreased again due to the dynamical sideplates branching though we do not have a strong evident for that at this time. So far, we have reasonably shown a qualitative relation between a composition field of interdendritic liquid and the overall microstructure evolution with a good agreement to the solute redistribution theory.

8.2 Phase fraction

In this section, a quantitative analysis of the interface structure and composition will be studied in terms of volumetric sense. As mentioned in the first overview of this chapter, tip temperature determination is critical but still remains in difficulty. From this point of view, finding any method of proper volumetric approach for the limited experimental techniques or even conceptional shortcomings is necessary. Thus, as a first step, we have measured phase fractions in two-dimension at the interfaces to quantify the overall growth behavior.

Fig. 8-7(a) and (b) are a series of microstructure evolution in the back order. Phase fractions for each phase namely Si, Al, and liquid are carefully measured in the inner envelope of four silicon dendrites. Thus the measured volume fraction is not a representative volume fraction for each silicon rod at the given distance because all four dendrite has a different distance from its tip. In this case, the reference tip is the upper left one. To make it easier, fraction adjustment based on this concern was ignored because the height differences between stems are less than 5μm. Measured phase fractions are shown in Fig.8-8(a). Si phase fraction is almost same behind

40μm and gradually decreases to the tip. A careful examination of this volumetric characteristic at the interfaces has revealed that there is a slight slope change of phase fraction as a function of distance, suggesting a quenched Al phase was counted for this slope changes around Z=20μm. Accordingly, this observation is corresponding to the increase of liquid composition between Z=20 and Z=0μm in Fig.8-6 (c) and (d).

It would be reasonable if we assume that the silicon volume fraction is constant at the distance regime far from the tip enough and there is no Al phase at all based on the above arguments. Thus, adjusted volume fraction is re-plotted assuming the very tiny (approximately 20μm), only primary silicon phase exist from Z=20μm to Z=0μm as shown in Fig.8-8(b). Scheil equation for the nonequilibrium solidification with assumptions of uniform liquid mixing and no solid back diffusion might be a simple but effective analytic model to be applied for interdendritic length scales. Average liquid composition as a function of solid volume fraction does not firmly support this as shown in Fig.8-9. However, in the regime of near the tip, measured average liquid composition is well matched to Scheil model. Note that the upper and lower lines are composition profiles from Scheil model, liquid and solid compositions respectively and triangles come from micro-probe measurements in this study. The reason for the significant deviation far from the tip are that our assumptions consider no quenching effect behind Z=20μm. The assumption of constant silicon fraction might be also a problem. Nevertheless, if we can find and adjust the phase fraction at the interface, the possibility of a strong analytical model for this may be increased.

8.3 Spacing-velocity relationship

We have measured silicon primary spacing in terms of average mean edge length and normalized length in primary silicon array in chapter 4. Primary spacing and interplates spacing as irregular eutectic spacing are also given in Fig.4-14 at near eutectic composition, 13 wt% Si to support various diffusive optimization processes observed in chapter4. Here, primary spacing-velocity plot at 13, 14, 15 wt% hypereutectic compositions is plotted in Fig.8-10, showing the similar diffusive growth mode. The significance of this length scale is that it can give us which growth mode is dominant and be a descriptive for the comparison to analytical and numerical model in the future.

8.4 The overall two phase structure

So far, a composition field in the vicinity of primary silicon tips has been studied and one problem has been arisen to quantitatively analyze the collected data for the strong analytical model. That is a quenched Al phase that must be removed for the exact understanding of the real microstructure evolution. Before proposing an overall growth model, we will verify how the quenching effect influences on the interface structure and analytical strategies.

Interestingly, sharp cusps have been observed everywhere in overall microstructure evolution as shown in Fig.8-11(a). Subsequent composition analysis results indicated by line1 to line 6 in (a) are shown in Fig.8-11 (b) and (c). Measurements of line 1, 2, and 3 are performed roughly at the cusps region and line 4, 5, and 6 may be not affected by Al phase that makes sharp cusps. Even though we do not have a good enough resolution of beam size, relatively gradual composition changes are observed in Fig.5-11(b), specially in line 2. This implies that the cusps might be from the quenching process because the end of secondary silicon plates should touch the interdendritic liquid during the growth to find efficient ways for the solute dissipation. The distance between the cusps and silicon plates in Fig.8-11(a) is too far for the silicon atom's attachment from liquid to the objective facets.

Fig.8-12 shows that interesting tertiary branching from the secondary sideplate occurs during the microstructure evolution. Right side of secondary plates of 8-pointed star-shaped dendrite is stretching to liquid with bunch of tertiary arms, responding to the local supersaturation. As noticed it already, there are also cusps at the end of tertiary sideplates, producing several nonfaceted Al interfaces that may compose sub-grains in Al phase. We have shown Al grain structure in Fig.5-15, showing the secondary branching may affect the orientation of Al phase. Accordingly, if there is no epitaxial orientation relationship between silicon plates and Al, we should have observed finer independent Al grains in the inverse pole figure images.

From Fig.8-12, we have observed three important key features at the crystal-melt interfaces. First, Al phase at the end of secondary branched silicon plates is thinner than that of interfaces quenched at lower rate as shown in Fig.8-3. It seems that the rapid quenching made the sharper deep cusps with clear quenched Al phase traces, while faceted silicon interfaces of secondary or tertiary plates still faced on interdendritic liquids to dissipate the rejected silicon atoms from the growing Al phase. Second, the shape of Al interfaces (well shape) between two secondary plates is not changing significantly in both cases. This was confirmed in line composition measurements in Fig. 8-11 (b) and (c). Third, as indicated by circles in Fig.8-12, there is no quenched eutectic between the two primary silicon dendrites. It means that Al phase

between two particles do not have a quenched Al phase. If there were a quenched phase of Al in the circle, there should have been interdendritic liquid too.

The only tiny silicon tip (less than 20 microns) is primarily growing and this silicon is leading phase during the directional growth of angular silicon bicrystal. Although Al phase are surrounding the silicon tip in the microstructure series as shown in Fig.8-13, t this phenomenon came from the quenching effect. This is clearly shown in the couple of snap-shots from 3-dimensional reconstruction in Fig.8-14. Note that this 3-dimensional structure was reconstructed from sequent images of Fig.8-13. Behind the tiny tip, Al is growing with silicon plates but there is no strong coupling between two phases. Thus, it is hard to say that this is eutectic coupling or even dendritic coupling since the little tiny tip is not strongly decoupled as a dendrite tip. Accordingly, we propose "coupling cellular" for overall growth mode. The diffusive coupling occurs in the envelope cell where Al and faceted silicon coexist. In addition to that, in the envelope, Al grows like a halo of primary silicon dendrites[111, 112], as shown in Fig.8-13. These microstructure series were taken after very rapid quenching, so growing Al is exactly similar to that of halo formation, where eutectic growth occurs between the second dendritic halo phases. The halo formation itself, however, has not been fully understood yet and several mechanisms have been proposed. In addition, a diffusive coupling still exits in the proposed cellular coupling envelope and this must be considered if one wants to try to modify the halo growth model to faceted bicrystal array evolution. The dynamical tertiary branching to the interdendritic liquid in this coupling cellular model might be a counterpart of eutectic coupled growth in the halo formation.

Summary of the key points in this chapter

- Phase fraction, composition, interface structure, and spacing in the interdendritic region behind the growing tip suggest that overall microstructure evolution is occurred by a very tiny decoupled primary tip, followed by an Al "halo-like" structure surrounding the silicon star-shape.
- Silicon composition in Al "halo-like" phase is almost uniform and it may be estimated by Sheil's model, combining with phase fraction measurements as a function of the distance to the tip.
- Primary and inter-plate spacing suggests that overall growth is a diffusive coupling "cellular" growth.

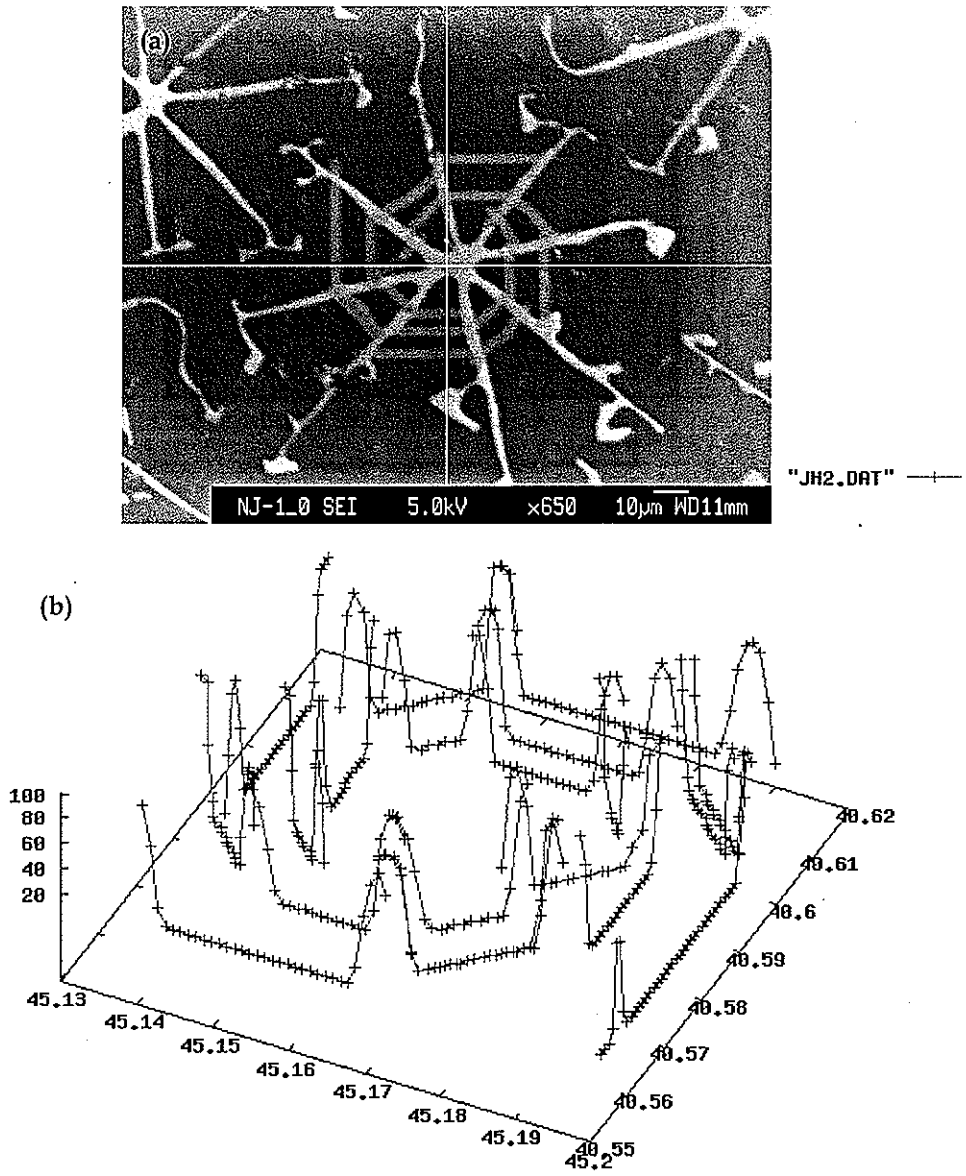

Figure 8-1. (a) Preliminary composition measurements with spiral movements of beam and (b) Three dimensional silicon composition plot from (a). Micro-probe beam step is 1µm.

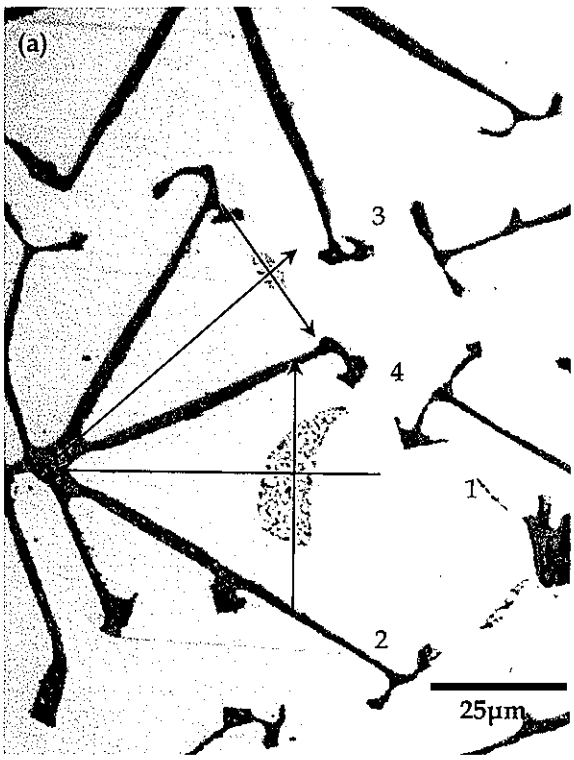

Figure 8 -2. (a) Preliminary composition measurements for interdendritic liquid region. Line 1 to Line 4 indicate μ-probe scanning pathways in 1μm steps.

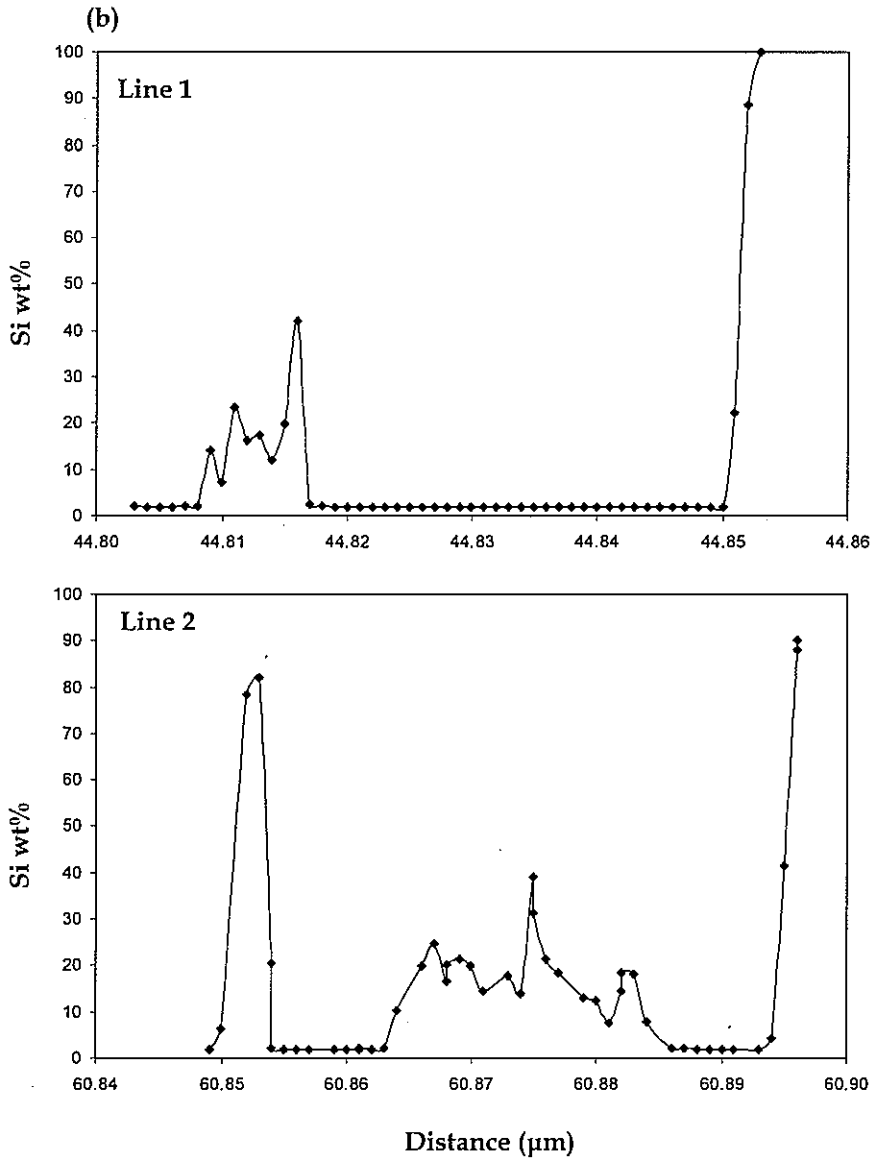

Figure 8-2. Continued. (b) Composition profiles of Line 1 and 2 from (a).

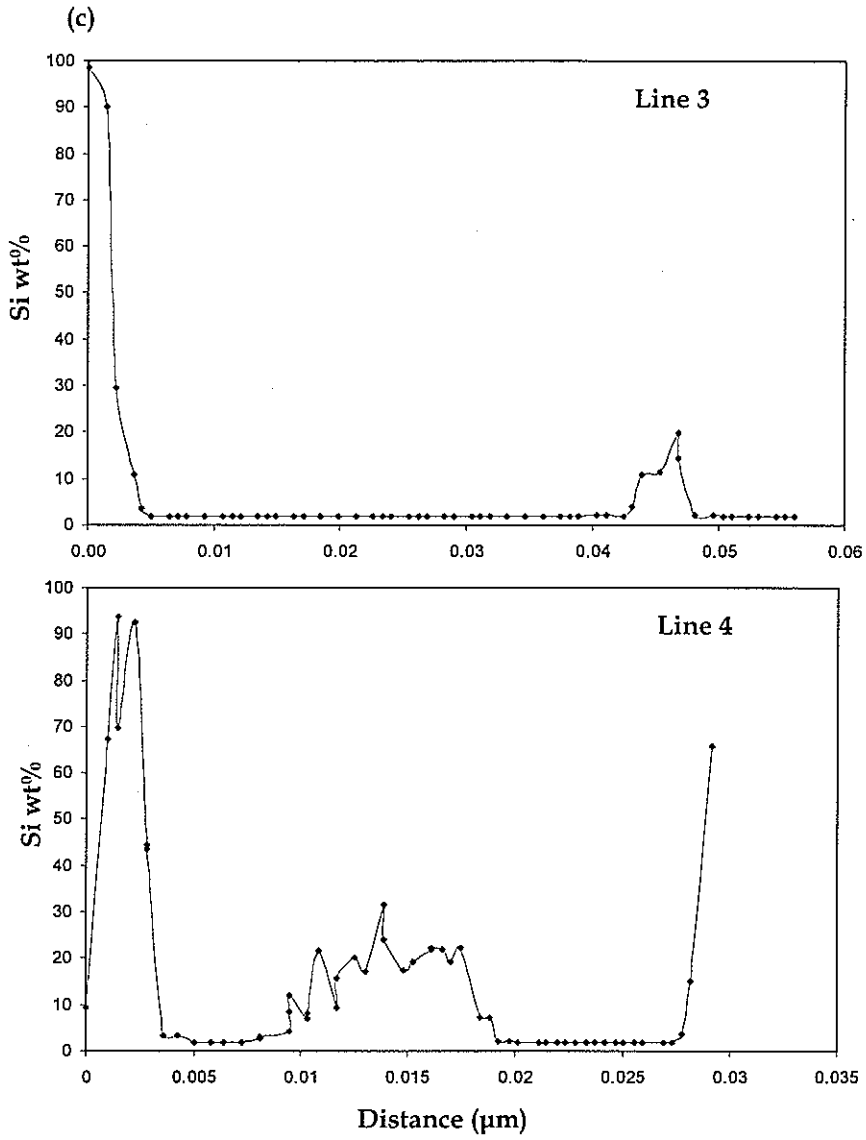

Figure 8-2. Continued. (c) Composition profiles of Line 3 and 4 from (a).

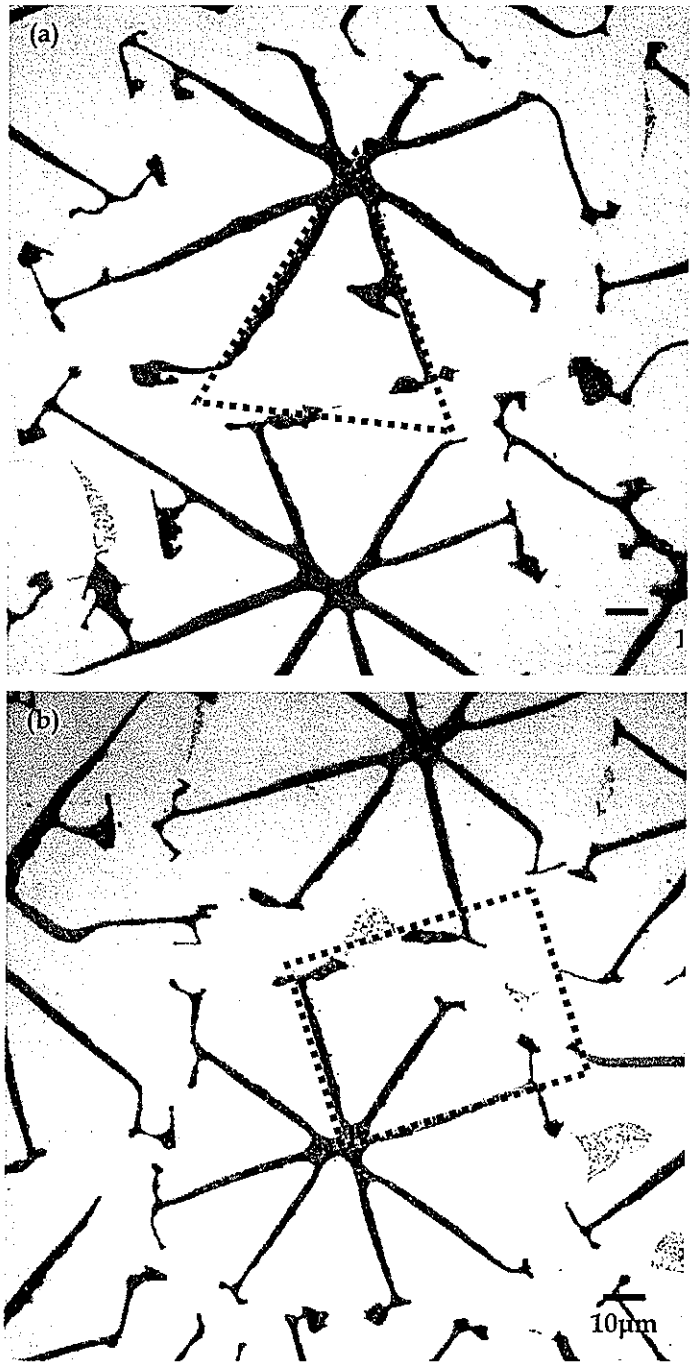

Figure 8-3. Two selected silicon dendrites for area composition measurements. (a) a triangle between two sideplates(z=180) and (b) a quadrant rectangle (Z=150μm). Z is the distance from the tip.

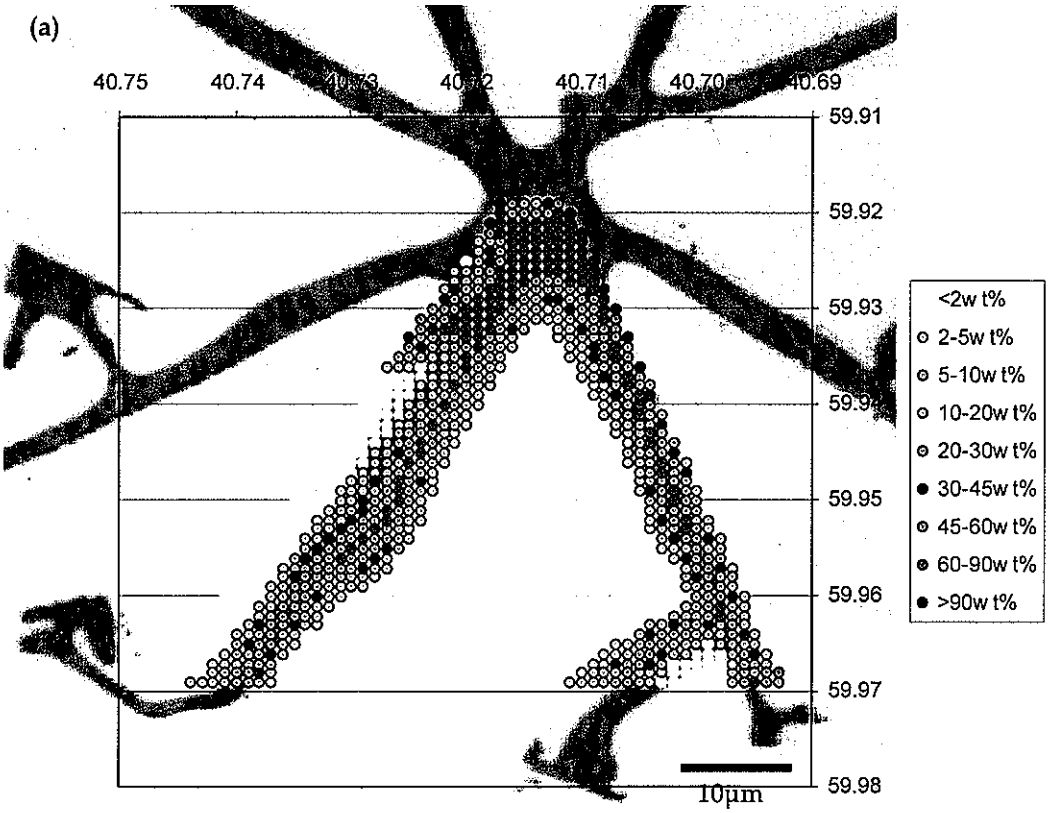

Figure 8-4. (a) Composition measurement for triangle area between secondary sideplates. This is roughly 150µm (Z) behind the tip. A tertiary sideplate is about to emerge at the inside of the right secondary plate.

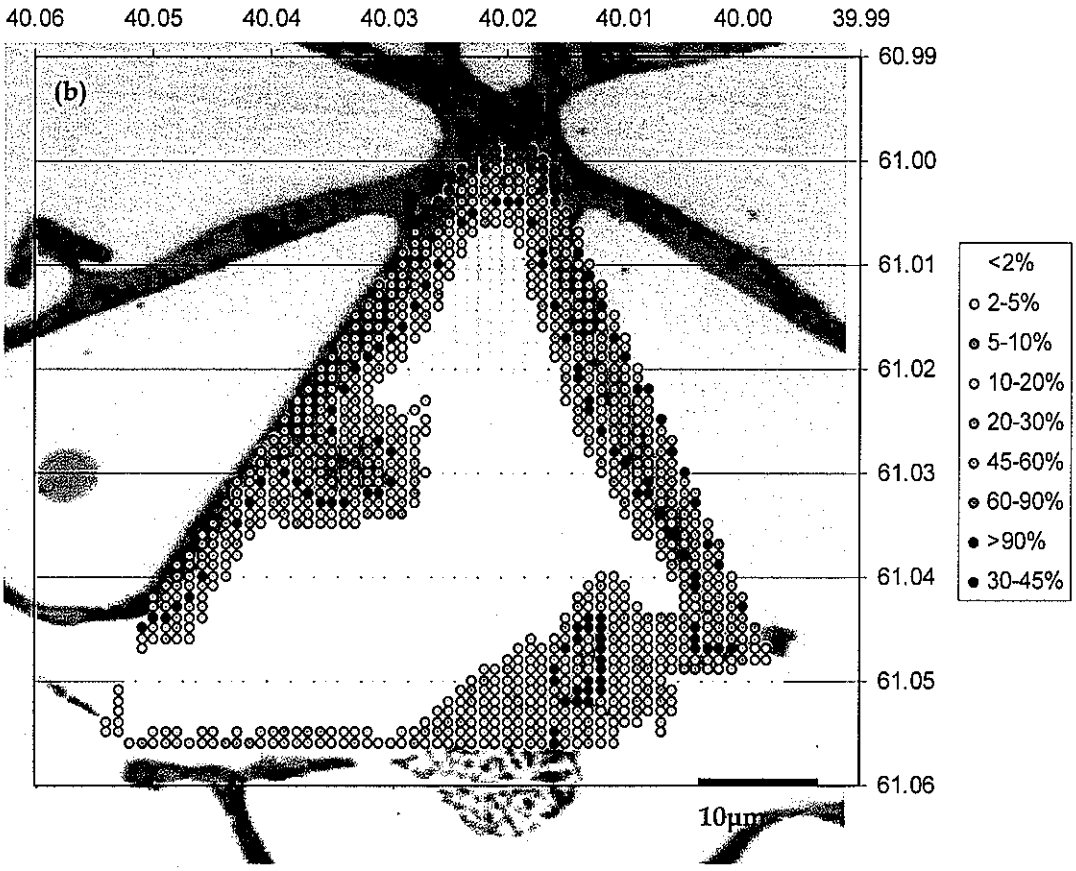

Figure 8-4. Continued. (b) Composition measurement for triangle area between secondary sideplates. Z=90μm. A tertiary sideplate is interacting with highly supersaturated liquid and a new tertiary branched from the expected point in Fig.5-4 (a).

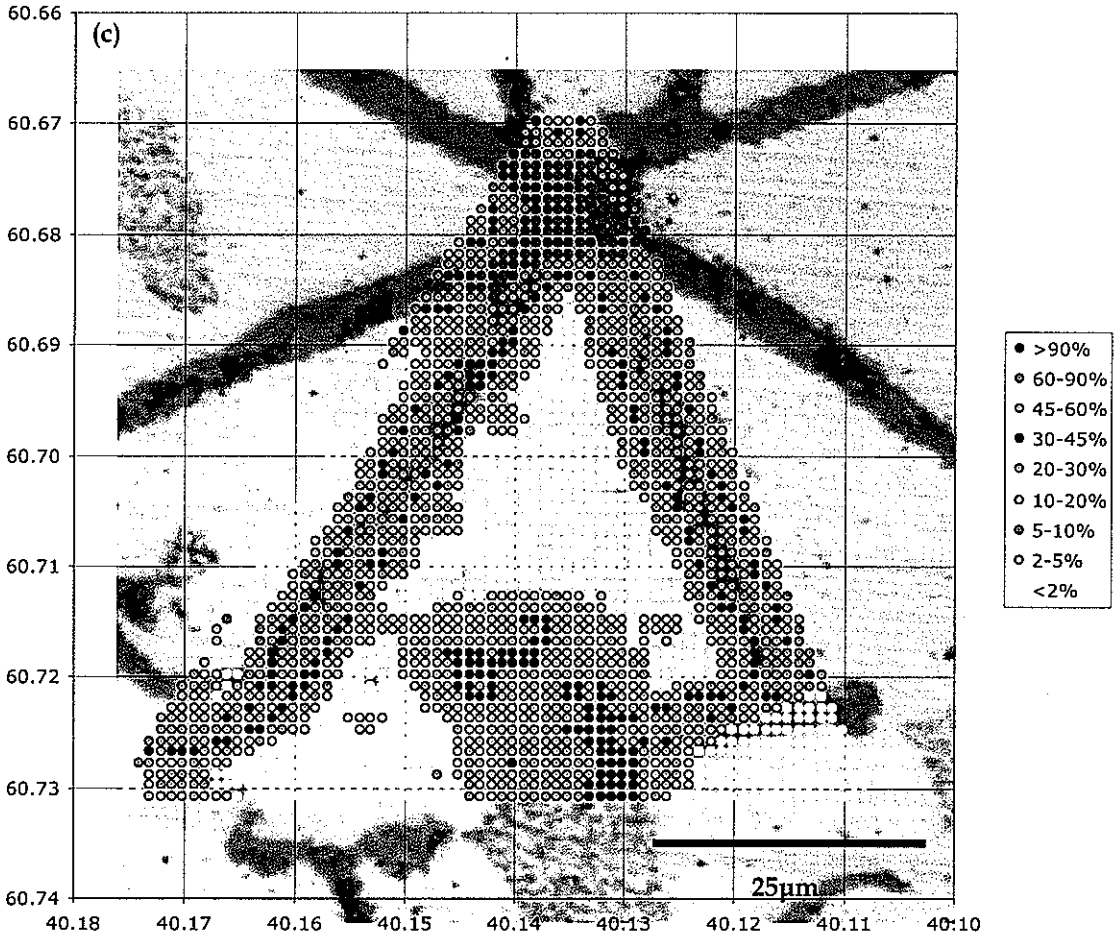

Figure 8-4. Continued. (c) Composition measurement for triangle area between secondary sideplates. This is roughly 70μm behind the tip. A tertiary sideplate is interacting with highly supersaturated liquid.

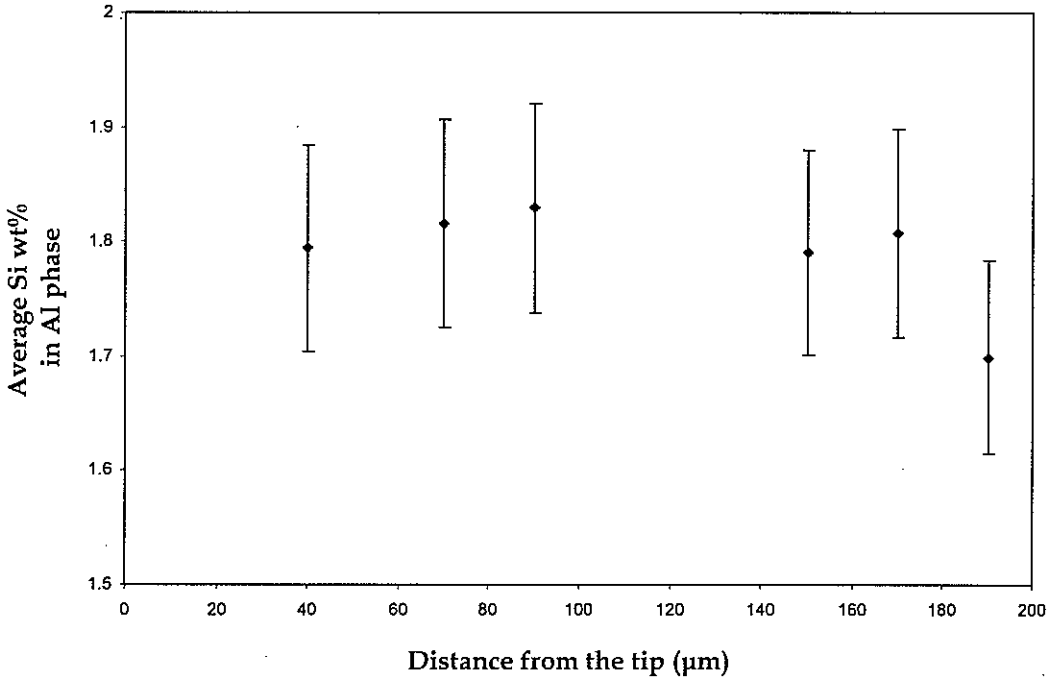

Figure 8-5. Composition of Al phase as a function of distance from the tip.

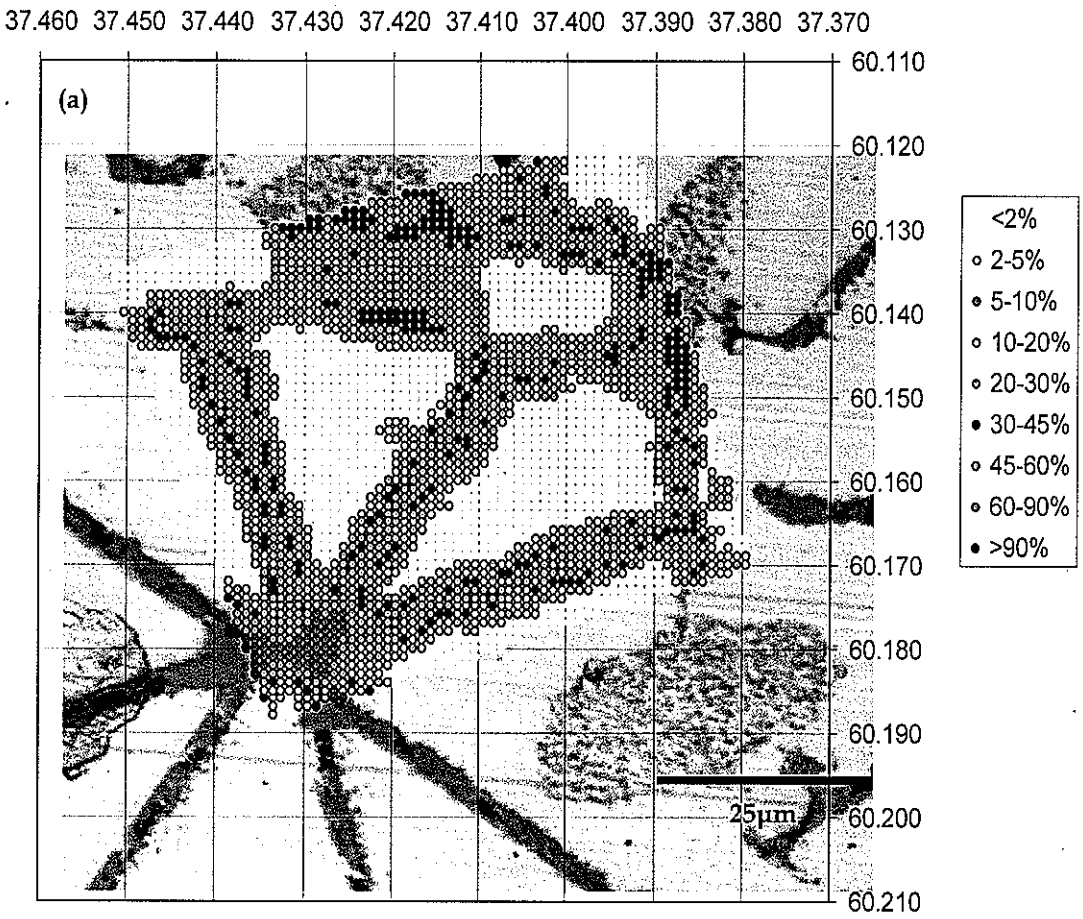

Figure 8-6. (a) Area with light blue (20-30 wt%) color is decreased. Liquid composition at closer position to the tip is decreasing qualitatively at z=70.

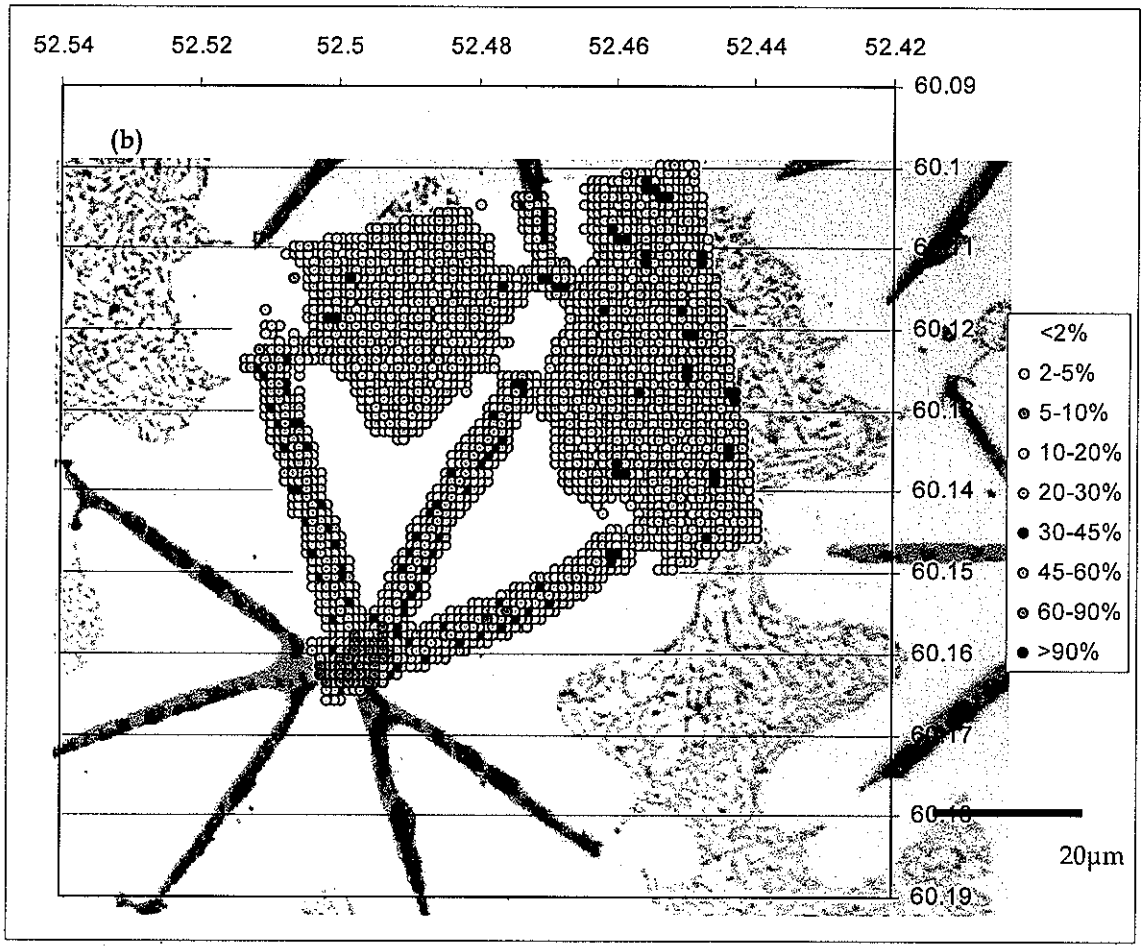

Figure 8-6. Continued. (b) Area with light blue (20-30 wt%) color is decreased. Liquid composition at closer position to the tip is decreasing qualitatively at z=40.

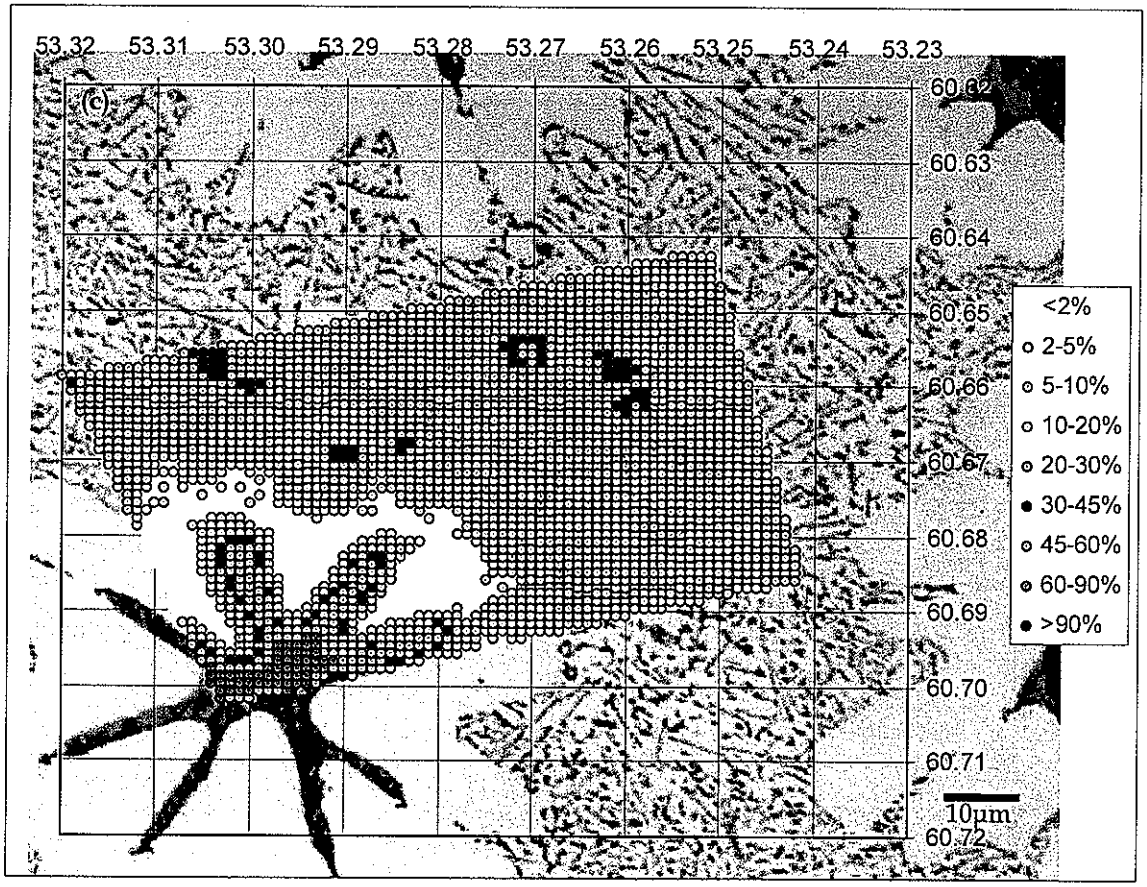

Figure 8-6. Continued. (c) Area with light blue (20-30 wt%) color is decreased. Liquid composition at closer position to the tip is decreasing qualitatively at z=20.

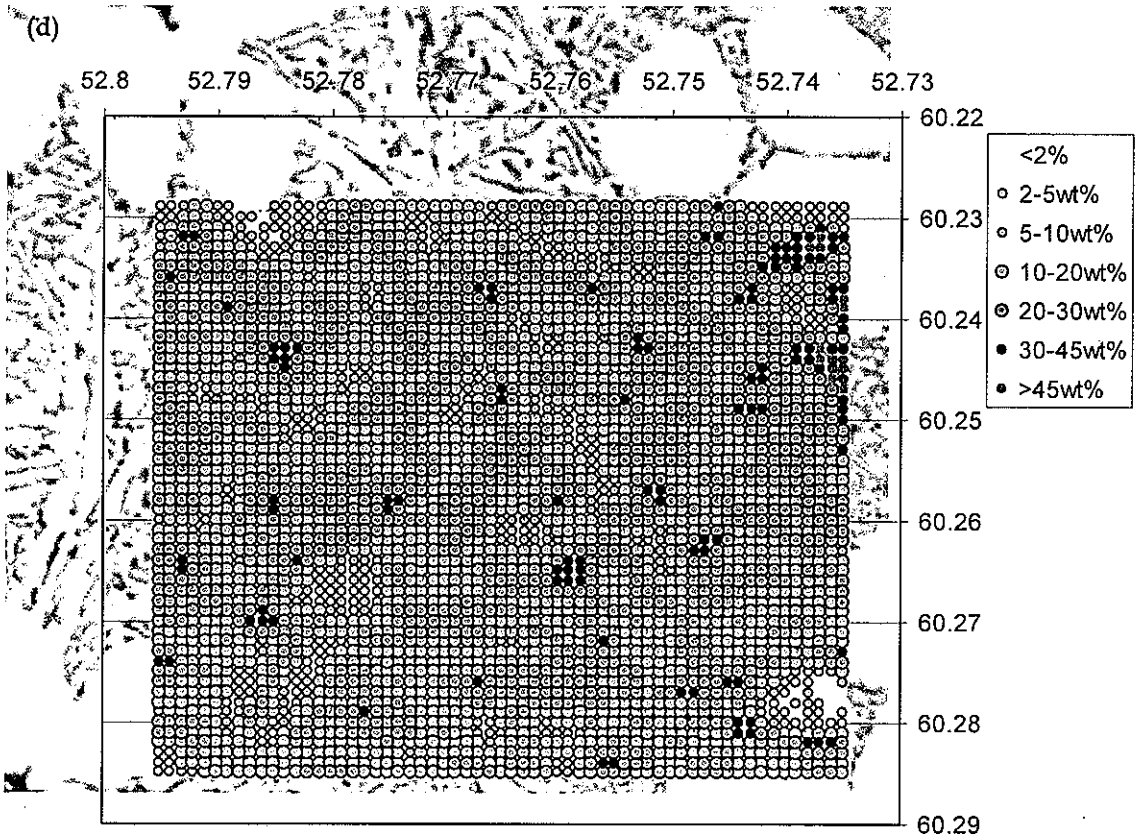

Figure 8-6. Continued. (d) Area of light blue (20-30 wt%) color is increased. Liquid composition at the tip is slightly increased from z=20, indicating quenching effect is much higher than deep groove at z=0.

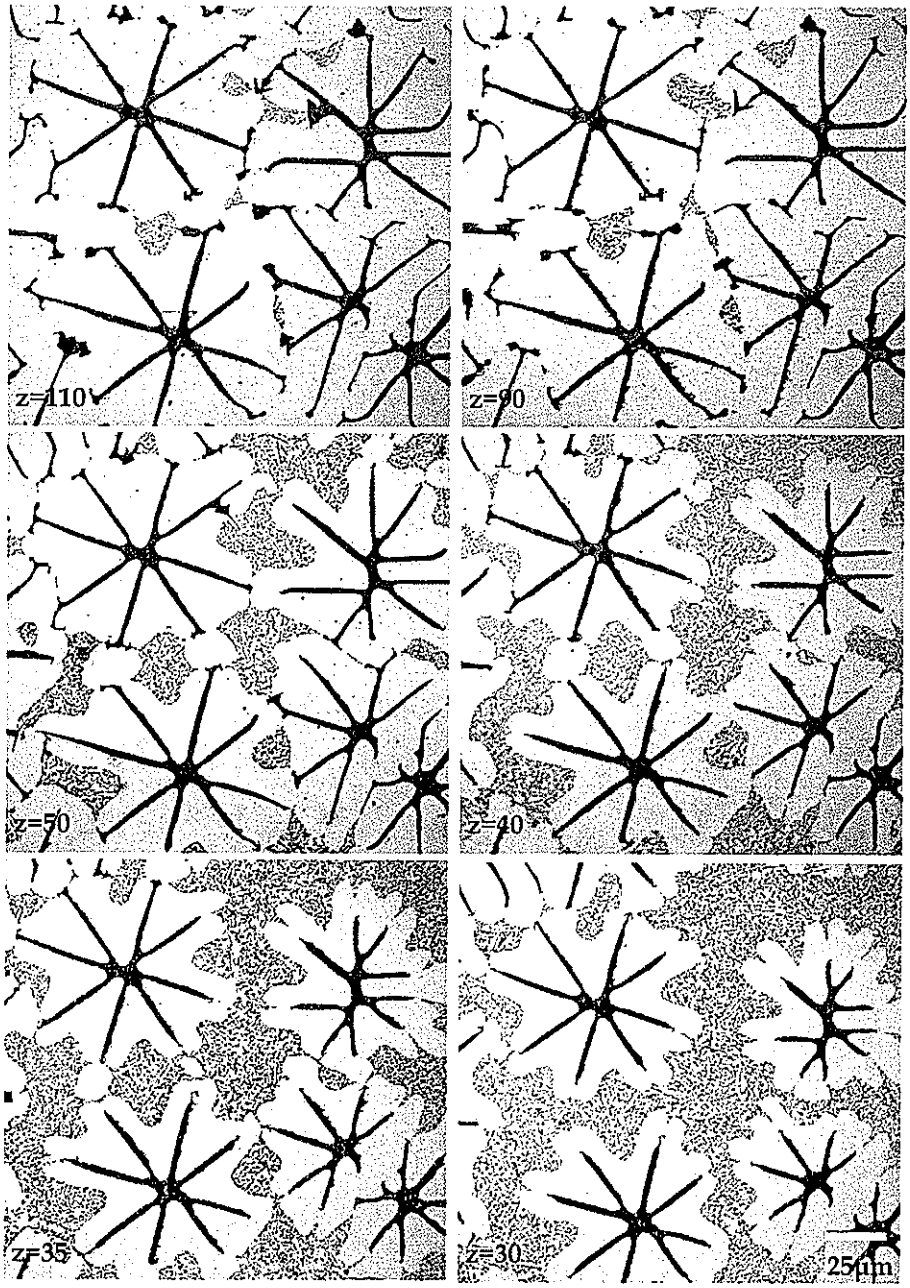

Figure 8-7. Microstructure series of crystal-melt interfaces. Z is the approximated distance from the tip (110μm-30μm). Growth conditions are 13wt%Si, V=1μm/s, G=7.5 K/mm, and quenched at V=17mm/s.

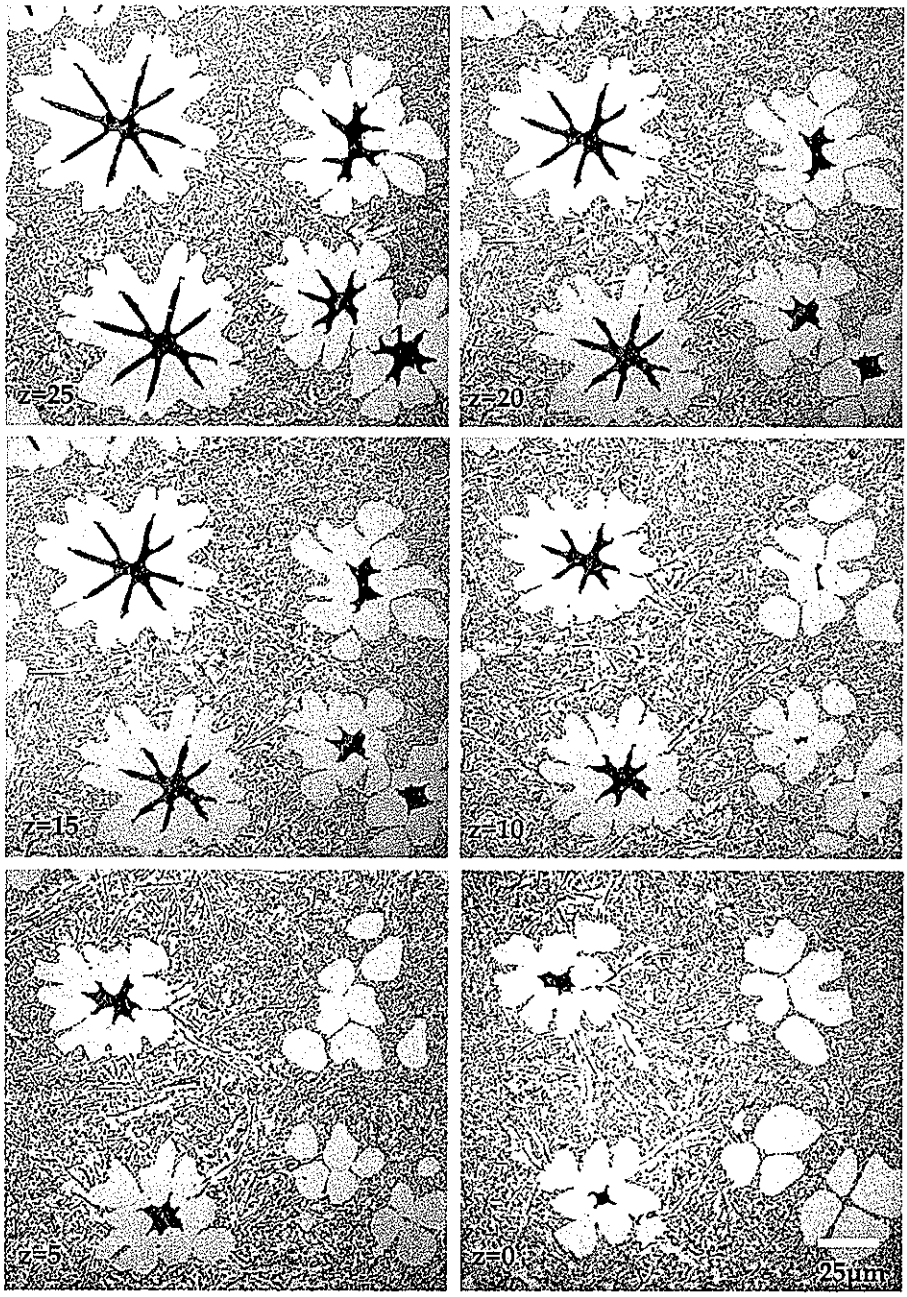

Figure 8-7. Continued. Microstructure series of crystal-melt interfaces. Z is the approximated distance from the tip(25μm-0μm). Growth conditions are 13wt%Si, V=1μm/s, G=7.5 K/mm, and quenched at V=17mm/s.

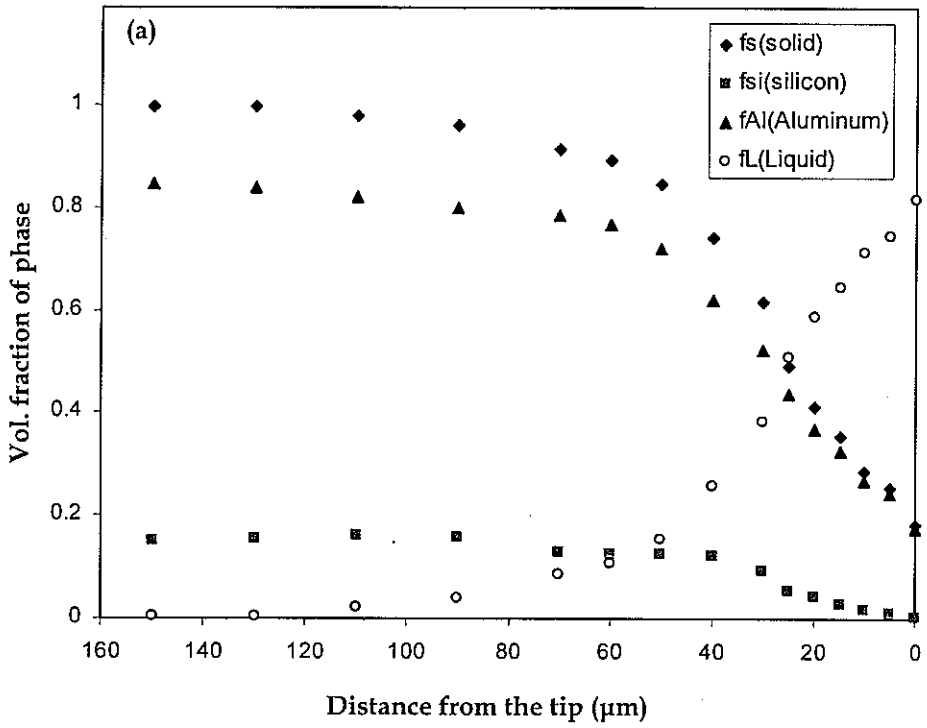

Figure 8-8. (a) Volume fraction of each phase as a function of distance from the tip.

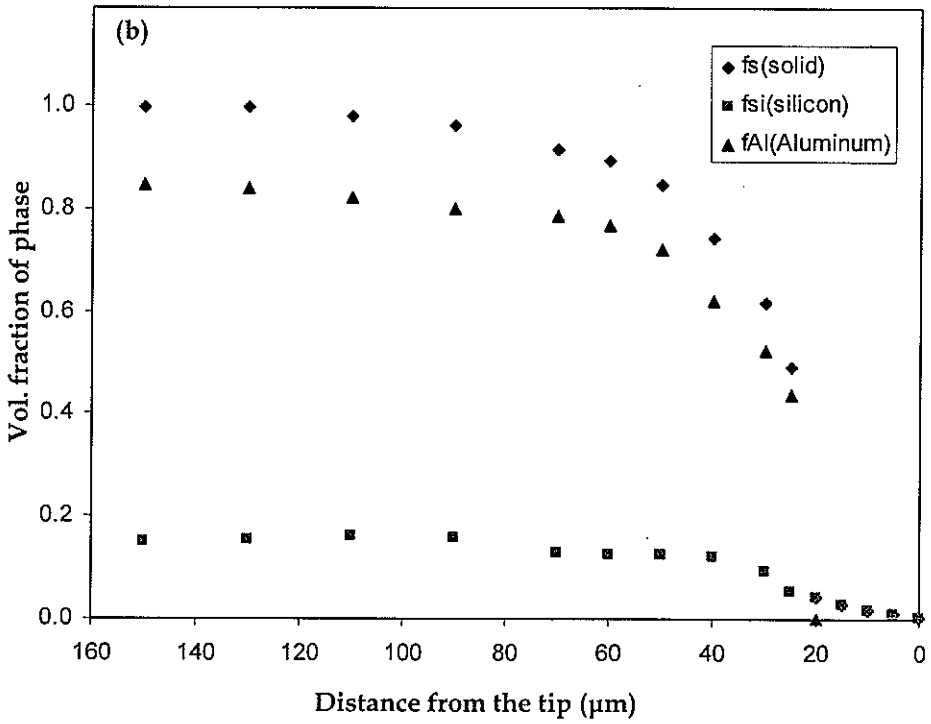

Figure 8-8. Continued. (b) Adjusted volume fraction as a function of distance from the tip, based on our assumption.

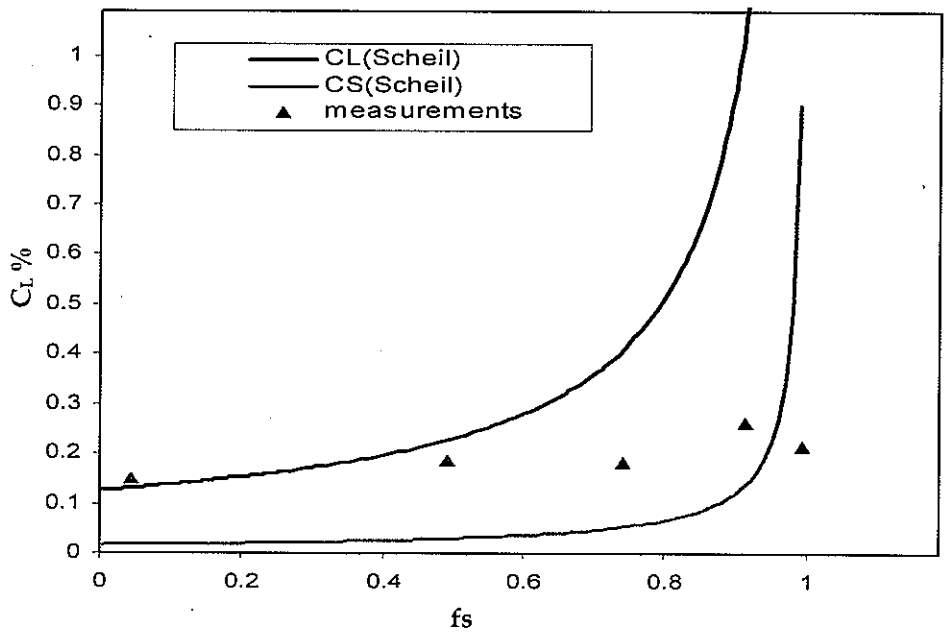

Figure 8-9. Comparison to Scheil model. Triangles came from μ-probe measurements.

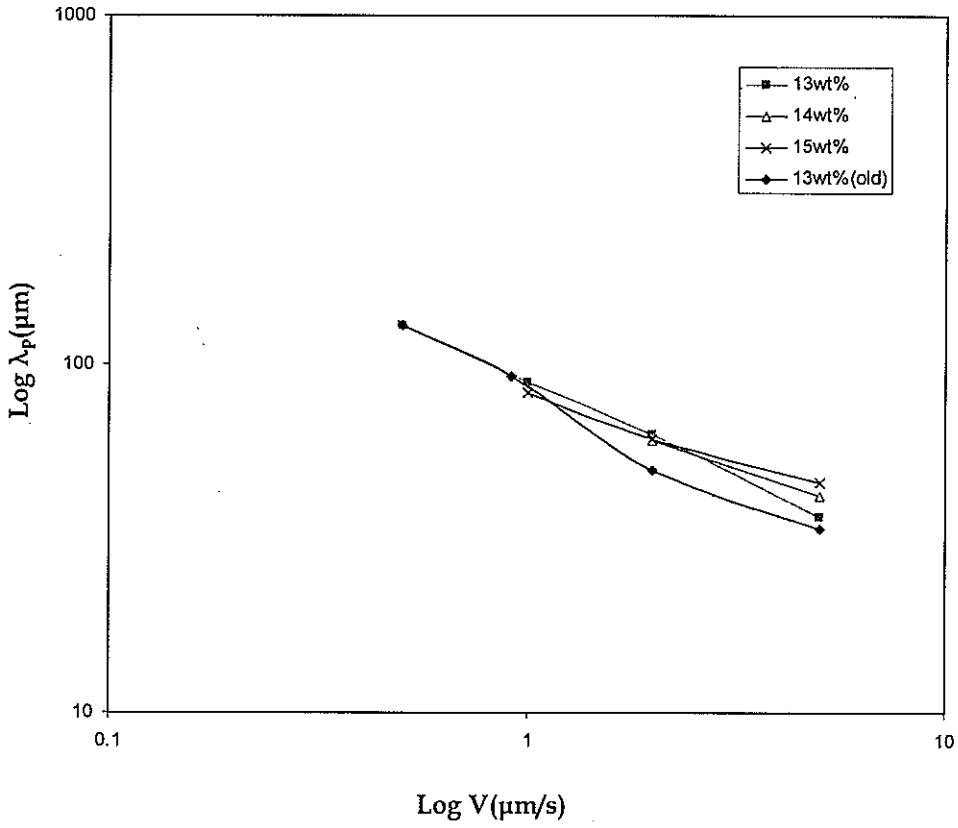

Figure 8-10. Primary spacing vs. growth velocity plot showing the similar diffusive growth mode in effect at various composition ranges.

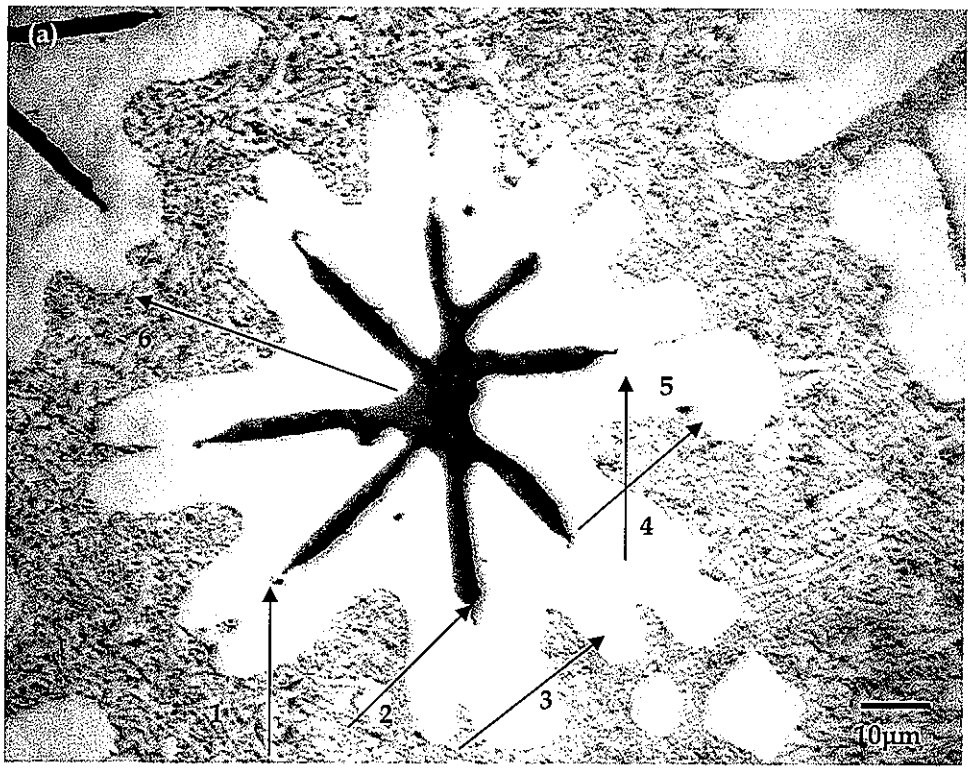

Figure 8-11. (a) Cusps and smooth well between two sideplates. Arrows indicate the direction of μ-probe beam movements of 1 μm step in order from Line 1 to Line 6. Growth conditions are 13wt%Si, 1μm/s, and 17mm/s quenching rate.

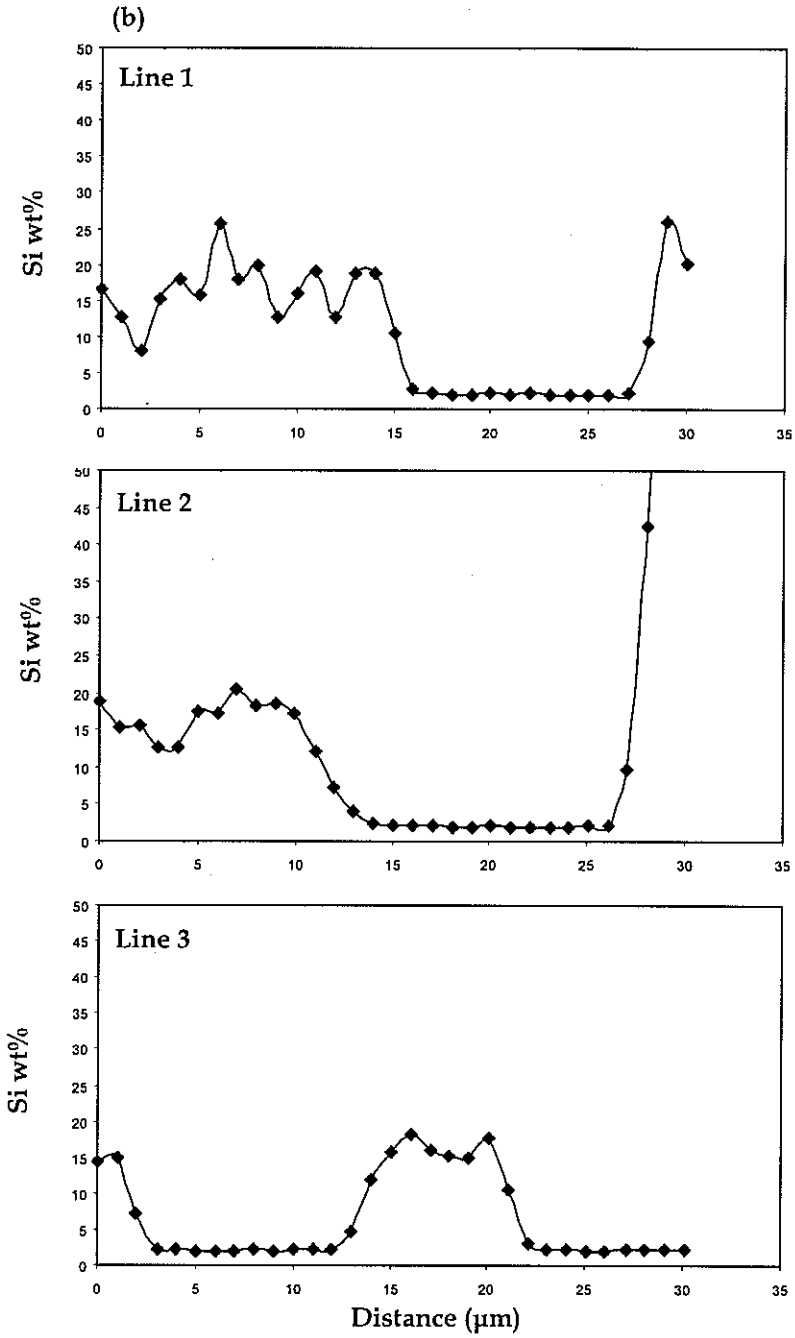

Figure 8-11. Continued. (b) Composition profiles of Line 1, 2, and 3 from (a).

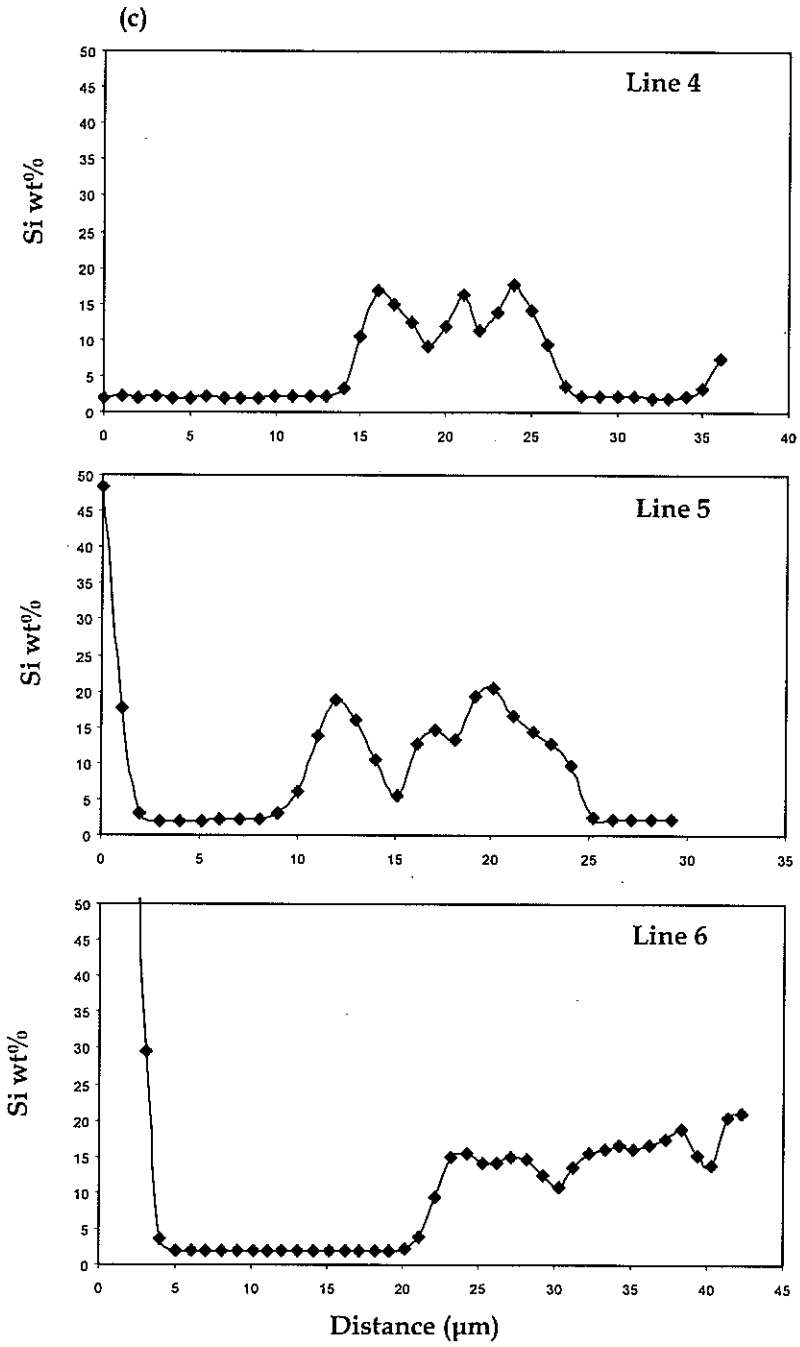

Figure 8-11. Continued. (c) Composition profiles of Line 3, 4, and 6 from (a).

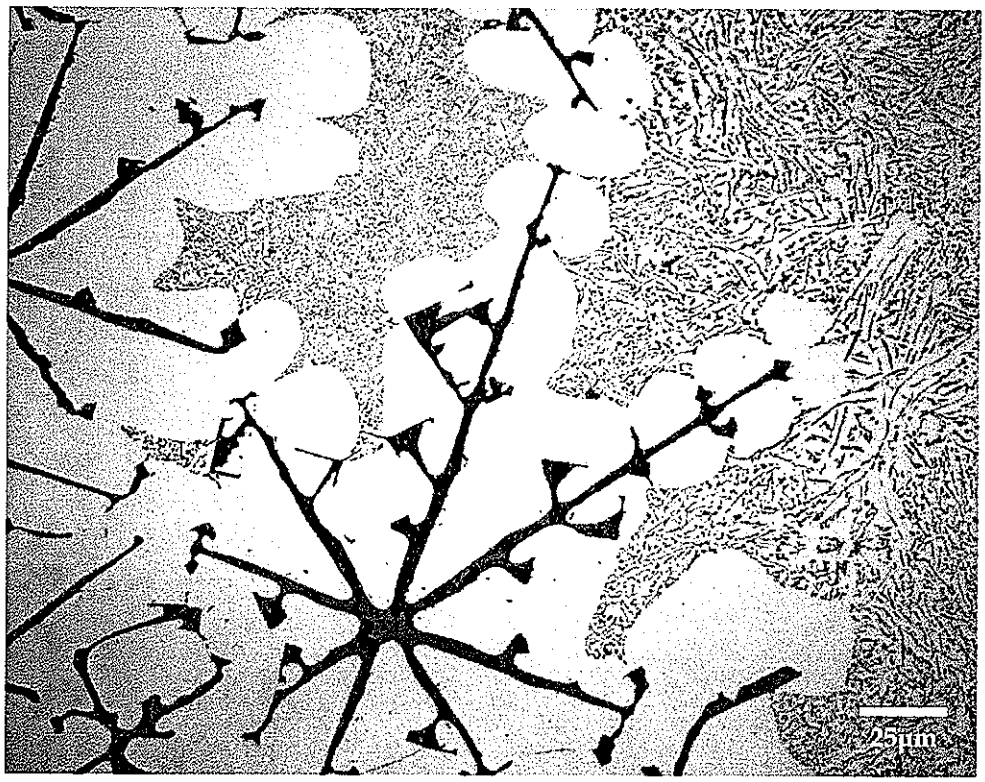

Figure 8-12. Tertiary branching and separate Al subgrains, showing cusps come from the little tertiary sideplates.

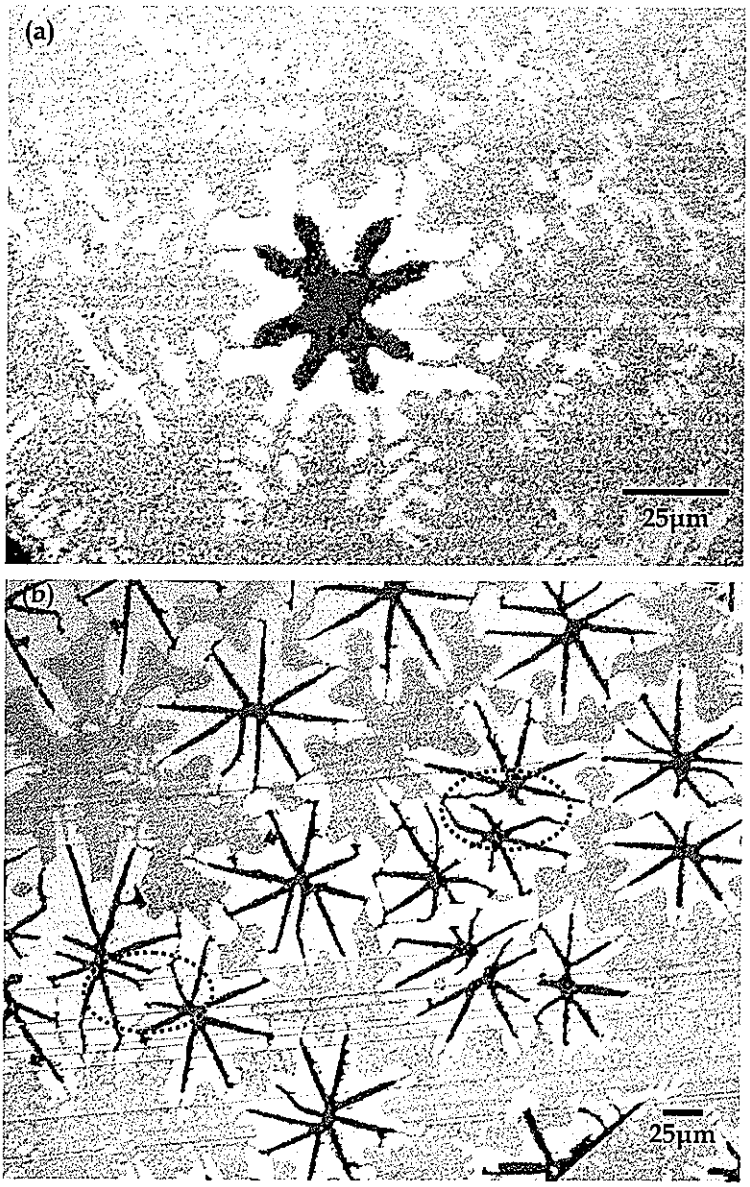

Figure 8-13. Transverse microstructures at crystal-melt interfaces quenched by very rapid rate (V=71mm/s) after 1μm/s growth. (a) Closer to the tip, showing quenched Al phase trails and (b) Local area of the array.

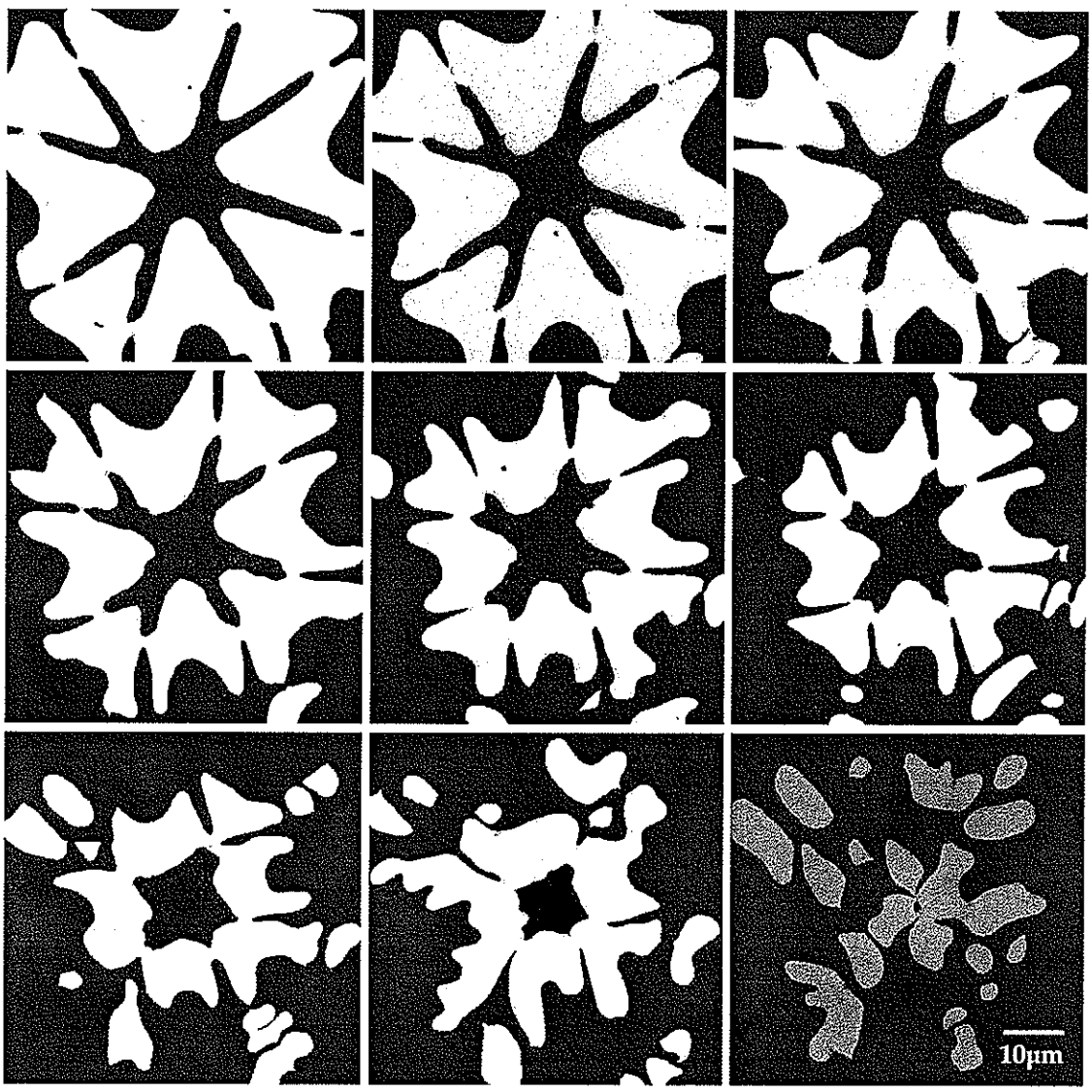

Figure 8-14. Microstructure evolution of 8-pointed silicon morphology. Quenched at 71mm/s after 1μm/s growth.

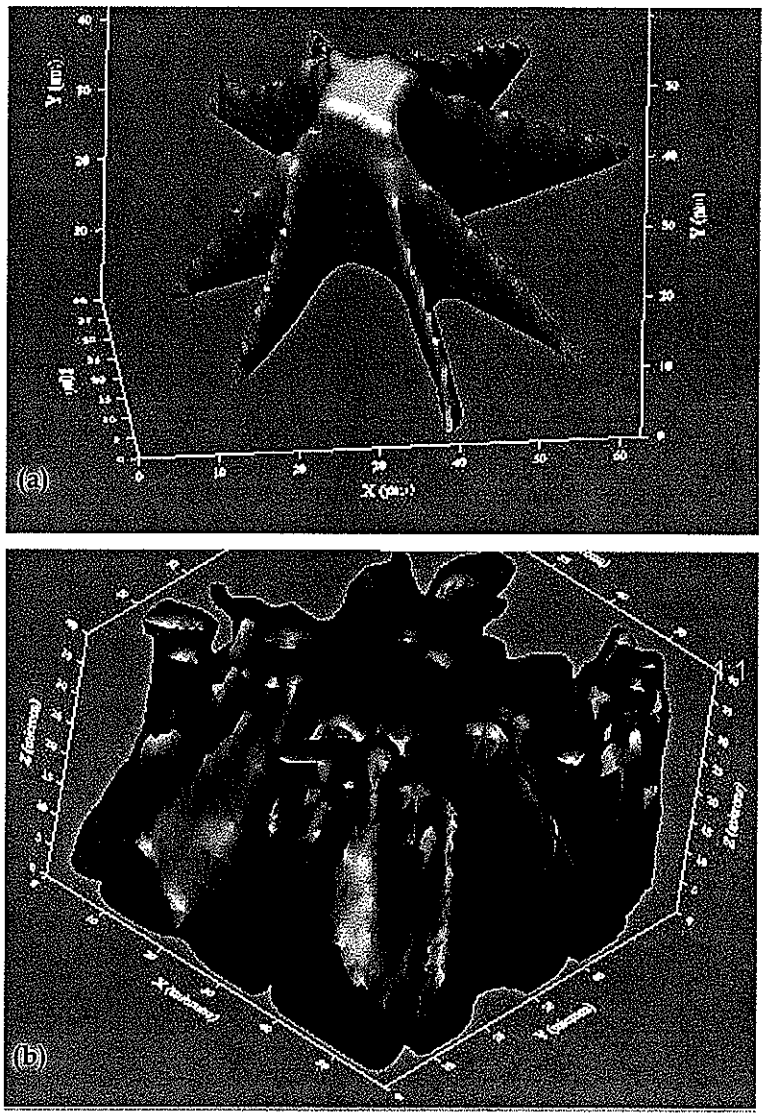

Figure 8-15. Three dimensional reconstruction of (a) Si and (b) Al phase near the tip region from Fig.8-14.

CHAPTER 9

Summary, Conclusions, and Suggestions for Further Investigation

Crystal-melt interfaces play a crucial role in microstructural evolution, and the intrinsic properties of crystal-melt interfaces determine how the crystal grows from its melt. We have discussed structure, thermodynamic treatments, and the intrinsic/extrinsic behavior of crystal-melt interfaces in Chapter 2. Most of all, anisotropic properties of interfaces, stiffness and mobility, may result in the faceted shape of the growing crystal. The crystal-melt interfacial properties of silicon have a relatively strong anisotropy, and Si exhibits a variety of growth morphologies in Al-Si alloys. Among these morphological transitions, a flake to angular or script morphology has been observed in directional growth (gradient ≈ 7 K/mm) at rates below ~ 1μm/s. Though twinning is the main mechanisms in other growth mode transitions, such as impurity modification, its role in the selection of the bicrystalline dendritic morphology is somewhat different.

Employing directional solidification techniques, we have grown faceted twinned bicrystalline primary Si at near eutectic compositions and examined detailed structures, crystallographic orientations, and chemical compositions of the dominant 8-pointed star-shaped growth morphology. Careful analyses of microstructure of the bicrystalline silicon array have been conducted by electron backscattered diffraction patterns and a high resolution microscopy, combining serial milling and computation techniques.

It was found that star-shaped Si grows at a preferred orientation which was determined to be <001>. There is a transient period where the preferred <001> texturing in Si develops from randomly oriented Si particles and, based on the rapid lateral propagation of textured domains, it is clear that star-like angular silicon morphology was strongly favored. The silicon dendrites formed as continuous textured domains. These domains of silicon dendrites spread laterally by branching events occurring at the periphery of the textured domains. In addition, the domains were single dendritic bicrystal twin-pairs, and their lateral growth required low-undercooling branching mechanisms that propagated both twins and new primary structures.

The 8-pointed star-like Si morphology is comprised of two interpenetrating grains formed by joining of 4 sub-plates extending at right angles from a central stem. {210} and {310} coherent twin boundaries in the core are essential to the primary tip kinetics, the secondary

structure, lateral propagation mechanisms and primary array adjustment. The selection through *mechanistic optimization* promoted an array of twin-dependent faceted primary growth structures which, unlike most faceted crystals, possess the required responsiveness to enable local adjustments in shape and spacing. This, in turn, provided a means for *morphological optimization* on a larger scale despite the faceted nature of the interface. Thus, we assert that it is the ability of the twin boundaries to migrate laterally under low driving forces and to assume various geometries within the central core (i.e. mechanistic selection) that is the essential feature enabling the requisite branching and rapid lateral propagation of the overall dendritic array.

We also found several mechanisms of lateral propagation and branching of silicon bicrystal during the array evolution. The branching occurred in the form of tip splitting and tertiary sideplate formation events. These branching processes were enhanced by the above mechanistic twin boundary migration, resulting in the overall array structure of identically oriented primary bicrystalline silicon. In addition, from the analysis of array dynamics, diffusion optimization occurred for spacing adjustments of primary silicon phase and spacing measurements has suggested that a diffusional coupling growth would be the overall growth mode of the faceted silicon array.

Composition analysis at the vicinity of the primary tip has supported the previous sideplates branching and overall octahedral morphological selection. Quenching effects in the crystal-melt interfaces made it difficult in analyzing overall microstructure evolution. It was found, however, that the overall microstructure evolution occurred by a very tiny decoupled primary tip, followed by an Al "halo-like" structure surrounding the silicon star-shape. In addition, interaction between secondary or tertiary branching and supersaturated interdendritic liquid behind the primary tip has been well explained, combining volumetric measurement for each phase with an analytical model.

We have successfully examined the angular or script morphology, particularly dominant 8-pointed morphology of faceted bicrystalline silicon. From all observations and analyses of the microstructural evolution of twinned silicon, symmetrical coherent {210} and {310} twin structure in the dendritic core and their mechanistic migration mechanisms enabled the strong anisotropic faceted crystal-melt interfaces to select star-shaped morphology and to adjust primary spacing, efficiently, responding to the local circumstances.

In this study, we have not measured silicon tip temperature, which might be very important to understand overall tip conditions. The best way is the direct measurements, inserting thermocouples into melts and letting interfaces go through it acquiring the temperature at the same time. Unfortunately, this method might be very painful because of difficulties in

positioning of thermocouple tip at the interfaces. However, we can still estimate the tip temperature. As described in Fig.9-1, corner experiments during the directional growth could provide us greater benefits for the understanding of faceted regular array. Tip undercooling can be estimated from several sets of experiments. Lateral spreading and branching phenomena to highly undercooled melts may be also observed from this experiment. Directional solidification experiments of hypoeutectic compositions are also strongly recommended. Cellular Al primary phase will be the leading phase and a faceted silicon halo phase or star-shaped silicon trail may be observed from the remained inter cellular liquid region with coupled eutectic compositions. As we can determine a cellular tip temperature of nonfaceted metallic phase experimentally or theoretically, using the equilibrium phase diagram and the coupled zone construction, for example, as shown in Fig.9-2, we might be able to estimate a faceted silicon tip temperature from them.

Another key issue remaining in this study is Al grain epitaxial orientations to silicon plates. This is significant because nucleation and growth of the Al phase should be identified to understand polycrystalline grain structure and to develop a strong analytical or numerical model for overall microstructure evolution. Actually, we have gathered enough data to investigate this and the analysis is in progress. Furthermore, a strong analytical model is necessary to predict thermal and diffusional characteristic length scales, namely primary spacing or tip temperature. This model, combined with our volumetric approach to the microstructure characterization, could give a deeper understanding of morphological selection and microstructural evolution of engineering materials. Also, 3-dimensional phase field simulation is strongly recommended for array spacing adjustment, sideplates branching, and Al halo formation behind the growing tip, applying 8-fold crystal symmetry. Finally, Al-Ge and Al-Al_3Fe are suggested for future research to proceed into the research for the faceted crystal growth. These systems have similar hopper-like growth morphologies in their microstructure due to the strong anisotropic interfacial properties of Ge and Al_3Fe. Even though silicon and germanium have been widely used as electronic packaging materials, bicrystals with preferred orientations and regular spacing may give rise to the development of new self-assembled electronic patterns and can be applied for other intermetallic compounds for the improvement of functional composite materials.

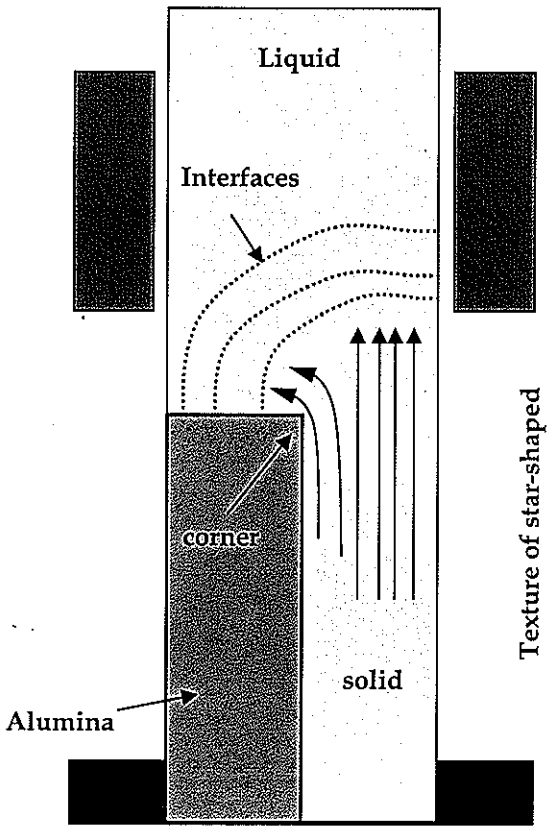

Figure 9-1. Schematic illustration of corner experiments.

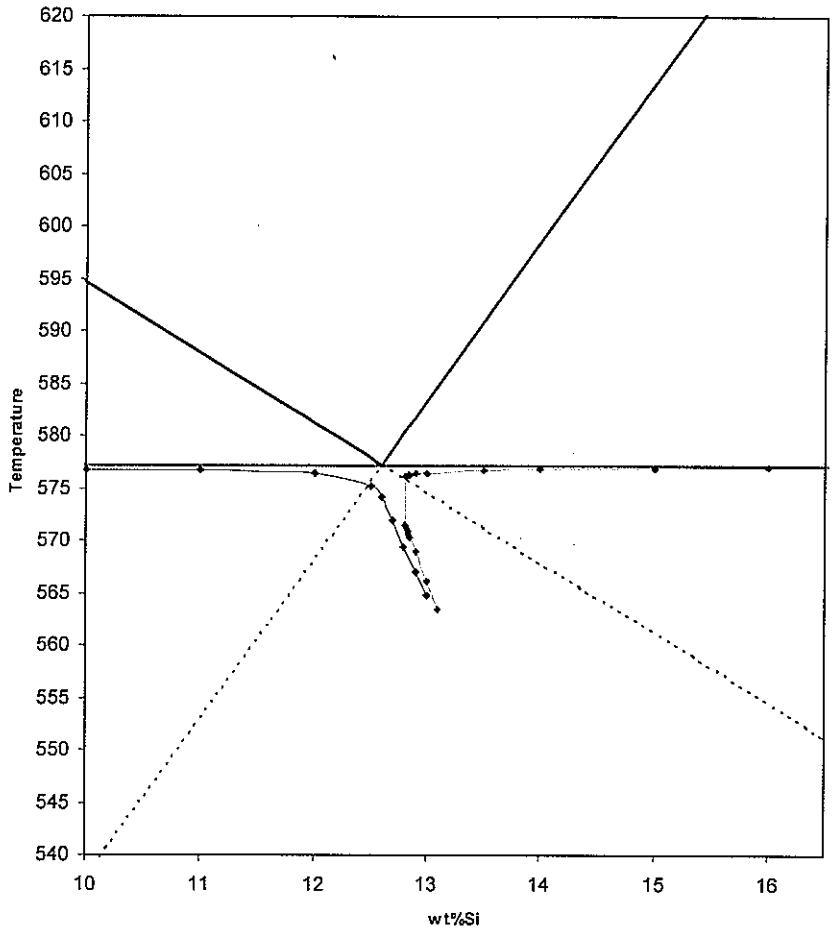

Figure 9-2. Computed coupled zone of Al-Si alloys, using needle like growth for Al and plate-like growth for Si from Kurz and Fisher[113].

REFERENCES

1. W. J. Boettinger, S. R. Coriell, A. L. Greer, A. Karma, W. Kurz, M. Rappaz, and R. Trivedi, Acta Mater. 48, 43 (2000)
2. S. Henry, T. Minghetti, and M. Rappaz, Acta. Mater. 47, 6431 (1998)
3. S. C. Huang and M. E. Glicksman, Acta Metal. 29, 717 (1981)
4. D. Turnbull, J. Chem. Phys. 18, 768 (1950)
5. K. A. Jackson and B. Charlmers, Can. J. Phys. 34, 473 (1956)
6. J. D. Bernal, Pro. Roy. Soc. A280, 299 (1964)
7. R. R. Fessler, R. Kaplow, and B. L. Averbach, Phys. Rev. 150, 34 (1966)
8. A. Filipponi, J. Phys.: Condens. Matter 6, 8415 (1994)
9. T. H. Kim, G. W. Lee, B. Sieve, A. K. Gangopadhyay, R. W. Heyers, T. J. Rathz, J. R. Rogers, D. S. Robinson, K. F. Kelton, and A. I. Goldman, Phys. Rev. Lett. 95, 085501 (2005)
10. J. A. Hayward and A. D. J. Haymet, J. Chem. Phys. 114, 3713 (2001)
11. H. E. A. Huitema, M. J. Vlot, and J. P. van der Eerden, J. Chem. Phys. 111, 4714 (1999)
12. W. J. Briels and H. L. Tepper, Phys. Rev. Lett. 79, 5074 (1997)
13. R. L. Davidchack and B. B. Laird, J. Chem. Phys. 108, 9452 (1998)
14. J. Q. Broughton, A. Bonissent, and F. F. Abraham, J. Chem. Phys. 74, 4029 (1981)
15. J. J. Hoyt, M. Asta, and A. Karma, Phys. Rev. Lett. 86, 5530 (2001)
16. J. A. Hayward and A. D. J. Haymet, J. Chem. Phys. 114, 3713 (2001)
17. D. Turnbull, J. Chem. Phys. 20, 411 (1952)
18. F. C. Frank, Proc. Roy. Soc. London A215, 43 (1952)
19. F. Spaepen, Acta Metall. 23, 729 (1975)
20. F. Spaepen and R. B. Meyer, Scripta Metall. 10, 257 (1976)
21. J. Q. Broughton, A. Bonnissent, and F. F. Abraham, J. Chem. Phys. 74, 4029 (1981)
22. B. B. Laird and D. J. Haymet, J. Chem. Phys 91, 3638 (1989)
23. R. L. Davidchack and B. B. Laird, J. Chem. Phys. 108, 9452 (1998)
24. L. Granasy, M. Tagze, and A. Ludwig, Mater. Sci. Eng. A133, 577 (1991)
25. F. Spaepen, in Solid State Physics, edited by H. Ehrenreich, and D. Turnbull (Academic, New York, 1994), Vol. 47 1-32 (1994)
26. J. W. Gibbs, The Scientific Papers of J. Willard Gibbs, Dover, New York (1961)
27. J. L. Finney, Proc. Roy. Soc. A319, 479 (1970)
28. J. W. Cahn and J. E. Hillard, J. Chem. Phys 28, 258 (1958)

29. J. D. Weeks, G. H. Gilmer, and H. J. Leamy, Phys. Rev. Lett. 31, 549 (1973)
30. J. B. Maxton, D. E. Savage, F. Liu, R. M. Tromp, M. C. Reuter, and M. G. Lagally, Phys. Rev. Lett. 85, 2152 (2000)
31. M. S. Hoogeman, M. A. J. Klik, D. C. Schlober, L. Kuipers, and J. W. M. Frenken, Surface Science 448, 142 (2000)
32. J. M. Kosterlitz and D. J. Thouless, J. Phys. C 6, 1181 (1973)
33. W. K. Burton, N. Cabrera, F. C. Frank, Philos. Trans. R. Soc. London, A243, 299 (1951)
34. J. M. Howe, Interfaces in Materials, John Wiley & Sons, Inc. New York (1997)
35. H. J. Leamy and G. H. Gilmer, J. Crystal Growth 24/25, 499 (1974)
36. M. Wortis, Mater. Sci. Forum 4, 69 (1985)
37. K. A. Jackson, Liquid Metal and Solidification American Society for metals Cleveland, Ohio (1958).
38. K. A. Jacson, Interface Science 10, 159 (2002)
39. K. A. Jackson, Growth and Perfection of Crystals J. Wiley & Sons Inc. New York 319 (1958)
40. C. Herring, in The physics of powder metallurgy, ed. W. E. Kinston, McGraw-Hill, New York, 143 (1951)
41. E. R. Rubenstein and M. E. Glicksman, J. Cryst. Growth 112, 97 (1991)
42. M. E. Glicksman and C. L. Vold, Acta Metall. 17, 1 (1969)
43. W. A. Miller and G. A. Chadwick, Proc. Roy. Soc. A312 257 (1969)
44. D. R. H. Jones, Phil. Mag. 20, 569 (1972)
45. R. J. Schaefer, M. E. Glicksman, and J. D. Ayers, Phil. Mag. 32, 725 (1975)
46. D. R. H. Jones and G. A. Chadwick, Phil. Mag. 22, 291 (1970)
47. M. Gündöz and J. D. Hunt, Acta Metall. 33, 1651 (1985)
48. N. Marasli and J. D. Hunt, Acta Metall. 33 1996 (1985)
49. S. C. Huang and M. E. Glicksman, Acta Metall. 29, 701 (1981)
50. M. E. Glicksman and N. B. Singh, J. Cryst. Growth 98, 277 (1989)
51. M. Muschol, D. Liu, and H.Z. Cummins, Phys. Rev. A 46, 1038 (1992)
52. Shan Liu, R. E. Napolitano, and R. Trivedi, Acta Materialia, 49 4271 (2001)
53. R. E. Napolitano and S. Liu, Phys. Rev. B 70, 1 (2004)
54. R. E. Napolitano, Shan Liu, R. Trivedi, Interface Science 10, 217 (2002)
55. M. E. Glicksman and R. J. Schaefer, J. Cryst. Growth 1, 297 (1967)
56. G. H. Rodway and J. D. Hunt, J. Cryst. Growth 112, 554 (1991)
57. J. Q. Broughton and G. H. Gilmer, J. Chem. Phys. 84, 5749 (1986)

58. W. E. McMullen and D. W. Oxtoby, J. Chem. Phys. 88, 1967 (1988)
59. R. L. Davidchack and B. B. Laird, J. Chem. Phys. 118, 7651 (2003)
60. J. J. Hoyt, M. Asta, and A. Karma, Phys. Rev. Lett. 86, 5530 (2001)
61. J. R. Morris, S. Y. Lu, and K. M. Ho, Interface Science 10, 143 (2002)
62. M. Asta, J. J. Hoyt, and A. Karma, Phys. Rev. B 66, 100101 (2002)
63. J. R. Morris and R. E. Napolitano, J. Metal Apr. 40 (2004)
64. R. L. Davidchack and B. B. Laird, Phys. Rev. Lett. 85, 4751 (2000)
65. J. R. Morris, X. Song, J. Chem. Phys. 116, 9352 (2002)
66. J. Morris, C. Wang, K. Ho, and C. Chan, Phys. Rev. B 49, 3109 (1994)
67. J. Q. Broughton, G. H. Gilmer, and K. A. Jackson, Phys. Rev. Lett. 49, 1496 (1982)
68. F. C. Celestini and J.-M. Debierre, Phys. Rev. B62, 14006 (2000)
69. C. J. Tymczak and J. R. Ray, Phys. Rev. Lett. 64, 1278 (1990)
70. J. J. Hoyt and M. Asta, Phys. Rev. B 65, 214106 (2002)
71. J. J. Hoyt, A. Karma, M. Asta, and D. Y. Sun, J. Metal Apr. 49 (2004)
72. R. Trivedi and W. Kurz, Inter. Mater. Rev. 39, 49 (1994)
73. J. D. Hunt and S. Z. Lu, Metall. Mater. Trans. A 27A, 611 (1996)
74. J. D. Hunt and Q. Han, and S. Z. Lu, Solidification Science and Processing, Edited by I. Ohnak and D. M. Stefanescu, The Minerals, Metals & Materials Society, 87 (1996)
75. J. D. Hunt and S. Z. Lu, Metall. Mater. Trans. A 27A, 611 (1996)
76. J. D. Hunt and Q. Han, and S. Z. Lu, Solidification Science and Processing, Edited by I. Ohnak and D. M. Stefanescu, The Minerals, Metals & Materials Society, 87 (1996)
77. K.A. Jackson and J.D. Hunt, Trans. AIME 236, 1129 (1966)
78. P. Magnin, J.T. Mason and R. Trivedi, Acta Metall., 39 469 (1991)
79. S.-Z. Lu and A. Hellawell, J. Cryst. Growth 73, 316 (1985)
80. L. M. Hogan and H. Song, Acta Metall. 35, 677 (1987)
81. A. Hellawell, Progress in materials science, 15 Editors: B. Chalmers, J. W. Christian, and T. B. Massalski, 3 (1970)
82. Binary Alloy Phase Diagrams 2nd Edition, Vol 1 ASM International 212 (1990)
83. D. J. Fisher and W. Kurz, Solidification and Casting of Metals, Metals Soc. London, 57 (1979)
84. S.-Z. Lu and A. Hellawell, Metall. Trans. *A* 18, 1721 (1987)
85. M. G. Day, *Nature* 219, 1357 (1968)
86. I. Obinata and N. Komatsu, Sci. Rep. Tohoku Univ. A 9, 107 (1957)
87. R. Wang, W. Lu, and L. M. Hogan, Metall. Mater. Trans. A 28, 1233 (1997)

88. H. Fredriksson, M. Hillert, and N. Lange, J. Inst. Met., 101, 285 (1973)
89. O. A. Atasoy, F. Yilmaz, and R. Elliott, J. Cryst. Growth 66, 137 (1984)
90. M. G. Day and A. Hellawell, Proc. Roy. Soc. A305, 473 (1968)
91. M. Shamsuzzoha and L. M. Hogan, Cast Metals 4, 103 (1991)
92. M. Shamsuzzoha and L. M. Hogan, and J. T. Berry, *AFS Transactions 100, 619* (1992)
93. J. A. E. Bell and W. C. Winegard, J. Inst. Metals 93, 318 (1965)
94. M. Shamsuzzoha and L. M. Hogan, Cast Metals 4, 103 (1991)
95. C. C. Chama, J. Mater. Sci. Lett. 17, 1857 (1998)
96. J. W. Faust ,Jr. and H. F. John, J. Phys. Chem. Solids 25, 1407 (1964)
97. T. F. Ciszek, J. Cryst. Growth 10, 263 (1971)
98. F. C. Frank, Disc. Faraday Soc. 5, 48 (1949)
99. S. Kodambaka, S. V. Khare, W. Swiech, K. Ohmori, I. Petrov, and J. E. Greene, Nature 429, 49 (2004)
100. R. P. Liu, W. K. Wang, D. Li, and D. M. Herlach, Scripta Mater. 41, 855 (1999)
101. Y. Shao and F. Spaepen, J. Appl. Phys. 79, 2981 (1996)
102. S. Ansell, S. Krishnan, J. J. Felten, and D. L. Price, J. Phys. 10, L73 (1998)
103. R. P. Liu, D. M. Herlach, M. Vandyoussefi, and A. L. Greer, Metall. Mater. Trans. A 35, 1067 (2004)
104. R. Wang, W. Lu, and L. M. Hogan, J. Cryst. Growth 207, 43 (1999)
105. E. Billing and P. J. Holmes, Acta Metall. 5, 53 (1957)
106. R. S. Wagner, Acta Metall. 8, 57 (1960)
107. D. P. Woodruff, The solid-liquid interface Cambridge University Press (1973)
108. J. Alkemper and P. W. Voorhees, J. of Microscopy, 201, Pt 3. 388 (2001)
109. http://www.edax.com/technology/EBSD/OIM/index.html
110. I. Hornstra, Physica 26, 409 (1959)
111. F. Yilmaz and R. Elliott, Met. Sci. 18, 362 (1984)
112. M. D. Nave, A. K. Dahle, and D. H. StJohn, Acta Mater. 50 2837 (2002)
113. W. Kurz and D. J. Fisher, Inter. Met. Rev. 5 and 6, 177 (1979)